UNIVERSITY OF SOUTHAMPTON

FACULTY OF ENGINEERING AND THE ENVIRONMENT

Engineering Materials Research Group

3D printing of Bone Tissue Engineering Scaffolds and Production of PEEK-based Biocomposites

by

Mohammad Vaezi

Thesis for the degree of Doctor of Philosophy

April 2017

UNIVERSITY OF SOUTHAMPTON

ABSTRACT

FACULTY OF ENGINEERING AND THE ENVIRONMENT

Engineering Materials Research Group

Thesis for the degree of Doctor of Philosophy

3D printing of Bone Tissue Engineering Scaffolds and PEEK-based Biocomposites

Mohammad Vaezi

In this research work, the possibilities and limitations of using solvent-based extrusion freeforming (SEF), a type of additive manufacturing (AM) technologies, for 3D printing of bone tissue engineering scaffolds is examined. Optimised SEF technique allowing production of the highest resolution of bioceramic scaffolds has been reported so far with filament diameter as fine as 30 μm, while retaining reasonable level of detail and accuracy. In vitro tests of the 3D printed hydroxyapatite (HA) scaffolds proved cell attachment and proliferation. The spacing of 200-250 μm between adjacent HA filaments in the scaffold was identified suitable for cell survival, adhesion and proliferation while for blood vessels' integration the pore size should be increased to the region of 350-400 μm. In addition, feasibility of using SEF method for low-temperature 3D printing of highly uniform polylactic acid (PLA)/HA biocomposite scaffolds with varying stiffness was demonstrated and an integrated synthetic bone graft/fracture fixation system was proposed in order to minimise graft migration.

A novel production technique is also outlined in this project that yields a bioactive polyether-ether-ketone (PEEK)/HA composite with a unique configuration in which the bioactive phase (i.e. HA) distribution is computer-controlled within a PEEK matrix. To this end, the relatively fragile 3D printed HA scaffolds were overmoulded with PEEK under optimised pressure, temperature, dwelling time, and loading method. The PEEK/HA biocomposites with different HA volume percentages ranging from approximately 35% to 78% were produced and analysed using computed tomography (CT). The proof of primary cell adhesion, sustained viability in contact with sample surface architecture over a 7 day period, and evidence of cell bridging were strongly supportive of biocompatibility. According to the results, incorporation of extrusion freeformed HA into PEEK eventuates in reduction in mechanical properties, although it enhances cell attachment. However, the biocomposites with HA content of 40 vol.% could survive in one million compression-compression cyclic loading at 30% of their compressive strength without any degradation in compressive properties. The application of these composites can be extended into porous PEEK scaffold, or PEEK microfluidic device, when the interconnected HA phase is removed by socking the composites in hydrochloric acid (HCl).

Direct low-cost extrusion freeforming of biomimetic porous PEEK parts with complicated external geometry and controlled pore size was also demonstrated for the first time in this project. The findings of this study suggest that 3D printed PEEK structures have promising compressive properties with potential for both load bearing and non-load bearing applications. According to the results, the 3D printed solid PEEK specimens with 100% infill rate had 14% porosity and ultimate tensile strength (UTS) of 75.06 MPa that is 33% less than solid injection moulded PEEK. The air gap between infill pattern and entrapped micro-bubbles inside filaments were identified as the main source of mechanical properties degradation. The 3D printed PEEK samples had flexural modulus and strength significantly higher than those various polymers/composites printed using other AM techniques.

Table of Contents

List of Tables

List of Figures

Acknowledgements

I would like to express my deepest gratitude to my project supervisor, Dr Shoufeng Yang, for giving me the opportunity to undertake the responsibility of this project, his constant guidance and support throughout the project. I would also like to thank to Dr Mohamed Moshrefi-Torbati, Prof. Martin Browne and Dr. Bram Sengers for their constructive comments and suggestions for improving my work.

I am grateful to Invibio biomaterial Solutions, Institute for Life Sciences (IfLS), and Faculty of Engineering and the Environments, University of Southampton for their financial support. My great thanks to Prof. Richard Oreffo, Mr. David Gibbs, and Mr. Cameron Black for their invaluable guidance and helps for conducting in vitro and in vivo assessments. I acknowledge the μ-VIS centre at the University of Southampton, and Dr. Orestis L. Katsamenis for provision of tomographic imaging facilities, Dr. Andrew Robinson at the TSRL for provision of mechanical tests, Miss Valeriya Griffiths, Mr. Kavindha Shehan Ratwatte, Mr. Lecheng Yang, and Mr. Gjermund Holm for their great helps.

I would very much like to thank to my family for their supports and all my friends; in particular: Kwan, Lin, Zongqi, Hamed, Fei–Fei, Gregor, Alina, Liping, Kiki, Ben, Simon, and all those I have forgotten to name.

Outcomes of this project

Book Chapter

1. **Vaezi, M.**, Yang, S., 2013. "Freeform fabrication of nano-biomaterials using 3D printing". In, Narayan, R. (ed.) Rapid Prototyping of Biomaterials: Principles and Applications. Woodhead Publishing, Cambridge, UK.
   Online: http://www.sciencedirect.com/science/article/pii/B9780857095992500027

Peer reviewed Journals

1. **Vaezi, M.**, Black, C., Gibbs, D., Oreffo, R., Brady, M., Torbati, M., Yang, S. 2016. "Characterization of New PEEK/HA Composites With 3D HA Network Fabricated by Extrusion Freeforming". Molecules, 21(6):687; doi:10.3390/molecules21060687
2. **Vaezi, M.**, Yang, S., 2015. "Extrusion-based Additive Manufacturing of PEEK for Biomedical Applications". Virtual and Physical Prototyping, 10:123-135
3. **Vaezi, M.**, Yang, S., 2015. "A novel bioactive PEEK/HA composite with controlled 3D interconnected HA network". International Journal of Bioprinting, 1(1): 66-76.
4. Gibbs, D., **Vaezi, M.**, Yang, S., and Oreffo, R., 2014. "Hope versus hype: what can additive manufacturing realistically offer trauma and orthopedic surgery?", Regenerative Medicine, 9,(4), 535-549.
5. **Vaezi, M.**, Chianrabutra, S., Mellor, B., Yang, S., 2013. "Multiple material additive manufacturing – Part 1: a review". Virtual and Physical Prototyping, 8, (1), 19-50.
6. **Vaezi, M.**, Seitz, H., Yang, S., 2013. "A review on 3D micro-additive manufacturing technologies". The International Journal of Advanced Manufacturing Technology, 67, (5-8), 1721-1754.

Conference papers

1. **Vaezi, M.**, Li, Z., Yang, S., Chant, J., Jarman-Smith, M., Wilson, J., 2013. "Novel method for making homogeneous bioactive PEEK compounds using an ultrasonic co-feeding and on-line mixing system". In, 1st PEEK conference, Philadelphia, US, 25-26 April
2. **Vaezi, M.**, Yang, S., Brady, M., 2014. "Extrusion freeformed hydroxyapitite (HA) incorporated into polyether ether ketone (PEEK)". 1st International Conference on Progress in Additive Manufacturing, Singapore, SG, 26 - 28 May
3. **Vaezi, M.**, Kruger, H., Yang, S., 2014. "3D printing of magnetorheological elastomers (MREs) smart materials". 1st International Conference on Progress in Additive Manufacturing, Singapore, SG, May 26-28
4. **Vaezi, M.**, Yang, S., 2014. "3D printing of acoustic metamaterials", 1st International Conference on Progress in Additive Manufacturing, Singapore, SG, 26-28 May

Awards

1. First prize, oral presentation of the paper entitled "High resolution extrusion freeforming of ceramics" at the 21st Joint Annual Conference of CSCST-SCI, Society of Chemical Industry (SCI), University of Surrey, UK. October 2014.

Definitions and Abbreviations

3DP- Three dimensional printing
AM- Additive manufacturing
AWGC- Alumina-wollastonite glass ceramic
BMP- Bone morphogenetic proteins
CAD- Computer-aided design
CFR-PEEK- Carbon fibre reinforced PEEK
CMF- Cranial maxillo-facial
CT- Computed tomography
CTD- Computational Topology Design
DBM- Demineralized bone matrix
DW- Direct writing
ECM- Extracellular matrix
FDA- Food and Drug Administration
FDC- Fused deposition of ceramics
FDM- Fused deposition modelling
FDMM- Fused deposition of multi-materials
HA- Hydroxyapatite
HCL- Hydrochloric acid
hBMSC- Human Bone Marrow Stromal Cells
MDM-Multi nozzle deposition manufacturing
M-LDM- Multi-nozzle low-temperature deposition
MRI- Magnetic resonance imaging
OCP- Octacalcium phosphate
PA- Polyanhydrides
PAEKs- Polyaryletherketones
PAM- Pressure-assisted microsyringe
PBT- Polybutylene terephthalate
PCL- Polycaprolactone
PDLLA- Poly(D, L-lactide)
PED- Precision extrusion deposition
PEEK- Polyether-ether-ketone
PEM- Precise extrusion manufacturing
PEK- Poly(ether ketone)
PEOT- Polyethyleneoxide terephthalate
PGA- Polyglycolide
PGS- Poly(glycerol-sebacate)
PHEMA - Poly (hydroyethyl methacrylate)
pHEMA- Poly(2-hydroxyethyl methacrylate)
PLA- Polylactic acid
PLLA- Poly-L-lactide
PMMA- Poly(methyl methacrylate)
POC- Poly (1,8) octane diol citrate
PPF- Polypropylene fumarate
RP- Rapid prototyping
RPRD- Rapid prototyping robot dispensing
SEF- Solvent-based extrusion freeforming
SFF- Solid freeform fabrication
SL- Stereolithography
SLS- Selective laser sintering
TE- Tissue engineering
TTCP- Tetracalcium phosphate
u-HA- Non-calcined/non-sintered HA
UHMWPE-Ultra-high-molecular-weight polyethylene
UTS- Ultimate tensile strength
β-TCP - β-tricalcium phosphate

List of Symbols

α Velocity-dependent factor for convergent flow (Pa s m^{-1})

β Velocity-dependent factor for parallel flow (Pa s m^{-1})

σ_o Initial bulk yield stress of the paste (Pa)

τ_o Initial paste-die wall shear stress (Pa)

V Mean extrudate velocity (m s^{-1})

P Extrusion pressure (Pa)

P_1 Pressure drop due to the change in cross-sectional area (Pa)

P_2 Pressure drop in die (Pa)

D Die diameter (m)

Do Syringe's barrel internal diameter (m)

L Die land length (m)

m Coefficients to take account of non-linear behaviour of paste

n Coefficients to take account of non-linear behaviour of paste

Chapter 1

Project Overview

Chapter 1: Project Overview

1.1 Additive Manufacturing of Tissue Engineering Scaffolds

In general, bones can regenerate most simple injuries relatively quickly (for instance a broken wrist in an adult should heal completely within 6–8 weeks), however, this is only the case provided the fracture is no more than a few millimetres in width, otherwise surgical intervention may be necessary. In such cases, several grafting procedure routes are possible: an autograft is taken from another part of the patient's own body (e.g. the hip); an allograft is taken from a donor's body; while synthetic implants can be made from biocompatible material with mechanical and structural properties similar to those of bone **(Griffiths V., 2013)**.

Using an autograft is currently considered to be the most effective method, due to its relatively low risk of rejection and disease transmission. However, this means the patient will have an additional surgical site, resulting in added discomfort and pain, as well as additional strain on the patient's body and possible extended recovery time. The additional surgical operation and complexity may also result in overall increased cost of the procedure **(Greenwald A.S. et al., 2003, Griffiths V., 2013)**.

Using an allograft eliminates all the above disadvantages. However, the chances of finding a matching bone donor in the necessary time frame are small and so allograft bone normally comes from tissue banks, having been previously harvested from cadavers. This presents obvious storage issues and storage time limitations. To reduce the risk of disease transmission the bone is disinfected and cleaned, though risk of infection is still slightly greater than it is for autografts, since standard sterilization processes are harmful to living tissue and so it cannot be disinfected to the same level as medical equipment. As a result of disinfection and storage processing, allograft bone may lack the growth-promoting cells and proteins found in autografts, and may see a reduction in mechanical strength. The risk of the patient's body rejecting an allograft transplant is also slightly greater, compared to autograft bone **(Griffiths V., 2013)**.

Since there are disadvantages to both autograft and allograft methods, a lot of research has been put into synthetic graft alternatives, which include certain metals and ceramic, coral, and graft composites. A bone tissue engineering (TE) scaffold is a highly porous artificial three dimensional (3D) structure made from biologically suitable materials to accommodate living cells which are seeded onto the scaffold. Its main role is to provide structural support and a favourable environment for these cells as they form new bone tissue.

Additive manufacturing (AM) technologies, aka 3D printing, have been extensively used for fabrication of synthetic TE scaffolds. AM technologies are automated techniques that can simply fabricate 3D structures with controlled internal and external geometry layer-by-layer using computer-aided design (CAD) file. Initially, these technologies were used for product design & development and rapid prototyping due to their significant

reduction in lead time and cost, while in recent years their applications have been expanded to high-value production and specialized manufacturing. A large number of AM processes have been developed allowing the use of various materials ranging from plastics and metals to advanced ceramics and composites for various industries **(Chua et al., 2014)**.

The AM technologies play an increasingly important role in the biomedical industry so that medical and dental has established itself as a strong sector for AM. The AM techniques have been used within medical/dental area for the production of assistive, surgical and prosthetic devices, customized surgical implants, dental implants, drug delivery devices, and TE scaffolds **(Chua et al., 2014)**. The use of these technologies for the manufacture of TE scaffolds is widely explored as they can overcome limitations of conventional porous material manufacturing methods (such as solvent casting/salt leaching and phase separation) in terms of geometry, and process consistency **(Yang et al., 2001)**. The additive nature of the AM processes ensures minimal waste of biomaterial and makes it suitable for mass production of scaffolds, multiple material porous bioactive structures **(Vaezi et al., 2013a),** and micro-scale woodpile structures **(Vaezi et al., 2013b)**. Extrusion-based and droplet-based AM systems have been developed specifically for processing of biological materials which are called "bio-printers". The bio-printers can deposit various biopolymers, hydrogels, and encapsulated multiple cell types in hydrogels to produce 3D bioconstructs with unique biological features.

1.2 Bioactive and Porous PEEK

Polyether-ether-ketone (PEEK) is a semi-crystalline thermoplastic which is an excellent alternative for metal biomaterials as it has good biocompatibility **(Sagomonyants et al., 2008)**, with no cytotoxic effects in vivo **(Rivard et al., 2002)**, and mechanical strength **(Edwards et al., 2010)**. Elastic modulus similar to cortical bone, high biostability, great resistance to compressive loading with reducing stress shielding, and radiolucency allowing clear fusion assessment are the main features which have made PEEK suitable for orthopaedic applications. Medical grade PEEK-OPTIMA has been developed by Invibio Biomaterial Solutions (Thornton-Cleveleys, UK) to meet the US Food and Drug Administration's (FDA) requirements and has been used in multiple clinical applications including spinal cage fusion and craniomaxillofacial (CMF) reconstruction **(Toth et al., 2006, Rao et al., 2014)**.

Despite possessing favourable biomaterial properties, PEEK is relatively bioinert, demonstrating poor osseointegration (i.e. infiltration of bone cells into the structure of PEEK implant) following implantation. Lack of bio-integration can result in graft migration, and failure of the reconstructive procedure. To overcome this problem, a lot of research has been put into production of PEEK biocomposites (e.g. PEEK and calcium

phosphates), surface modification, coating PEEK implants with bioactive materials, and creating porous PEEK structures for better bone in-growth and osseointegration.

Calcium phosphates including hydroxyapatite (HA) (the primary mineral component of natural bone) and β-tricalcium phosphate (β-TCP), or Bioglass are utilised as a composite filler to produce PEEK compounds **(Ma and Tang, 2014, Li et al., 2014).** In fact, the addition of bioactive fillers into PEEK is an efficient strategy to improve biological performance and surgical function of PEEK-based implants, although it can have adverse effects with regard to mechanical strength **(Roeder and Conrad, 2012)**.

In addition to incorporation of the bioactive fillers into PEEK, the use of biomimetic porous PEEK implants with a structure that is physically closer to the natural bone has been identified useful method to improve fixation of PEEK-based implants and devices **(Jarman-Smith et al., 2012)**.

1.3 Aims and Objectives

There are a number of publications on application of extrusion-based AM techniques to process various biomaterials from soft (e.g. hydrogels) to hard (e.g. ceramics) materials for different biomedical applications. These results have proved that this low-cost AM method offers a good control on macro/microarchitecture, and guarantees the pore interconnectivity. Solvent-based extrusion freeforming (SEF) process, first developed by Evans and Yang **(Yang et al., 2008c, Lu et al., 2009d, Lu et al., 2010, Lu et al., 2009b, Lu et al., 2009c, Lu et al., 2009a, Lu et al., 2008, Yang et al., 2008b, Lu et al., 2012a, Yang et al., 2006, Yang et al., 2008a)**, has been used for low-temperature 3D printing of ceramic lattice structures with controlled filament/pore size and distribution. In this method, solidification is based on solvent evaporation upon material deposition which has advantages over similar techniques. The technique can deliver very fine filaments and avoids the thermal management issues of other extrusion-based techniques. The versatility of SEF method is not just in terms of structure and filament size but its capability to process various high-demanding ceramics (such as zirconia, alumina, HA, β-TCP, Bioglass, etc.) to serve different applications. However, there is still demand for more in-depth research on SEF process and problems which will be addressed in this project:

- There is no further quantitative information about sintering-induced porosity and qualitative information about microscopic defects such as micro-cracks of printed ceramic parts
- There is very few quantitative information about sintering-induced shrinkage and uniformity of the printed scaffolds
- There has been no in-depth study on effective parameters in SEF process, characterizing ceramic pastes using analytical and experimental methods, and extrusion analysis

- It has been a great challenge to increase printing resolution while the higher resolution can expand the applications of SEF process
- *In vitro* and *in vivo* tests has not been done on the printed ceramic scaffolds using SEF process to assess biocompatibility and cell attachment
- The application of biopolymer/bioceramic materials in SEF process has not been explored with the aim of tailoring mechanical properties of printed scaffolds

Here are the main contributions of this project to the field:

- The initial goal of this project focused on providing consistent and high-quality bone scaffolds using SEF method and verifying previous findings. A 'good' scaffold would demonstrate well defined and even filaments, consistent pore sizes and distribution, as well as uniform overall geometry of scaffold layers
- This project also aimed to increase the amount of available data by conducting computed tomography (CT) analysis, measuring micro-porosity, and evaluations of microscopic defects
- The next objective was to expand recorded knowledge of the SEF method by characterization of HA paste and optimising the production process with the aim of printing ceramic scaffolds with the highest resolution has been reported so far, while retaining reasonable level of uniformity and accuracy
- Further works was also planned to be performed with regard to both scaffold material composition and geometry, specifically, examining the feasibility of low-temperature 3D printing of polylactic acid (PLA)/HA biocomposite scaffolds with excellent uniformity, and development of integrated synthetic bone graft/fracture fixation system.
- This project also provides additional information on biological performance of the HA scaffolds 3D printed using SEF method by conducting biomedical *in vitro* and *in vivo* tests

As discussed earlier, different methods of bioactive PEEK processing are currently used effectively with the aim of improving osseointegration and biological performance. Each of these methods has different advantages and disadvantages which may be best suited to a particular biomedical sector. However, there are some obstacles that limit their application:

- The current methods of bioactive PEEK processing do not permit control on distribution of bioactive phase within the PEEK matrix. These techniques rely on simple mixing of PEEK with bio-active material powders/granules, and thus less control on distribution.
- In addition, the wide range of physical properties of different particles (size, shape, density) negates efficient and consistent mixing, and thus process consistency
- A few techniques can be used to incorporate both porosity and bioactivity into PEEK

- Limitation on amount of bioactive filler loading
- Limitation on interconnectivity of both bioactive network and PEEK

A novel PEEK processing is proposed in this project to address the above limitations. **Figure 1.1.** depicts workflow of the technique used in this project to make both bioactive PEEK/HA composite and porous PEEK structure. It comprises low-temperature 3D printing of porous bioactive scaffolds using SEF method, followed by PEEK melt infiltration into the scaffolds through the compression moulding process (procedure 1 in Fig. 1.1). Here are the main contributions of this project to the field:

- Development of a novel technique that would permit greater control on incorporation of bioactive materials into PEEK than the existing techniques.
- The proposed technique integrates extrusion-based AM (in this project SEF method) and compression moulding processes to produce bioactive PEEK/HA composite.
- The approach enables designers to control precisely the distribution of bioactive phase within the PEEK matrix and hence tailor biological and mechanical properties of the final composite.
- In addition to PEEK/HA composite, the proposed technique can be served to produce porous PEEK structures with fully interconnected pores with controlled size and distribution.
- Both bioactive phase and PEEK matrix are fully interconnected, which is superior to existing microstructural designs.
- This is the first report of PEEK/HA composite displaying 100% interconnectivity of the bioactive HA network phase.
- Although HA as a well-known osteoconductive material was used in this research work, the technique is versatile such that a range of bioactive materials such as Bioglass and β-TCP with different rates of biodegradation can be used. The interconnected bioactive network can be fully absorbed in vivo, leaving 3D interconnected channels for further in-growth and proliferation. Thus, a 3D locked bone–PEEK structure could be achieved in vivo which can dramatically improve implant fixation compared with existing techniques
- The PEEK/HA composite produced can be used directly with the HA bioactive phase inside. Alternatively, it can be further soaked into hydrochloric acid (HCl) solution to remove the HA network and produce a fully interconnected porous PEEK. Clearly, when this alternative process is used to produce porous PEEK, HA can be replaced with other solvent soluble materials. This is also the first report on fully interconnected porous PEEK structure with controlled pore size, porosity, and channel direction and distribution

The other objective of this research work was to develop a low-cost extrusion freeforming technique for direct high-temperature 3D printing of porous PEEK which can create a more durable and biomimetic material with potential clinical application

(procedure 2 in Fig. 1.1). The device needs to be able to print highly uniform porous PEEK with great reproducibility and control on porosity. This provides more design freedom to designers of PEEK-based biomedical or microfluidic devices than current porous PEEK manufacturing techniques.

As is documented both HA and PEEK are biocompatible but it is not known if the new proposed method of PEEK/HA sample preparation in this project, maintains or perhaps improves biocompatibility. Any improvements should be demonstrated with further comprehensive in vivo testing including various controls utilizing previously described PEEK and HA manufacturing methods. The focus in this project is merely on preparation of the PEEK/HA samples, and in vitro cell compatibility and growth over a short period of time.

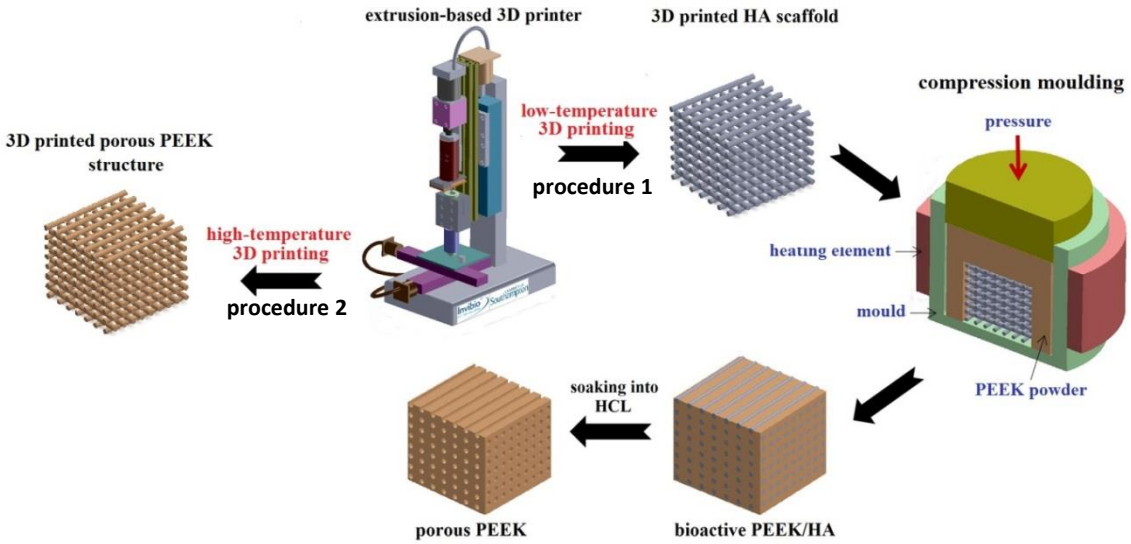

Figure 1.1 Process steps to produce bioactive PEEK/HA composite and porous PEEK

The outlined objectives of this PhD project can be summarised as follows:

- To Modify/programme the existing 3D stage suitable for low-temperature extrusion freeforming of TE scaffolds from bioceramics such as HA, alumina, zirconia, etc.
- To provide consistent and reproducible scaffold samples with different filament/pore sizes using various materials, and characterize the scaffolds using CT analysis
- To optimise and document the SEF process for production of very high resolution ceramic lattice structures
- To provide preliminary data on low-temperature printing of PLA/HA scaffold, and design suggestions for development of bone scaffolds integrated with fracture fixation system
- To assess the biological performance of the 3D printed HA scaffolds for further use in production of the bioactive PEEK/HA

- To infiltrate the 3D printed HA scaffolds with PEEK through an optimized compression moulding process
- To produce porous PEEK by socking the PEEK/HA into HCl solution
- To characterize the produced PEEK/HA composite and porous PEEK using scanning electron microscope (SEM), CT, laser profilometer, etc.
- To study mechanical properties of the produced PEEK/HA composites
- To develop a high-temperature 3D printer suitable for direct low-cost extrusion freeforming of porous PEEK structures
- To determine applicable nozzle temperature range for successful 3D printing of PEEK parts without defects such as warpage and delamination
- To study mechanical properties of the 3D printed PEEK

This project has been built on established relationships between the University of Southampton's Faculties of Engineering and the Environment, and the industrial partner, Invibio Ltd. which is the market leader in providing PEEK-based biomaterial solutions to medical device manufacturers around the world.

In chapter 1, a brief introduction to extrusion-based 3D printing and different PEEK processing techniques is presented and the main objectives of this project are specified. In chapter 2, a literature review is presented to establish the state–of–the–art of the technology and background knowledge of the extrusion-based AM and bioactive PEEK-based composites, thereby providing insights for the project objectives, experimental design, and interpretation of the results. In chapter 3, the application of SEF technique in low-temperature production of lattice structures is investigated. High accuracy lattice structures printed from various highly demanded ceramics such as alumina, zirconia, and HA for tissue engineering application are demonstrated in this chapter. In addition, ceramic paste characterization using Benbow's model are discussed in this chapter. An exploration on paste formulation suitable for low-temperature 3D printing of PLA/HA scaffolds and the *in vitro* tests on the 3D printed HA scaffolds using SEF method are presented in this chapter. In chapter 4, the new technique for production of bioactive PEEK/HA composite and porous PEEK is presented and preliminary evidence supporting initial biological safety of the new technique developed is demonstrated in this chapter. In chapter 5, successful extrusion AM of medical grade PEEK structures is reported for the first time with in-depth discussion on extrusion system, the main challenges, and the process parameters need to be adjusted. Furthermore, mechanical properties of the extrusion freeformed porous PEEK parts are investigated for the first time in this chapter. Chapter 6 presents the principal conclusions and major findings for this research work.

Chapter 2

Literature Review

Chapter 2: Literature Review

2.1 Additive Manufacturing

General reviews and books on AM processes have emerged over the past three decades which varied considerably in scope and methods of classification **(Pham and Dimov 2000, Gebhardt 2003, Tay et al. 2003, Hopkinson et al. 2006, Liou 2007)**. Chua and co-authors' book **(2010)** has kept tracing the development of Rapid Prototyping (RP) technology and its applications in industry and has now been revised in the fourth edition. Fundamentals and the working principle behind the various AM systems are clearly explained and illustrated. Wohler's report **(Wohlers, 2015)** is updated every year and provides broad and timely information though with less academic depth. Some reviews and books have been presented in the fields of medical AM **(Bartolo and Bidanda 2008, Bartolo et al. 2012, Yang et al., 2001, Melchels et al. 2012, Gibbs et al., 2014, Gibson 2006)**. Vaezi et al. **(2012)** presented a comprehensive review on 3D micro-additive manufacturing technologies and their recent developments toward "rapid micro-manufacturing". Gibson and co-authors **(2010)** have a short chapter in their book which provides a review on multiple material additive manufacturing (MMAM), while a broader and updated review on MMAM was further published by Vaezi and co-authors **(Vaezi et al., 2013a)**. Oxman **(2011)** focused on variable property RP (VPRP) in which functional components can be printed by dynamically mixing, grading and varying the ratios of material properties. Her proposed approach can be used in production of biomimetic scaffolds as the human tissues are multi-material hierarchical structures. The approach can be used to produce functional bio-constructs with continuous gradients, highly optimized to fit their biological and mechanical performance with efficient use of biomaterials, reduction of waste and production of highly customizable features with added functionalities. In particular, her proposed novel software approach entitled Variable Property Modelling allows designers to create structural bio-components defined by their desired biomaterial behaviour.

The field of AM encompasses a variety of unique processes, with varying characteristics, which were previously categorized by several researchers. AM technologies have been standardized and classified by the American Society for Testing and Materials (ASTM) International Committee F42 on AM technologies. The committee has classified AM processes and their variants into seven main categories including: vat polymerization, powder bed fusion, directed energy deposition, sheet lamination, material jetting, binder jetting, and material extrusion (which is subject of this study) **(Stucker 2011)**. Several AM techniques have been modified to work at a small scale to deposit passive electronic structures and components (conductors, insulators, resistors, antennas, integrated circuit (IC), etc.). These techniques are often known as direct writing (DW) **(Stucker, 2011)**. An overview of the various AM processes based on the ASTM standard, their specifications and medical applications is provided in **Table 2.1**.

Table 2.1 Various AM technologies classified by ASTM international committee F42 **(Stucker 2011, Vaezi et al., 2014)**

Process	Description	Typical AM techniques	Advantages	Disadvantages	Applications	Living cells /growth factors
Vat polymerization	Liquid photopolymer is selectively cured using a light source	SL, 2PP	High-dimensional accuracy, offering transparent materials	Only photopolymers, single composition, cytotoxic photoinitiator, incomplete conversion thus postcuring required, limited cells for incorporation, nonhomogeneous cell distributions	Printing clinical implants and surgical guides, tissue engineering scaffolds, 3D micro-vasculature networks, biological chips, cell-incorporated 3D biological constructs	Yes
Binder jetting	Liquid bonding ink is selectively spread to join solid powder material	3DP	Low-temperature process, rapid process, multiple compositions	Requirement of powder, high porosity, low surface quality, accuracy limited by the particle size of materials, powder entrapment, cell-challenging environment	Printing clinical implants and tissue-engineering scaffolds	No
Powder bed fusion	Thermal energy selectively fuses regions of powder bed material	SLS, SLM, EBM, SMS	Wide range of materials, great material properties, high material strength	Thermal stress, degradation, accuracy limited by the particle size of materials, requirement for atmosphere control for metals	Printing surgical implants with complex internal and external structures, tissue-engineered scaffold, medical devices	No
Material extrusion	Material is selectively dispensed through a nozzle or extruder	Melting extrusion: FDM, PED, MJS, 3D fiber deposition	Rapid, no toxic materials, good material properties	Low-dimensional accuracy, delamination, weak bonding between dissimilar polymers	Printing clinical implants, tissue-engineering scaffolds	No
		Extrusion without melting: PAM, 3D bioplotting, SEF, LDM, robocasting, direct-write assembly	Simple and cheap mechanism, no trapped materials, low material waste, fairly high fabrication speed, cell-friendly	Relatively low-dimensional accuracy and mechanical strength, solvent is sometimes used, precise control of ink rheology is crucial	Printing tissue-engineering scaffolds, cell-incorporated 3D biological constructs, organ bioprinting	Yes
Sheet lamination	Material sheets are bonded together and selectively cut in each layer to create a desired 3D object	LOM, UC	Low-temperature effects	Shrinkage, significant amount of waste, delamination	Printing orthopedic implants	No
Directed energy deposition	Focused thermal energy melts materials as deposited	LENS, DMD, LC	Wide range of materials, good material properties	Low-dimensional accuracy, thermal stress, requirement for atmosphere control, requirement for machining process for finishing the part	Printing orthopedic implants	No
Material jetting	Droplets of build material are selectively deposited layer by layer	DoD inkjet printing, PJT	Rapid process, wide range of biomaterials, yet jettable materials, use of existing inexpensive technology, multiple compositions, multicell printing	Nozzle blockage an issue, low viscosity prevents build-up in 3D, low strength	Printing clinical implants and surgical guides, printing tissue-engineering scaffolds, printing cell incorporated biological constructs, organ bioprinting	Yes

2PP: Two-photon polymerization; 3DP: 3D printing; DMD: Directed metal deposition; DoD: Drop-on-demand; EBM: Electron beam melting; FDM: Fused deposition modeling; LC: Laser cladding; LENS: Laser engineering net shape; LOM: Laminated object manufacturing; MJS: Multiphase jet solidification; PAM: Pressure-assisted microsyringe; PED: Precision extrusion deposition; PJT: PolyJet technology; SL: Stereolithography; SLM: Selective laser melting; SLS: Selective laser sintering; SMS: Selective mask sintering; UC: Ultrasonic consolidation.

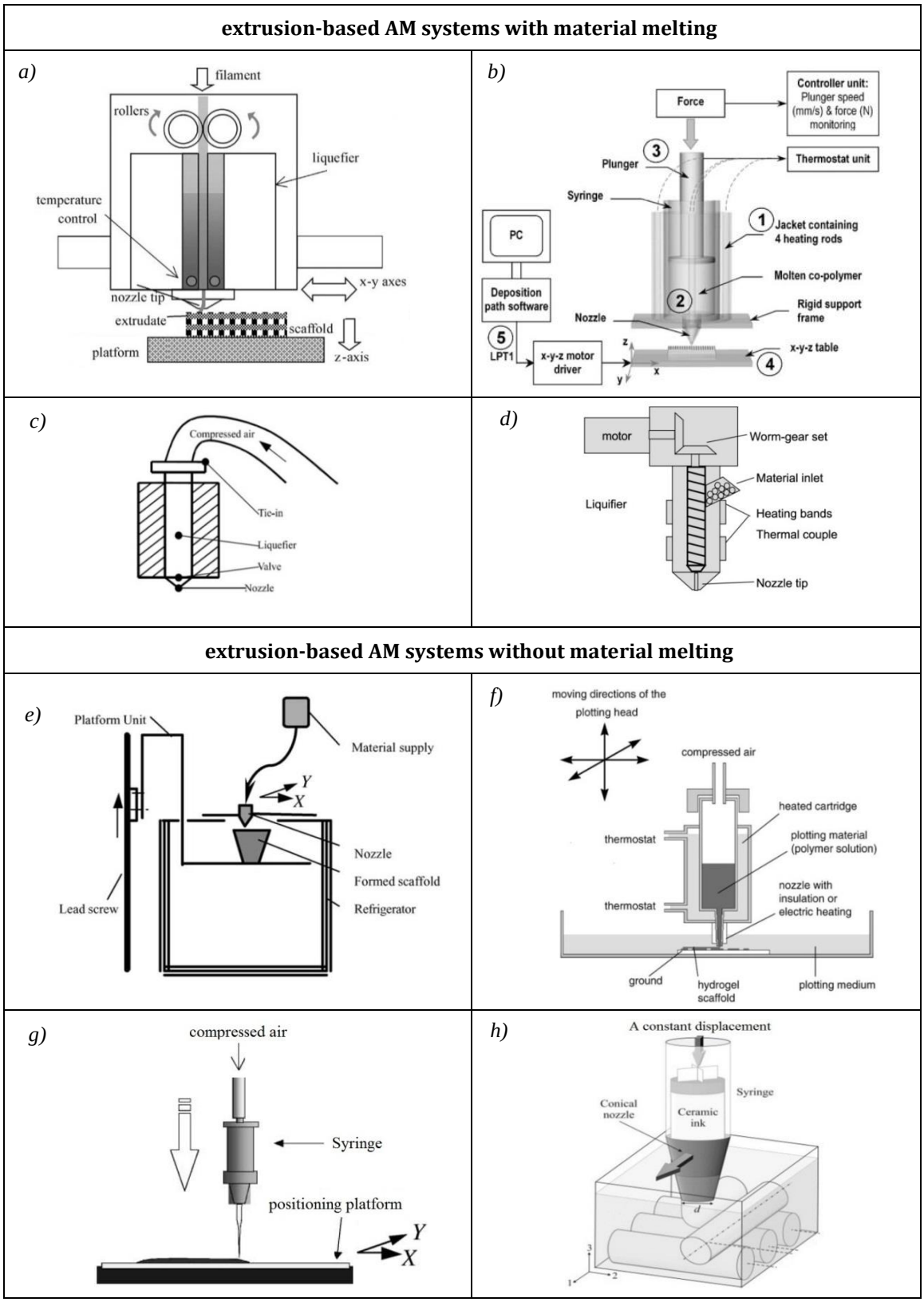

Figure 2.1 Schematic illustration of different extrusion-based AM systems, including processes with and without material melting: **(a)** FDM process **(Zein et al., 2002)**, **(b)** 3D fiber deposition process **(Woodfield et al., 2004)**, **(c)** PEM process **(Xiong et al., 2001)**, **(d)** PED process **(Wang et al., 2004)**, **(e)** LDM process **(Zhuo et al., 2002)**, **(f)** 3D bioplotting process **(Landers et al., 2002)**, **(g)** pressure-assisted writing processes such as PAM and direct-write assembly techniques **(Vozzi et al., 2002)**, **(h)** paste extrusion techniques such as robocasting and SEF techniques **(Miranda et al., 2008)**

The application of the material extrusion AM systems comprising a movable extrusion head controlled by computer has spawned a range of construction methods. In these processes, continuous flow of materials in form of paste or thick ink is dispensed layer-by-layer using the extrusion nozzle(s) incorporated with a 3D motion system. Much attention have been paid to material extrusion AM systems in tissue engineering in recent years as they are mechanically simple in comparison to other AM techniques and a wide range of biomaterials can be processed effectively. The material extrusion systems are classified into two main sub-groups as seen in **Table 2.1**: processes based on material melting and processes without material melting **(Vaezi and Yang, 2014)**. Fused deposition modelling (FDM), precision extrusion deposition (PED) **(Wang et al., 2004)**, 3D fiber deposition **(Woodfield et al., 2004)**, precise extrusion manufacturing (PEM) **(Xiong et al., 2001)**, and multiphase jet solidification (MJS) **(Greulich et al., 1995)** are AM techniques based on melting process. Pressure-assisted microsyringe (PAM) **(Vozzi et al., 2002)**, low-temperature deposition manufacturing (LDM) **(Zhuo et al., 2002)**, 3D bioplotting **(Landers and Mulhaupt, 2000)**, robocasting **(Cesarano, 1999)**, direct-write assembly **(Smay et al., 2002)**, and SEF **(Grida and Evans, 2003)** are the most commonly used AM techniques without material melting. Four major nozzle designs have been exploited in non-heating processes: pressure-actuated, volume-driven injection nozzles (normally using a stepper-motor), solenoid and piezoelectric-actuated, whereas two main nozzle designs, namely, filament driving wheels and mini-screw extruder have been used in processes with material melting **(Vaezi et al., 2013a)**. **Fig. 2.1** illustrates the working principle of the key extrusion-based methods schematically. A broader review on extrusion-based methods and their application in biofabrication of TE scaffolds will be presented further in section 2.3.

2.2 Tissue Engineering Scaffolds

One of the standard routines behind TE includes developing cells in vitro into the required 3D organ or tissue. Cells can not inherently develop in favoured 3D structures and characterize the anatomical state of the tissue however they arbitrarily relocate to frame a two-dimensional (2D) layer of cells. Scaffold is a permeable structure that functions as a synthetic extracellular matrix (ECM), which allows cell to develop in favoured directions and encourages cell attachment, expansion, and differentiation **(Sachlos and Czernuszka, 2003)**. One of the most important challenges in tissue engineering is to design and manufacture an ideal scaffold. Several aspects should be taken into consideration in the design of scaffolds for tissue engineering. The scaffolds need to be made from a biocompatible material with sufficient porosity to allow the infiltration of cells and nutrients and removal of waste materials, and possess an appropriate surface chemistry for cell attachment and growth **(Yang et al., 2001)**. In addition to mimic the structure and biological functions of ECM, TE scaffolds should provide a proper stress environment for the neotissues by their appropriate mechanical properties. Two

main aspects for scaffold design are material and macro/microstructure which are discussed further.

2.2.1 TE Scaffold Materials

Selection of suitable biomaterials for fabrication of TE scaffolds is an important design step since the scaffold characteristics are determined by the inherent properties of the scaffold materials. Three main biological requirements for scaffold material are **(Yang et al., 2001)**:

- Biocompatibility: not to stimulate any unwelcome tissue response to scaffold
- Bioactivity: possessing an appropriate surface chemistry to assist cell adhesion and proliferation and integration with surrounding tissues
- Biodegradability: being able to be decomposed into non-toxic products after specific period of time

The TE Scaffolds are normally produced from metals, biopolymers, bioceramics, and their composites. Bioceramics such as calcium phosphate family including HA, β-TCP, and bioactive glasses have demonstrated a good bioactivity and biocompatibility which are widely served as artificial bone matrix and filler material for bone injury repair. Bioceramics suitable for TE scaffolds can be classified into three main groups: bioinert ceramics such as alumina and zirconia; bioactive ceramics such as Bioglass, sintered HA (s-HA), alumina-wollastonite glass ceramic (AWGC); and biodegradable ceramics such as non-calcined/non-sintered HA (u-HA), α or β-TCP, tetracalcium phosphate (TTCP), octacalcium phosphate (OCP). The rate of their biodegradation is in the following order: OCP>α-TCP>β-TCP>u-HA **(Yang et al., 2001).**

Natural polymers including chitosan, glycosaminoglycan, collagens, starch, and chitin have been exploited for regeneration of different tissues such as cartilage, bone, nerves and skin. While naturally occurring biomaterials may most closely simulate the native cellular milieu, large batch-to-batch variations upon isolation from biological tissues is the main limitation for their wide applications **(Vaezi and Yang, 2014).** In addition, scaffolds made from natural polymers such as collagen and chitin have shown insufficient mechanical properties. To complement these limitations, synthetic resorbable biopolymers such as polyphosphazens, polyanhydrides, poly (a-hydroxy ester)s, and polyorthoesters are being used. Polyglycolic acid (PGA), PLA, polycaprolactone (PCL), polyanhydrides (PA), polyorthoesters, and polydioxanone are biodegradable synthetic polymers which have been used for years in surgical sutures, and have a long and proved clinical record. Some biodegradable polymers such as poly-L-lactide (PLLA) can be used in composite systems with bioceramic fillers due to their initial high strength. PLLA and PGA exhibit a high degree of crystallinity and degrade relatively slowly, while copolymers of PLLA and PGA (i.e. PLGA) are amorphous and degrade rapidly **(Yang et al., 2001).** Scaffolds made from some other biodegradable polymers such as polypropylene fumarate (PPF), poly (1,8-octanediol–co-citrate) (POC), and poly(glycerol-sebacate) (PGS) have exhibited good mechanical properties. **Table 2.2** shows properties of some biodegradable polymers.

Hydrogels are also used for tissue regeneration scaffolds which are biodegradable biomaterials in form of a colloidal gel in which water is the medium of dispersion and is formed by the cross-linking network of hydrophilic polymer chains **(Bartolo and Bidanda, 2008, Nguyen and West, 2002)**. Hydrogels are normally formulated from a wide range of materials including silicon, cellulose derivatives, poly (vinyl alchol), poly (ethylene glycol), calcium alginate and the most widely used poly (hydroyethyl methacrylate) PHEMA **(Bartolo and Bidanda, 2008)**.

Despite the favourable biological properties of biopolymers highlighted above, they are relatively ductile and not rigid enough for some tissue engineering applications. Scaffolds with mechanical properties more comparable with load bearing tissues can be obtained by combining ductile biopolymers with bioceramics which are too stiff and brittle by themselves **(Yang et al., 2001)**.

Table 2.2 Properties of some biodegradable polymers suitable for TE scaffolds **(Yang et al., 2001)**

Polymer	Melting point (°C)	Glass trans. temp. (°C)	Degradation time (months)*	Density (g/cm^3)	Tensile strength (MPa)	Elongation (%)	Modulus (GPa)
PLGA	Amorphous	45-55	Adjustable	1.27-1.34	41.4-55.2	3-10	1.4-2.8
DL-PLA	Amorphous	55-60	12-16	1.25	27.6-41.4	3-10	1.4-2.8
L-PLA	173-178	60-65	>24	1.24	55.2-82.7	5-10	2.8-4.2
PGA	225-230	35-40	6-12	1.53	>68.9	15-20	>6.9
PCL	58-63	65	>24	1.11	20.7-34.5	300-500	0.21-0.34

*Time to complete mass loss

Biocompatible metals such as stainless steels, cobalt-based and titanium-based alloys have also been employed extensively for different biomedical applications such as surgical implants. However, lack of biodegradability and low level of processability are two main obstacles for tissue engineering applications. Thus, polymers and polymer/ceramic composites are considered as the main current biomaterials for TE scaffold applications.

2.2.2 TE Scaffold's Macro/Microstructure Design

Both macro and microstructure of scaffolds need to be designed based on the desirable performance and application. Scaffold may have simple or complicated macrostructure depending on the application. For example, the macrostructure of the scaffold can be complicated when reconstruction of a damage organ/tissue of patient is desired. In such cases the macrostructure is designed based on acquired medical images such as magnetic resonance imaging (MRI) or CT scans.

Microstructure (e.g. porosity and pore size) of the scaffold is the factor that affects the regeneration of specific tissues using synthetic substances. Basically, cell attachment and in-growth is promoted by increasing surface area. Highly porous scaffolds are favourable for improving nutrients diffusion and removing waste products and more efficient vascularization. In particular, mass transport (that is permeability and diffusion) control is a momentous issue since the high rates of nutrient and oxygen transfer at the surface of the scaffold promote the mineralization of the scaffold surface, further limiting the mass transfer to the interior of the scaffold **(Sachlos and Czernuszka, 2003).** Thus cells would be only able to survive close to the surface. Using larger pore size in the external areas of the scaffold would not be an efficient strategy as it may result in reduction in mechanical properties of the bone scaffolds.

The minimum pore size of scaffold is usually defined by the diameter of cells in suspension which differ from one cell type to another. Experiments provide optimum pore size of 5 μm for neovascularization, 5–15 μm for fibroblast in-growth, close to 20 μm for the in-growth of hepatocytes, 20–125 μm for regeneration of adult mammalian skin, 40–100 μm for osteoid in-growth, and 100–350 μm for regeneration of bone **(Yang et al., 2001).** For rapid vascularization and survival of transplanted cells fibrovascular tissues pore sizes bigger than 500 μm is suggested **(Wake et al., 1994).** Interconnectivity of pores within scaffold is another important issue that should be taken into consideration. If the pores are not interconnected within scaffold, mass transport and cell migration are not done appropriately even if porosity of scaffold is high.

Techniques in macro/microstructure design for patient-specific scaffold must be able to 1) offer hierarchical porous structures so that the required mechanical function and mass transport is satisfied and 2) these structures must be embedded in a complicated and arbitrary 3D anatomical shapes. The main advantage of AM techniques is that they are able to fabricate TE scaffolds with both predefined macro and microstructures.

Computational Topology Design (CTD) is an effective design procedure which can be integrated with AM for design and fabrication of TE scaffold. CTD-based scaffold design may start with creation of unit cell libraries that can be assembled to form scaffold architectures. Unit cell libraries may be created by either using approaches based on CAD **(Cheah et al., 2004, Fang et al., 2005, Van Cleynenbreugel et al., 2002)** or using image-based design approaches **(Hollister et al., 2000, Hollister et al., 2002, Lin et al., 2004b).** Homogenization theory **(Hollister and Kikuchi, 1994)** can then be exploited to calculate effective properties based on these unit-cell designs. Surpassing effective property calculation from defined microstructures, topology optimization approaches **(Lin et al., 2004a, Sigmund, 1994)** actually compute new microstructures to attain desired properties. It is possible to either optimize the functional elastic properties or maximize permeability with a constraint on porosity, or a constraint on required elastic properties, respectively **(Hollister, 2006).** Scaffold architecture creation within a complex 3D anatomic shape is the final stage of the scaffold design process. 3D anatomic shape is generated from patient's CT or MRI images. Both CT and MRI produce structured voxel datasets where patient anatomy is defined by density distribution. These datasets can be used in

design process either by converting the voxel anatomic data into solid geometric models for use in CAD **(Cheah et al., 2004, Fang et al., 2005, Van Cleynenbreugel et al., 2002),** or by directly using voxel data base structures in image-based methods **(Hollister et al., 2000, Hollister et al., 2002).** Finally, boolean techniques are used to intersect the defined anatomic defected shape with the microstructure design database, resulting in the final patient-specific scaffold design **(Hollister, 2006).**

2.3 Fabrication of TE Scaffolds using Extrusion-Based AM Systems

Various fabrication methods including traditional chemical engineering methods and advanced AM techniques (known as solid freeform fabrication (SFF)) are used for fabrication of TE scaffolds. The main traditional techniques to construct TE scaffolds include: solvent casting/salt leaching, phase separation, foaming, and textile meshes. These techniques subject to limitations such as shape restrictions, manual intervention, inconsistent and inflexible processing procedures. In addition, the traditional techniques usually cannot control pore size, pore geometry and spatial distribution of pores properly. To complement these limitations, there has been a trend in recent years to fabricate TE scaffolds using AM processes directly (building final scaffold) or indirectly (building negative scaffold to be used as a mould). In particular, extrusion-based AM systems have been widely investigated for fabrication of TE scaffolds due to their ability of processing different biomaterials, their possibility of manufacturing scaffolds in a cell-friendly environment, their high reproducibility and flexibility, and their simple process control in comparison with other AM techniques **(Vaezi and Yang, 2014)**.

2.3.1 Extrusion-Based AM Systems with Material Melting

FDM process is the first extrusion AM system developed based on polymer melts extrusion for 3D printing of high strength functional parts. Thermoplastic materials in form of filament are used as feedstock and a pinch roller or screw feed mechanism is used to push the filament into liquefier, and subsequently extruding from a computer-controlled nozzle. By repeating the extrusion process the final part is fabricated layer-by-layer. Extrusion temperature needs to be controlled precisely to achieve desirable accuracy. Variety of modified FDM systems have been developed for fabrication of biomaterials 3D scaffolds with micron size pores and struts. Highly porous PLGA scaffolds for cartilage tissue engineering were fabricated by Hung-Jen et al. **(2009)** using FDM process and were further modified by type II collagen. Tellis et al. **(2008)** used micro CT to create biomimetic polybutylene terephthalate (PBT) trabecular scaffolds.

Bone biocomposite scaffolds produced from polymer and calcium phosphates (such as HA and TCP) using FDM process have good mechanical and degradation properties, improved cell seeding, and enhanced incorporation and immobilization of growth factors. Calcium phosphates phase brings about higher structural strength and polymer phase provides plasticity and toughness to the scaffold. Hutmacher's group **(Zein et al., 2002)** has extensively investigated

the process parameter for PCL and they printed various composites including PCL, PP/TCP, PCL/HA, PCL/TCP and PCL/TCP scaffold with resolution of 250 μm using FDM process. Kalita et al. **(2003)** produced controlled porosity polymer-ceramic composite PP/TCP scaffolds, with 3D interconnectivity designed to promote richer supply of blood, oxygen and nutrients for healthy in-growth of bone cells. Controlled porosity alumina and β-TCP ceramic scaffolds with pore sizes in the range of 300–500 μm and pore volumes of 25–45% have also been produced using the indirect FDM process **(Bose et al., 2003)**. Safari's group **(Allahverdi et al., 2001)** produced hybrid scaffold from alumina and wax (as support structure) directly using multi nozzle fused deposition of ceramics (FDC).

Two major limitations of FDM process are the need to use filamentary materials as feedstock and the high heat effect on the raw biomaterial which can result in degradation of the biomaterial. In particular, preparation of filamentary feedstock makes it difficult/time consuming to process new biomaterial. To overcome this problem, variety of modified FDM systems with new melt extrusion configurations such as 3D fiber deposition, PED, PEM, and MJS processes have been developed which are reviewed further.

In 2004, Woodfield and co-workers **(2004)** developed the 3D fiber deposition process with the aim of extrusion of highly viscous polymers. The technique allowed them to print scaffolds by accurately controlling the deposition of molten co-polymer fibres from a pressure-driven syringe onto a computer controlled moving table. They produced 3D poly(ethylene glycol)-terephthalate-poly(butylene terephthalate) (PEGT/PBT) block co-polymer scaffolds **(Woodfield et al., 2004)**, polyethyleneoxide terephthalate (PEOT) and polybutylene-terephtelate (PBT) scaffolds **(Moroni et al., 2006)** with a 100% interconnecting pore network.

PED process is another adjuration of melt extrusion AM process developed by Wei Sun's group **(Wang et al., 2004)** in which biomaterial in form of pellet or granule is liquefied in a chamber and a rotating screw (mini-extruder) expels the molten biomaterial through nozzle. Shor et al. **(2007)** used this method to build PCL and PCL/HA 3D scaffolds with uniform pore size of 250 μm. The test results proved the structural integrity, controlled pore size, interconnectivity, a favourable mechanical property, and basic biocompatibility of the printed PCL scaffolds using PED process **(Shor et al., 2009)**. Hoque et al. **(2009)** developed a desktop robot based rapid prototyping (DRBRP) system with the ability of processing a wide range of synthetic polymers in form of pellet, lump, or powder to build 3D scaffolds. Biocompatibility tests using rabbit smooth muscle cells proved excellent performance of fabricated scaffolds in terms of cell adhesion and tissue formation.

Xiong et al. **(2001)** developed PEM process in which compressed air is used instead of piston or rotating screw to expel the melted biomaterial through deposition nozzle. PLLA and PLLA/TCP filaments with enough accuracy could be deposited onto the substrate using a computer controlled digital valve with high switch response speed.

MJS process was developed by Fraunhofer-Gessellschaft research centre to produce high density metallic and/or ceramic parts using low-melting point alloys or a powder-binder

mixture **(Greulich et al., 1995)**. Heated paste is pushed out through a nozzle and deposited on a computer-controlled build table. The feedstock is normally supplied as powder, pellet, or bar and the extrusion temperature of the molten material can reach up to 200 ºC. Powder-binder feedstock is heated in a process chamber above the melting point of the binder, and thus only the binder is liquefied during the process. A piston is used to push out the low viscous flow through nozzle and the material is deposited layer-by-layer. MJS process was used to print 3D scaffolds made of poly(D, L-lactide) (PDLLA) for bone and cartilage tissue engineering. The scaffold pore size was found to be in the range of 300–400 μm and the structure supported ingrowth of human bone tissues **(Koch et al., 1998)**.

The Polytechnic Institute of Leiria developed a variation of FDM called "BioExtruder" **(Domingos et al., 2012, Domingos et al., 2009)** for printing PCL scaffolds. The BioExtruder comprises two different deposition systems: a rotational system for multi-material deposition that uses a pneumatic mechanism for extrusion, and a single material deposition system that serves a rotating screw to assist the deposition process.

2.3.2 Extrusion-Based AM Systems without Material Melting

New configurations for melt extrusion highlighted in the previous section could open up the possibility for the use of a wider range of biomaterials, making the extrusion-based systems more versatile and applicable alternative manufacturing process for composite scaffold materials. However, the main concern was the high heat effect on raw biomaterial, and thus new extrusion configurations without material melting were proposed that could better preserve bioactivity of the scaffold's materials.

PAM process is a technique developed by Vozzi and co-workers **(Vozzi et al., 2002)** without the need for heating. PAM uses a pneumatic driven microsyringe to deposit biomaterial on a substrate. Material viscosity, deposition speed, nozzle diameter and the applied pressure correlate with the final deposited filament dimensions **(Vozzi et al., 2003)**. High resolution polymeric scaffolds with various compositions such as PCL, PLLA, PLGA, and PCL/ PLLA, gelatin, and alginate hydrogels scaffolds with three different geometries-square grids, hexagonal grids, and octagonal grids could be printed successfully using PAM method **(Mariani et al., 2006, Tirella et al., 2009, Tirella et al., 2008, Vozzi and Ahluwalia, 2007, Vozzi et al., 2004)**. In addition to scaffolds, PAM was used to deposit a polyurethane dielectric layer and an additional carbon black electrode layer above it **(Tartarisco et al., 2009)**. Vozzi's group further used a modified system called "piston assisted microsyringe (PAM2)" for microfabrication of viscous, sol-gel or gelled inks (e.g. alginate solutions at different concentrations). PAM2 uses a stepper motor instead of compressed air to move the plunger of the syringe with a controlled speed **(Tirella et al., 2012)**. PAM2 has also a temperature controlled syringe (TCS) module to control the temperature of processed materials using an aluminium jacket.

LDM process is another low-temperature extrusion AM method proposed by Xiong et al. **(2002b)** that its key feature is a non-heating liquefying processing of materials. In this process,

material slurries are fed into the material supply that is connected to a screw pump nozzle using a soft pipe and fabrication process is accomplished in low temperature environment under 0 ºC in the refrigerator. The layer of deposited materials is frozen on the platform. After the forming process, the frozen scaffolds need to be freeze-dried for a rather long time (~38 h) to remove the solvent. Biomolecules can also be applied in the LDM process to fabricate a bioactive scaffold directly. The bone scaffolds made by LDM system had good biocompatibility and bone conductive property as a molecular scaffold for bone morphogenic protein (BMP) in the implantation experiment of repairing segment defect of rabbit radius **(Yongnian et al., 2003)**. LDM process has been used to print multi material **(Liu et al., 2009a)**, and various hydrogel scaffolds **(Li et al., 2009a, Li et al., 2009b)**. Cong Bang et al. **(2008)** developed a special LDM system based on rapid freeze prototyping (RFP) technique to produce scaffolds from chitosan solution. Multi nozzle low-temperature deposition and manufacturing (M-LDM) and multi nozzle deposition manufacturing (MDM) systems **(Liu et al., 2009a, Liu et al., 2009b)** were further developed by incorporation of multiple nozzles with different designs into the LDM technique. M-LDM system was proposed to fabricate scaffolds with heterogeneous materials and gradient hierarchical porous structures.

Ang et al. **(2002)** set up a special robotic extrusion device called "rapid prototyping robot dispensing (RPBOD)" for the design and fabrication of chitosan-HA scaffolds. The RPBOD system consists of a computer-guided desktop robot and a one-component pneumatic dispenser. Mixture of sodium hydroxide solution and ethanol with different ratios were used as plotting medium to produce chitosan-HA scaffolds. Further, the RPBOD system was improved to include a new manufacture method, called dual dispensing system as besides the pneumatic dispenser, a mechanical dispenser which was driven by a stepper motor was set up to deposit plotting medium. The dual dispensing method excrete the high sensitivity to material concentration compared with the method of dispensing plotting materials into a fluid medium, as the precipitation occurs when the dispensing material and the coagulant medium merge on the base or on the previous layer. There is then no precipitated lump forming at the nozzle and no movement of the fluid medium to affect the shape of the precipitated strands of the scaffold. The chitosan scaffolds printed using RPBOD exhibits excellent uniformity, interconnectivity, sufficient strength, good reproducibility, and calibration **(Li et al., 2005)**.

3D bioplotting is a technique that was first developed by Landers and Mulhaupt **(Landers and Mulhaupt, 2000)** to produce scaffolds for soft tissue engineering purposes, and simplifying hydrogel manufacturing. In this process, the material dispensing head normally moves in three dimensions, while the fabrication platform is stationary. Either a filtered air pressure (pneumatic nozzle) or a stepper-motor (volume-driven injection nozzle) is used to plot a viscous material into a liquid (aqueous) plotting medium with a matching density. The filament thickness can be adjusted by varying viscosity of plotting solution, nozzle diameter, and the applied pressure **(Billiet et al., 2012)**. The work by Landers and Mulhaupt led to the commercialization of the first 3D-Bioplotter™ by EnvisionTec GmbH (www.envisiontec.com) to

fulfil the demand for 3D scaffolds with well-defined external and internal structures in tissue engineering and controlled drug Release.

In comparison to other extrusion-based AM processes, 3D bioplotting can process a wider range of biomaterials. The plotting of biomaterials such as melts of PLA, PLGA, PCL, biopolymer solutions of agar and gelatin, natural polymers such as collagen, reactive biosystems involving fibrin formation and polyelectrolyte complexation, and cells and thermally sensitive biocomponents is possible **(Landers et al., 2002)**. In particular, the processing of materials with low viscosities benefits from buoyancy compensation **(Pfister et al., 2004)**. The 3D-Bioplotter™ has the capacity of fabricating scaffolds using the widest range of materials from soft hydrogels over polymer melts up to hard ceramics and even metals.

Further surface treatment is normally applied to the scaffolds produced by 3D bioplotting technique as they mostly have smooth surfaces that are not desired in terms of cell attachment. To make scaffolds with rough surface, Geun Hyung and Joon Gon **(2009)** used a piezoelectric transducer (PZT) generating vibrations during plotting to make PCL scaffolds with a rough surface. Maher et al. **(2009)** developed a device based on bioplotting technique with the ability of heating plotting materials and produced TE scaffolds using a variety of materials including poly(ethylene glycol) (PEG), gelatin, alginic acid and agarose at various concentrations and viscosities.

Different low-temperature extrusion AM techniques have also been developed for printing hard tissue engineering scaffolds from ceramics. Robocasting is a ceramic processing technique in which a computer controls the robotic deposition of highly concentrated (typically 50-65 vol.% ceramic powder) colloidal ceramic slurries. The slurry is deposited layer-by-layer from a syringe using constant displacement at a controlled rate. Miranda et al. **(Miranda et al., 2008, Miranda et al., 2006)** used robocasting process to produce β-TCP scaffolds with designed 3D architecture and mesoscale porosity using concentrated inks with suitable viscoelastic properties. The deposition was done in a non-wetting oil bath to prevent non-uniform drying during printing.

Direct-write assembly is a low-temperature extrusion AM system developed by Lewis and co-workers **(Smay et al., 2002)** whereby a wide range of inks can be printed in both planar and 3D structures. Robocasting and direct-write assembly are essentially identical-the primary difference is the way in which ink is extruded. Robocasting relies on a constant displacement process, whereas direct ink writing relies on a constant pressure process. In direct-write assembly, compressed air is employed to push inks with controlled rheological properties through an individual nozzle (diameter ranging from 1 to 500 μm). This process deposits inks at room temperature or a proper coagulation reservoir using a controlled-printing speed and pressure which depend on ink rheology, and nozzle diameter. A wide range of inks including colloidal suspensions and gels, nanoparticle-filled inks, polymer melts fugitive organic inks, hydrogels, sol–gel and polyelectrolyte inks have been processed using direct-write assembly. Ink rheology strongly depends on solid loading for nanoparticle inks so that viscosity decreases by

decreasing solid loading. Concentrated inks with solid loading of 70-85 wt% are normally required for printing planar and spanning filaments **(Smay et al., 2002)**. Writing of some inks such as polyelectrolyte inks need to be performed into a reservoir-induced coagulation to enable 3D printing, whereas some other inks such as sol-gel inks can be directly printed in air providing excellent control over the deposition process (e.g., the material flow can be started/stopped repeatedly during print process).

In recent years, Lewis and co-workers have focused on extending direct-write assembly to biomedical applications. Using biocompatible inks they printed 3D scaffolds and microvascular networks for tissue engineering and cell culture. Different 3D HA scaffolds with 250 μm strut width **(Michna et al., 2005, Simon et al., 2007)**, and scaffolds composed of a gradient array of silk/ HA with filaments at size 200 μm were fabricated by direct-write assembly **(Sun et al., 2012)**. The 3D silk/HA scaffolds are used to support the growth of co-cultures of human bone marrow derived mesenchymal stem cells (hMSCs) and human mammary microvascular endothelial cells (hMMECs) to assess in vitro formation of bone-like tissue. In addition, 3D microperiodic scaffolds of regenerated silk fibroin have been fabricated using direct-write assembly for tissue engineering **(Ghosh et al., 2008)**. Biocompatible silk optical waveguides as fine as 5 μm was printed by direct-write assembly of a concentrated silk fibroin ink through a micronozzle into a methanol-rich coagulation reservoir **(Parker et al., 2009)**. 3D microperiodic hydrogel scaffolds with 1 μm **(Barry et al., 2009a)** and 10 μm **(Shepherd et al., 2011)** filaments were also printed for guided cell growth by direct writing of a poly(2-hydroxyethyl methacrylate) (pHEMA)-based ink through a gold-coated deposition micro-nozzle that is simultaneously photopolymerized via UV illumination.

SEF is another extrusion AM technique developed by Evans and Yang's group **(Yang et al., 2008a, Lu et al., 2008a, Yang et al., 2008b, Lu et al., 2012a, Yang et al., 2006)** to produce ceramic scaffolds. SEF is relatively simple process in which phase change is based on solvent evaporation **(Grida and Evans, 2003)**. Paste with high yield strength is prepared by blending polymer, ceramic, and a solvent with specific ratios. Defects such as dilatancy, drying cracks and surface fracture which happens in water-based extrusion systems can be eliminated by appropriate adjustment of polymer content **(Yang et al., 2008d)**. A range of bioceramic scaffolds have been fabricated using SEF method with various compositions (different HA/β-TCP ratios) and sintered from 1100°C to 1300°C **(Yang et al., 2008b)**. Scaffolds with varying porosities and pore sizes were printed, filament width down to 70 μm and interconnected pores with interstices from 50 to 500 μm **(Yang et al., 2008a, Yang et al., 2008b, Yang et al., 2008d)**. Other ceramic pastes such as alumina, alumina/silica, zirconia, and alumina/graphite have been also used successfully for fabrication of 3D lattice structures with fine filaments **(Xuesong et al., 2009, Xuesong et al., 2010)**. In addition to bioceramics, 3D carbon scaffolds were produced using two different paste compositions, different polymers in the paste **(Lu et al., 2012b)**. **Fig. 2.2** shows a high resolution HA scaffold with filament diameter of 70 μm printed using SEF process.

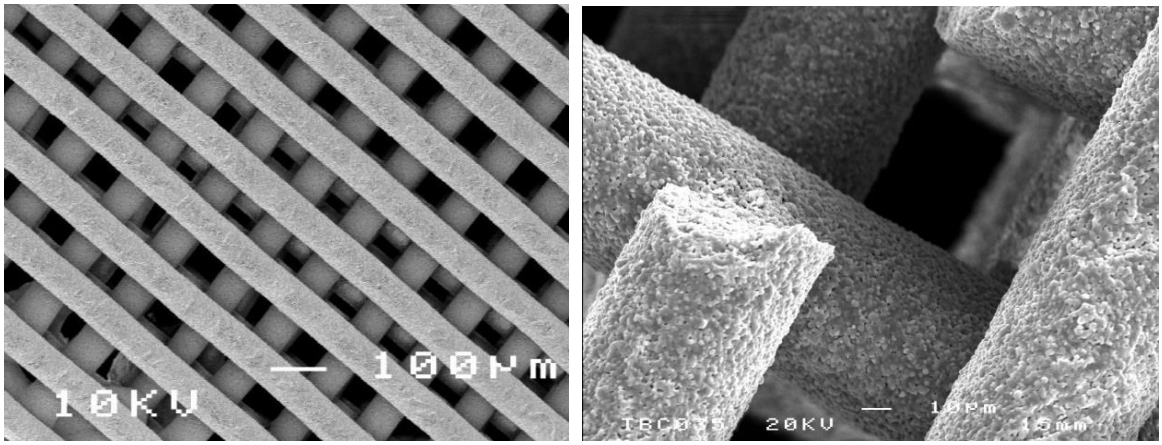

Figure 2.2 (a) Plane view of HA scaffold with filament diameter of 70 µm produced by SEF method, **(b)** fracture of a sintered filament near to a weld area **(Yang et al., 2008e)**

As a consequence of what was discussed above, extrusion-based AM processes can be employed as a standard tool in biofabrication of tissue engineering scaffolds. However, choosing the right extrusion-based process to use requires a careful evaluation of the capabilities and limitations of each process. **Table 2.3** provides a comparison between the key extrusion-based AM techniques in terms of resolution, materials, and their characteristics.

Scaffolds-based tissue engineering is a proven approach in regenerative medicine but still subjects to some limitations and challenges including: (i) complications posed by host acceptance (immunogenicity, inflammatory response, mechanical mismatch), and; (ii) problems related to cell cultures (cell density, multiple cell types, specific localization) **(Billiet et al., 2012)**. Cell-based printing techniques have been intensively investigated and many innovative approaches such as organ bioprinting **(Mironov et al., 2007)**, laser writing of cells **(Schiele et al., 2009)**, bio-electrospraying **(Jayasinghe, 2007)**, and biological laser printing (BioLP) **(Barron et al., 2004)** have introduced to complement limitations in scaffold-based tissue engineering. Billiet and co-workers **(2012)** define organ bioprinting as the engineering of 3D living structures supported by the self-assembly/organizing capabilities of cells delivered through the application of AM techniques based on laser, inkjet, or extrusion freeforming technologies.

Inkjet and extrusion-based systems are used in a similar way for direct bioprinting: balls or continues flows of bioinks are deposited in well-defined topological patterns into biopaper layers. The bioink building blocks typically have a spherical or cylindrical shape, and consist of single or multiple cell types. In a post-processing step, the construct is transferred to a bioreactor and the bioink spheres are fused. The biopaper, an inert and biocompatible hydrogel, can be removed after construction in post-processing step **(Billiet et al., 2012)**. Several extrusion-based systems such as 3D bioplotter described earlier can be served as a bio-printer, if sterile conditions can be acquired. Different living structures have been produced using

hydrogel structures containing viable cells, but the designs have been simple and isotropic, and mechanical properties and printing resolution were not satisfactory **(Melchels et al., 2012)**. **Fig. 2.3** depicts a pig smooth muscle cell (SMC) printed using an extrusion-based bio-printer.

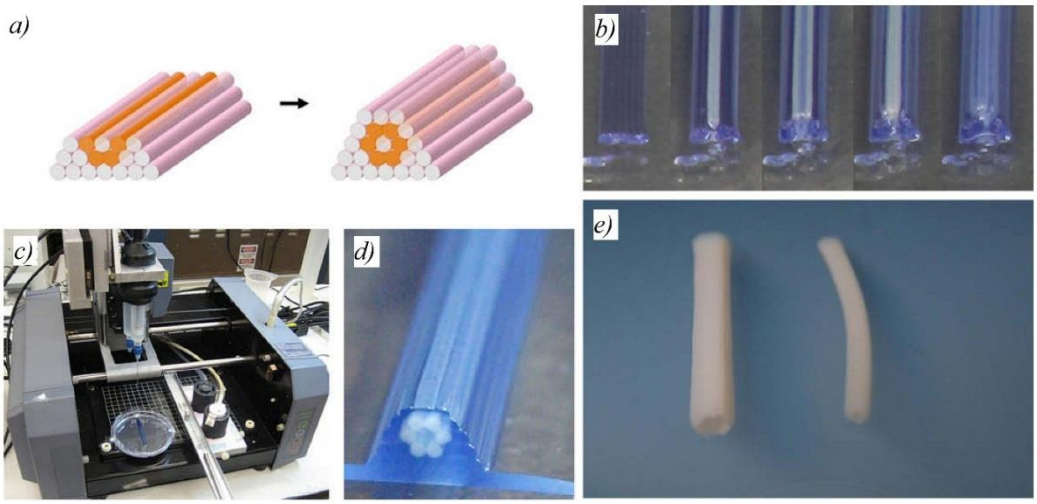

Figure 2.3 Bioprinting of tubular structures using scaffold-free extrusion-based AM; **(a)** designed print template, **(b)** layer-by-layer deposition of agarose cylinders (stained in blue) and multicellular pig smooth muscle cell (SMC) cylinders (white), **(c)** the bioprinter outfitted with two vertically moving print heads, **(d)** the printed construct, **(e)** engineered pig SMC tubes of different diameters resulted after 3 days of post-printed fusion and hydrogel removing **(Norotte et al., 2009)**.

The scaffold-free cell printing technologies has opened up new possibilities, however, an ideal 3D tissues or organs have not yet been printed successfully since gel-state cell-embedded hydrogels are unable to maintain the desired 3D structure due to their insufficient mechanical strength **(Vaezi et al., 2013a)**. Hybrid scaffolds were developed to overcome this problem **(Khalil et al., 2005, Schuurman et al., 2011)**. Lee et al. **(2013)** printed a hybrid scaffold in which PCL and cell (MC3T3-E1)-embedded alginate struts are stacked in successive layers to build a 3D bioconstruct. The PCL struts provide controllable mechanical support of the cell-laden alginate struts which provide biological activity **(Vaezi et al., 2013a)**. The subsequent mechanical properties of the scaffolds were fundamentally enhanced and could be engineered as those of local tissues. Besides, since the hydrogel is bolstered by the thermoplastic material, a more choice of hydrogels and concentrations can be utilized in comparison with scaffold-free method, which can result in enhancing the conditions for encapsulated cells to proliferate and deposit new matrix **(Melchels et al., 2012)**. **Fig. 2.4** shows an example of hybrid biopolymer/cell bioconstruct printed by Shim et al. **(2012)** using multi-head tissue/organ building system (MtoBS). Two different alginate solutions were infused into the previously prepared PCL framework to create the 3D construct for osteochondral printing **(Shim et al., 2012, Vaezi et al., 2013a)**.

Table 2.3 Comparison of the key extrusion-based AM techniques

Technique	Lateral Resolution	Materials	Strengths	Drawbacks	References
FDM	250 µm	PCL, PP-TCP, PCL-HA, PCL-TCP, PLGA, polybutylene terephthalate (PBT), etc.	Good mechanical strength, versatile in lay-down pattern design, no trapped particles or solvents	High temperature, need to produce filament material, rigid filament, Limited material range, difficult to prepare structures with microscale porosity	**(Bose et al., 2003, Hung-Jen et al., 2009, Kalita et al., 2003, Tellis et al., 2008, Zein et al., 2002)**
RPBOD/dual dispensing	400 µm	Chitosan-HA, Chitosan	Enhanced range of materials can be used, can incorporate biomolecule	Low mechanical strength, Precise control properties of material and medium, requires freeze drying	**Ang et al., 2002, Li et al., 2005)**
PAM	5-10 µm	PCL, PCL-PLLA, PLGA, PLLA, Polyurethane elastomer (Polytek 74-20), alginate, gelatin and viscous inks (using PAM2)	Enhanced range of materials can be used, can incorporate biomolecule, high resolution, not subject to heat, can be used for multilayers	Small nozzle inhibits incorporation of particle, narrow range of printable viscosities, solvent is used, highly water-soluble materials cannot be used	**(Mariani et al., 2006, Tirella et al., 2009, Vozzi and Ahluwalia, 2007, Vozzi et al., 2004)**
PED	250 µm	PCL, PCL-HA	Input material in pellet form	High temperature, rigid filament	**(Shor et al., 2009, Shor et al., 2007, Wang et al., 2004)**
3D bioplotting	45 -250 µm	Bone regeneration and drug release applications: HA, titanium, TCP, PCL, PLGA, PLLA Soft tissue fabrication/organ printing applications: Agar, chitosan, alginate, gelatine, collagen, fibrin, PU, silicone Hybrid scaffolds: PCL hybrid with alginate	Remarkably wide variety of different materials, can incorporate biomolecule, use of hydrogel materials (agar, gelatin, etc.)	Low mechanical strength, smooth surface which are not desired for appropriate cell attachment, low accuracy, slow processing, precise control of properties of plotting material and medium is required	**(Landers et al., 2002, Landers and Mulhaupt, 2000, Maher et al., 2009, Pfister et al., 2004)**

Table 2.3 Comparison of the key extrusion-based AM techniques (continue)

Technique	Lateral Resolution	Materials	Strengths	Drawbacks	References
LDM/ MDM/ M-LDM	300 µm	PLLA-TCP, PLGA, collagen, PLGA-collagen, chitosan, gelatin, alginate	Input material in grain form, preserve bioactivities of scaffold materials because of its non-heating liquefying processing of materials, Can incorporate biomolecule	Solvent is used, requires freeze drying	**(Li et al., 2009a, Liu et al., 2009b, Yongnian et al., 2003)**
3D fiber deposition	250 µm	poly(ethylene glycol)-terephthalate/poly(butylene terephthalate) (PEGT-PBT), polyethyleneoxide terephthalate (PEOT) and polybutylene-terephtelate (PBT)	Input material in pellet form; preparation time is reduced	High temperature, rigid filament, difficult to prepare structures with microscale porosity	**(Moroni et al., 2006, Woodfield et al., 2004)**
PEM	200-500 µm	PLLA; PLLA-TCP	Input material is grains	High temperature, rigid filament	**(Xiong et al., 2001)**
Robocasting	100 µm	Ceramic and organic inks	Enhanced range of materials can be used, High ceramic content, multimaterial scaffold is possible	Precise control of ink properties is crucial	**(Cesarano, 1999, Miranda et al., 2008, Miranda et al., 2006)**
Direct write assembly	250 nm for so-gel inks 1-20 µm for nanoparticle inks, hydrogel, and polyelectrolyte inks 200-250 µm for ceramic inks such as HA; silk-HA	Ceramic inks; fugitive organic inks; nanoparticle inks; polymer inks; sol-gel inks	A wide range of materials, very high resolution, non-heating process	Precise control of ink properties is crucial	**(Lewis and Gratson, 2004, Shepherd et al., 2011, Sun et al., 2012)**
SEF	70 µm	HA, HA-β-TCP, zirconia, alumina, alumina/silica	Simple process yet high resolution, low sintering shrinkage, controlled microprosity of filaments	Precise control of ink properties is crucial	**(Xuesong et al., 2009, Xuesong et al., 2010, Yang et al., 2008a, Yang et al., 2008c, Yang et al., 2008e)**

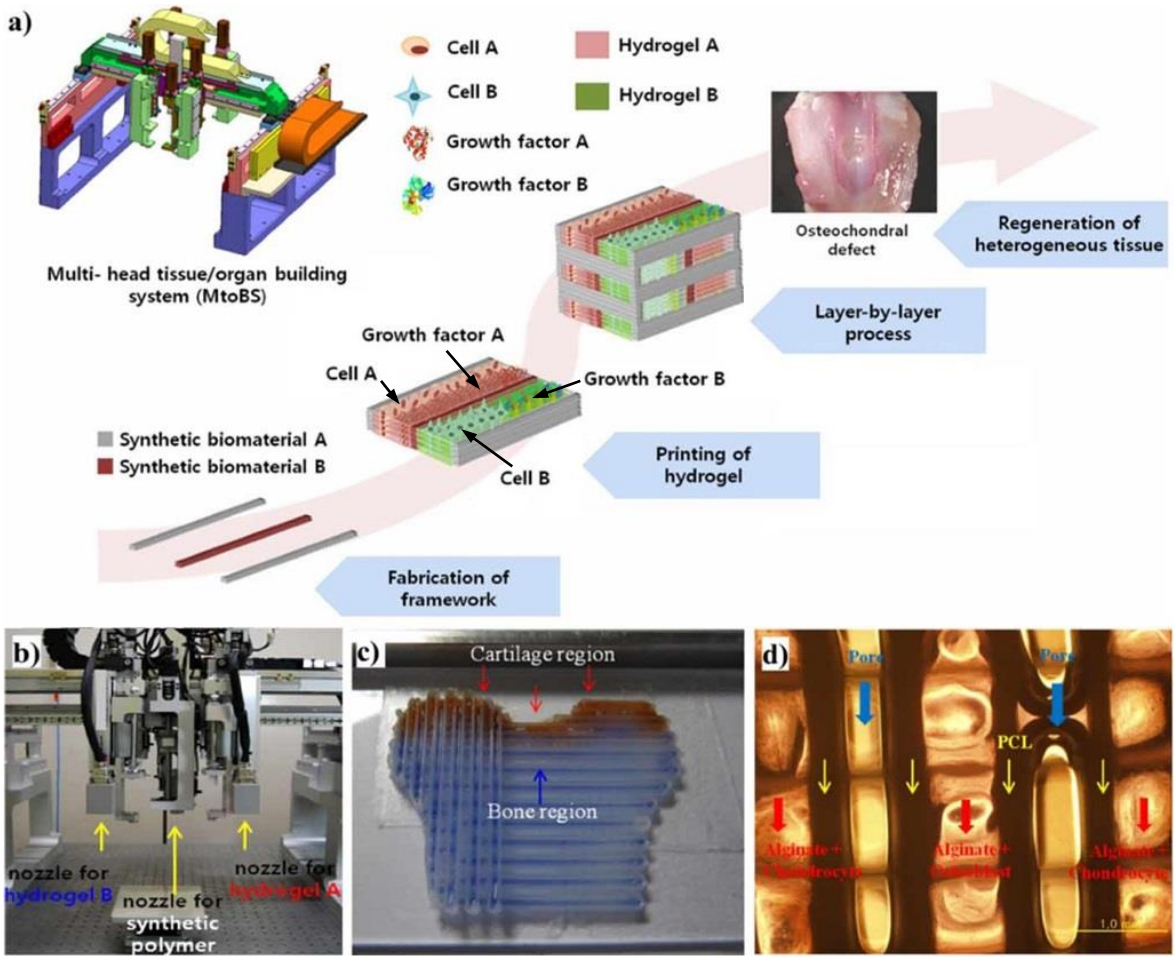

Fig. 2.4 (a) Schematic diagram of hybrid scaffold printing using MtoBS: First, a framework made up of synthetic biomaterials such as PCL and PLGA is fabricated, next the hydrogel which is able to encapsulate cells and growth factors is dispensed into the pores. The sequential dispensing of synthetic biomaterials and hydrogel is repeated and stacked to build a 3D bioconstruct, **(b)** MtoBS components: three extrusion heads, where one is for synthetic biomaterials and the remaining two are for hydrogels, **(c)** a conceptual 3D osteochondral structure made up of PCL and two different alginates. Cartilage and bone regions are filled with red stained alginate and blue stained alginate, respectively, **(d)** microscopic image of the printed bioconstruct using chondrocyte and osteoblast encapsulated in the alginate. Every second pore is filled with alginate. The others are empty for oxygen and nutrient transportation **(Shim et al. 2012)**.

2.4 Polyether-Ether-Ketone (PEEK)

Polyaryletherketones (PAEKs) is a family of high temperature polymers which contains an aromatic backbone molecular chain, interconnected by ketone and ether functional groups **(May, 2002).** Polyether-ether-ketone (PEEK), poly(ether ketone) (PEK), poly(etherketoneketone) (PEKK), and poly(aryl-ether-ketone-ether-ketone-ketone (PEKEKK) are different polymers in PAEK family which are used mostly in orthopaedic and implants. **Fig 2.5** depicts chemical formula of PEEK which is the subject of this research work. PEEK is an organic semi-crystalline thermoplastic with great mechanical properties and chemical resistance which is used in different demanding applications, not only medical sector, such as bearings, piston parts, pumps,

compressor plate valves, thermal insulation, etc. PEEK is highly resistant to thermal degradation as well as attack by both organic and aqueous environments.

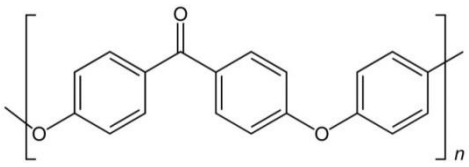

Figure 2.5 Chemical structure of PEEK **(Nandan et al., 2003)**

PEEK had emerged by the late 1990s as an efficient thermoplastic which could be used as implants components, especially in orthopaedics and trauma instead of metal implants **(Liao, 1994)**. In 1998, PEEK was offered commercially as a biomaterial for implants by Invibio because of its excellent mechanical properties which are retained in high temperatures, and its resistance to in vivo degradation (such as damage caused by lipid exposure). Extensive research works have proved the successful clinical performance of PEEK in orthopaedic and spine patients, and PEEK composites as bearing materials and flexible implants used for joint arthroplasty **(Toth et al., 2006, Wang et al., 1999, Joyce et al., 2006)**.

2.4.1 Mechanical Properties and Processing Methods of Medical Grade PEEK

Mechanical properties of PEEK depend on both temperature and strain rate like other semi-crystalline polymers **(Boinard et al., 2000, Hamdan and Swallowe, 1996, Rae et al., 2007)**. In addition, molecular weight, size and orientation of the crystalline regions can affect mechanical behaviour of PEEK **(Chivers and Moore, 1994, Rae et al., 2007, Cebe et al., 1987)**. Unfilled PEEK has good ductility and can subject to large plastic deformation in both uniaxial tension and compression, although it has a rather rigid molecular chain structure. Studies on mechanical properties of both 150G **(Hamdan and Swallowe, 1996)** and 450G PEEK **(Rae et al., 2007)** provided a good understanding of PEEK's engineering and true stress–strain behaviour. **Fig. 2.6** depicts uniaxial tension and compression curves of 450G PEEK with different rates. Effect of strain rate on stress-strain curves at 23°C can be realized from **Fig. 2.6**. PEEK at room temperature shows a linear relationship between stress and strain in both tension and compression at small strains (<0.03), the slope of which is characterized by an elastic modulus. As the strain increases, room temperature PEEK exhibits a clear yield transition in the slope of the stress–strain curve. The yield transition in compression is 30–40% higher than in tension **(Kurtz and Devine, 2007)**.

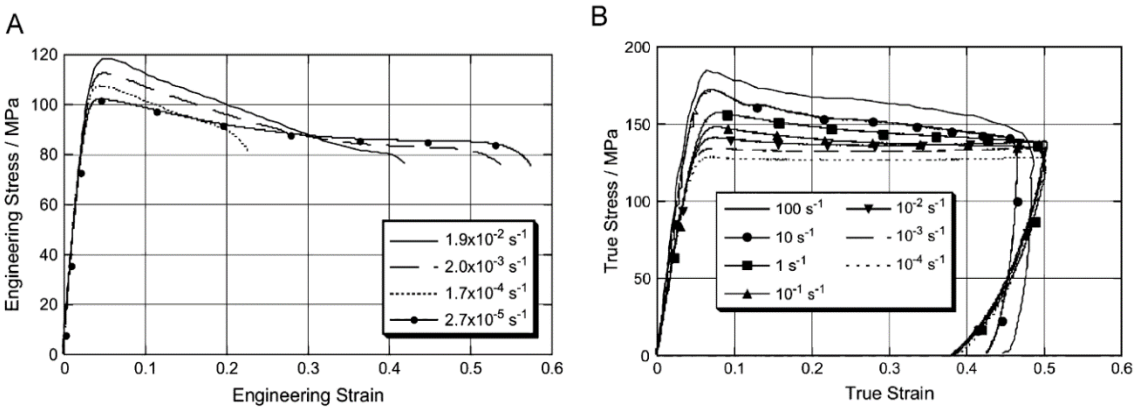

Figure 2.6 Stress–strain curves at 23°C in **(a)** uniaxial tension and **(b)** compression of 450G PEEK **(Rae et al., 2007)**

Mechanical properties of PEEK and carbon fibre-reinforced PEEK (CFR-PEEK) composites are summarized in **Tables 2.4** which can merely provide a general idea for biomaterial selection and is useful for comparison purposes.

Table 2.4 Typical properties of PEEK and CFR-PEEK structural composite biomaterials, compared with Ultra-high-molecular-weight polyethylene (UHMWPE) and Poly(methyl methacrylate) (PMMA) **(Kurtz and Devine, 2007)**

Property (ISO)	Invibio PEEK-OPTIMA LT1			UHMWPE	PMMA
	Unfilled	30% carbon fibre reinforced (LT1CA30)	68% continues carbon fiber reinforced (Endolign)		
Polymer type	Semi-crystalline	Semi-crystalline	Semi-crystalline	Semi-crystalline	Amorphous
Molecular weight (106 g/mole)	0.08-0.12	0.08-0.12	0.08-0.12	2-6	0.1-0.8
Poisson's ratio	0.36	0.40	0.38	0.46	0.35
Specific gravity	1.3	1.4	1.6	0.93-0.94	1.18-1.25
Flexural modulus (GPa)	4	20	135	0.8-1.6	1.5-4.1
Tensile strength (MPa)	93	170	>2000	39-48	24-49
Tensile elongation (%)	30-40	1-2	1	350-525	1-2
Degree of crystallinity (%)	30–35	30–35	30–35	39-75	-

Various manufacturing techniques are currently used for fabricating PEEK-based implants and medical devices, as follow **(Kurtz and Devine, 2007)**:

- Injection moulding: a conventional plastic part manufacturing process suitable for mass production of PEEK-based parts with desired geometry

- Extrusion: a manufacturing process to produce long stock shapes such as PEEK rods, sheets, and fibers. Thin film of PEEK are produced by extruding PEEK using suitable die and haul-off equipment, which controllably handles and stores the film. PEEK films are produced in either crystalline or amorphous forms by controlling the temperature of the casting drums in the haul-off equipment. PEEK monofilaments can also be produced by extrusion followed by drawing of the PEEK extrudate
- Compression moulding: a manufacturing process for production of relatively simple stock shapes like plates and thick sheets
- Machining: a conventional manufacturing process which is generally used for low volume production of PEEK
- Selective Laser Sintering (SLS): a type of powder-based AM technologies that uses a high power laser beam to sinter fine powders layer-by-layer. This process is normally used for low volume production when PEEK implants with complex macro/microstructure is required

2.4.2 Bioactive and Porous PEEK Compounds

There are many evidences to support the biocompatibility of PEEK and its composites. Several biocompatibility tests such as systemic and intracutaneous toxicity and intramuscular implantation, sensitization tests, and gene toxicity have been performed on PEEK and its compounds to meet the requirements of FDA **(Wenz et al., 1990, Petillo et al., 1994, Hunter et al., 1995, Morrison et al., 1995, Lin et al., 1997, Katzer et al., 2002)**. However, a potential clinical concern is that PEEK is not bioactive enough and has limited fixation with bone. Three main strategies are being developed to enhance osseointegration of PEEK-based implants for different orthopaedic applications **(Ma and Tang, 2014, Kurtz and Devine, 2007, Abu Bakar et al., 2003a, Wang et al., 2011):**

- Incorporating of bioactive materials such as calcium phosphates into PEEK,
- Coating PEEK implants with biomaterials such as titanium and/or calcium phosphates,
- Incorporating porosity into PEEK implants

Calcium phosphates or other bioactive materials are used to produce PEEK compounds with enhanced biological properties **(Ma and Tang, 2014)**. Recent study on nano-TiO_2/PEEK biocomposites **(Wu et al., 2012)** revealed that pseudopods of osteoblasts preferred to anchor at areas where nano-TiO_2 was present on the surface. Also, the addition of nano-calcium silicate into PEEK can significantly promoted cell attachment, proliferation, and spreading compared with PEEK **(Ma et al., 2014b)**. A review of strategies to improve the bioactivity of PEEK has been reported recently **(Ma and Tang, 2014).**

In addition to improving bioactivity of PEEK, the incorporation of bioactive fillers into PEEK provides control on mechanical properties. The preliminary research works on the addition of HA into PEEK were to characterize the composition and investigate thermal characteristics of the

compound **(Abu Bakar et al., 1999, Abu Bakar et al., 2003a)** whereby it was proved that HA filler does not have adverse effect on crystallization and melting processes of the compound. Mechanical behaviour of PEEK/HA composites has also been studied extensively **(Fan et al., 2004, Abu Bakar et al., 2003c, Tang et al., 2004, Abu Bakar et al., 2003b, Abu Bakar et al., 2003a).** According to the results, elastic modulus, compressive strength and micro hardness is enhanced by increasing HA loading, while tensile strength, toughness and strain to failure is decreased. Loading PEEK with 40% HA has been shown to decrease the ultimate tensile strength (UTS) of the PEEK by 45%, to 44MPa, which is within the range of cortical bone **(Kurtz and Devine, 2007)**. Therefore, the bioactive PEEK/HA biocomposites have the potential for use as an alternative biomaterial for load-bearing orthopaedic application.

Micromechanical analysis on the injected moulded PEEK/HA biocomposites **(Fan et al., 2004, Tang et al., 2004)** revealed that HA and β-TCP do not show a strong bonding to the PEEK matrix, unlike carbon and/or glass fibre additives. **Fig. 2.7** depicts the fracture surface of PEEK-HA composites in which HA particles are debonded from the PEEK matrix. To overcome this problem, a novel PEEK/HA biocomposite prepared using well-dispersed HA nanoparticles by Wang et al. **(Wang et al., 2010, Wang et al., 2011)** which exhibited enhanced mechanical properties and a high surface HA content. In particular, a good PEEK-HA interface could be achieved and no PEEK-HA debonding occurred. However, their proposed technique suffers from agglomeration of HA nanoparticles when the loading gets more than 10 vol.%.

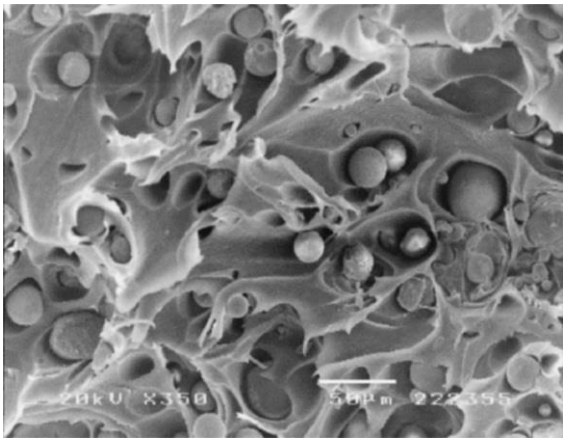

Figure 2.7 SEM of the fracture surface of a PEEK- 10% HA composite, reproduced from **Tang et al. (2004)**

In vitro bioactivity study of PEEK/HA and β-TCP composite conducted by **Yu et al. (2005)** and **Petrovic et al. (2006)** provided encouraging results regarding the bioactivity of PEEK/HA and β-TCP composites. Petrovic et al. **(2006)** studied the viability and proliferation of normal human osteoblasts onto PEEK and PEEK compounded with 5-40 vol.% β-TCP. Their results showed that PEEK possesses good biological interaction even without the addition of

traditionally bioactive components as enhancements. Invibio performed in vitro studies on PEEK/HA biocomposite with 20 vol.% HA loading in their specialized medical grade PEEK called "PEEK-OPTIMA" and they observed apatite formation in the correct Ca/P ratio of 1.67 after immersion in simulated body fluid (**Fig. 2.8**).

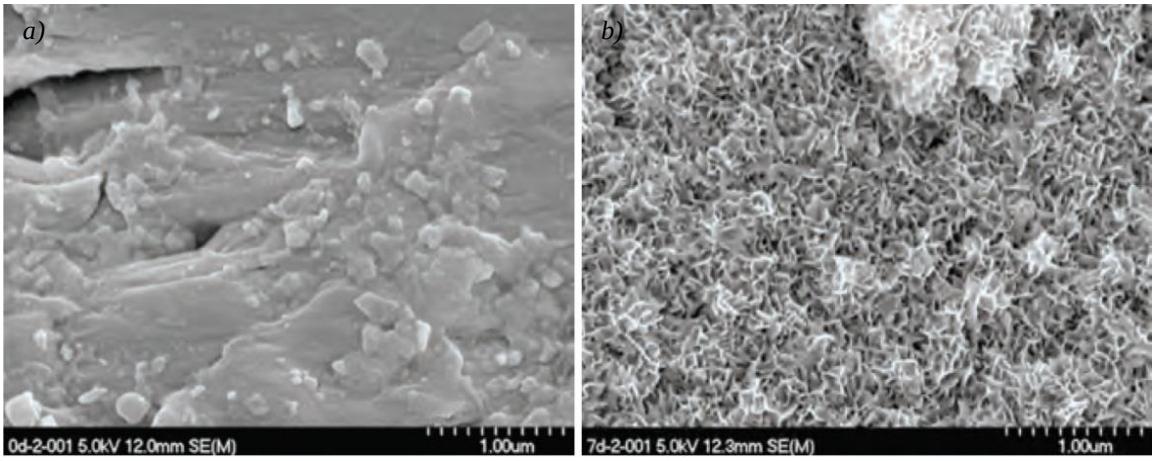

Figure 2.8 SEM of **(a)** PEEK/HA (20 vol.% HA loading) composite before immersion in simulated body fluid, and **(b)** Showing formation of apatite on the surface after 7 days' immersion **(Invibio Ltd)**

Different processing methods such as compounding and injection moulding **(Abu Bakar et al., 2003c, Tang et al., 2004, Abu Bakar et al., 2003a)**, compression moulding **(Wong et al., 2009, Converse et al., 2007, Converse et al., 2009, Converse et al., 2010)**, cold press sintering **(Yu et al., 2005, Hengky et al., 2009, KIM et al., 2009)**, and SLS **(Tan et al., 2003, Tan et al., 2005b, Schmidt et al., 2007)** have been used to produce bioactive PEEK/HA or β-TCP composites. Functionally graded PEEK/HA biocomposites can also be produced via layer-by-layer casting method **(Pan et al., 2013)**.

Compounding and injection molding has been used extensively to make PEEK/HA compound with maximum 40 wt.% HA loading **(Abu Bakar et al., 2003c, Tang et al., 2004, Abu Bakar et al., 2003a)**. Injection moulding is a low-cost process suitable for high-volume commercial manufacturing of near net shape PEEK compounds. However, the quantity at which bioactive fillers may be loaded is strictly limited, as high loading increases melt viscosity resulting in inconsistent and unreliable mixing **(Roeder and Conrad, 2012)**. Furthermore, material removal may be required to reveal bioactive fillers on the surface of injection moulded PEEK compound.

Yu et al. **(2005)** used pressure-less sintering to make PEEK/HA specimens for biocompatibility testing. In cold press sintering, there is no limitation on the loading of bioactive fillers but the process suffers from residual porosity in composite due to pressure reduction during sintering.

Conversely, compression moulding is a manufacturing platform offering greater flexibility, and shown to be well-suited to the synthesis of PEEK/HA composites. It is low-cost, suitable for

high-volume production of high-density PEEK compounds, and more critically tailored porosity. Porous PEEK compounds can be realized by integration of compression moulding and particulate leaching. In particulate leaching, a fugitive particle (e.g. sodium chloride) is added into the compound that is further leached out by soaking the compound into a solvent post-moulding **(Roeder and Conrad, 2012)**. **Fig. 2.9** is schematic illustration of the integrated compression moulding and particulate leaching method developed by Roeder's research group **(Converse et al., 2010, Converse et al., 2007, Roeder and Conrad, 2012)** for the production of bioactive and porous PEEK composites of various sizes and shapes.

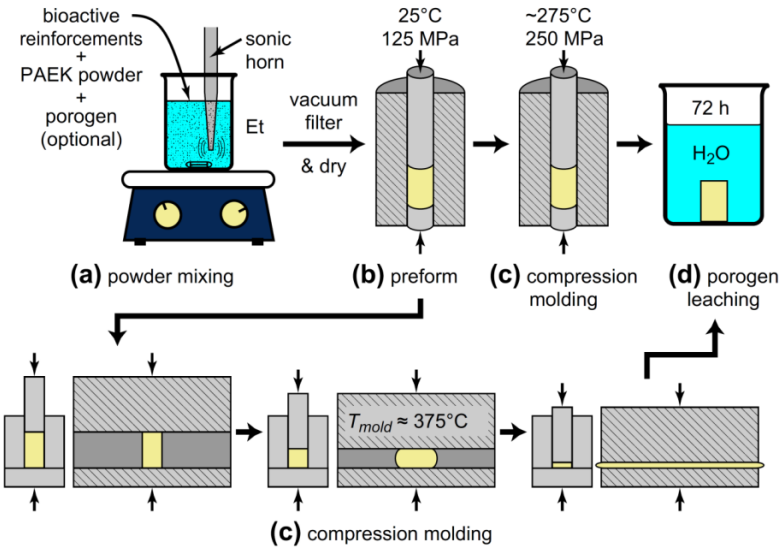

Figure 2.9 Schematic diagram showing integrated compounding and compression molding. The process steps include **(a)** powder mixing in suspension and wet consolidation, **(b)** cold pressing a composite preform, **(c)** compression molding in dies designed for controlled flow and final shapes, **(d)** leaching the porogen (if applicable) **(Roeder and Conrad, 2012)**

SLS is capable of fabricating bioactive porous structures with very complex architecture, thus permitting greater design freedom. This process has been applied to form both porous natural grade PEEK and porous bioactive PEEK components. Tan et al. **(2003)** used SLS process for the first time to produce biocomposite PEEK/HA tissue engineering scaffolds. Use of SLS technique has been hampered by difficulty in loading the quantity of bioactive filler beyond 22% by volume (v/v), and exceeding porosity beyond 70%–74% (v/v) **(Tan et al., 2005, Kim et al., 2009)**.

Table 2.5 depicts summary of different medical grade PEEK compounds produced using different processing techniques with their bioactivity test results. Compression moulding is perhaps the most appropriate form of material processing to produce bioactive PEEK compounds due to its ability to incorporate both porosity and bioactivity into PEEK with fewer limitations in terms of cost, pore interconnectivity, and level of bioactive filler loading in comparison to other techniques.

Table 2.5 Summary of the PEEK compounds produced using various processing techniques **(Ma and Tang, 2014)**

PEEK composites	Fillers	Processing techniques	Research results related the bioactivity of the composites	References
PEEK/HA	Conventional HA particles	SLS	Cell tests: with improved osteoblast growth compared to TMX and PVC; higher HA contents with enhanced cell proliferation and osteogenic differentiation	**(Zhang et al., 2009)**
Porous PEEK/HA	Conventional HA particles	SLS	SBF immersion test and cell tests: with precipitation of apatite-layers; with positive cell adhesion and growth compared to control (no specimens)	**(Tan et al., 2003, Tan et al., 2005a)**
PEEK/Carbon black/ β-TCP	Nano-sized carbon black powders, Conventional β-TCP powers	SLS	Cell tests: with no improvement of cell proliferation compared to pure PEEK and carbon black/PEEK	**(Pohle et al., 2007, von Wilmowsky et al., 2008)**
PEEK/Carbon black/ bioglass	Nano-sized carbon black powders, Conventional bioglass powders	SLS	Cell tests: with improvement of cell proliferation compared to PEEK, carbon black/PEEK, and carbon black/β-TCP/PEEK	**(von Wilmowsky et al., 2008)**
PEEK/HA	Conventional HA particles	Melt compounding, granulation and injection molding	N/R	**(Abu Bakar et al., 2003b, Tang et al., 2004, Abu Bakar et al., 2003c, Abu Bakar et al., 2003a)**
PEEK/HA	Conventional HA whiskers	Powder processing and compression molding	N/R	**(Converse et al., 2007)**
PEEK/HA	Conventional HA powders	In situ synthetic process	In vivo: the new bone tissues surrounding the composite grow faster with a higher HA content	**(Ma et al., 2012a, Ma et al., 2013)**
PEEK/HA	Conventional HA powders	Mixing, compaction and pressureless sintering	SBF immersion test: the 40 vol %-HA composite was covered by apatite-layer after 3 days; the growth rate increased with HA volume fraction	**(Yu et al., 2005)**
PEEK/Sr-HA	Conventional Sr-HA powders	Mixing, compression and molding	SBF immersion test and cell tests: with improved apatite-formation ability and mineralization compared to HA/PEEK or pure PEEK	**(Wong et al., 2009)**
PEEK/bioglass	Conventional Chopped E-glass fibers	N/A	Cell tests: with improved cell proliferation, ALP activity and OC production compared to polystyrene	**(Lin et al., 1997)**
PEEK/β-TCP	Conventional β-TCP powders	Injection and molding	Cell tests: with inhibited cell proliferation, but with no concentration-dependent decrease	**(Petrovic et al., 2006)**
PEEK/HA	Nano-sized HA particles	Compounding and injection molding	N/R	**(Wang et al., 2010, Wang et al., 2011)**
PEEK/HA	Nano-sized HA particles	In situ synthetic process	N/R	**(Ma et al., 2012b)**
PEEK/HA	Nano-sized HA rods	Powder processing and sintering	Cell tests: with improved apatite-formation ability, cell adhesion and proliferation compared to pure PEEK	**(Li et al., 2012)**

Alternatively surface modification has been used to enhance the mechanical and biological properties of PEEK **(Wang et al., 2010b, Lu et al., 2015, Xu et al., 2015, Wakelin et al., 2015)**. PEEK-bone interface is improved (i.e. higher bone-to-implant contact ratio) by coating PEEK and/or PEEK composites with titanium **(Han et al., 2010, Rust-Dawicki and Cook, 1995)** or HA **(Lee et al., 2013, Briem et al., 2005, Ha et al., 1994)** with no adverse effects on strength and toughness. Uncoated and titanium coated CFR-PEEK rods were implanted by Rust-Dawicki and Cook **(1995)** in dogs for 8 weeks to assess bone apposition as well as bone–implant interface strength using push-out testing. According to their results, apposition of bone for both coated and uncoated PEEK was observed but coated implants exhibited significantly greater bone apposition than the uncoated implants, although no significant difference in interface strength between the two groups of implants was realized. Plasma deposition techniques **(Schröder et al., 2002)** and wet chemistry **(Noiset et al., 2000)** can be served to improve biocompatibility and bioactivity. Thermal plasma spraying is used for coating of commercial PEEK orthopaedic implants with HA. Current commercial implants are coated by plasma spraying with titanium, followed by thermal plasma coating with HA **(Kurtz and Devine, 2007)**. Dual coating with titanium and HA is used to provide bone with titanium (the well-proven biocompatible implant surface) after HA absorption in vivo **(Ha et al., 1997)**.

Furthermore, controlled porosity in surface/structural of PEEK implants has been identified as an asset to improve bone apposition **(Jarman-Smith et al., 2012, Zhao et al., 2013, Wang et al., 2014)**, while it adds more complexity from manufacturing prospective. The channels in the porous materials can help the alignment and differentiation of cells **(Bhuthalingam et al., 2015)**. Formation of pores within PEEK results in a physical form that more closely replicates the natural tissue and allows the integration with cellular component, orientation of cells in configuration closer to nature, and enhanced fixation of device **(Jarman-Smith et al., 2012)**.

Manufacturing of porous PEEK materials has been widely investigated for use in different industries but has been limited for medical application by either the type of manufacturing technology or its ability to fulfil the key end-user requirements for orthopaedic application that are **(Jarman-Smith et al., 2012)**:

- The pore interconnectivity needs to be sufficient for cells infiltration and perfusion, and
- The pore size must be suitable (~100-600 μm) to permit cells and vascularization of the biomaterial, and yet able to retain desirable structural integrity to resist the mechanical forces

This is not easily achievable by direct utilization or modification of the current available industrial porous material manufacturing technologies, due to their limitations such as unsuitable producible geometries and process contamination. For instance, some industrial processes use chemical blowing agents such as magnesium hydroxide, pyromellitic acid or sodium borohydride which requires concentrations up to 20% of the foaming agent and leave metal oxide or carbonized organic residues in the porous foam **(Jarman-Smith et al., 2012)**. It is possible to use

gas-assisted injection molding (such as that of MuCell, USA) to avoid the use of blowing agents, however, the closed cell porosity is merely possible with pore size up to 100 μm **(Jarman-Smith et al., 2012)**. A few industrial techniques have been identified as transferable into medical. Techniques such as particulate leaching, heat and compression sintering, injection moulding, micromachining, sulfonation treatment, and SLS have been used to make porous PEEK for medical applications **(Zhao et al., 2013, Jarman-Smith et al., 2012**). These processes have been assessed extensively to provide controlled surface texture and porosity with medical grade PEEK implants.

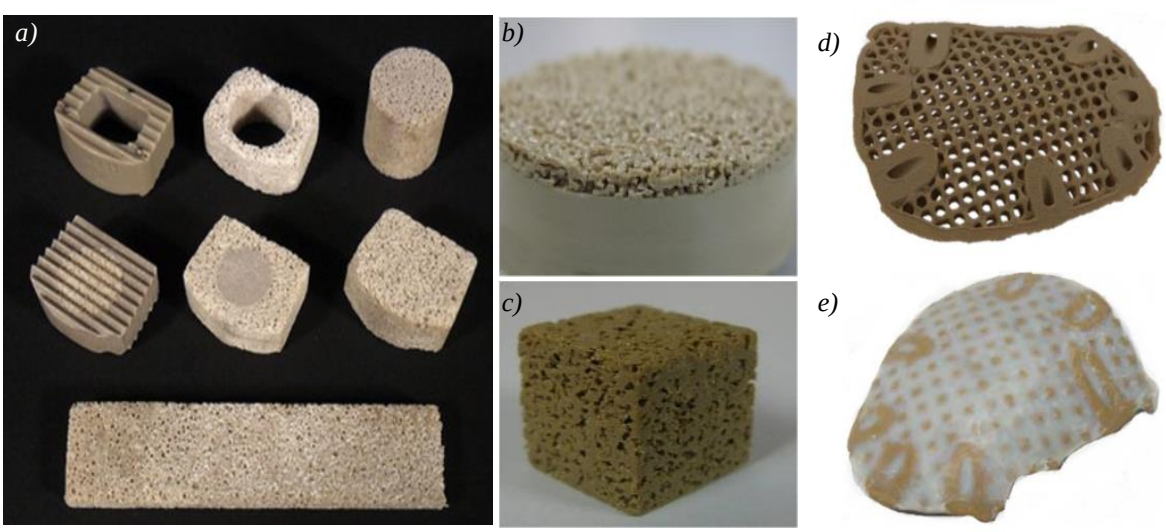

Figure 2.10 (a) Porous bioactive PEEK composites of varying pore size and simple external shape produced by compression molding and particulate leaching, compared with a commercial cervical spinal fusion cage (upper left) **(Roeder and Conrad, 2012), (b,c)** porous PEEK structures with simple external shape made by Invibio using particulate leaching method **(Invibio Ltd), (d)** Cranial porous PEEK implant with computer-controlled complex external shape made by EOS P800 SLS machine, the grade of PEEK has been modified (PEEK-HP3) by EOS and Victrex to cater for unique demands of laser sintering such as the high energy needed and optimizing the flow of the material for distribution **(Manning, 2012) (e)** Infiltrated PEEK implant with a bioabsorbable polymer/HA biocomposite **(Manning, 2012)**

Particulate leaching is a flexible and economic platform among currently available porous PEEK manufacturing techniques but it lacks versatility and suffers from limitations such as manual intervention, inconsistency, and has less control on microstructure (e.g. porosity) and macrostructure (e.g. architecture) so that very simple geometries can be produced (see **Fig. 2.10a, b,** and **c**). The porous PEEK implants produced by machining or injection moulding can include simple holes for bone in-growth but SLS process can fabricate much more complex external shape and greater control on pore size/shape that brings more design freedom to implant designers. As mentioned earlier, SLS have been employed to produce both porous PEEK and porous bioactive PEEK compounds **(Tan et al., 2003, Tan et al., 2005b, Schmidt et al., 2007, von Wilmowsky et al., 2008).** EOS GmbH, leading laser-based AM system provider (www.eos.info), produced the first commercial high-performance selective laser sintered PEEK part with a tensile strength up to 95 MPa and a Young´s modulus up to 4.4 GPa. Smithers Rapra

group (http://www.smithersrapra.com) employed EOS' specialized laser sintering machine through Custom IMD project to fabricate custom-made cranial implant (**Fig. 2.10d**). To further promote bone growth, the finished laser sintered PEEK implant was infiltrated with a bioabsorbable polymer filled with 50% HA nanoparticles (**Fig. 2.10e**).

2.5 Summary

A tissue scaffold plays a very important role in the process of tissue engineering for the growth of new, or repairs of defected tissue. A scaffold provides the necessary support for cells to proliferate and maintain their differentiated functions, and its architecture defines the ultimate shape of a new organ. As such, without the presence of a scaffold, the cells for growth would not have an appropriate medium in which to propagate and grow around, preventing the generation of new tissue. Extrusion-based AM systems are favourable to print scaffolds because of their ability to process a wide range of biomaterials, great control on porosity, and pores interconnectivity which is important to allow the proper cell in-growth. Extrusion-based AM systems with and without material melting were reviewed comprehensively in this chapter. Direct-write assembly and 3D bioplotting methods can process a wide range of soft biomaterials, while SEF method has shown to be well-suited to print hard ceramics. Scaffold-free approach can also be used for direct cell-based bioprinting of living structures, although the printed bioconstructs lack of sufficient mechanical strength and resolution. Hybrid scaffolds are printed by computer-controlled dispensing of cell-embedded hydrogels and growth factors within biodegradable polymers struts such as PCL which is used to improve mechanical strength.

PEEK is an excellent biomaterial choice for development of medical devices and orthopaedic applications, although it does not have sufficient bone apposition in vivo. Addition of bioactive fillers, and incorporation of porosity into PEEK have been shown to be effective strategies for improving bone-implant interfaces and osseointegration of PEEK-based devices. Different manufacturing techniques such as compounding and injection moulding, compression moulding, particulate leaching, and SLS are being served for production of the bioactive and/or porous PEEK compounds. Each of these bioactive PEEK manufacturing methods has its own advantages and disadvantages. The techniques such as compression moulding and particulate leaching are cost effective while they subject to limitations in terms of micro/macrostructure and consistency. Injection moulding has higher level of control on part architecture but the quantity at which bioactive fillers may be loaded is limited. SLS process provides a great control on pore size and part external geometry but it is expensive technology to run, and thus non-economic approach. The main limitation in all of these techniques is lack of control on distribution of bioactive fillers within the PEEK matrix.

Chapter 3

Low-Temperature Extrusion Freeforming of Ceramics

Chapter 3: Low-Temperature Extrusion Freeforming of Ceramics

3.1 3D Printer Set up

An existing 3D stage (Parker Hannifin Automation, UK) was used and programmed for low-temperature 3D printing of lattice structures from range of ceramics such as HA, alumina, zirconia. As seen in **Fig. 3.1**, the designed device possesses four main features including three X, Y, and Z axis and a paste extrusion head. The paste extrusion head comprises a stainless steel syringe which can move in Z direction and the build substrate can move in X and Y directions. The extrusion head extrudes ceramic paste into fine filaments and movement of XY table results writing of paste on substrate. For 3D writing, the extrusion head moves up for a fine pre-set amount, called "nozzle/layer gap", and dispenses a new layer on the previous printed layer. By repeating this procedure the whole lattice structure can be printed layer-by-layer.

The experimental set up for fabrication of bioceramic scaffolds comprises three-axis table (Parker Hannifin Automation, UK) with three linear servo motors driving the XY table and Z axis, and a stepper motor (200 steps/rev, SL0-SYN step motor, Warner Electric, USA) driving a 2mm-pitch lead screw to make continuous force on syringe plunger containing HA paste. A 100-1 reduction gear box was used to decrease speed of the stepper motor to reach a smooth displacement. The extrusion pressure is measured by a load cell which is mounted on the extrusion axis. In the meantime, load cell is necessary to provide the over-load alarm. A 6K4 motion controller (Parker Hannifin Automation, UK) was used to controls the driving motors for the movement of X, Y and Z-axes and extrusion. In this operating system, Motion Planner (Parker Hannifin Automation, UK) was used to control extrusion freeforming worktable as "engine" and LabVIEW 8.2 (Laboratory Virtual Instrument Engineering Workbench, National Instrument) was used to develop a user friendly graphical user interface (GUI). LabVIEW is a powerful and flexible graphic programming language and provides a platform to efficiently develop user interfaces and to display data. A labVIEW program was constructed in two parts: the front panel and the block diagram. The Front Panel was used for the user to input data, adjust process parameters such as extrusion speed, number of layers, XY table moving speed, etc. Compucam 1.4 (Parker Hannifin Corporation, UK) was used to convert the CAD files into the Motion Planner program. In short, desired 2D structures were first drawn by the Solidworks software and then transferred into Motion Planner program. The programs written by Motion Planner were then exported to LabVIEW and changed to sub-programs by entering the paths and names of the files. So, the extrusion freeforming worktable was controlled by the Front Panel of the LabVIEW.

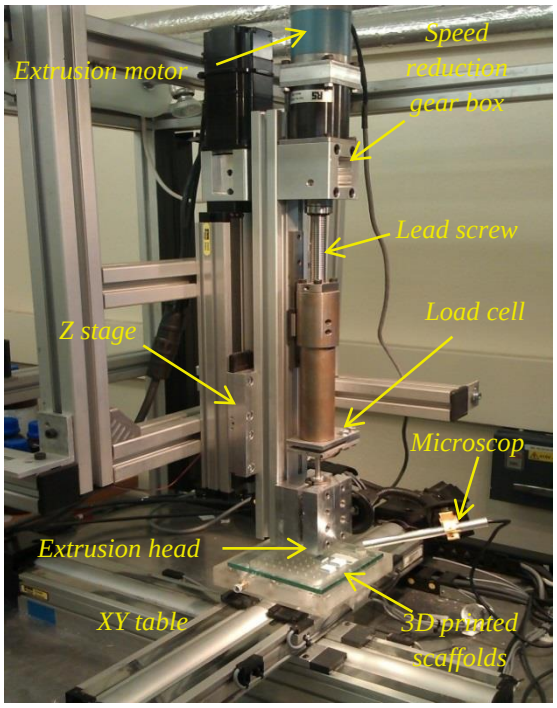

Figure 3.1 Experimental set up for 3D printing of bioactive scaffolds

3.2 Materials and Method

The process of solvent-based extrusion freeforming of the ceramic scaffolds involved the following steps: (i) preparation of ceramic paste, (ii) 3D printing, and (iii) drying, debinding and sintering of the 3D printed scaffold **(Fig. 3.2)**.

For production of ceramic paste, adhesive binder polyvinylbutyral (PVB), and plasticizer polyethyleneglycol (PEG) were fully dissolved in propan-2-ol solvent, with the ratio of 75% (w/v) PVB and 25% (w/v) PEG. Ceramic powder was then added (60% (v/v) of ceramic based on the dried paste) to the solution, and stirred for 2 hours to achieve a well-dispersed solution. The addition of binder and plasticizer into ceramic powder provides adequate rheological characteristics and allows the extruded filaments to have plastic deformation and retain their shapes after extrusion. Following this, excess solvent was evaporated by fast stirring, and blowing hot air using hairdryer until a viscous ceramic paste was achieved. Ceramic paste was then loaded into a homemade stainless steel syringe for 3D printing. The extrusion process formed lattice-shaped 3D scaffolds (scaffold length is within the range of 5-20 mm), by incrementing regularly arranged 2D layers in the vertical axis. Following the printing process, it is necessary to dry the scaffolds. Standard practice to achieve this is to leave the scaffold at room temperature for 24 hours to allow evaporation of excess solvent, and subsequently to place the scaffold in an oven for debinding and sintering. Different heating procedures can be applied depending on the type of ceramic. The sintering protocol

for HA was developed from Evans and Yang' previous studies **(Yang et al., 2008c)** in which the maximum sintering temperature was 1300°C with a dwelling time of two hours.

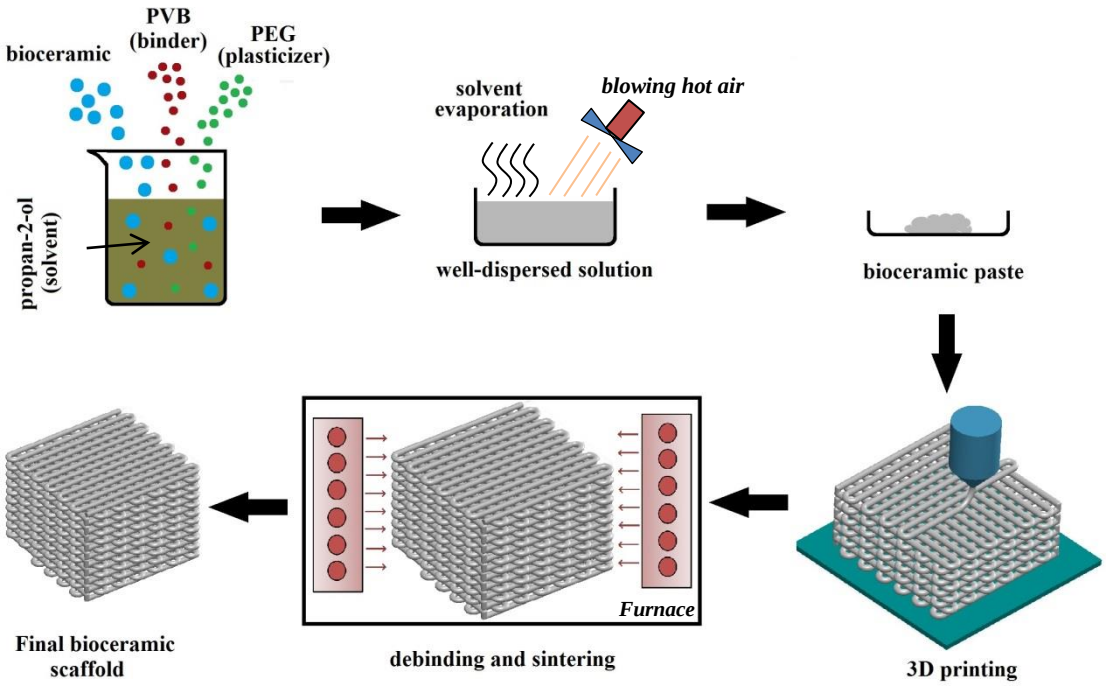

Figure 3.2 The SEF process steps

The following materials were used to form the ceramic pastes: (i) hydroxyapatite powder (HA, $Ca10(PO4)_6(OH)_2$, Grade P221 S, Plasma Biotal Ltd. UK) with particle size within the range of 1-5 μm and density of 3156 kgm^{-3}; (ii) alumina powder (Al_2O_3, ex Condea Vista, Tucson Arizona), having a purity of 99.99%, typical particle size of 0.48 μm and density of 3960 kgm^{-3}; (iii) zirconia powder (HSY-3, Daichii Kingenso, Japan) with density of 5.68 g/cm^3; (iv) poly(vinyl butyral) (PVB, Grade BN18, Whacker Chemicals, UK) with density of 1100 kgm^{-3}; (v) poly(ethylene glycol) (PEG, MWt = 600, Whacker Chemicals, UK) with density of 1127 kgm^{-3}; (vii) propan-2-ol (Fisher Scientific, UK) with density of 789 kgm^{-3}.

3.3 Analysis of Paste Extrusion

There are four stages in paste extrusion as shown in **Fig. 3.3**: 1. Compaction, 2. Transient, 3. Steady stage, and 4. Dead zone stage.

By applying extrusion force, paste volume is decreased and the entrapped air in the paste can be excreted. The pressure gets higher by compression of paste in a short period of time. The pressure augments quickly and reaches to the point that paste extrusion is taken place. The extrusion pressure needs to be higher than the resistance pressure to allow extrusion of the paste from nozzle. The shear pressure at barrel wall, the paste deformation resistance in

the die entry, and flow pressure in the die are the main resistance pressure for paste flow in extrusion freeforming **(Liu et al., 2013)**. These strongly depend on the paste's rheological properties and the die geometry which will be discussed further.

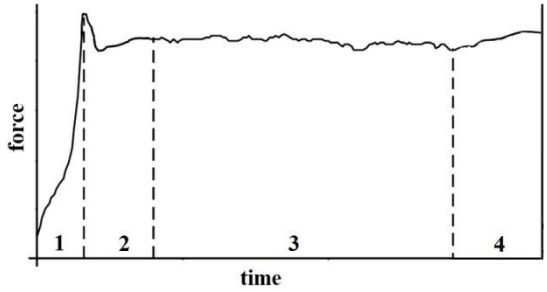

Figure 3.3 Schematic diagram of pressure transient during paste extrusion: 1. compaction, 2. transient, 3. steady stage, and 4. dead zone stage

In ceramic paste extrusion, there is normally a peak point in the end of compaction stage (as can be seen in **Fig. 3.3**) that is due to quick solvent loss/evaporation of the paste in the outlet of die land. In particular, the ceramic paste suitable for 3D printing applications has normally a low solvent content which can easily evaporate when the paste is exposed to air. Therefore, the paste in the outlet is rapidly dried, and consequently the friction force between the die wall and the drier paste gets higher which results in resisting paste flow. Upon the extrusion pressure overcomes this resistance, the drier paste is expelled from nozzle and the paste flows out rapidly to release the excessive pressure. This results in a quick pressure drops and formation of the peak point in the extrusion pressure profile. In extrusion without paste drying in the outlet (i.e. no peak point in the extrusion), the pressure may increase ceaselessly after the paste can be extruded out, that is called "transient stage", till the paste extrusion also reaches a relatively steady status. The stage from starting ram movement to the steady status of paste extrusion is called "initial stage" (compaction and transient steps) **(Liu et al., 2013).**

After the initial stage, the paste extrusion will continue for the period of stable status and the pressure remains relatively constant that is called "steady stage". Normally, little fluctuations occur in extrusion pressure due to temporary inhomogeneity in the paste that is induced by air bubbles and agglomerates. After steady stage, ram reaches to the dead zone (where the paste is stationary in the syringe) which yields to increasing extrusion pressure. The dead zone is dynamically changed in the paste extrusion process. From the point pressure increases to stop of extrusion is called "dead zone stage". Using a faster paste flow (i.e. using a higher ram velocity) the dead zone stage is shorter as it gets less chance to grow **(Liu et al., 2013)**.

It is incumbent to review the principles of paste flow in SEF process before ceramic paste characterization. Although the techniques of generating pressure may differ remarkably in

extrusion freeforming but paste flow through nozzle is common in all techniques. Benbow and Bridgwater **(1993)** presented a general analysis for paste extrusion where they consider only the viscous, plastic, and elastic effects associated with liquid flow as turbulence is absent from paste flows. **Fig. 3.4** depicts the essential parts in a simple system and illustrates the terminology adopted.

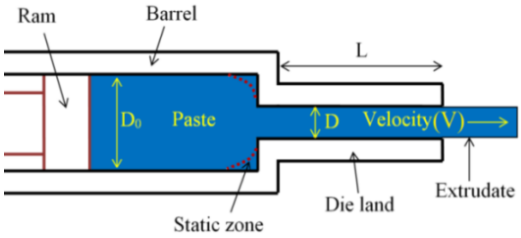

Figure 3.4 Schematic view of extrusion through a square die in a ram extruder

Paste is contained in a barrel of diameter D_0 and is forced by a ram into a die land of diameter D and length L. In proceeding from the barrel into the die land, the paste extends in the direction of flow and its cross-section decreases. In the die land, where the mean extrudate velocity is V, the paste has to overcome the wall shear stress exerted by the wall of the die land. There are thus two parts to the system: flow from the barrel into the die land and flow in the die land. As described earlier, a small static region of paste is produced at the very end of the barrel in the square entry as illustrated in **Fig. 3.4**. The equation proposed by Benbow and Bridgwater, which is used to predict the extrusion pressure consists of the aggregate of two terms **(Benbow and Bridgwater, 1993)**:

$$P_1 = 2(\sigma_0 + \alpha V)Ln(D_0 / D) \tag{3.1}$$

$$P_2 = 4(\tau_0 + \beta V)(L / D) \tag{3.2}$$

where σ_0 is the initial bulk yield stress of the paste, τ_0 is the initial paste-die wall shear stress, α is a velocity-dependent factor for the convergent flow, β is the velocity-dependent factor for parallel flow. The term P_1 liaises to the pressure drop due to the change in cross-sectional area during paste plastic deformation and the term P_2 liaises to the pressure drop induced by paste flow through the die. The shear at the barrel wall causes an extra pressure drop:

$$P_0 = 4(\tau_0 + \beta V_0)(L_0 / D_0) \tag{3.3}$$

where V_0 is the ram velocity and L_0 is the height of the paste in the barrel. This pressure drop can be relatively remarkable for long ram displacements but for the characterization

process it was realized to be negligible in comparison with P_1 and P_2. Therefore, the total extrusion pressure can be determined by:

$$P = P_1 + P_2 = 2(\sigma_0 + \alpha V)Ln[D_0 / D] + 4(\tau_0 + \beta V)(L / D) \quad (3.4)$$

In some pastes it is necessary to treat the liquid-phase terms α and β in a manner that takes account of non-linear behavior. Therefore **(Benbow and Bridgwater, 1993)**:

$$P = P_1 + P_2 = 2(\sigma_0 + \alpha V^m)Ln[D_0 / D] + 4(\tau_0 + \beta V^n)(L / D) \quad (3.5)$$

This increases the maximum number of characterizing parameters to six, namely, σ_0, α, m, τ_0, β and n, three being associated with flow from the barrel into the die land and three with flow along the die land. In the derivation of these equations it has been assumed that the wall shear stress is independent of the local pressure. This is generally found to be true provided there is sufficient liquid to surround the particles completely and this liquid remains in position during extrusion **(Benbow and Bridgwater, 1993)**.

The parameters σ_0 and τ_0 depend strongly on the paste formulation. Previous research has shown that small changes in liquid content (in this study propan-2-ol) in paste affect σ_0 and τ_0, and thus extrusion pressure significantly **(Rough et al., 2002)**. In ceramic paste extrusion, liquid phase migration (LPM) phenomenon may occur which can be described by faster movement of the liquid phase than the solid components in the paste flow process. LPM results in inhomogeneity and temporary variation in liquid content of the paste. Paste's segments of low liquid content are stiffer and therefore require higher stresses to extrude, and extrudate composition can deviate from the desired content; in extreme cases, the extruder nozzle is clogged **(Liu et al., 2013)**.

An alternative analysis approach proposed by Benbow and Bridgwater **(1993)** relies upon a numerical separation of the effects in the die entry and the die land. For a paste flowing from a circular cylinder into a circular die land with a square entry, the Eq. 3.5 can be generalized as:

$$P = f(V)2Ln[D_0 / D] + g(V)4(L / D) \quad (3.6)$$

where f(v) and g(v) are the functions of extrudate velocity.

To enable a better control on the SEF process and getting high resolution bioceramics scaffolds, the parameters affecting paste extrusion needed to be investigated. In this research work both Equations 3.5 and 3.6 are used to characterize the bioceramic paste extrusion.

3.4 3D Printed Ceramic Scaffolds

Different scaffolds were 3D printed successfully from HA, alumina, and zirconia using the bespoke developed extrusion freeforming device by proper adjustment of printing parameters (**Fig. 3.5**). Consistency between scaffolds was achieved through preliminary design calculations, as well as trial-and-error procedures to breach the gap between behaviors of different materials and scaffold designs. HA scaffolds with a range of filament and pore sizes were printed to be used for further PEEK infiltration. Through control of the printing parameters such as solvent content in the paste, nozzle size, paste deposition speed, and build layer thickness it was possible to determine the microstructure of the scaffolds. As seen in the **Fig. 3.5**, the 3D printed scaffolds have quite uniform filament and pore size which proves the ability of the process to accurately control microstructure. This makes the overall process very consistent and repeatable for further use in PEEK compression moulding process.

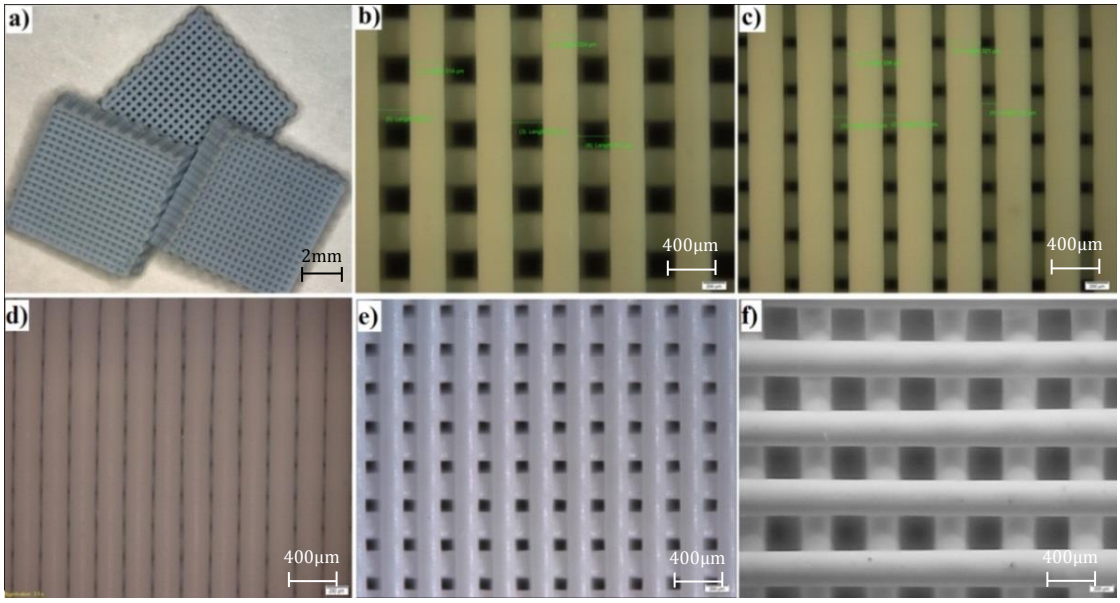

Figure 3.5 (a) Typical 3D printed HA scaffolds, **(b)** top view of HA scaffold, filament size 250 µm, pore size 250 µm, **(c)** top view of HA scaffold, filament size 250 µm, pore size 120 µm, **(d)** top view of HA scaffold, filament size 250 µm, pore size 30 µm, **(e)** 3D printed alumina scaffolds filament size is 250 µm, pore size150 µm, **(f)** 3D printed zirconia scaffold filament/pore size is 250 µm, pore size 250 µm- scale bars are 200 µm

Fig. 3.6 depicts SEM image of a sintered 3D printed HA scaffold and a magnified view of a filament fracture surface (specified by the red rectangle). As seen in **Fig. 3.6b**, the external surface of the sintered HA filament possesses relatively rough surface with micropores within the range of 1-5 µm. The rough surface of HA filaments can play a positive role when

the scaffolds are used as bone scaffold. In the meantime, the sintering-induced micropores in the fractured surface are evident.

The macroporosity is the porosity formed due to spacing between the filaments which are open pores. The microporosity is the porosity inside the filament due to the not-fully-sintered HA and they are closed pores. Both macroporosity of scaffold and microporosity of filaments are controllable in SEF process; macroporosity of scaffold by computer design and microporosity of filaments via alternation in sintering temperature and dwell time **(Yang et al., 2008c)**. The macroporosity and microporosity of the 3D printed HA samples are of key importance in the quality of the scaffold. The macroporosity is a defining factor in the ability of any other materials (such as a tissue culture solution or PEEK) to penetrate the scaffold. As this is a target function of the scaffold, it is important that the scaffolds have optimum levels of macroporosity. The microporosity of the filament defines the volume of sintering-induced micropores and any other micro-air bubbles/spaces inside the filament compared to the total volume of the extruded filament, it is an important factor as high microporosity can greatly decrease the mechanical strength of the scaffold. Generally, there is a need for high compressive strength tissue scaffolds and more specifically in this study for further PEEK infiltration, and therefore a low level of microporosity is desirable.

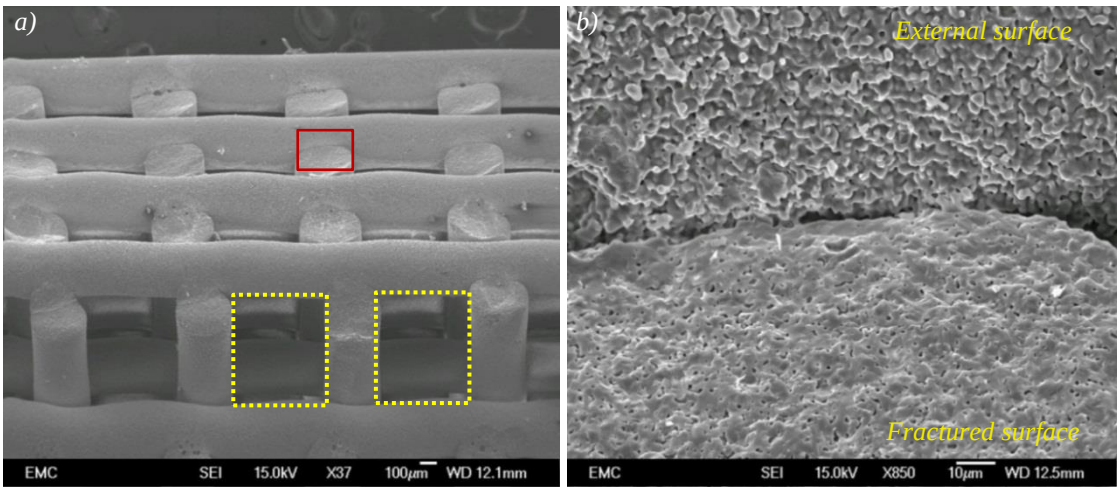

Figure 3.6 (a) A typical sintered HA scaffold with uniform microstructure, **(b)** a magnified image of the selected region (red rectangle) which includes both external and internal surface of filaments

Archimedes' principle was used to measure macroporosity and microporosity of the scaffolds of various pore and filament sizes. The porosity measurement method was developed from **(Spierings et al., 2011)**. To this end, the weighing pan of the balance, onto which the specimen to be measured is usually placed, has been replaced by a specially made arm from which it is possible to suspend the sample from above. The mass of the suspended

HA scaffold (m_s) is measured and then the sample is placed into a small beaker of water (which does not contact the scale), which is boiled in order to evacuate air from within the internal pores of the lattice and the body of water, allowing water to fill the pores. The sample, whilst still submerged in water, is then suspended once more from the balance, and the "wet mass" of the sample (m_w) is measured (The mass that results from the sample being suspended in water). From Archimedes' principle, it is expected that this measured "wet mass" will be lower than that measured when the sample was not submerged, as the liquid will exert a force upwards against the scaffold. The magnitude of this force corresponds to the weight of the water that the scaffold displaces. Initially a cotton thread was used to suspend the sample from the scales; however, due to the absorbent nature of the thread, water saturated the thread, affecting the readings obtained from the scale. In order to prevent this, a very thin, strong and water resistant material was used. Using the data obtained from this experiment, it is possible to calculate the microporosity and macroporosity of the samples by Equations 3.11 and 3.12, respectively:

$$m_{dw} = m_s - m_w \tag{3.7}$$

$$\rho_{water} = 0.998\ \text{g/mL at } 25\ ^\circ\text{C} \simeq 1.000\ \text{g/mL} \rightarrow |m_{dw}\ (\text{g})| = |V_{dw}\ (\text{cm}^3)| \tag{3.8}$$

$$V_{dw}\ (\text{cm}^3) = V_{af}\ (\text{cm}^3) \tag{3.9}$$

$$V_{tf} = \frac{m}{\rho_{HA}} \tag{3.10}$$

$$\text{microporosity of filaments } (\%) = \frac{V_{af} - V_{tf}}{V_{af}} \times 100 \tag{3.11}$$

$$\text{macroporosity of scaffold}(\%) = \frac{V_l - V_{af}}{V_l} \times 100 \tag{3.12}$$

where

m_{dw}: mass of displaced water

$m_{s:}$ mass of suspended scaffold

m_w: mass of wet scaffold

V_{dw}: volume of displaced water

V_{af}: apparent volume of filaments

V_{tf}: theoretical volume of filaments

V_l: total volume of scaffold (determined by measurement of external dimensions using calliper)

Macroporosity and microporosity of HA scaffolds of various pore and filament sizes measured is presented in **Table 3.1.** The macroporosity could be controlled in a wide range, from 33% to nearly 70% in the four samples, with the macroporosity of sample 400.250 being significantly smaller than the others due to its larger filament size. Actually the macroporosity range could be further increased to 20-80% by changing the filament diameter and/or the filament distance. However too low or too high macroporosity might not be ideal for this

application. If the porosity is too low (more HA phase) it will be difficult to infiltrate enough PEEK to provide sufficient mechanical strength to the composite. If the porosity is too high (too little HA) there could be insufficient bioactive phase after infiltration. The microporosity calculated across all samples lies within the range of 7-10% with little variability, showing consistency in the properties of the material used to produce each sample and minimal presence of pores within the filaments.

Table 3.1 Results of macro and micoporosity measurement for HA scaffolds with different filament and pore size

HA scaffold filament(µm).pore(µm)	m_s (g)	m_w(g)	V_l (mm^3)	Macroporosity (%)	Microporosity (%)
240.250	0.5914	0.3892	382.1	56.32	7.17
240.400	0.5701	0.3746	494.3	60.45	7.42
400.250	0.9691	0.6335	505.3	33.50	8.84
240.550	0.4668	0.3035	509.5	67.95	9.25

CT analysis of 3D printed scaffolds revealed that in addition to sintering-induced micropores there are two kinds of air bubbles/voids produced in the scaffolds: air trapped within filaments, and voids at the point of welding between the extruded filaments. These micro air bubbles/voids can affect the structural integrity of scaffolds, and it is important to minimize them to enable compression moulding to be performed without damaging the HA network. **Fig. 3.7** shows a CT image taken of an oblique cross section of a typical 3D printed HA scaffold in which air bubbles/voids are seen. Air bubbles inside extruded filaments (red arrows) are produced during paste preparation (e.g. paste stirring, solvent evaporation, and loading the paste into the syringe).

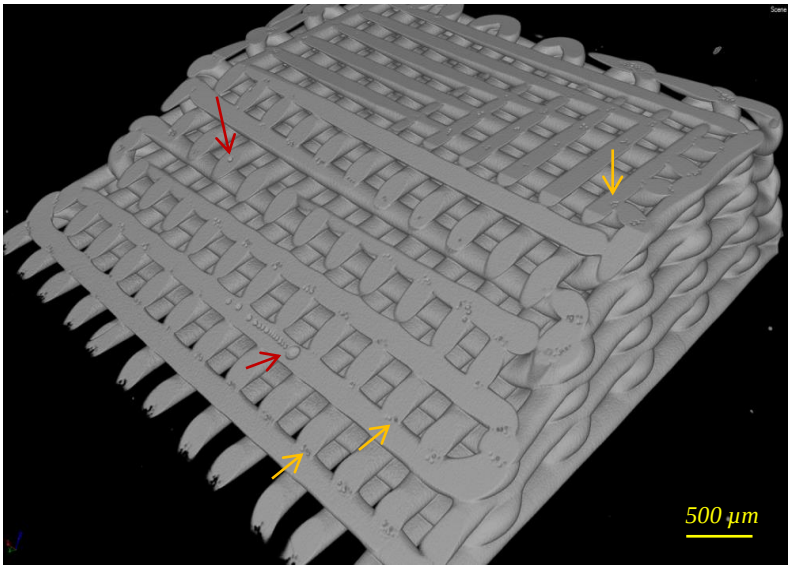

Figure 3.7 CT image of a typical 3D printed HA scaffolds sectioned by horizontal and oblique plans, micro-air bubbles inside filaments (red arrows), and in filaments' welding areas (yellow arrows)

It was found that it is important to initialize the printing by dumping a few centimetres of filament until a stable extrusion started to minimise air bubbles inside extruded filaments. This is because during the paste loading stage, in which the paste is manually pushed into the syringe, the recess of the syringe is not fully loaded and air pockets can be trapped. During the initialization of extrusion, the trapped air is expelled and then extrusion became stable. The finishing of the initialization stage could be determined by reading the extrusion force, which fluctuates during initialization stage but becomes stable later. After paste extrusion reaches a relatively steady state, scaffold printing maybe commenced with a reduction of air bubbles within the filaments. In addition, selection of a finer nozzle in the initial stage requires higher extrusion pressure, and thus more chance for air in the HA paste to be expelled through the outlet in this stage. According to results, air bubbles can be realized inside of filament simply due to large size of nozzle and insufficient initial stage extrusion (see **Fig. A_1**). The mechanism of micro-bubble formation between filaments in the welding zone (yellow arrow in **Fig 3.7**) is yet to be understand.

Solvent content in the prepared HA paste must be also sufficient for formation of a strong weld between layers. If solvent content is too low, resulting in faster extrudate drying and insufficient weld formation, it can affect mechanical strength of the 3D printed scaffold which is critical to sustain subsequent compression moulding. **Fig. 3.8a** demonstrates a sample printed using paste with adequate solvent content in which bonding formed between layers in the slurry state is retained after sintering, and provides a strong bridge between layers. In **Fig. 3.8b**, the weld formed in the slurry state lacks sufficient mechanical strength for compression moulding as the HA paste does not contain sufficient solvent.

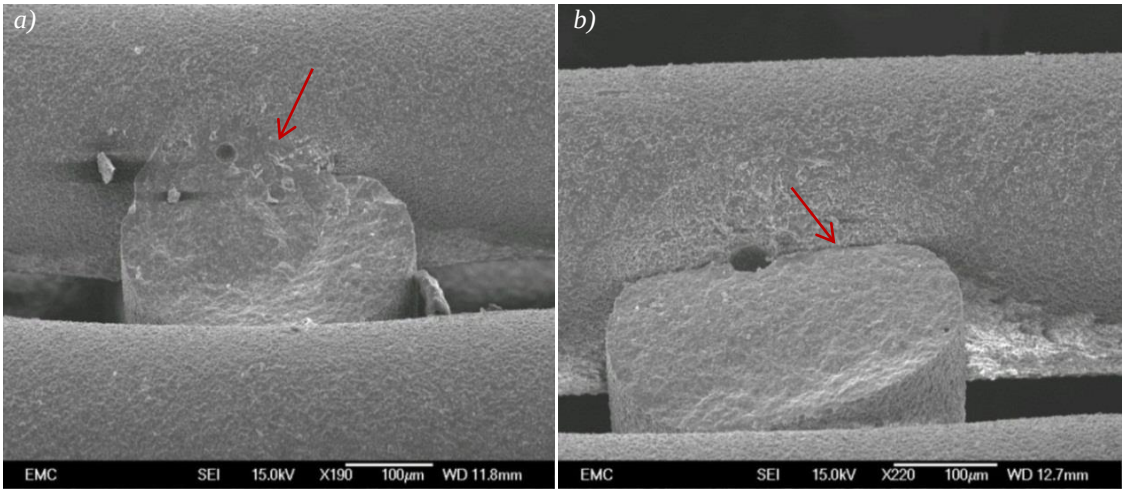

Figure 3.8(a) strong inter-layer bonding due to sufficient solvent content, **(b)** weak layer bonding due to insufficient solvent content

The quality of the lattices produced depended largely on paste rheology and the subsequent paste extrusion settings. The viscosity of the paste when loaded into the extrusion syringe affects the formability and more importantly shape sustainability of the filament that is extruded during the print procedure; a paste with too low viscosity (high solvent content) would result in a filament that is less able to retain its shape, and more likely to deform upon settling on the built layer. This can also bring about deformation of scaffold's edges due to tension on printed filaments during printing (**Fig. 3.9a**). Moreover, in high height scaffolds (heights more than 6 mm), as the print progresses, gravity of printed soft filaments is represented by a characteristic sinking of the middle of the scaffold, causing a concave shaped upper surface to arise (**Fig. 3.9b**). In the case of printing scaffold with a high height using too soft paste, a concave shape may observe on the top surface, but additionally, the sides may take up a slightly concave, skewed profile (**Fig. 3.9c**). In addition, deceleration of XY moving table in the end of extrusion path results in overflowing, and thus more material extrusion in the edges called "overfill" (**Fig. 3.9d**). The error resulted from exceed materials in corners accumulates layer by layer which eventually makes a concave shape. Furthermore, delamination defect may occur when a paste with inadequate solvent is used that yields in insufficient interlayer bonding (**Fig. 3.9e**).

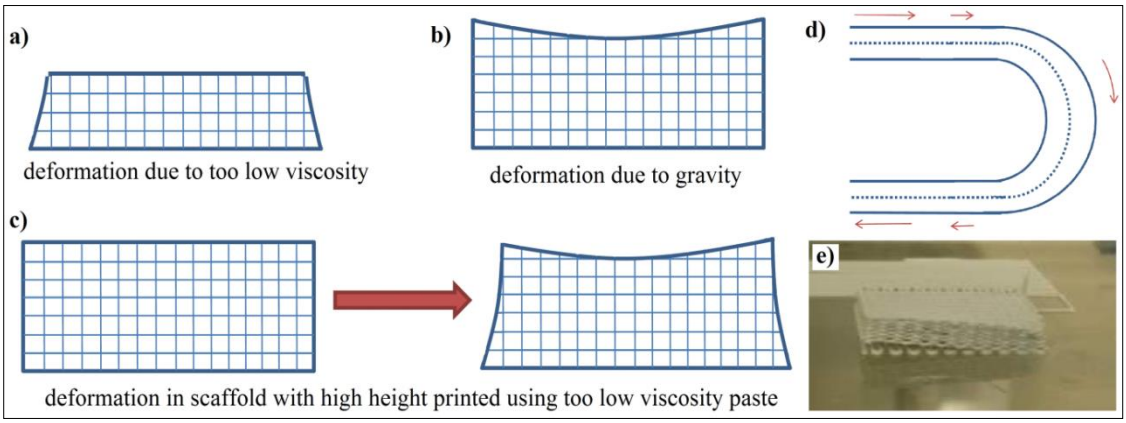

Figure 3.9 Schematic illustration of different deformation in scaffolds; **(a)** deformation in the scaffold printed using a paste with too low viscosity, **(b)** deformation in scaffold due to gravity of filaments when the scaffold has too many layers, **(c)** deformation in scaffolds which has too many layers and printed using a paste with too low viscosity, **(d)** illustration of material accumulation in end of path which can cause concave shape on the top surface after printing, **(e)** typical scaffold printed using a zirconia paste with insufficient solvent caused delamination

In addition to paste viscosity, adjusting the gap between nozzle and built layer affects uniformity and dimensional accuracy of the printed filaments. It was observed that the filaments obtain curved shape upon deposition when the gap between nozzle and built layer is too large as the extrudate is free to deform before laying down on underlying layer. On the other hand, when nozzle/layer gap is not sufficiently large it causes smash of stacked

filaments. The results for adjustment of nozzle/layer gaps for a typical zirconia scaffold fabricated using 200 μm nozzle with various nozzle/layer gap settings including 200 μm, 190 μm, and 170 μm are presented in **Figs. A_2** to **A_4**.

In addition to drying-induced shrinkage, the filaments and pores of the scaffolds experience a noticeable shrinkage after sintering. HA, alumina, and zirconia pastes were prepared and two scaffolds at size 10×10×3mm and various filament/pore size were printed for each ceramic paste to assess sintering-induced shrinkage. Shrinkage for different ceramics were calculated by measuring filament and pore size before and after sintering using an optical microscope. According to the results, zirconia filaments had the highest shrinkage of 21.3%, while alumina had the least shrinkage of 15.3% (See details in **Tables A_1** to **A_3)**.

3.5 Increasing Resolution

As a consequence of what was discussed earlier, extrusion freeforming offers the ability to rapidly print functional materials in complex 3D structures from a diverse array of materials with different resolutions. Extrusion freeforming resolution depends on several factors such as precision of motion system, appropriate adjustment of process parameters (e.g. extrusion speed with regard to XY motion), type of material and paste delivery system. In particular, paste formulation is a crucial factor which determines extrudability, extrusion pressure, and viscoelastic behavior of the paste that needs to be designed for successful high resolution 3D printing. Three main current types of inks/pastes formulation have been designed and served by Lewis and co-workers, leaders in extrusion-based 3D direct writing, for high resolution printing are **(Lewis, 2008)**:

I. Colloidal and nanoparticle inks
II. Polyelectrolyte inks
III. Sol-Gel inks

(I) Colloidal and Nanoparticle Inks

Colloidal inks are great materials for extrusion freeforming of complex 3D structures since their viscoelastic properties can be tailored to facilitate flow through nozzles. These kinds of inks can be extended to any type of colloidal material if their inter-particle forces are controlled to produce the desired solids concentration and rheological properties **(Lewis, 2008)**. 3D lattice structures with minimum feature size of about 100 μm is reported using colloidal inks but further reduction in filament size is possible by using polymeric and metallic nanoparticle inks with maximum particle diameter less than 100 nm **(Lewis, 2008)**.

(II) Polyelectrolyte Inks

Lewis' group **(Gratson and Lewis, 2004)** first drew inspiration from nature to develop concentrated polyelectrolyte complexes that mimic spider silk in a simplistic way **(Lewis,**

2008). This ink design utilizes polyelectrolyte complexes composed of non-stoichiometric mixtures of polyanions and polycations. They first explored mixtures of poly(acrylic acid) (PAA), and poly(ethyleneimine) (PEI) that were nominally 40 wt.% polyelectrolyte in an aqueous solution **(Lewis, 2008)**. Inks with a broad compositional range were formulated with requisite viscosities needed for flow through micro-capillary nozzles of varying diameter. The concentrated polyelectrolyte inks rapidly coagulate to yield self-supporting filaments upon deposition into an alcohol/water coagulation reservoir. The exact coagulation mechanism, driven by electrostatics in a water-rich or solvent quality effects in an alcohol-rich reservoir, as well as the magnitude of ink elasticity depend strongly on the alcohol/ water ratio **(Lewis, 2008)**. By carefully tuning this parameter, the deposited ink filament is elastic enough to promote shape retention, while maintaining sufficient flexibility for continuous flow and adherence to the substrate and underlying patterned layers **(Lewis, 2008)**. Minimum filament size of ~1 μm could be printed using polyelectrolytes inks **(Gratson et al., 2004)**.

(III) Sol-Gel Inks

Sol-gel inks use a sol-gel precursor solution based on a chelated titanium alkoxide, titanium diisopropoxide bisacetylacetonate (TIA). An organic polymer, poly(vinyl pyrrolidone) (PVP), is also included to mitigate stresses that occur during drying and calcination of the as-patterned structures **(Lewis, 2008)**. Unlike the polyelectrolyte inks highlighted above, these sol-gel inks can be printed directly in air. To convert the 3D printed structures to the desired oxide phase, in this case TiO_2, they are calcined at temperatures above 450 °C. This sol-gel ink design and patterning approach can be readily extended to other organometallic precursors. For example, by simply varying the organometallic precursors, inks for microscale patterning of electrically (e.g., doped-TiO_2), transparent (e.g., indium tin oxide), and ionically (e.g., doped-zirconium oxide) conducting oxides can be formulated **(Lewis, 2008)**. The main advantage of these inks is that after calcination the printed structures are subjected to a remarkable, yet uniform shrinkage so that nano-size features can be achieved (**Fig. 3.10**).

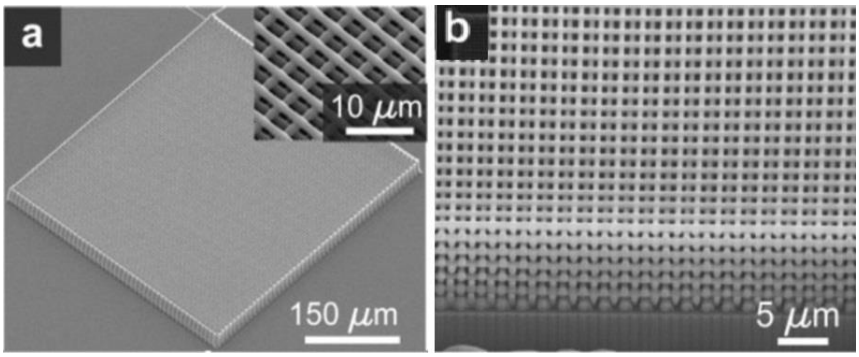

Figure 3.10 (a) lattice structure printed using sol-gel ink (before calcination, filament of 1.212 ± 0.024 μm and pore of 4.002 ± 0.053 μm, **(b)** calcined TiO_2 structure (24-layers) with filament of 520 ± 6 nm and pore of 2.097 ± 0.095 μm heated to 715 °C **(Duoss et al., 2007)**

The unremitting drive toward printing materials at high resolution with faster speed gives rise to many opportunities and challenges. Lewis and co-workers reported printing features as fine as 250 nm for sol-gel inks **(Duoss et al., 2007)**, ~10μm for hydrogel inks **(Barry et al., 2009, Shepherd et al., 2011)**, ~ 1μm for polyelectrolyte inks **(Gratson et al., 2004)**, while they have reported the minimum feature size of ~200 μm for ceramic inks **(Michna et al., 2005, Simon et al., 2007).** The highest resolution ceramic lattice structure is that of has been reported by Evans and Yang's group **(Yang et al., 2008d)** with filaments circa 70 μm printed using SEF method (see **Fig. 2.2**). The main Challenges to decrease nozzle size with the aim of increasing ceramic 3D printing resolution are:

- Increased extrusion force: scaling down the nozzle size for better resolution will make the required extrusion pressure unpractical high for high viscosity ceramic colloidal inks, since the extrusion pressure scales up much faster when the nozzle diameter is decreased according to the Hagen–Poiseuille equation **(Sutera and Skalak, 1993, Chuang and Jingyan, 2013)**.
- Nozzle jamming or clogging due to dilatancy, agglomerates, impurity, process contamination, and quick drying of colloidal ink in outlet of nozzle

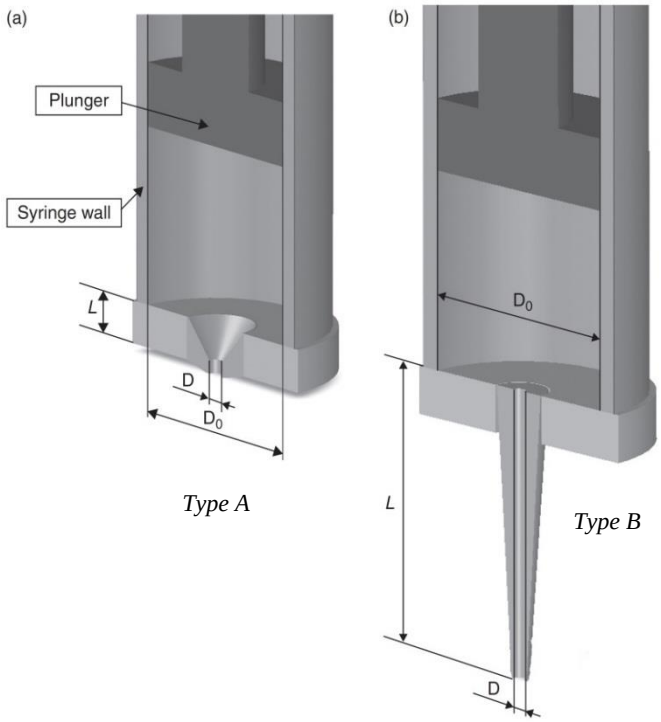

Figure 3.11 Schematic of different nozzle design for extrusion freeforming: **(a)** short die land length to decrease extrusion pressure, **(b)** needle-like nozzle used in PAM and direct-write assembly techniques

According to Equation 3.5, increase in die land length can theoretically result in increment of extrusion pressure which is an obstacle for high resolution printing. That is why extrusion

pressure is remarkably higher in PAM or direct-write assembly processes than SEF method as they use needle-like nozzles (design type B in **Fig. 3.11)**. Therefore, these processes are normally used for printing soft materials like hydrogel or biopolymer inks, while Evans and Yang's group used a novel nozzle design with a short die land length (similar to the design type A in **Fig. 3.11**), and a unique paste formulation which allowed them to reduce extrusion pressure and avoid nozzle jamming for printing ceramic scaffolds.

The objective of this research work is to investigate the control factors affecting the ceramic extrusion resolution including paste formulation, extrudate velocity, and nozzle geometry, in order to increase the resolution of ceramic extrusion freeforming. In this project, Benbow's model was used effectively to characterize HA paste extrusion. In addition, factorial design of experiment (DOE) was served for statistical analysis of contribution of each control factor on the extrusion pressure and the results were considered as a guide for 3D direct writing of high resolution ceramic scaffolds. HA scaffolds with filaments as fine as 30 μm could be printed for the first time by carefully adjusting the process parameters.

A series of experiments were performed to investigate the influence of paste formulation (solvent content), die land length and geometry (L and D), and extrudate velocity on the extrusion process using the Benbow's model. Three different HA pastes with solvent content of 10.2 wt.%, 13.4 wt.%, and 15.2 wt.% were prepared and extruded through nozzles with die diameter (D) of 200 μm and different die length of 6.4 mm (L/D=32), 12.8 mm (L/D=64), 25.4 mm (L/D=127) (**Fig. 3.12**). The dimensions are all based on the information provided by the nozzles' manufacture (FISNAR, USA). The nozzles are made from stainless steel tubes epoxy sealed to a polypropylene hub with the ability to work in high pressures. Microliter glass syringes with barrel diameter of 4.6 mm (Hamilton, USA) were used and for each setup different extrudate velocities of 1.0 mm/s, 2.7 mm/s, 5.3 mm/s, and 8.0mm/s were applied. For all the experiments, the extrusion pressure was read in steady state stage (after 120s pre-extrusion as initial stage). The pressures had still fluctuation in steady state zone due to imperfection between ram and the syringe wall, or local agglomerates. The pressures have been reported in this study are the mean of four reading during extrusion with standard deviation varying between 0.02 MPa to 0.25 MPa (more details on standard deviation can be found in statistical analysis section, **Table 3.3**).

The f(v) and g(v) functions for each paste were determined using experimental data whereby the behavior of any other die design can be predicted providing the die has a square entry. To assess accuracy of the determined f(v) and g(v) functions, a series of experiments were conducted through nozzles with die diameters of 0.41 mm and 0.84 mm with different die land length of 6.4 mm, 12.8 mm, 25.4 mm and then the resultant pressures were compared with those calculated from determined f(v) and g(v) functions. In addition, using the four-parameter Benbow's approach the σ_0, τ_0, α, β parameters were calculated for two different pastes with solvent content of 10.2 wt.% and 15.2 wt.% and a linear model was developed

whereby these four parameters can be estimated for other HA pastes with any solvent percentage. To assess accuracy of the developed linear model, these four parameters were calculated through experiment for a paste with solvent content of 13.4 wt.% and the results were compared with those predicted using the linear model.

After characterizing HA paste using the Benbow's model, DOE method was employed for statistical analysis of the effects of different factors on extrusion pressure. Totally 27 experiments for three control factors including L/D, extrudate velocity and solvent content were conducted so that each factor has three levels. Details of control factors and their levels are presented in **Table 3.3**. The experiments were executed with the guidance of the MINITAB 17 software to avoid biased errors based on the experimental sequence. Contour plot of pressure versus different control factors were determined using Akima's polynomial interpolation method **(Akima, 1970)**. Analysis of variance (ANOVA) was then performed using MINITAB's general linear model to determine the statistical significance and contribution of each factor on extrusion pressure.

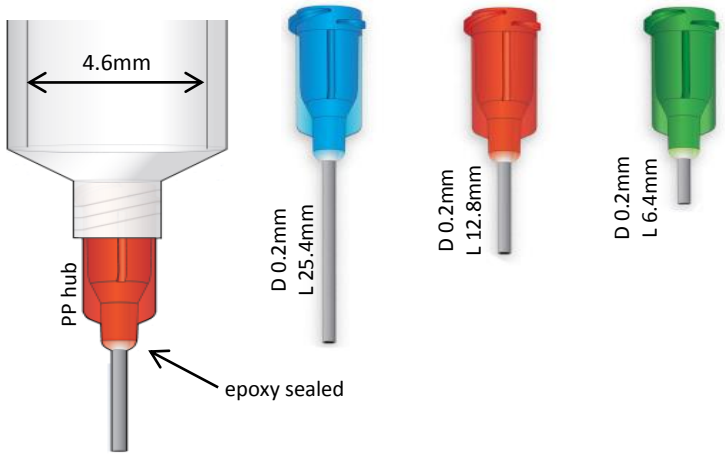

Figure 3.12 Schematic illustration of the syringe and the nozzles with different L/D ratios used for characterization of HA paste using Benbow's model (schematic images reproduced from information provided by FISNAR, USA)

Fig. 3.13 depicts extrusion pressure versus L/D and extrudate velocity for the paste with 10.2 wt% solvent content and die diameter of 0.2 mm. It should be noted that error bars have not been put in the diagrams due to very small variations. The data set for L/D=0 can be determined either extrapolation or estimation based on available experimental date points. In this case, the data for L/D=0 is estimated using the data points for L/D of 32 and 64; as the increment in L/D from 32 to 64 equals the increment from 0 to 32, it was supposed that the extrusion pressure is changed by a same slope. As can be seen in **Fig. 3.13a**, extrusion pressures increase by enhancement of L/D value (i.e. by increasing die land length) which is expected from the Benbow's model as well. **Fig. 3.13b** is extrusion force as a function of

extrudate velocity (cross-plot of Fig. **3.13a**) which indicates that extrusion pressure increases by increasing velocity from 2.7 mm/s to 8.0 mm/s for various L/D in the steady stage which the Benbow's model again provides a qualitative explanation about this.

In **Fig. 3.13b,** in a specific extrudate velocity, when L/D $\rightarrow$0, using the Benbow's alternative model P= f(v)2Ln(D_0/D) and thus the f(v) can be calculated. In addition, when L/D=127, P= f(v)2Ln(D_0/D)+g(v)4L/D, and thus g(v) can be calculated. Similarly for all extrudate velocities of 1.0 mm/s, 2.7 mm/s, 5.3 mm/s, and 8.0 mm/s the f(v) and g(v) were calculated and the result were plotted in **Fig. 3.13c**. Polynomial curves fitted to the points to determine equations for both f(v) and g(v) functions which are independent to die parameters. Therefore, die performance can be predicated and the extrusion pressure for any other die designs with various L/D can be estimated through this approach. For this end, the HA paste from the same batch was extruded through nozzles with different die diameters of 0.41 mm, and 0.84 mm with various die land lengths of 25.4 mm, 12.8 mm, and 6.4 mm. **Fig. 3.13d** depicts the estimated (using f(v) and g(v) functions) and experimental data for the HA paste with 10.2 wt.% solvent extruded through 0.41 mm, and 0.84 mm nozzles with various die lengths. Although the estimated extrusion pressures do not match perfectly with the experimental data, yet they have enough closeness so that the largest deviation observed is 0.68 MPa which is for the velocity of 2.5 mm/s and L/D of 62.

Figs. 3.14 and **3.15** depict the results for HA pastes with solvent content of 13.4 wt.% and 15.2 wt.%, respectively. According to Benbow's equation, the paste formulation (here solvent content of paste) can affect the σ_0, and τ_0 so that when solvent content increases the extrusion pressure decreases which is evident in these experimental results. In addition, by comparing the extrusion pressure in the three different HA pastes, it can be concluded that applying a small decrement in solvent content can result in noticeable increase in the extrusion pressure. The largest deviation for the HA paste with 13.4 wt.% solvent in **Fig. 3.14d** is 0.95 MPa which is for the velocity of 2.5 mm/s and L/D of 62, while that is 0.48 MPa for the HA paste with 15.2 wt.% solvent in **Fig. 3.15d** for the velocity of 0.6 mm/s and L/D of 15. The larger deviation for the HA paste with 13.4 wt.% might be due to inaccuracy of the f (v) function in **Fig. 3.14c** where the deviation between determined points and fitted curve is relatively high.

Although the Benbow's model doesn't provide a highly accurate estimation, yet it was found as a good general model for characterization of HA paste extrusion and quick estimation of extrusion pressure with varying die design and ram velocity. It should be noted that in addition to the assumptions which reduce accuracy of the Benbow's model, experimental noise factors can also be considered as source of these variations. For example, ignoring the paste volume change inside syringe over time induces inaccuracy in the final extrusion pressure. It is almost impossible to make two batches of paste with a same solvent content as the solvent used in this study (e.g. propan-2-ol) is highly volatile, and thus very

difficult to control solvent content within the paste. Even if solvent content is controlled during paste preparation, the solvent can evaporate quickly during paste loading into syringe which is totally uncontrollable. Therefore, in this study a batch of HA paste was prepared and loaded into the syringe and extruded through a nozzle with specific die diameter and length. After extrusion with desired extrudate velocities, the nozzle was simply replaced with a new nozzle and the remaining paste inside syringe was extruded. This is to make sure the solvent content is not changed due to nozzle change, although there is a change in paste volume inside syringe for different nozzles. As extruded paste in each step is a low fraction of the total paste inside syringe using fine nozzles (e.g. 0.2 mm nozzle), the error was assumed to be ignorable in this study. However, as die diameter gets higher (e.g. 0.41 mm or 0.84 mm) the volume change inside syringe over time get higher which results in more inaccuracy in the measured pressure. Therefore, fewer experiments were conducted with limited ram velocities of only 2.5 mm/s and 0.6 mm/s for 0.41 mm and 0.84 mm nozzles.

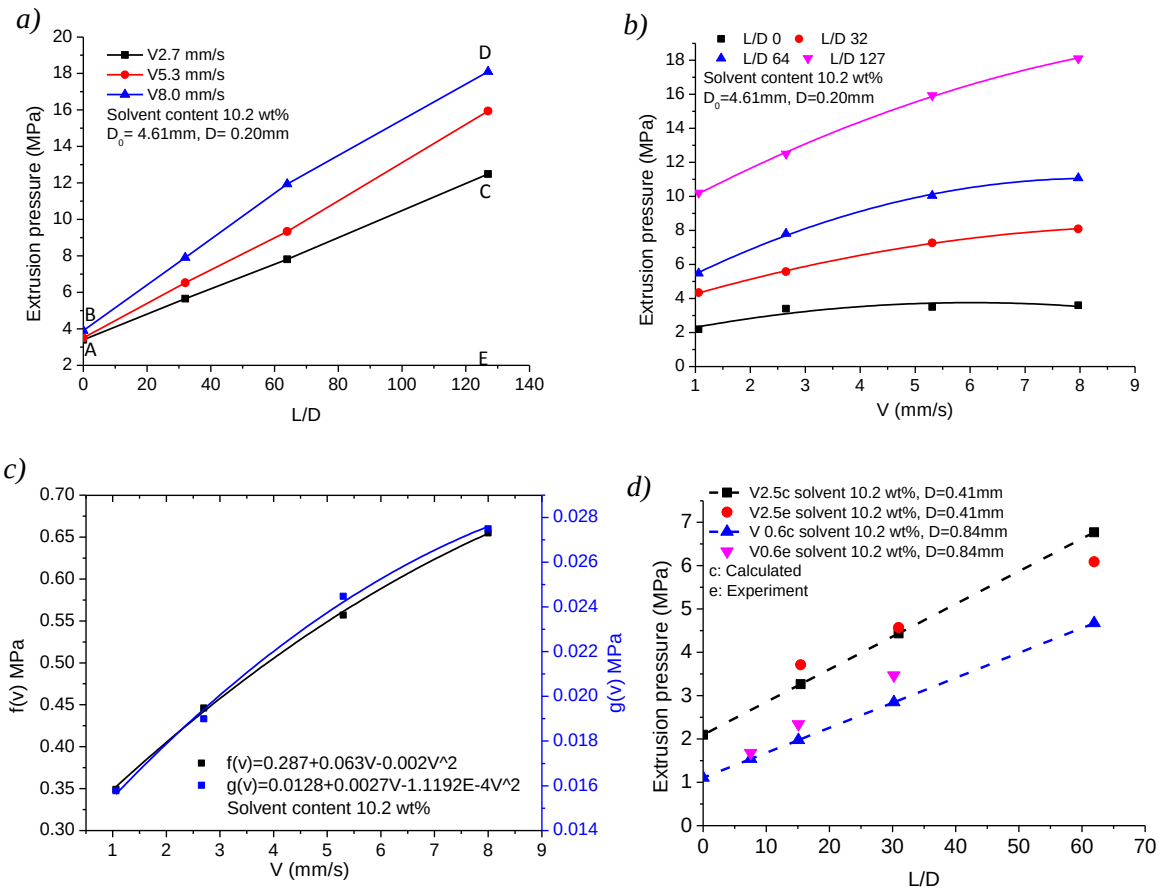

Figure 3.13 (a) extrusion pressure versus die land lengths for various extrudate velocities in the HA paste with solvent content of 10.2 wt.%; **(b)** extrusion pressure versus extrudate velocity for various L/D in the HA paste with solvent content of 10.2 wt.%,; **(c)** f(v) and g(v) functions determined using the Benbow's alternative model for characterization of the HA paste with solvent content of 10.2 wt.%,; **(d)** predicted extrusion pressure versus experimental data for dies with D=0.41mm, and D=0.84mm

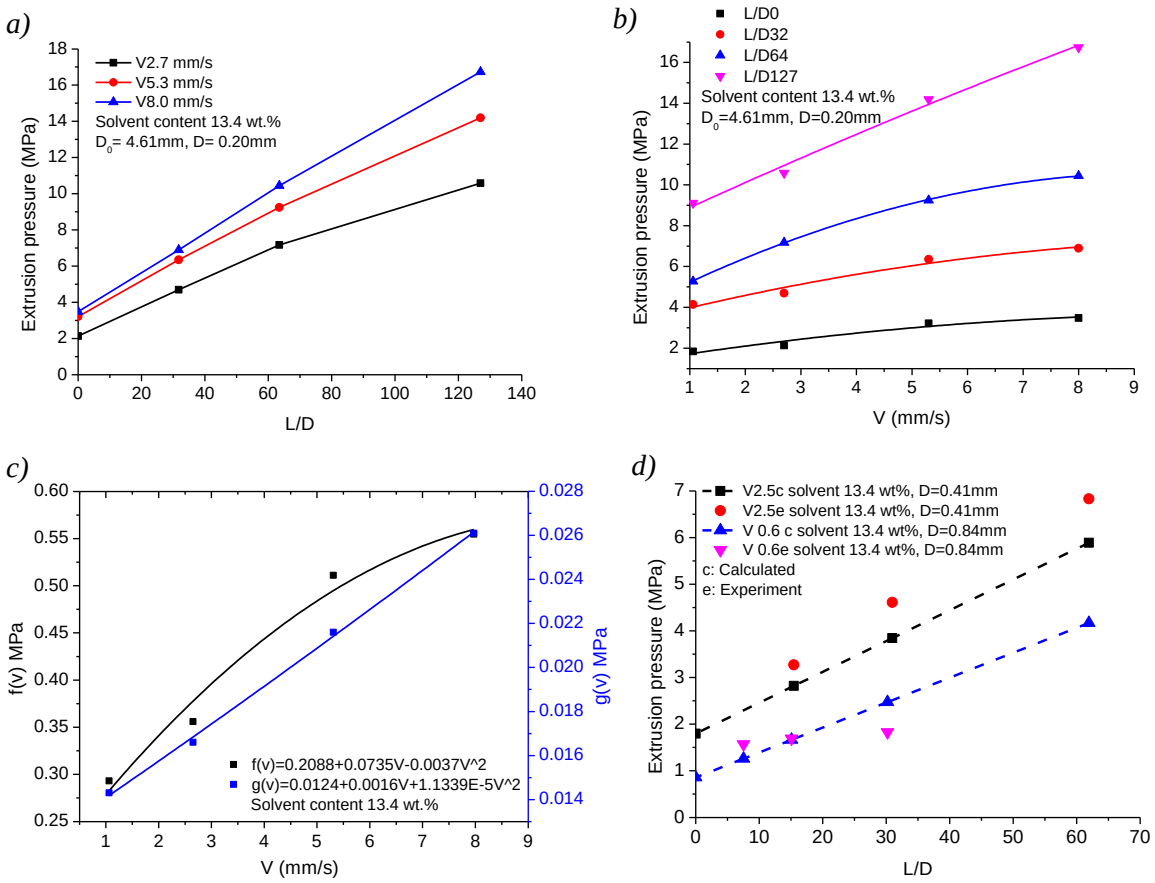

Figure 3.14 (a) extrusion pressure versus die land lengths for various extrudate velocities in the HA paste with solvent content of 13.4 wt.%; **(b)** extrusion pressure versus extrudate velocity for various L/D in the HA paste with solvent content of 13.4 wt.%,; **(c)** f(v) and g(v) functions determined using the Benbow's alternative model for characterization of the HA paste with solvent content of 13.4 wt.%,; **(d)** predicted extrusion pressure versus experimental data for dies with D=0.41mm, and D=0.84mm

Using the Benbow's four-parameters approach the σ_0, τ_0, α, and β can be calculated as follows with assumption of m=1 and n=1 **(Benbow and Bridgwater, 1993)**:

$$\sigma_0 = \frac{OAV_2 - OBV_1}{2(V_2 - V_1)Ln(D_0/D)} \quad (3.13)$$

$$\alpha = \frac{OB - OA}{2(V_2 - V_1)Ln(D_0/D)} \quad (3.14)$$

$$\tau_0 = \frac{V_2(CE - OA) - V_1(DE - OB)}{4OE(V_2 - V_1)} \quad (3.15)$$

$$\beta = \frac{(DE - OB) - (CE - OA)}{4OE(V_2 - V_1)} \quad (3.16)$$

The definition of terms OA, OB, CE, OE, and DE can be realized from **Fig. 3.13a**. Equations 3.13 to 3.16 were used for calculating these four parameters for the HA pastes with 10.2 wt.% and 15.2 wt.% with die diameter of 0.2 mm. Afterward, a linear model could be developed for other HA pastes with solvent content between 10.2 wt.% and 15.2 wt.% (**Fig. 3.16**). **Table 3.2** depicts the four parameters values calculated through experimental data for HA pastes with

10.2 wt.% and 15.2 wt.% solvent contents, and the calculated parameters through experimental data for pastes with 13.4 wt.% solvent along with those estimated using the linear model developed in **Fig. 3.16** for the HA paste. The parameters calculated using experimental data for the paste with 13.4 wt.% solvent have also been presented in **Fig. 3.16** (single dots) for comparison.

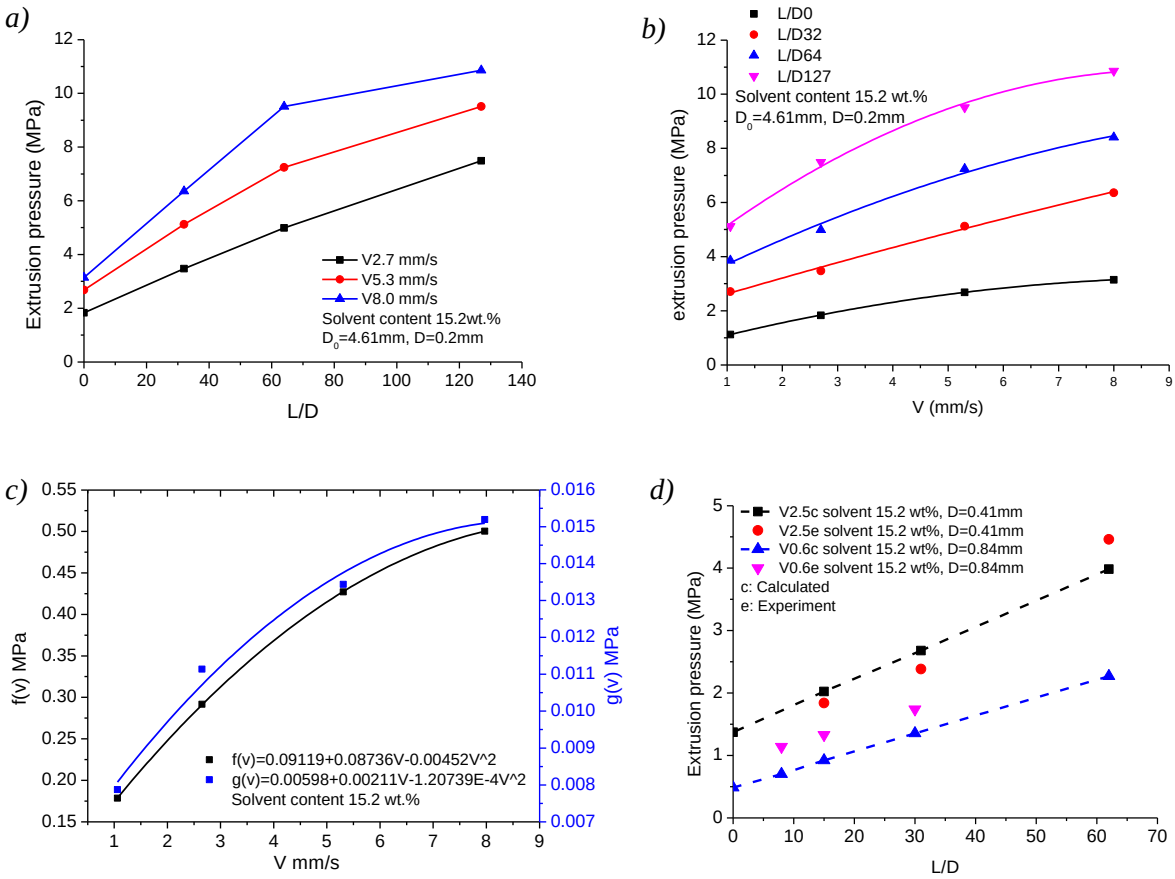

Figure 3.15 (a) extrusion pressure versus die land lengths for various extrudate velocities in the HA paste with solvent content of 15.2 wt.%; **(b)** extrusion pressure versus extrudate velocity for various L/D in the HA paste with solvent content of 15.2 wt.%,; **(c)** f(v) and g(v) functions determined using the Benbow's alternative model for characterization of the HA paste with solvent content of 15.2 wt.%,; **(d)** predicted extrusion pressure versus experimental data for dies with D=0.41mm, and D=0.84mm

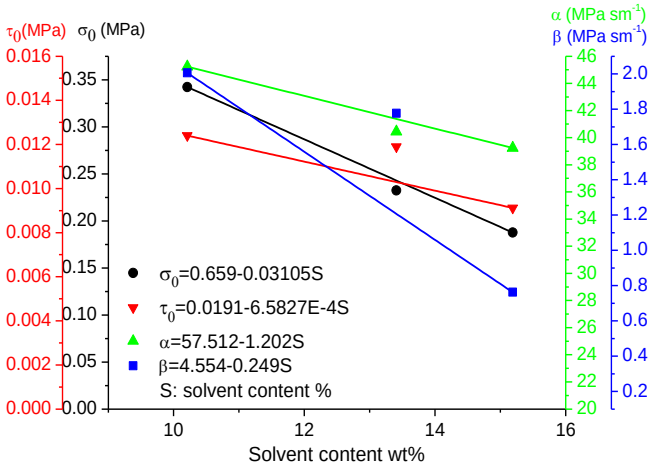

Figure 3.16 The result of Bebow's four parameter prediction for HA pastes with different solvent contents, D=0.2 mm

As seen in **Fig. 3.16**, the estimated values for σ_0 and α are quite close to those calculated using experiments, while the difference for τ_0 and β parameters are considerable. In particular the error for β parameter is relatively high. However, the small variations in the σ_0 and α parameters predicted and experimentally determined for the paste with 13.4 wt.% solvent is an indication of the Benbow's four parameter approach's accuracy that could be achieved with a normal care in experimental work. The main potential factors affecting accuracy of the Benbow's model in this study can be described as follows:

- Estimation of pressure for L/D=0; as discussed earlier the extrusion pressure for L/D=0 needs to be estimated in the Benbow's four parameter approach. As this estimation gets more accurate the resultant calculated parameters would be more accurate as well. A small error in L/D=0 pressure value (OA and OB in the Eqs. 3.13-3.16) has a remarkable effect on calculated τ_0 and β parameters. A more efficient way to estimate pressure for L/D=0 is extrapolation when the interval between L/D=0 and the next data points is small enough. In this study, unfortunately it was not possible to reduce the interval between data points to use extrapolation method as nozzles with limited L/D ratios were provided by the supplier.
- Scaling problem; the Benbow's four parameter approach is a general model which have been developed and verified for extrusion of pastes through dies with a rather large diameter (almost above 2 mm) and L/D ration less than 20 **(Powell et al., 2013, Rough et al., 2002).** The flow behavior of ceramic paste through the die with a large die land and fine outlet in this study (L/D ratio as high as 127) may not follow the Benbow's model perfectly. Using a large L/D ratio can alter the velocity and shear stress profile within the die land. For instance, it may reduce paste slippage or results in varying shear stress through die land. This can affect the parameters τ_0 and β which are related to pressure drop caused by flow of the paste through the die land.
- The Benbow's model provides a good first order model for axisymmetric extrusion and provides reasonable design information, however, the assumptions involved in the analysis (for example m=1, n=1) affect its precision. Meanwhile, errors in preparation of the pastes as well as in the extrusion needs to be controlled by applying excessive care in laboratory work which can be an asset for achieving more accurate results using Benbow's model.

After characterizing HA paste with the use of the Benbow's model, factorial DOE method was applied for statistical analysis of the effects of different factors on extrusion pressure. **Table 3.3** illustrates the selected control factors and their levels along with the resultant

extrusion pressure. It is necessary to check the normality assumption of ANOVA before drawing conclusions. The population normality was checked using MINITAB software with a normal probability plot of residuals (see **Fig. A_5**) in which the straight line indicates the distribution of residuals is normal.

Table 3.2 The Benbow's parameters calculated using four parameter approach for HA pastes with 10.2 wt%, 15.2wt%, and 13.4wt% solvent along with the estimated values for HA paste with 13.4% solvent from **Fig. 3.16**

	σ_0 (MPa)	τ_0 (MPa)	α (MPa sm^{-1})	β (MPa sm^{-1})
HA paste with 10.2 wt% solvent, calculated using experimental data	0.3422	0.0124	45.23	2.00
HA paste with 15.2 wt% solvent, calculated using experimental data	0.1876	0.0091	39.24	0.76
HA paste with 13.4 wt% solvent Estimated using the linear model developed (Fig. 3.16)	0. 2429	0. 0117	41. 38	1. 06
HA paste with 13.4 wt% solvent calculated using experimental data	0.2323	0.0119	40.44	1.77

Table 3.3 Factorial DOE parameters used for statistical analysis of HA paste extrusion

Run no.	L/D	Solvent wt%	Velocity (mm/s)	Mean pressure (MPa)	Standard deviation
1	32	10.2	2.7	5.4	0.17
2	32	10.2	5.3	6.5	0.23
3	32	10.2	8.0	8.1	0.22
4	64	10.2	2.7	7.8	0.09
5	64	10.2	5.3	9.3	0.12
6	64	10.2	8.0	11.9	0.13
7	127	10.2	2.7	12.5	0.05
8	127	10.2	5.3	15.9	0.18
9	127	10.2	8.0	18.1	0.12
10	32	13.4	2.7	4.7	0.05
11	32	13.4	5.3	6.3	0.11
12	32	13.4	8.0	6.9	0.05
13	64	13.4	2.7	7.2	0.04
14	64	13.4	5.3	9.2	0.02
15	64	13.4	8.0	10.4	0.03
16	127	13.4	2.7	10.6	0.04*
17	127	13.4	5.3	14.2	0.04*
18	127	13.4	8.0	16.7	0.02*
19	32	15.2	2.7	3.5	0.05*
20	32	15.2	5.3	5.1	—
21	32	15.2	8.0	6.4	0.06*
22	64	15.2	2.7	5.0	0.25*
23	64	15.2	5.3	7.2	0.15*
24	64	15.2	8.0	9.5	0.18*
25	127	15.2	2.7	7.5	0.17*
26	127	15.2	5.3	9.5	—
27	127	15.2	8.0	10.9	0.13*

Overall mean of pressure = 9.1MPa
* determined from three readings
— less than three readings is available
The L/D values were calculated based on the die diameter and length provided by supplier

Investigation of ANOVA results is necessary to find out which control factor has more contribution in response (here extrusion pressure). **Table 3.4** depicts the ANOVA results obtained from MINITAB software. The P-value is a measure of how likely the sample results are, assuming the null hypothesis is true. P-values range from 0 to 1 and a small (<0.05, a commonly used level of significance) p-value indicates that the control factor has statistically significant effect on the response comparing other factors. Since the p-value for all the control factors are below 0.05, the null hypothesis can be rejected, and thus it can be concluded that all the factors have significant effect on the extrusion pressure at 95% confidence level. The ANOVA table also shows that there is significant interaction between "L/D" and "solvent content".

Table 3.4 The ANOVA results

Source	Degree of freedom	Adjusted sum of squares	Adjusted mean squares	F-Value	P-Value	Contribution percentage (%)
L/D	2	224.19	112.09	329.84	0.000	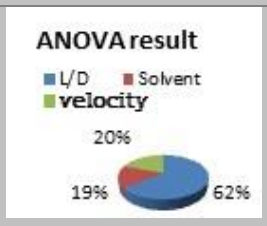
Solvent (%)	2	56.53	28.27	83.17	0.000	
Velocity	2	67.79	33.89	99.74	0.000	
L/D×Velocity	4	4.80	1.20	3.53	0.061	
L/D×Solvent	4	19.58	4.89	14.40	0.001	
Velocity×Solvent	4	0.54	0.14	0.40	0.805	
Error	8	2.72	0.34			
Total	26	376.16				

As all control factors have significant effect (P-value below 0.05), the main effect plot is not presented in this study, while it is worth to consider interaction plots (**Fig. 3.17**). In the interaction plots, as graphs look more like parallel lines less interaction between control factors can be interpreted so that interaction between "velocity" and "solvent" is interpreted less than others. This is also indicated by P-value (0.805) in **Table 3.4**, and thus less significance.

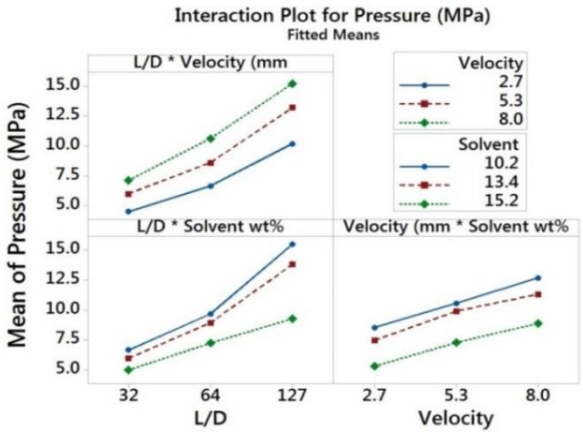

Figure 3.17 Interaction plots for extrusion pressure

The contour plots of pressure versus different control factors are presented in **Fig. 3.18**. The results totally confirm the previous observations about the effect of each control factors:

- Higher extrudate velocity and less solvent content results in higher pressure (a, b, c)
- Higher extrudate velocity and larger L/D results in higher extrusion pressure (d, e, f)
- Less solvent content and larger L/D results in higher extrusion pressure (g, h, i)

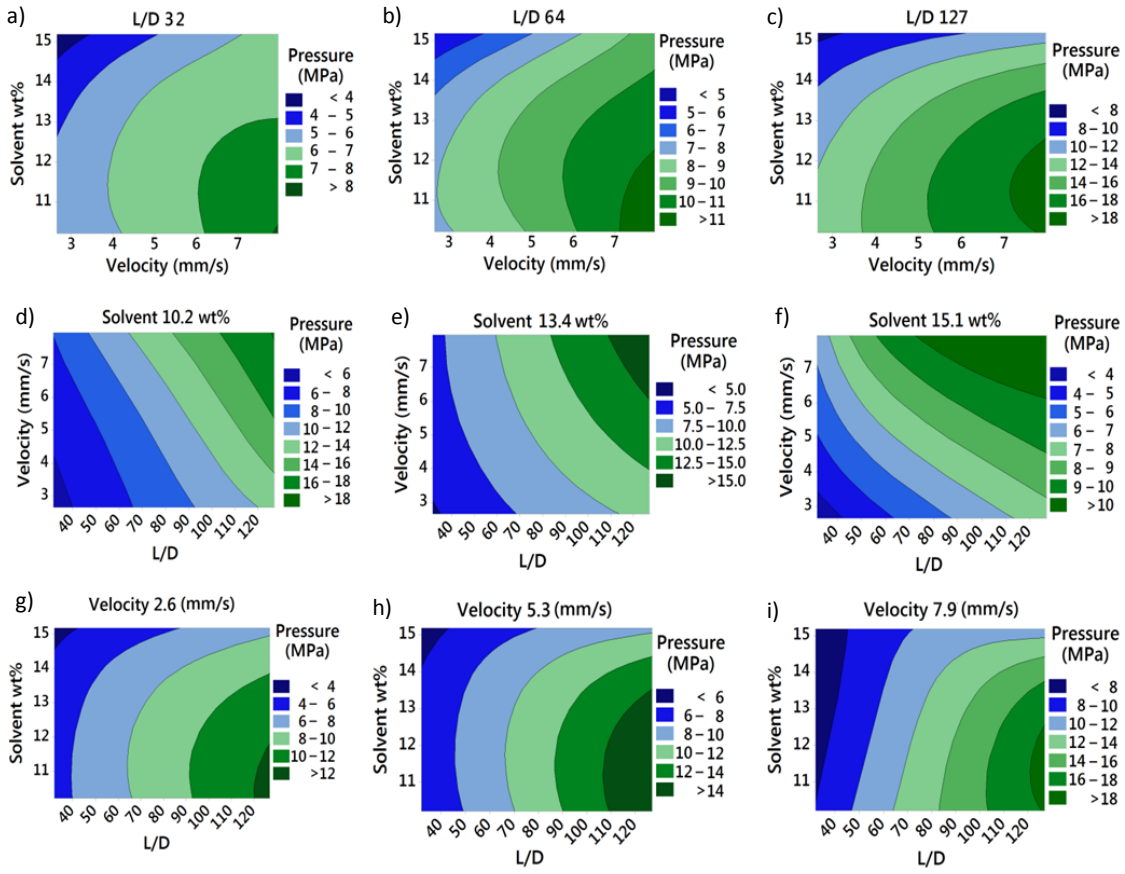

Figure 3.18 Contour plot of extrusion pressure versus different control factors: **(a-c)** pressure versus velocity and solvent content for fixed L/D values, **(d-f)** pressure versus velocity and L/D for fixed solvent contents, **(g-i)** pressure versus L/D and solvent content for fixed velocities

After characterization of the HA paste, the obtained data were used as a guide for providing the optimum condition for printing high resolution HA scaffolds. According to the ANOVA results, die land length and ram velocity needs to be selected as less as possible while solvent content should be increased sufficiently (to decrease σ_0, τ_0) to have minimum effect on extrusion pressure by decreasing die diameter. In addition, using a small syringe's barrel size can be useful for reduction of extrusion pressure (according to Equation 3.5) and the paste needs to be prepared with a high level of stabilization (to avoid agglomerates) with enough lab work cares to avoid any contamination. In short, decreasing extrusion force can be accomplished by:

- Reduce nozzle die land
- Reduce barrel size

- Increase solvent content (to decrease σ_0, τ_0)
- Reduce ram velocity
- Minimize agglomerates

Reduced nozzle die land:

Two different nozzle designs were selected for high resolution extrusion freeforming of HA scaffolds, including: sapphire water-jet cleaning nozzles (Quick-OHM Küpper & GmbH) with die diameter of 80 µm and die land of 500 µm (**Fig. 3.19a**), and a conical shape nozzle manufactured from electroless nickel silver (UNS C73500) with die diameter of 50 µm (Micron-S precision nozzles, FISNAR, USA) and die land as fine as 30 µm (**Fig. 3.19b**). The commercial sapphire water-jet cleaning nozzles had been previously used by Evans and Yang's group for printing of HA scaffolds with 70 µm filament. These nozzles were also used in this study with a paste with more solvent content to increase sintering-induced shrinkage, thus a bit finer filaments. Using more solvent content can also decrease extrusion force using these nozzles. In the meantime, it was necessary to use the conical shape 50 µm nozzles to increase the resolution significantly.

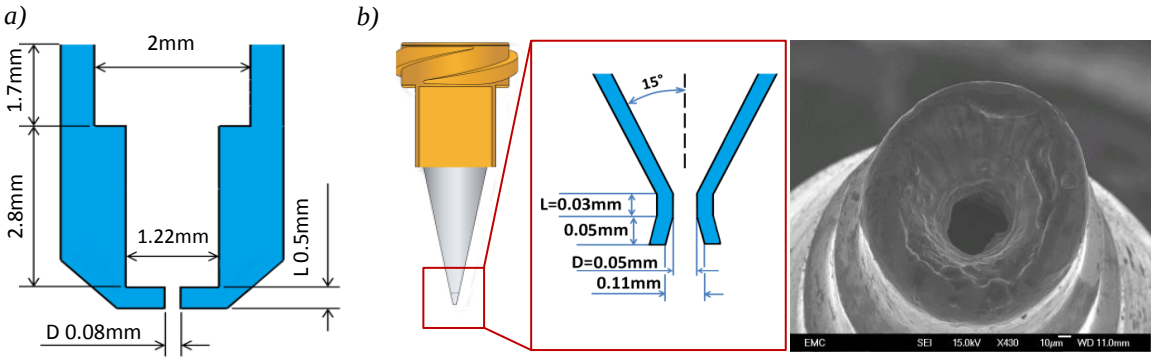

Figure 3.19 (a) Schematic drawing of the nozzle with 80 µm die diameter used for printing HA scaffolds, **(b)** the Micron-S precision conical shape nozzle with 50 µm outlet used for printing high resolution HA scaffolds

Agglomerates and paste drying on outlet:

Agglomerates, impurity, and contamination during paste preparation are the main sources result in nozzle clogging. Particle agglomerates is the most common defect in fine filament extrusion which is often produced in the paste preparation stage **(Lu et al., 2009c)**. To avoid nozzle clogging, the colloidal system (here ceramic/polymer solution) needs to be stabilize before solvent evaporation. The prepared bioceramic/polymer solution left on rolling table for 7 days to make a well-dispersed uniform solution before solvent evaporation. In addition, it was observed that quick drying on the nozzle outlet is the main reason of nozzle jamming when the nozzle diameter is below 50 µm (see **Fig. A_6** as an example of the home-made 40 µm glass nozzle clogged due to quick solvent evaporation on the tip before printing). To solve this

problem, the conical shape nozzles were maintained in a small bottle containing propan-2-ol solution before and after printing (see **Fig. A7**).

Reduced barrel size and increased solvent content:

It is necessary to use a syringe with the least possible barrel size (D_0) with a paste with sufficiently high solvent content to provide an ideal condition for printing high resolution HA scaffolds. Two different syringes with different barrel diameters were used:

- In-house made stainless steel syringes with barrel diameter of 7 mm used with the 80 μm nozzle
- The microliter glass syringes with barrel diameter of 4.61mm (Hamilton 1001 TLL 1mL Syringe, USA) used with the conical shape 50 μm nozzles.

Solvent content is normally within a range of 8-9 wt.% in SEF process for printing ceramic scaffolds with filaments above 200 μm. The HA pastes with solvent content of 10.3 wt.% and 11.7 wt.% were prepared for use with 80 μm and 50 μm nozzles, respectively.

Reduced ram velocity:

A series of experiments have already been conducted to define the most significant factors that should be taken into consideration to reach fine filaments **(Lu et al., 2009c)**. They found equipment accuracy (in particular levelling error), and appropriate adjustment of XY table velocity and nozzle path according to extrusion ram velocity are the most important factors for fine filament extrusion freeforming. The relationship between XY table velocity and extrusion ram velocity under steady state extrusion conditions follows Equation 3.17 **(Lu et al., 2009c)**:

$$\frac{V_{ram}}{V_{paste}} = \left(\frac{D_{nozzle}}{D_{barrel}} \right)^2 \tag{3.17}$$

where V_{ram} is ram velocity, V_{paste} is extrudate velocity, D_{barrel} syringe barrel diameter and D_{nozzle} the nozzle diameter. From the Equation 3.17, the XY table velocity can be a thousand times higher than the extrusion ram velocity for extrusion of very fine filaments, depending on the ratio of syringe barrel diameter to nozzle diameter. Hence, some control difficulties are introduced to make the XY table and extrusion work in harmony. Therefore, the ratio of barrel to nozzle diameter should be selected to adjust these two velocities **(Lu et al., 2009c)**. In practice, ram velocity of 15-18 μm/s with XY table moving speed of 5-7 mm/s is normally set for a successful printing of ceramic paste from nozzle of 300-400 μm. For high resolution printing with nozzles 50 μm to 80 μm, ram velocity was set within the range of 1.5 to 2 μm/s with XY table moving speed of 12-15 mm/s.

3D printed high resolution HA scaffolds:

A paste with solvent content of 10.3 wt.% was prepared and HA scaffolds with different spacing of 400 µm, 200 µm, and 120 µm were designed and 3D printed using the 80 µm nozzle with die land of 500 µm and average extrusion pressure of 13.2 MPa (**Fig. 3.20**). Solvent content of paste determines viscoelastic characteristics of paste which enables printing of self-supporting (spanning) features. It can be seen in **Fig 3.20a** the printed HA filaments could not span in case spacing size was designed as 400 µm and the printed filaments could not retain their shape due to low yield strength. This is less in 200 µm spacing (**Fig. 3.20b**) yet it is considerable and as for 120 µm spacing (**Fig. 3.20c**) the filaments could span sufficiently. Using a higher solvent content results in more drying-induced shrinkage, and thus finer filaments than those reported by Evans and Yang **(Yang et al., 2008d)** using a same die design. Sintering-induced nano-pores inside filaments can be seen in **Fig. 3.20d**, while external surface of the filaments possess a rather closed surface, yet rough suitable for in vivo cell attachments.

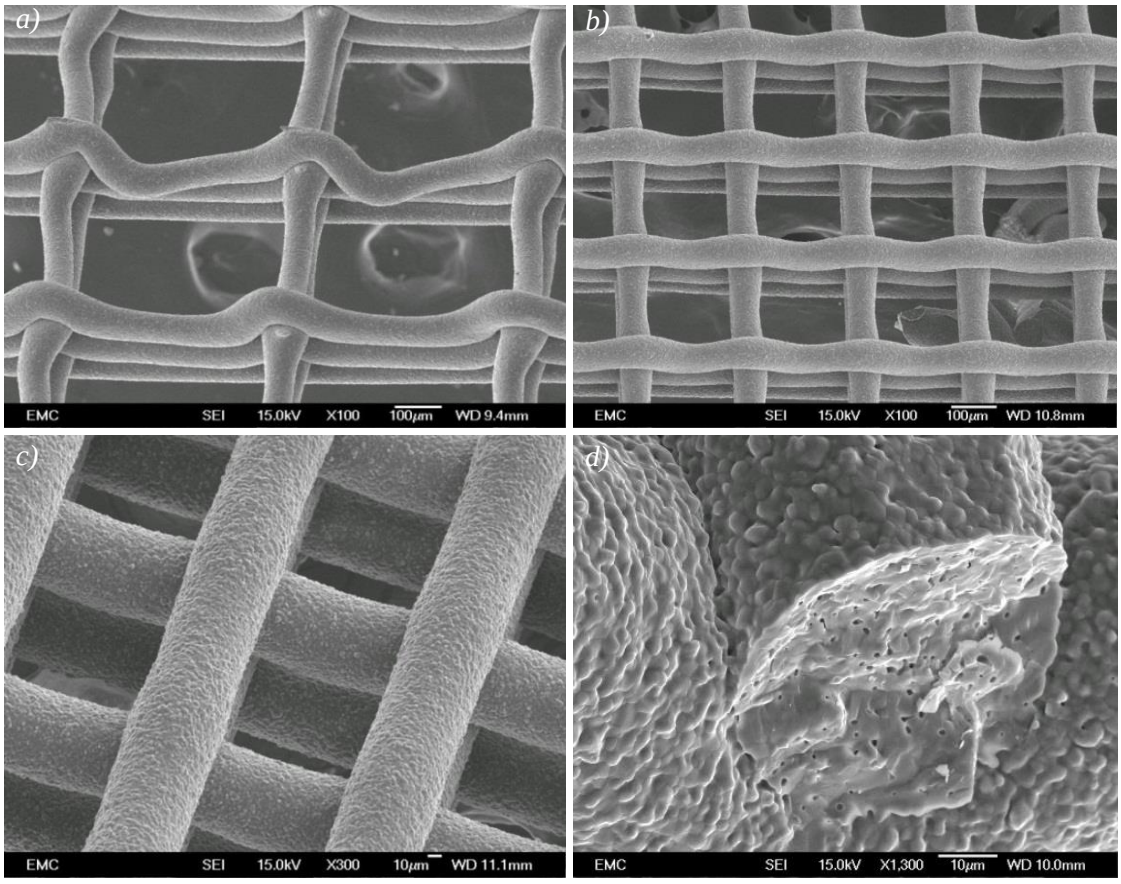

Figure 3.20 HA scaffolds with approx. 60 µm filaments printed using 80 µm nozzle and different spacing: 400 µm **(a)**, 200 µm **(b)**, and 120 µm **(c,d)**. Solvent content: 10.3 wt.%, die land 500 µm, extrusion pressure 13.2 MPa

Fig. 3.21 depicts a typical 4 layer 3D printed HA scaffold using 50 µm conical nozzle, solvent content of 11.7 wt.%, ram velocity of 1.5 µm /s, and average extrusion pressure of 17.9 MPa. The 3D printed scaffold has filaments as fine as approx. 30 µm. In comparison with normal HA paste extrusion with 8-9 wt.% solvent content and die diameter within the range of 200-300 µm the pressure is much higher, although using the conical shape nozzle was an efficient measure to minimize the extrusion pressure.

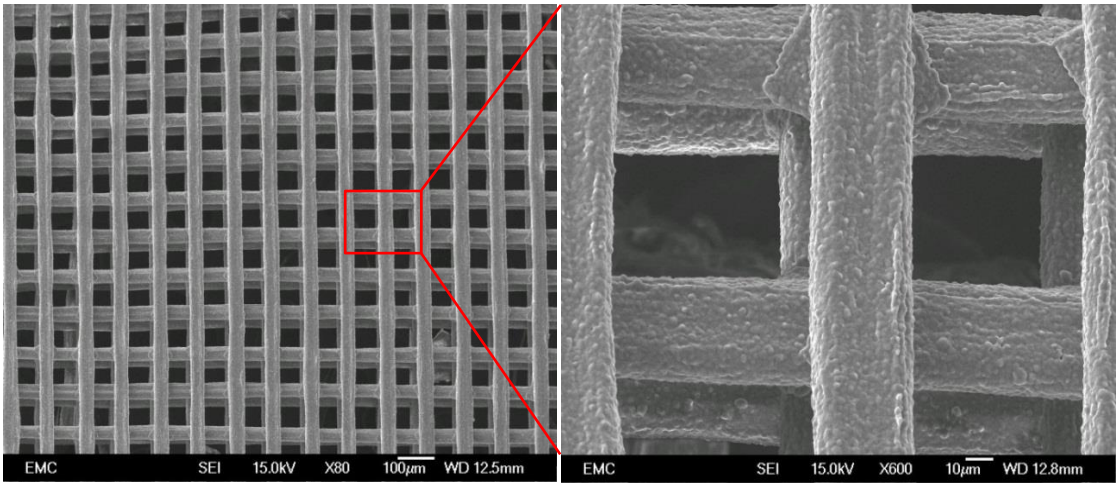

Figure 3.21 HA scaffolds with ~30 µm filaments printed using 50 µm nozzle, solvent content: 11.7 wt.%, ram velocity 1.5 µm/s, average extrusion pressure of 17.9 MPa

It was observed that dimensional uniformity is not as good as those printed using 80 µm nozzle so that filaments ranging from 20 µm to 45 µm (after sintering) were measured in some areas of the scaffold with no change in process parameters such as XY table speed or ram velocity. **Fig. 3.22a** depicts an example of 20 µm and 30 µm filaments printed without change in process parameters. This phenomena might be due to agglomerates within the HA paste which could resulted in a remarkable extrusion pressure fluctuation during print process. **Fig. 3.23** illustrates the effect of agglomerates on printed filament width schematically. As local agglomerates can increase extrusion pressure, more paste is extruded in a short period of time after releasing the agglomerate which results in filaments with larger width (zone C). In addition, there is less paste extrusion for a short period of time before the local agglomerates which results in smaller filaments (zone B). This effect can be seen in **Fig. 3.22b**, where there is a filament with varying width size of 30 µm, 20 µm, and 45 µm. The order of the width sizes intensifies the supposition of agglomerates effect so that 30 µm width is the normal situation with ignorable fluctuation in pressure (zone A), and next 20 µm width which is the period before agglomerates (zone B), and then the 45µm width which is after releasing agglomerate (zone C).

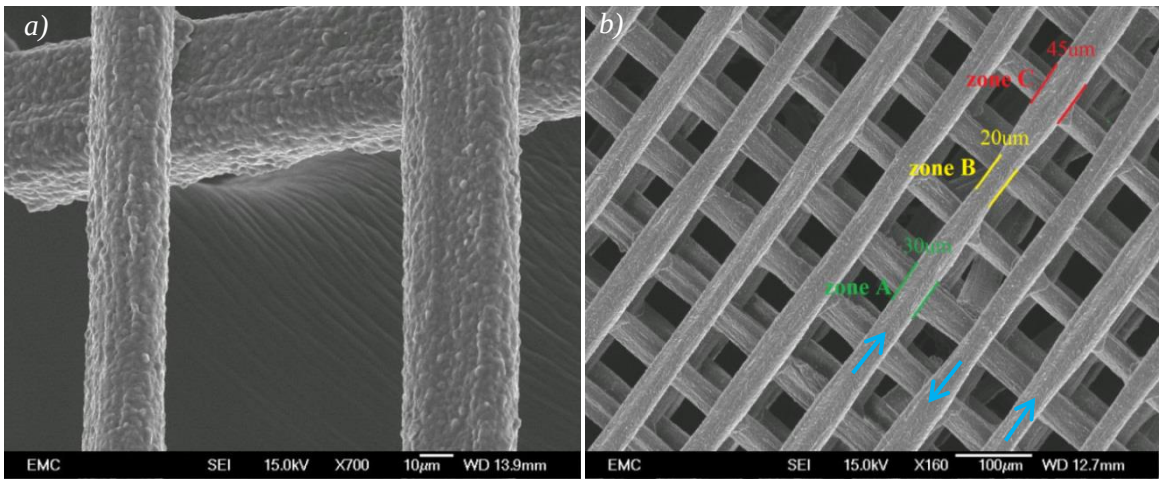

Figure 3.22 20 μm and 30 μm HA filaments printed using 50 μm nozzle, solvent content: 11.7 wt.%, ram velocity 1.5 μm /s, the blue arrows indicate print head movement direction

The dimensional inaccuracy can also be due to inconsistency and variation in liquid content of paste due to LPM phenomena using a low ram velocity. Previous researches reported there is normally a velocity threshold above which LPM doesn't happen **(Rough et al., 2000)**. A highly viscous binder system was used in this research work to minimize LPM and improve the stability of the paste. However, using a very low ram velocity (to decrease extrusion pressure) and more solvent content than a normal paste might result in LPM and thus, inconsistency of HA paste composition during extrusion. In addition, using increased solvent content the printed filaments have less yield strength and thus easier to deform after extrusion using relatively high XY table moving speed. Conversely, the use of a low ram velocity could limit die swell (i.e. increasing extrudate diameter upon exiting from outlet), and thus printing uniform filaments. The die swell equation for the PTT (Phan-Thien-Tanner) family of models is as follows **(Tanner, 1970)**:

$$\frac{D}{D_{die}} = \left[1 + \frac{\tau_w^2}{2G_0^2}\right]^{\frac{1}{6}} \tag{3.18}$$

where D_{die} is the die diameter, D is the diameter of the extrudate, τ_w is the wall shear stress and $G_0 = \eta_0/\lambda$, where η_0 is the zero-shear viscosity and λ is the relaxation time. Thus, die swell is mainly attributed to the wall shear stress and is affected by extrusion ram velocity and the die configuration **(Liang, 2004).** A die with a short land length may also result in a large amount of swell as elastic extensional strain produced in the entrance region does not completely recover and flow in the die is mainly elongational in a short die **(Liang, 2004, Lu et al., 2009c, Masood and Song, 2004).** Therefore, using a low ram velocity can decrease extrusion pressure and die swell, while using a small die land in this study might act inversely and increase die swell which affect the resolution of the final printed HA scaffolds. In addition, using a slow XY table moving speed may affect

filaments' bonding mechanism after deposition when nozzle size gets finer. When XY table moving speed gets lower it takes more time to print one layer and when the next layer is deposited the previous layer sometimes get already too dried (as the filaments are very fine there is less solvent, and thus easier to dry) so that the bonding can't be mutual. This can affect mechanical strength and structural integrity of the 3D printed scaffolds.

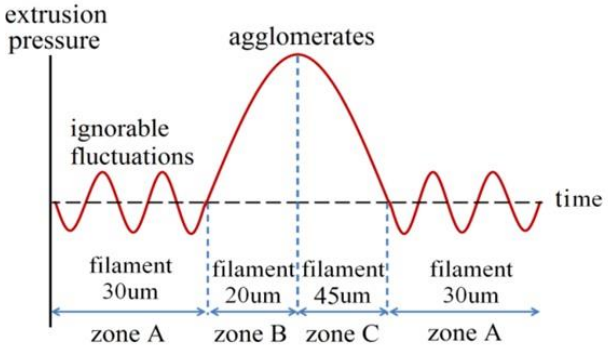

Figure 3.23 Effect of local agglomerates on printed filament width

3.6 Low-temperature 3D printing of PLA/HA Scaffolds

Synthetic bioactive and bioresorbable composite materials are becoming increasingly important as scaffolds for tissue engineering. Biomaterials should combine bioactive and bioresorbable properties to activate in vivo mechanisms of tissue regeneration, stimulating the body to heal itself and leading to replacement of the scaffold by the regenerating tissue. Certain bioactive ceramics such as HA as well as TCP and bioactive glasses, react with physiologic fluids to form tenacious bonds with hard (and in some cases soft) tissue. However, these bioactive materials are relatively stiff, brittle and difficult to form into complex shapes. In particular, HA possesses too slow biodegradation rate which makes it unsuitable choice as a single material for bone scaffolds. Conversely, synthetic bioresorbable polymers are easily fabricated into complex structures, yet they are too weak to meet the demands of surgery and the in vivo physiologic environment. Composites of tailored physical, biologic and mechanical properties as well as predictable degradation behavior can be produced combining bioresorbable polymers and bioactive inorganic phases **(Boccaccini and Blaker, 2005)**.

3D printing of PLA/HA composite is explored in this study in which PLA acts as the phase with a high biodegradation rate and HA provides strength to the composite. This can represent the effective optimal solution for tailored tissue engineering scaffolds, making tissue engineering a realistic clinical alternative in the near future. 3D printing of

PLA and PLA/CaP have already been widely reported through several papers using melt extrusion freeforming **(Landes et al., 2006, Yamada et al., 2008, Park et al., 2012)**, compression molding **(Mathieu et al., 2006),** and indirect AM **(Li et al., 2010)** methods while there are very few reports on low-temperature extrusion freeforming of PLA/CaP composites **(Xiong et al., 2002a, Chen et al., 2012, Serra et al., 2013)**. It is quite challenging to print PLA/CaP composite scaffolds via low-temperature extrusion freeforming with sufficient strut uniformity and resolution. The objective of this research work is to assess capability of SEF method to print high resolution PLA/HA scaffolds with higher level of uniformity than the existing reports. To this end, suitable paste formulation needed to be developed. Different pastes were prepared using various PLA/HA ratios and solvents:

I. 3D printing grade PLA/HA (40 vol.% HA)−dioxin solvent
II. 3D printing grade PLA/HA (20 vol.% HA)−dioxin solvent
III. 3D printing grade PLA/HA/PEG (20 vol.% HA)−dioxin solvent
IV. 3D printing grade PLA/HA/PEG (40 vol.% HA)−acetonitrile solvent
V. 3D printing grade PLA/HA/PEG(40 vol.% HA)−acetonitrile+dichloromethane solvent
VI. 3D printing grade PLA/HA/PEG (40 vol.% HA)−chloroform solvent
VII. Medical grade PLA/HA/PEG (40 vol.% HA)−chloroform solvent

3D printing grade PLA granules (http://reprap.org/wiki) were prepared and dissolved in different solvents. In order, PLA had the highest dissolution rate in chloroform (approx. 2 hours for %4 w/v PLA), next in dioxin (about 3 hours for %4 w/v PLA), and the least in acetonitrile which could not fully dissolve PLA (%4 w/v). HA powder with different ratios was added to the suspension and stirred using magnetic stir for 5 hours. PEG was added (as used in ceramic pastes described in the previous sections) as well in some solutions as a plasticizer to improve extrudability of the paste. The suspensions were put on rolling table for 5 days to avoid HA particle accumulation. Afterward, solvent was evaporated by blowing heated air to make extrudable polymer/ceramic pastes.

(I), (II) PLA/HA (40 vol.% and 20 vol.% HA)−dioxin solvent

It was very difficult to have a well-dispersed PLA/HA solution using the normal procedure used for preparation of HA paste. In fact, the addition of PLA into the ceramic colloidal system had adverse effect on dispersion of HA particles. Accumulated bits formed by HA agglomerates inside the paste during solvent evaporation. Consequently, the extruded filaments were non-uniform and extrusion was not continuous due to temporary nozzle

clogging. HA loading was reduced from 40 vol.% to 20 vol.% to avoid formation of the accumulated bits in the paste but no significant improvement was observed in extrusion (see **Fig. A$_8$**). In the meantime, the printed filaments could not stick to glass build plate because of high rate of drying and warpage during assembly.

(III) PLA/HA/PEG (20 vol.% HA)–dioxin solvent

Adding PEG to the paste formulation could improve extrudability (more uniform filaments could be delivered), although it could not avoid formation of the accumulated bits. To investigate the effect of solvent content on extrusion process three different pastes were prepared: very high solvent content of 23.4 wt.% paste, high solvent content of 19.7 wt.% paste, and less solvent content paste of 16.1 wt.% (still not as thick as normal HA paste). Using the paste with 16.1 wt.% solvent it was not possible to print uniform filaments as extrusion was non-continuous due to existence of accumulated bits and nozzle clogging. On the other hand, two adjacent filaments spread and join together due to surface tension using the soft paste with 23.4 wt.% (see **Fig. A$_9$**). Conversely, using the paste with 19.7 wt.% solvent it was possible to print scaffolds, although there was still non-continuous extrusion and the printed scaffolds did not possess sufficient level of uniformity (see **Fig. A$_{10}$**). In particular, due to the high solvent content a significant distortion and deformation was observed in the deposited materials where adjacent filaments get welded. Therefore, the PLA/HA paste with HA loading of 20 vol.% and 19.7 wt.% dioxin was identified as an applicable formulation to print PLA/HA scaffolds, yet insufficient print quality and consistency.

(V) PLA/HA/PEG (40 vol.% HA)–acetonitrile+dichloromethane (DCM) solvent

As mentioned earlier, dissolution of PLA in acetonitrile was observed insufficient through experiments. Thus, a solvent containing 30 vol.% acetonitrile and 70 vol.% DCM was prepared. Acetonitrile can dissolve PLA with a low rate and its boiling point is approx. 82 °C which is relatively close to propan-2-ol that is used as solvent for preparation of HA paste. DCM can dissolve PLA with higher rate but its boiling point is much less at 40 °C. The purpose of mixing DCM and acetonitrile was to formulate a paste with fully dissolved PLA and suitable solvent evaporation rate. The LPM occurred during extrusion test through 400 μm nozzle using this new formulation. The variation in liquid content was evident with discrete extrusion, and consequently a long filament could not be extruded (only filaments with length of 5-10 mm could be extruded) (**Fig. 3.24a**). The extrusion syringe containing the paste was also kept for 3 days in order to homogenize the paste but still discrete filaments could be extruded with insufficient strength (**Fig. 3.24b**). Change in acetonitrile/DCM ratios (ratio vol./vol.%: 40/60, 50/50, and 20/80) was found useless to avoid LPM.

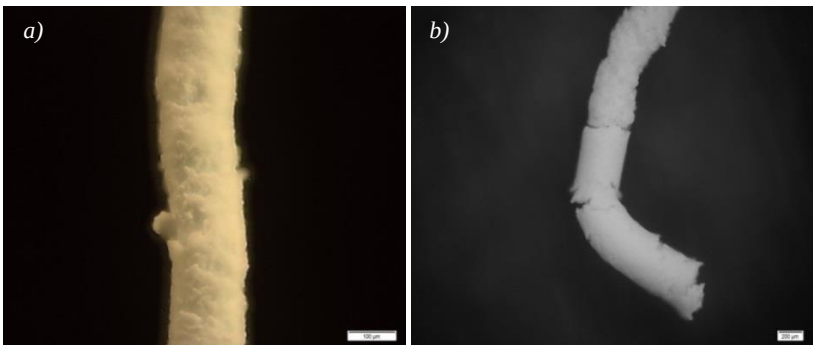

Figure 3.24 The short filament extruded from a paste with PLA/HA/PEG (40 vol.% HA)-acetonitrile+ DCM solvent, **(a)** soft paste, scale bar 100 µm, **(b)** paste left for 3 days inside syringe, scale bar 200 µm

(VI) PLA/HA/PEG (40 vol.% HA)–chloroform solvent

Much less accumulated bits were realized during paste preparation using chloroform solvent in comparison with dioxin, although non-continuous extrusion occurred using a thick paste with 15.4 wt.% chloroform. To minimize nozzle clogging, paste with higher solvent content of 18.3 wt.% was used and highly uniform PLA/HA scaffolds at different sizes (5×5×3mm and 10×10×3mm) could be printed successfully (**Fig. 3.25**) using 350 µm nozzle. HA particles expose on the surfaces of the printed scaffold suitable for cell attachment (**Fig. 3.25c**). Due to low boiling point of chloroform (64 °C) drying effect was remarkable and scaffolds tended to separate from build plate during printing process. Chloroform drops were injected manually on the corner of scaffolds during print process to avoid detachment of scaffold and build plate. The addition of PLA allowed making flexible structures as elastic modulus of the printed filaments could be controlled by adjusting PLA percentage. A flexible double layer sheets was roll out to make porous tubes (**Fig. 3.25d**) which is suitable structures with a significant number of areas can be pursued.

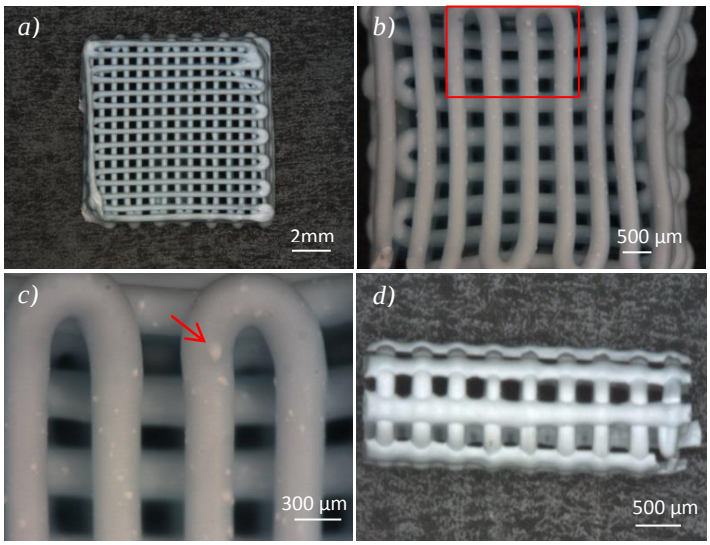

Figure 3.25 (a, b) PLA/HA/PEG (40 vol.% HA)–chloroform solvent biocomposite scaffold at size 10×10×3mm and 5×5×3mm, **(c)** close view of the PLA/HA scaffold (the red inset box), **(d)** The porous PLA/HA tube

(VII) Medical grade PLA/HA/PEG (40 vol.% HA)−chloroform solvent

Medical grade PLA PURASORB PLDL 8038 (ratio m/m%: 80/20) was used as received from PURAC to print composite scaffolds. The paste prepared from PURAC's medical grade PLA exhibited higher uniformity (with noticeably less agglomerated HA) with better extrudability than those prepared using 3D printing grade PLA. The higher paste uniformity may conceivably eventuate from the difference in molecular weight of the used medical grade PLA and 3D printing grade PLA. According to the experiments, the printed scaffolds experienced a significant drying-induced shrinkage due to higher content of chloroform solvent rather than propan-2-ol in normal HA pastes. The short extruded PLA/HA filaments with diameters at size 491±20 μm, 396±20 μm and 343±20 μm prepared using paste with 19.6 wt.% chloroform had diameter of 339±20 μm, 255±20 μm and 220±20 μm after drying at room temperature, respectively (average shrinkage of %33). The use of high solvent content in the paste made it challenging to print scaffolds with small pore size since two printed adjacent filaments join together (as illustrated in **Fig. A$_9$**) when the pore size is designed to be less than 200 μm, resulting failure of print process.

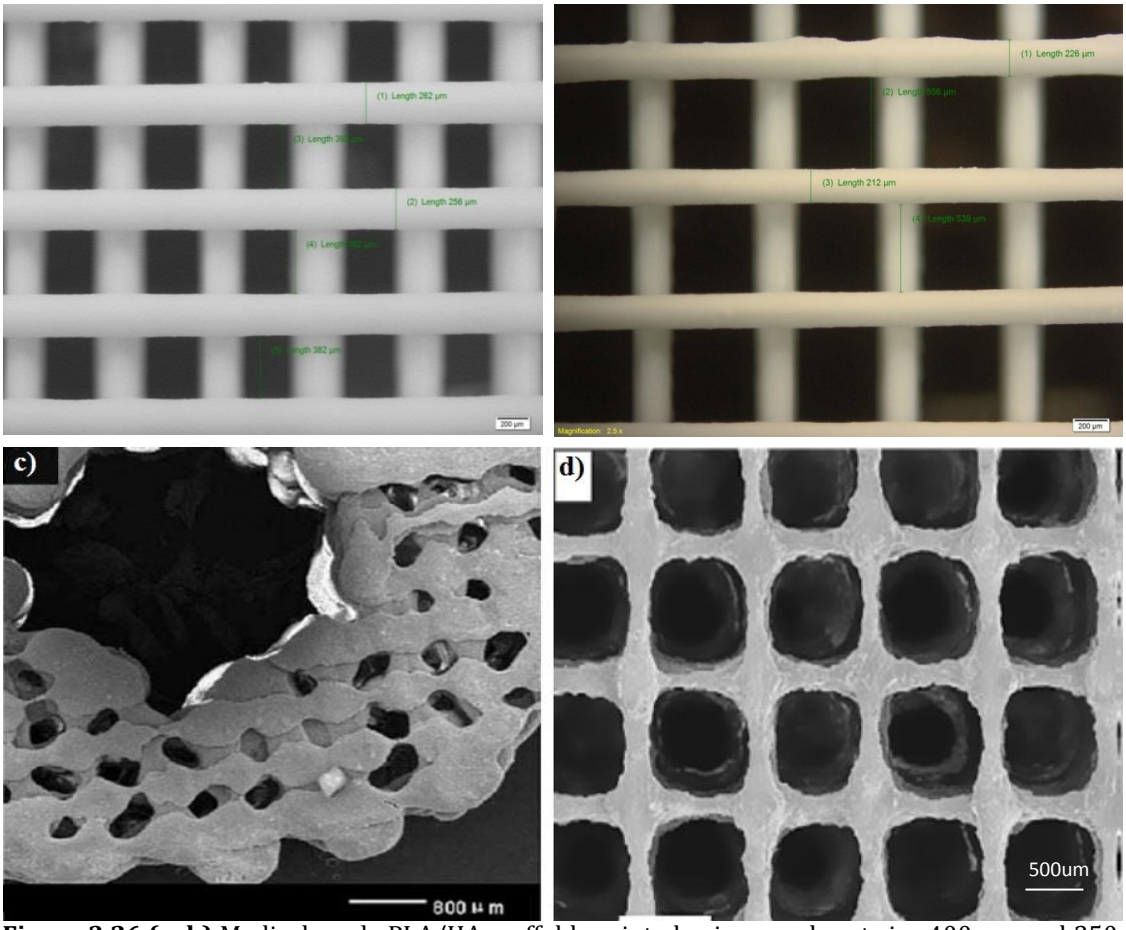

Figure 3.26 (a, b) Medical grade PLA/HA scaffolds printed using nozzles at size 400 μm and 350 μm, printed filaments were at size approx. 260 μm and 220 μm, respectively **(c)** PLA/CaP scaffold made using dioxin solvent **(Xiong et al., 2002a)**, and **(d)** chloroform solvent **(Serra et al., 2013)**

Fig. 3.26 depicts a typical 3D printed PLA/HA scaffolds in this study versus the two main PLA/CaP scaffolds printed by previous researchers via low-temperature extrusion freeforming. As seen the printed composite scaffolds by other researchers have poor quality and low level of struts uniformity. In comparison, the printed PLA/HA scaffolds in this study possess uniform struts, and thus greater control on porosity. Although scaffolds with high level of uniformity could be printed, the consistency of the method remains debatable. Measurement of filament diameter using optical microscopy in some printed scaffolds showed a relatively high dimensional deviation (in the worst case deviation up to 26% of filament size). The variation in the diameter of filaments in different locations of scaffold can be explained by inconsistency of paste containing micron-size accumulated bits, and high solvent content that yields LPM and reduced yield strength which results in material deformation.

3.7 Biological Performance of the 3D printed HA Scaffolds

Cell works and in vitro analysis were accomplished in collaboration with Bone & Joint Research Group, Faculty of Medicine. The collaborator has the facilities and home office approval in place to perform all the in vitro and in vivo studies. Cells were seeded into 3D printed HA scaffolds using the following protocol to assess biological performance:

Femoral heads taken from human bone are used to harvest bone marrow cells. The sample is processed in a centrifuge machine which rotates at about 1200 rev/min and 20 °C, which enables it to extract maximum number of cells and collect them in the form of a pellet. The cell pellet is then seeded into a culture flask with solution containing nutrients and the cells are left in the flask for a few days to proliferate (depending on the number of cells required for the experiment; normally order of 10^6). The medium (nutrients solution) is changed every few days to feed the cells such that a final concentration of +500,000 cells per 50 microliters of media is achieved. Nutrient solution may involve Alpha-MEM, fetal calf serum, modified eagle's medium; environment held at 37 °C. Next, cells in flask were dissolved using a salt solution and trypsin enzyme, in order to break down cells attachments to the flask walls and to each other (need single cells for seeding). Cells are then placed in an autoclave for sterilization. Afterward, cells are seeded into scaffolds and left for specific period of time for further analysis.

48-well plate was used as cell seeded scaffolds container. A scaffold placed in each well with 1ml of media containing cells. Basically, a few scaffolds are left un-seeded as control variable). Scaffolds are immersed in medium (Alpha-MEM) then the plate was placed in an incubator (CO_2 5%, temp. 37 °C); is needed to be turned over after about 2 days. Stem cells can differentiate into any other possible kind of cell–cartilage, osteoblast, fibroblast, etc. Osteogenic supplements can be placed in medium (e.g. dexamethasone, vitamin D, ascorbic acid) to encourage bone formation over other types of tissue.

After some time in vitro, the samples are stained to see what kind of tissue has formed. This method can 'stain' specific components of cells and used to differentiate between different types and parts of cells. For example, presence of alkaline phosphates and osteocalcium indicate presence of bone cells specifically (these substances will comes through as fluorescent in the staining test)

3.7.1 Live/Dead Cell Viability and MTT Test

In vitro test scaffolds are normally designed in small size and should have same porosity and material composition and all of the questions; cell adhesion, viability, proliferation and biointegration can be answered regardless of scaffolds size. For large animal testing larger scaffolds are needed, or could possibly stack some smaller scaffolds. A series of scaffolds with pore of 130 μm, and 250 μm were 3D printed at size of 5×5×5mm for cell seeding and assessment of biological performance after four time points, day 1, day 7, and day 14.

LIVE/DEAD cell Viability was conducted by Cell Tracker Green/Ethidium Homodimer in which:

- Cell Tracker™ Green identifies metabolically active cells (green color in figures)
- Ethidium homodimer-1 labels necrotic cells, or membrane damaged cells (red color in figures)
- Diamidino-2-phenylindole (DAPI) for staining nuclei of cells (blue color in the figures)

Excellent cell adhesion and viability was observed by Cell Tracker Green/Ethidium Homodimer staining. **Fig. 3.27** illustrates two microscope images of the scaffolds with 1 day cultured cells on in which the red indicates dead cells, the green indicates the cells are alive and also the boundary of each cell and the blue stains the nuclei of the cells.

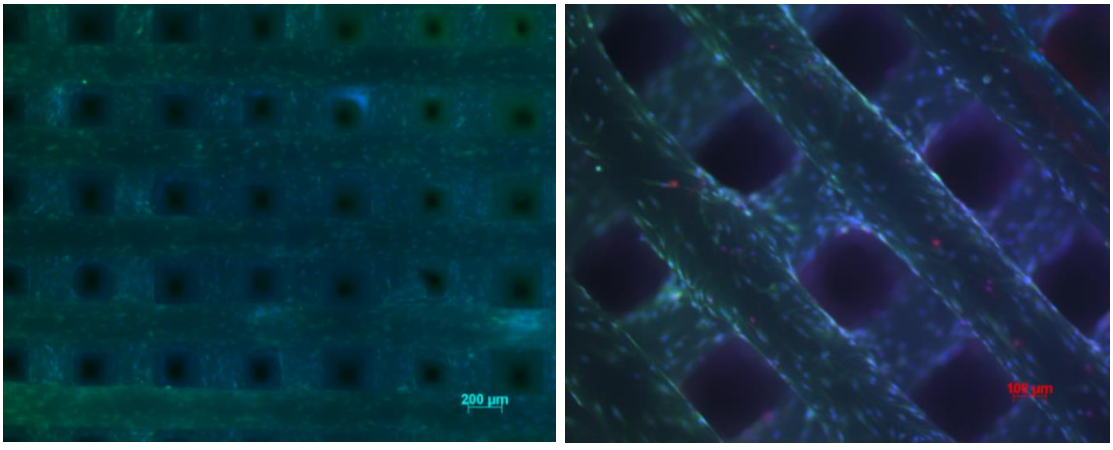

Figure 3.27 Cell viability assessed by Cell Tracker Green/Ethidium Homodimer for HA scaffold

The really interesting bit of results was that cells tend to row/bridge from one portion of filament to the adjacent filament, even after just one day (**Fig. 3.28**). Microscopic images at day 7 proved widespread cell growth, proliferation and pores filling (**Fig. 3.29**).

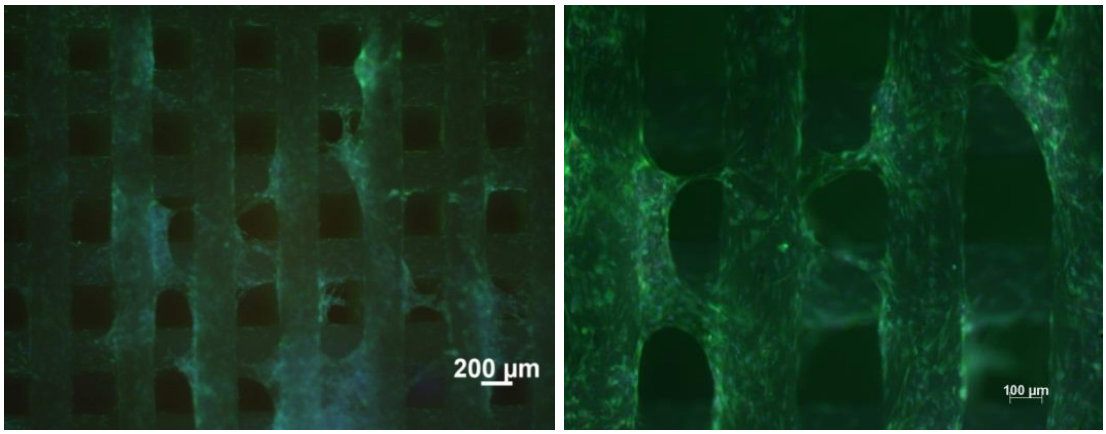

Figure 3.28 Evidence of cell bridging in day 1 for HA scaffold with 250 µm pores

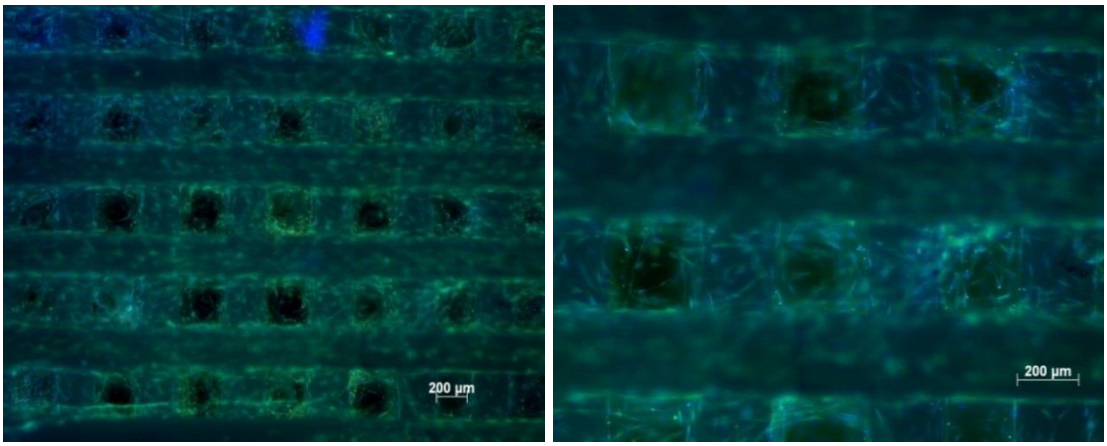

Figure 3.29 Widespread scaffold proliferation and pores filling evidenced at day 7 for HA scaffold with 250 µm pores

The MTT assay was also conducted for study of metabolic activity. The MTT assay is based on the conversion of MTT (3-[4,5-dimethylthiazol-2-yl]-2,5 diphenyl tetrazolium bromide) into formazan crystals by living cells, which determines mitochondrial activity. Since for most cell populations the total mitochondrial activity is related to the number of viable cells, this assay is broadly used to measure the in vitro cytotoxic effects of drugs on cell lines or primary patient cells. MTT is a chemical that is normally yellow. When it is put into cell culture medium it is exposed to cells. Enzymes on the cell surface called superoxidases (anti-oxidant enzymes that protect the cell) reduce the MTT by formation of formazan and change its color to blue/black. The degree of change can then be quantified and is an indication of overall metabolic activity. The larger the color changes the more cells it has been exposed to, and/or the higher the metabolic activity.

Fig. 3.30 depicts the result of the MTT assay for scaffolds with 250 µm pores at day 1, day 7, and day 14. As seen, the scaffold at day 7 has the highest metabolic activity due to cell proliferation over time which is expected. MTT absorbance of cells gets a bit less in day 14

than day 7. The reduction in metabolic activity conceivably eventuate from lack of nutrient supply into 3D scaffolds and removal of waste materials over time. To avoid this problem, bioreactors are used for a continuous and more efficient nutrient supply but unfortunately there was no access to a bioreactor in this project.

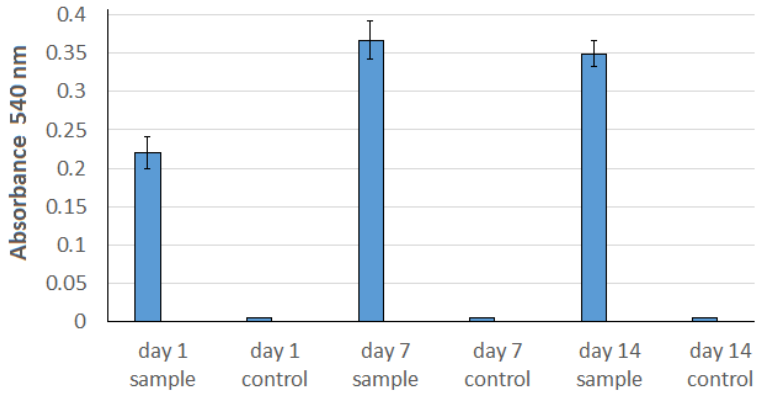

Figure 3.30 The result of MTT assay (2 hours MTT incubation and measured at 540 nm) for HA scaffolds with 250 µm pore size, control: MTT incubation on unseeded scaffolds

For the HA scaffolds with 130 µm pores, the metabolic activity declined from day 7 which was assumed to be related to the poor nutrient supply and subsequent cell death. MTT needs to be exposed to a cell surface to work. So, if the cells were all single layer covering the scaffold filaments (like the 250 µm) there is more exposure and more color change. If the cells clump or block the pores, like the 130 µm, then the MTT has a far lower exposure and less color change. Thus, the work shows justification for the larger pore which allows cell and nutrient access throughout the scaffold structure and the smaller pore size limits cell and nutrient infiltration. Large pore size promotes cell proliferation and viability compared to smaller.

3.7.2 Chorioallantoic Membrane Model (CAM)

Neovascularisation is a crucial step in bone regeneration and fracture healing and is highly dependent on pore size. Chorioallantoic membrane model(CAM) **(Kanczler et al., 2012)** is used to ascertain the optimal pore size for neovascularistion. The CAM model is uniquely suited for this due to huge vascularity, low cost, and the ability to measure vascular invasion with angiography and micro computational tomography (µCT). Graft material containing pore sizes which mediated greatest neovascularistion will then be assessed in a subcutaneous mouse model. Subcutaneous implantation of graft material in mice is an accepted technique for assessment of Osteogenic potential of graft material **(Barradas 2012)**.

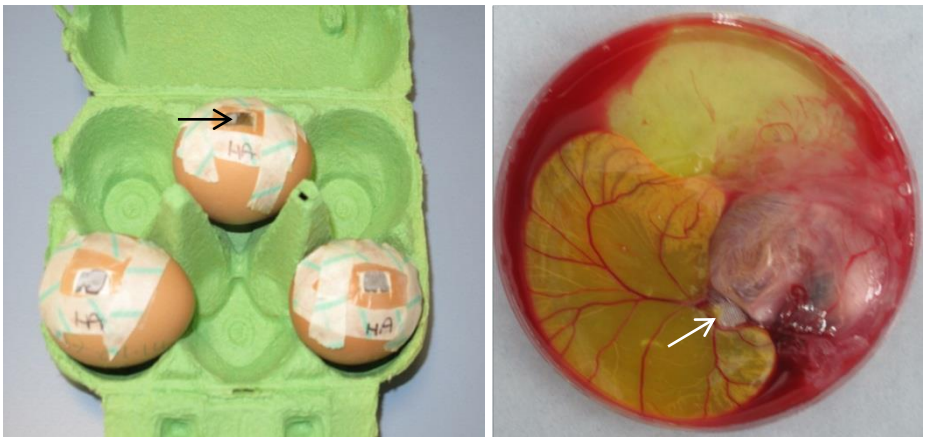

Figure 3.31 (a) Scaffolds implantation into day11 CAM, **(b)** HA scaffold after harvesting, in-situ 7 days on CAM membrane

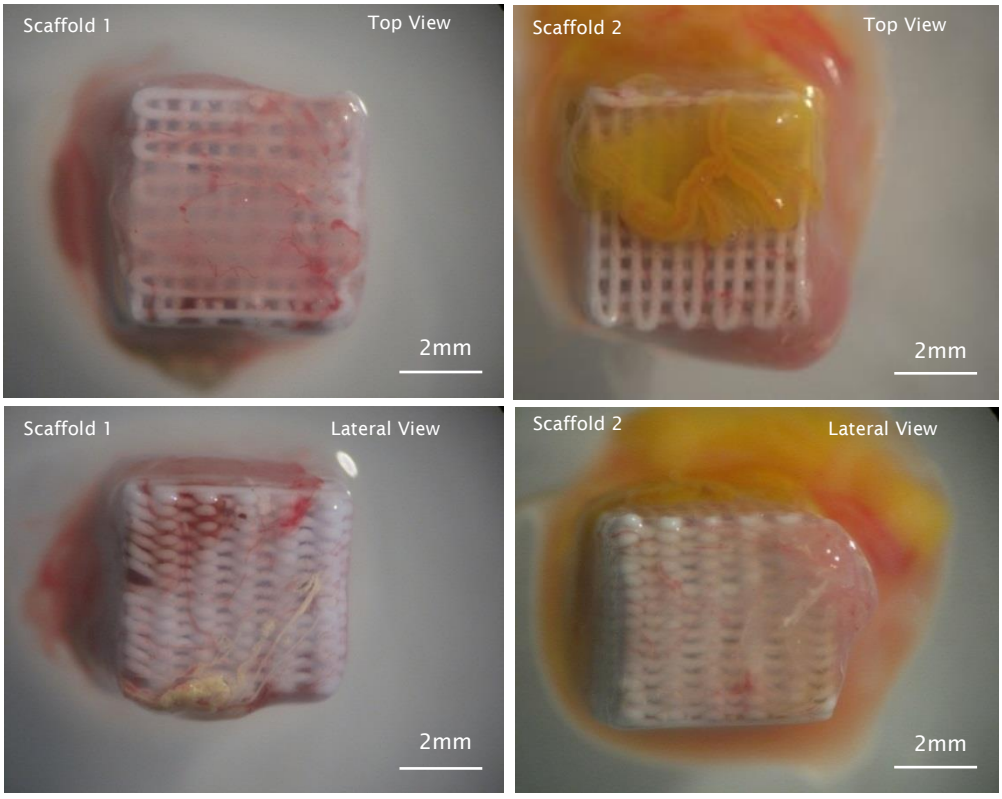

Figure 3.32 The scaffolds implanted into day11 CAM, in-situ 7 days

In this study, CAM model was used to investigate blood vessel generation; that's where a window through the shell of a fertilized egg is cut, the scaffold is placed on top of the chick membrane, the egg is closed back up and then let it develop for a week. This gives a really good idea of how blood vessels and other tissue incorporate with the scaffold. For this end, scaffolds with 250 μm were implanted into Day 11 CAM so that the eggs were incubated at 37°C and environmental CO_2 for 7 days. **Fig. 3.31a** shows eggs at Day 18, prior to scaffold harvest. Arrow indicates access window cut into egg shell at implantation and the window

then was covered with sterile waterproof membrane. After 7 days, scaffolds were harvested ensuring attached membrane is not disturbed (**Fig. 3.31b**). Location intimate with yolk sac (yellow) indicates good CAM integration and membrane is visible surrounding HA scaffold.

Fig. 3.32 depicts two scaffolds with generated blood vessels after CAM implantation. As seen, there is a good blood vessel formation and adhesion but not so great blood vessel integration with scaffold. For a better analysis, the scaffolds needed to be cut and observing inside to see if blood vessels could grow into scaffolds or not. This will be an asset for assessment of blood vessels integration level. However, it was very difficult to cut/section the fragile HA scaffolds. The scaffolds were cut on a tungsten carbide microtome knife, that is what the routinely use for bone samples but HA scaffolds collapsed. Further supportive resin infiltration into the scaffolds was necessary for cutting the samples without damage, however, further analysis was planned to be postponed as it was not within the scope of this research work. To summarize, from the initial in vitro results the conclusion can be drawn that pore of 200-250 μm should be suitable for cell adhesion and proliferation while for blood vessels integration the pore size may need to be increased to the region of 350-400 μm.

3.7.3 Integrated Bone Graft

Synthetic graft is commonly used in trauma and reconstructive surgery to facilitate anatomic restoration of bone fragments including joint surfaces. Standard cross sectional imaging such as CT permits pre-operative measurement of bone defects. The scaffold produced using extrusion freeforming technique can be tailored to fit the required defect and produced within hours. Migration of the synthetic or human derived bone graft material from the desired location is a frequently encountered problem and can result in failure of the procedure. In cases of parotid bone or severe disruption secondary to trauma reconstructive surgery frequently employs locking plates to provide adequate mechanical stability during fracture healing. In such devices threads in the screw head itself result in the screw being held rigidly at the desired angle allowing the screw to provide mechanical support to the reconstruction. These locking plates are currently unable to rigidly hold synthetic bone graft, consequently graft is at risk of migration and may lead to failure of the procedure.

The main feature of the developed 3D printer is the ability to generate 3D porous structures with highly uniform interconnected pores, great control on porosity, and more importantly control on external shape of scaffolds. Possibility of controlling external shape allows production of a graft enabling direct integration with a fracture fixation/stabilization system via a customized region in the synthetic bone graft. 3D printed bone graft integrates directly with a locking plate fracture fixation system, as such the graft is rigidly held and able to resist applied forces and thus not migrate. So, the ultimate goal will be production of a graft in which the region of integration will contain screw threads able to engage screws in

currently used commercial fracture fixation systems. The progress should be toward this ultimate goal via fabrication of a variety of coupling mechanisms.

The proposed integrated synthetic bone graft fixation system permits:

- Tailoring of graft shape and size to match defect
- Integration with fracture fixation system to avoid graft migration
- Precise control of porosity to match clinical requirements

System advantages are:

- The resulting fabricated bone graft is directly held by the fixation system – thus the bone graft is less likely to migrate than graft applied using current conventional clinical techniques
- No other currently available synthetic or naturally derived bone graft permits direct integration with a fixation system via fabricated customized region in the graft material
- Synthetic bone graft is pure HA, a natural constituent of bone which is FDA approved for clinical use in humans
- The 3D fabrication technique affords precise control of filament and pore size of the scaffold which is known to be a key determinant in both cellular migration and resorption rate **(Vaccaro, 2002)**. The proposed technique represents a significant improvement on current methods of manufacture as they are unable to exercise such fine control on porosity

While the developed 3D printer represents advancement in bone scaffold printing technology it has limitations. Namely it lacks adequate control on external shape and geometry and thus is suboptimal when attempting to produce graft tailored to specific bone defects which have been mapped with cross sectional imaging. In addition, the 3D printer was designed to print biomaterials which do not require melting (such as bioceramic pastes). It is anticipated the need to incorporate biopolymers or high performance biocompatible polymers such as PEEK to improve the mechanical properties of graft material beyond those that HA in isolation can provide. So, the idea needed to be simplified so that to 3D print a pure HA graft enabling direct integration with a fracture fixation/stabilization system via a customized region in the synthetic bone graft. As there was limitation on designing and printing complex fixation mechanism (e.g. cross or screw threads), a simple hole through bone graft was used as proof of concept. Graft material produced with extrusion freeforming of optimal porosity with central defect to accommodate wire fracture fixation system (**Fig. 3.33**). This research work was done by researchers at Bone & Joint Research Group, Faculty of Medicine. They developed original ideas and done cell works and analysis. The author contributed in printing the scaffolds.

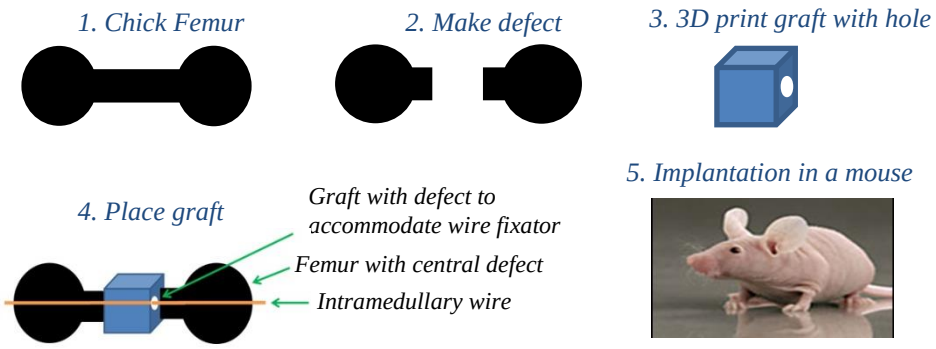

Figure 3.33 Fixation system with integrated 3D printed synthetic bone graft

A 3D printed graft was placed within a Chick femoral defect and implanted subcutaneously in a mouse. Following 28 days implantation the mouse was euthanized and the device retrieved. Photographic and μCT analyses (**Fig. 3.34**) demonstrate integration between fixation system and excellent localization of graft within the defect site with the absence of any migration of scaffold material/graft during the in vivo experimental period.

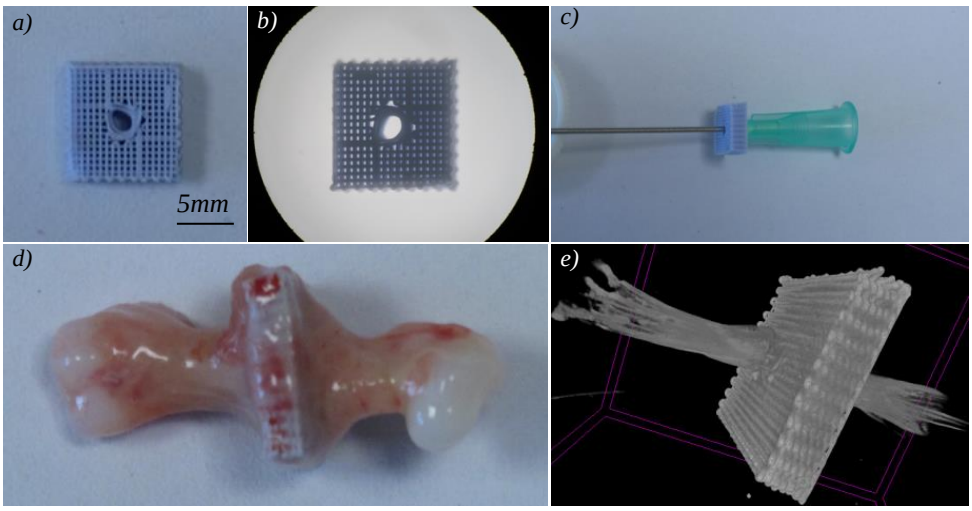

Figure 3.34 Illustration of the prototype device as a proof of concept, **(a)** photographs of scaffold, **(b)** magnified Photograph of scaffold, **(c)** scaffold accommodating a standard gauge needle, **(d, e)** photograph and uCT reconstruction of scaffold held in Chick femur defect by integrated fixation system (28 days subcutaneous implantation in a mouse)

Following successful in vitro and in vivo tests on the 3D printed scaffolds, the design for an ideal integrated synthetic bone graft fracture fixation system for clinical application can be presented. According to the in vitro results, Cells have acceptable adhesion and proliferation within the 200-250 μm pores, while larger pore size confers better blood vessels integration and vascularization. So, the ideal bone graft should be a hierarchical scaffold with different

pore sizes to allow both cell attachment and vascularization. In the meantime, a desirable defect needs to be designed to accommodate fixator to minimize bone graft migration as showed earlier. **Fig. 3.35** illustrates the ideal design of an integrated bone graft schematically in which there are different pore sizes for cell attachment and vascularization, and a desirable defect for fixation. It should be noted that the proposed design is merely based of cell response and other aspects such as mechanical strength and degradation rate of biomaterial need to be considered for a successful design of the final scaffold.

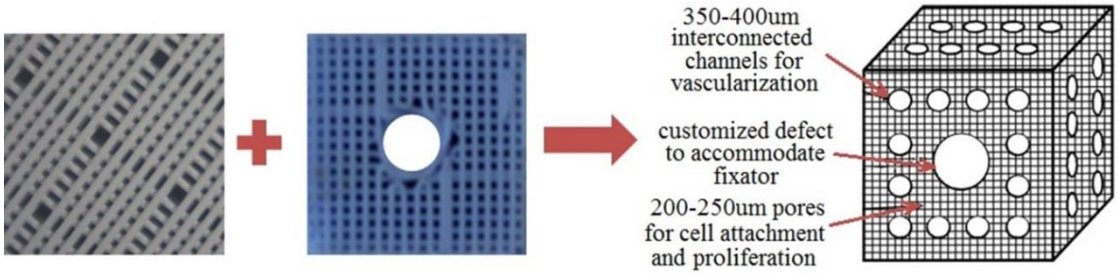

Figure 3.35 Schematic illustrates of an ideal bone graft in which hierarchical scaffold need to be combined with a desirable defect

3.8 Summary

In this chapter, the application of SEF technique in low-temperature production of lattice structures was comprehensively investigated. SEF process was used effectively to print high accuracy lattice structures from various highly demanded ceramics such as alumina, zirconia, and HA for tissue engineering application. The solvent content was identified as an important control factor for successful printing of ceramic structures with great uniformity and dimensional accuracy, although printing scaffolds with high height (above 6mm) remains the challenging part due to drying-induced deformation. Through microscopic observations it was realized that the gaps between nozzle and build layer along with solvent content can affect scaffold's struts uniformity and inter-layer bonding, and thus mechanical properties of the 3D printed scaffolds.

HA paste was characterized using Benbow's model and the results presented in this chapter proved the applicability of the method to estimate the Benbow's four parameters. The DOE approach along with ANOVA analysis were used to investigate the effect of die geometry, solvent content, and ram velocity on the extrusion process experimentally. The understanding of the behaviour of HA paste gained from the experiments were used for optimizing process parameters in order to increase resolution of printing. HA scaffolds with filaments as fine as 30 µm could be printed using a conical nozzle design and a paste with sufficiently high solvent content, and carefully tuning ram velocity. Agglomerates and LPM were identified as the main source of dimensional inaccuracy in printing of fine HA filaments.

In addition, an exploration on paste formulation suitable for low-temperature 3D printing of PLA/HA scaffolds was performed. Chloroform solvent of 18-20 wt.% and HA loading of 40 vol.% was found the most suitable formulation for printing PLA/HA composite scaffolds with tailored stiffness. The in vitro tests on the 3D printed HA scaffolds using SEF method proved their biocompatibility and bioactivity suitable for further use in production of the PEEK/HA biocomposites. According to in vitro test results, pore sizes of 200-250 μm and 350-400 μm are suitable for bone cells attachment and blood vessel integration with scaffolds, respectively. The use of SEF technique allowed the customized design of scaffolds with features to be integrated with bone fixation system to avoid migration after implantation.

Chapter 4

Production of Bioactive PEEK/HA

Chapter 4: Production of Bioactive PEEK/HA

4.1 Introduction

The proposed technique in this project comprises PEEK melt infiltration into the 3D printed HA scaffold. A number of researchers have reported the use of polymer infiltration into bioceramic scaffolds to increase mechanical properties **(Martínez-Vázquez et al., 2010, Seol et al., 2013, Lee et al., 2008, Fedotov et al., 2013, Alge and Chu, 2010, Bang et al., 2013)**. In these studies, bioceramic porous structures were immersed in molten polymer or solution to achieve infiltration of either the filaments or the entire structure. Martínez-Vázquez et al. **(2010)** immersed extrusion freeformed β-TCP scaffolds into molten PLA and PCL for 2 hours to produce bioceramic/polymer composite. The immersion technique was not suitable for use in this study as viscosity of easy flow medical grade PEEK is much greater than other biopolymers such as PCL or PLA. This renders the process of infiltration of fine pores by immersion unreliable, resulting in scaffold material being retained on the surface of viscous PEEK melt. In addition, medical grade PEEK tends to degrade when it is held in excess of 30 minutes at temperatures above 400°C in the absence of a vacuum. For these reasons, PEEK/HA composite are being proceeded by injection moulding or compression moulding as discussed in chapter 2. Ma et al. **(2014)** used compression moulding to make a simple functionally graded PEEK/HA composites. Roeder's group reported successful integration of compression moulding and particulate leaching processes to make porous bioactive PEEK/HA-whisker composite **(Wong et al., 2009, Converse et al., 2007, Converse et al., 2009, Converse et al., 2010).** In their technique, bioactive particles and/or a fugitive particle are mixed with PEEK powders, and then the mixture is densified by pressure, and finally, compression moulded. A similar compression moulding process was used in this study for infiltration of the 3D printed HA lattice structures, barring the fact that there is no requirement for mixing and densification of PEEK and HA powders.

The main features of these new PEEK/HA composite are **(Vaezi and Yang, 2015)**:

- ✓ Greater control on distribution of bioactive phase within PEEK matrix (controlled by computer design)
- ✓ Ability to tailor mechanical and biological properties by varying percentage of bioactive phase (by either varying HA filament or pore size)
- ✓ Various bioactive materials such as Bioglass and β- TCP with faster biodegradation rate than HA can be served so that the bioactive network leaves 3D interconnected channels after absorbing in vivo for further bone cells in-growth and proliferation
- ✓ 100% interconnectivity of both bioactive network and PEEK
- ✓ Ability to incorporate bioactive materials with a high volumetric percentage, yet fully connected PEEK matrix (in this study up to 78 vol.% HA) for non-load bearing applications such as craniomaxillofacial plates, etc.

- ✓ Ability to remove HA network to produce porous PEEK materials with controlled porosity

4.2 Preparation of PEEK/HA and porous PEEK

The sintered HA scaffolds were overmoulded with PEEK OPTIMA®LT3 UF (Invibio Biomaterials Solutions, UK, used as received) through a compression moulding process using both static and dynamic loads to produce a PEEK/HA composite. The PEEK OPTIMA®LT3 UF has a median particle size of 10 μm, and an average molecular weight of 83000 Da, which is an easy flow grade PEEK, with a melt index of 36.4 under conditions of 2.16 kg load in 10 min. A mould with an internal diameter of 25 mm was prepared from tool steel, with appropriate ventilation on the inferior surface to avoid trapping air within the composite. Both static and dynamic loading methods were performed as follows:

- Static Loading: mould was heated up to 250°C, then load applied, and pressure maintained until the temperature reached 400°C. Temperature and load were maintained for a further 20 minutes (dwelling time), then heating was stopped, and the mould was left to cool under pressure, whereby the PEEK matrix crystallized and solidified. Composites were removed from the mould when the temperature had fallen to just below the glass transition temperature (143°C), followed by cooling to room temperature, thus mitigating thermal stress and cracking.
- Dynamic Loading: Mould was heated up to 400°C and maintained for 20 minutes. Load was applied for 5 seconds before heating was stopped, then the mould was left to cool under pressure, until the temperature fell below 143°C, at which the sample was removed.

A series of HA scaffolds with a range of filament and pore sizes were 3D printed, and subsequently overmoulded using dynamic loading to investigate the effects of filament/pore size on PEEK infiltration depth into the HA scaffold. The effect of dwelling time at the target temperature on the formation of PEEK/HA composites was also explored. Through experimentation of the effect of load application during load and dwelling time, it was possible to optimize infiltration of molten PEEK through the HA pores without causing degradation of the polymer. **Table 4.1** shows the details of the samples and the condition of the experiments. Samples were cut using diamond cutter (Mecatome T210, Presi, France). Infiltration depth was measured with the use of the optical microscopy (Olympus BH2-UMA, Japan). Scanning electron microscope (SEM) (JEOL JSM-6500F, Oxford Instruments, UK) was used for analysis of the samples. The optimal temperature of 400°C was determined through experimentation on overmoulding HA scaffolds with external dimensions of 10×10×3 mm, 250 μm filaments, and 200 μm pore sizes, with an optimal pressure of approximately 0.39 MPa.

Another set of PEEK/HA composites with a range of HA scaffold filament and pore sizes as shown in **Table 4.2** were prepared using Static loading for CT scanning. The CT analysis

(Custom 225 kV Nikon/Metris HMX ST) with a resolution of 9 μm per pixel (or 9×9×9 μm voxel) was performed to (i) determine HA percentage volume in the composite; (ii) investigate fractures in the HA network; and (iii) evaluate presence of air bubbles within the biocomposites after moulding. CT scanning of the composites was performed with a 225 kV X-ray source and tungsten target and peak voltage was set to 120 kV with no pre-filtration. In order to achieve sufficient flux, 93 μA current was used (11.16 W). Throughout the 360 degrees rotation, 3142 projections were taken, with an average of 8 frames per projection to improve the signal to noise ratio. Exposure time of each projection was 177 ms with a gain of 30 dB. To reduce the effect of ring artefacts, shuttling was applied with a maximum displacement of 15 pixels. Projection data was reconstructed using Nikon's CTPro and CTAgent reconstruction software, which uses a filtered back projection algorithm. VG Studio Max 2.1 image processing application was used to standardize the volume (average volume of 220.14 mm^3) analysed from each sample.

Table 4.1 Specifications of the samples overmoulded under different conditions

HA scaffold size	Designed scaffold filament/pore size (μm)	Moulding pressure (MPa)	Loading type	Dwelling time (min)	Moulding temp. (°C)	Heating rate (°C/min)
10×10×3mm	250/200	0.39	static	20	400	20
10×10×3mm	400/400	0.39	dynamic	20	400	20
10×10×3mm	400/500	0.39	dynamic	4, 12, 16, 20	400	20
10×10×3mm	400/550	0.39	dynamic	20	400	20
10×10×3mm	400/670	0.39	dynamic	20	400	20
20×18×3.7mm	910/1200	0.39	dynamic	20	400	20

Table 4.2 Details of the PEEK/HA samples prepared for CT analysis; pressure 0.39 MPa, static loading, moulding temperature 400 °C, dwelling time: 20 min, heating rate 20°C/min

Designed scaffold filament/pore size (μm)	250/200	250/250	250/400	400/250	400/400	400/550
Qt.	2	2	1	1	1	1

Porous PEEK structures were produced by cutting off the composite from the overmoulded sample to expose the HA filament, then soaking the PEEK/HA composites in HCl (37%, Fisher Scientific, UK) solution for 72 hr. The HCl solution dissolved the HA network, leaving interconnected channels within the composite.

4.3 Compression Moulding

A comparative plot of melt viscosity versus temperature for a range of conventional polymers in comparison with PEEK-OPTIMA LT1 (Invibio Ltd., UK) is shown in **Fig. 4.1.** As seen, like most conventional polymers, the viscosity of PEEK decreases with increasing temperature. The melting temperature of PEEK is approximately 340 °C, and at temperatures of 360 °C to 400 °C, the shear viscosity of PEEK varies from ~77×10^3 Pa·s to ~66×10^3 Pa·s **(Kurtz, 2012)**. Therefore, to enable minimum shear viscosity for better PEEK infiltration into HA scaffolds with very fine pores, the highest possible mould temperature needs to be selected. Conrad et al. **(2013)** demonstrated that this increased mould temperature may also increase the compressive modulus, yield strength and strain of the traditional PEEK/HA composites produced through compression moulding of PEEK–HA mixed powders. Working temperatures greater than 380 °C have been shown to reduce crystallinity, which is known to be beneficial for ductility and toughness **(Jaekel et al., 2011, Nieminen et al., 2008)**, with no adverse effect on biocompatibility in vivo **(Nieminen et al., 2008)**. Given the positive effects described on both shear viscosity and mechanical properties of the resulting PEEK samples, a mould temperature of 400 °C was selected for this study.

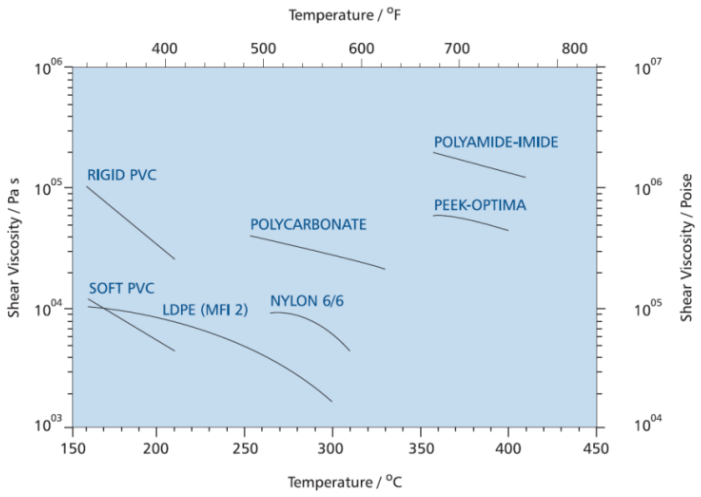

Figure 4.1 Shear viscosity versus temperature for a range of thermoplastics (source: Invibio Ltd., UK)

While mould temperatures of 400°C guarantee minimum viscosity, caution must be exercised when working at temperatures in excess of 380°C as there is a risk of thermal oxidation **(Conrad et al., 2013)**. Potential of oxidation can be decreased by a reduction in dwelling time at the target temperature; as such optimisation of dwelling time is crucial. An insufficient dwelling time will result in inadequate melting of PEEK and therefore, failure to perfuse the scaffold pores at low pressure. Dwelling time must be sufficient to permit adequate heat transfer throughout the powder, including powder residing at a distance from

the heat source. Conversely, prolonged time at the target temperature will result in thermal oxidation and degradation of the polymer. HA samples with 400 µm filament and 500 µm pore sizes were overmoulded using dwelling times of 4, 12, 16, and 20 minutes, under dynamic loading (details in **Table 4.1**). Four minutes dwelling time was insufficient to melt the PEEK, 12 minutes resulted only in partial melting (**Fig. 4.2a**), and 16 minutes dwelling time resulted in complete melting of the PEEK, but inadequate scaffold infiltration (**Fig. 4.2b**). It was determined that 20 minutes was the optimal dwelling time for compression moulding of PEEK at 400°C, permitting adequate melt flowability to fill the lattice structures with no apparent polymer degradation. PEEK degradation was realized by visual observation (i.e., colour change in PEEK) in this study.

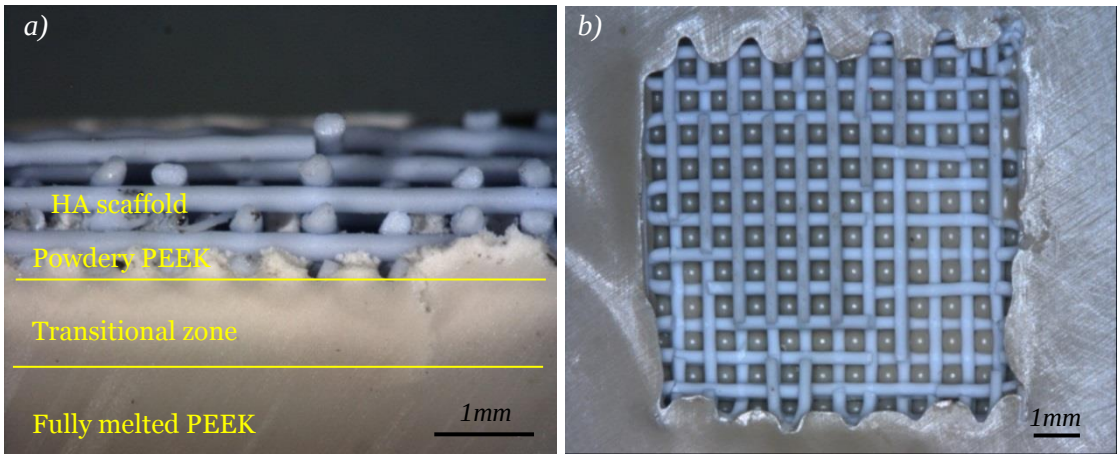

Figure 4.2 Bioactive PEEK/HA composites, scaffolds size 10×10×3 mm, filament size: 400 µm, pore size 500 µm, moulding temperature: 400ºC, pressure: 0.39 MPa, dynamic loading for 5 s; **(a)** dwelling time: 12 min, heating rate: 20°C/min, and **(b)** dwelling time: 16 min, heating rate: 20°C/min.

3D printed HA scaffolds are relatively fragile and moulding pressure must be carefully regulated to permit flow of molten PEEK and perfusion of fine pores without resulting in fracturing of the HA network. CT analysis was used to visualize the PEEK/HA composite and to detect over-load-induced defects in HA network following compression moulding. Defects manifested in the form of either a partial crush, or micro-cracks (red arrows) in the HA filaments (**Fig. 4.3**).

The results of previous mechanical tests on extrusion freeformed HA scaffolds indicated that compressive loading must be less than 1 MPa **(Yang et al., 2010)**, which is remarkably less than what has been reported for moulding of PEEK–HA powders. Roeder's group densified PEEK and HA-whisker dry powders at 125 MPa first, to avoid porosity, and then compression moulded at 250 MPa and 350°C–370°C **(Converse et al., 2010)**. Wong et al. **(2009)** described an alternative technique in which PEEK and strontium-containing HA (Sr-

HA) powders were densified at 35 MPa and then compression moulded at 12–15 MPa and 350°C –375°C. The use of injection pressures of 11–14 MPa and temperature of 395°C was previously used in the injection moulding of PEEK/HA compounds **(Abu Bakar et al., 2003a)**. Through experimentation, the optimal pressure to ensure full infiltration of a scaffold at size 10×10×3 mm without resulting in damage, was determined to be in the region of 0.39 MPa.

The optimal pressure used in this study is similar to that used by other researchers in the compression moulding of reinforced carbon fibre-PEEK composites **(Luo et al., 2014, Tai et al., 1995, Mrse and Piggott, 1993).** Luo et al. **(2014)** tested pressures ranging from 0.5 to 2.0 MPa and found that 0.5 MPa is the most suitable pressure for making 3D carbon-fibre reinforced PEEK (CFR-PEEK) composites prepared by 3D co-braiding and compression moulding techniques. Mrse and Piggott **(1993)** employed 0.4 MPa pressure for the preparation of AS-4 CFR-PEEK using lay-up followed by compression moulding process to avoid fibre damage.

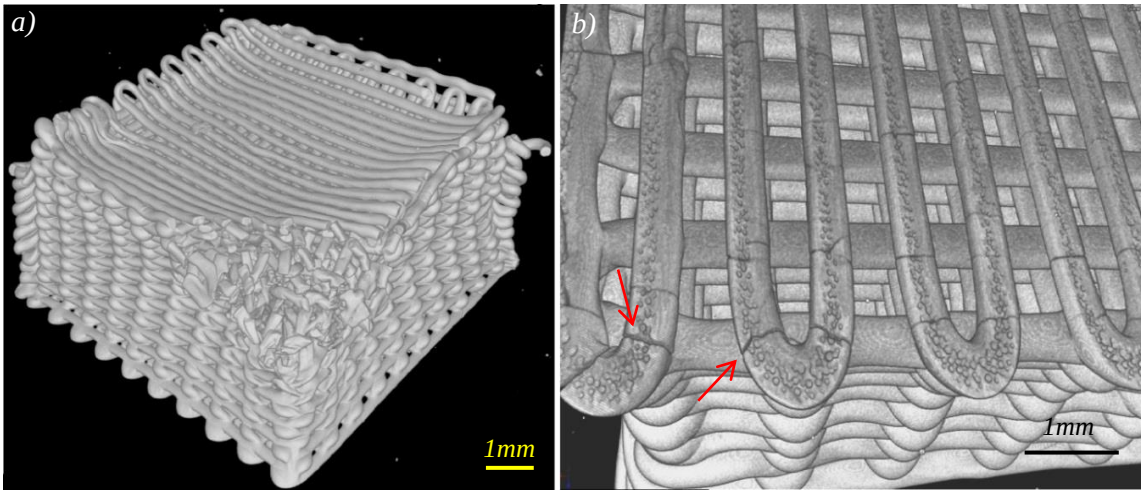

Figure 4.3 CT images of two typical damaged HA scaffolds after PEEK infiltration using excessive pressure; **(a)** partially crushed scaffold where filament is 250 µm and pore is 250 µm, **(b)** HA scaffold with micro-cracked filaments where filament is 400 µm and pore is 550 µm.

While the mechanical and biological functions of the composites can be tailored by varying the filament and pore size of the scaffold, there are lower limits for these parameters. Small filaments can fracture during compression moulding and molten PEEK is too viscous to infiltrate small pores. It was found that for scaffolds of 10×10×3 mm exposed to a moulding pressure of 0.39 MPa, the filament size and the spacing are required to be greater than 250 µm and 200 µm respectively to ensure successful PEEK infiltration without HA fracture. Dynamic compression was applied on PEEK/HA composites produced using scaffolds with a range of filament and pore sizes through conditions presented in **Table 4.1**. Infiltration depth was shown to be proportional to the pore size so that the scaffold, with dimensions of 20×18× 3.7 mm, and filaments sized 910 µm while pores are 1200 µm, was found to be fully

infiltrated by PEEK in both lateral and vertical directions, and HA network retained its structure and shape. For similar sized scaffolds that are 400 μm in filament size but of differing pore sizes (400, 500, 550 and 670 μm), the respective infiltration depths are as follows: 1.4, 1.9, 2.4 and 2.9 mm.

When the infiltration depths—using dynamic loading—are compared with the infiltration as seen following static loading, it can be concluded even in scaffolds with pores of 200 μm that dynamic loading of the molten PEEK does not permit sufficient time for flow through the scaffold. Infiltration depth was found to be more dependent on the temporal application of pressure than the absolute magnitude of the pressure. Thus, different pore sizes ranging from 200 μm to 700 μm can be fully infiltrated easily using static loading without filament fracture. Furthermore, dynamic loading was found to result in greater entrapment of air in the PEEK matrix than static loading. This implies that during dynamic loading, air is unable to escape from the PEEK matrix with a resulting decrease in mechanical strength. A static pressure of 0.39 MPa, dwelling time of 20 min and temperature of 400°C were identified to be optimal for compression moulding of HA scaffolds of 10×10×3 mm in size with filament size above 250 μm and pore size above 200 μm.

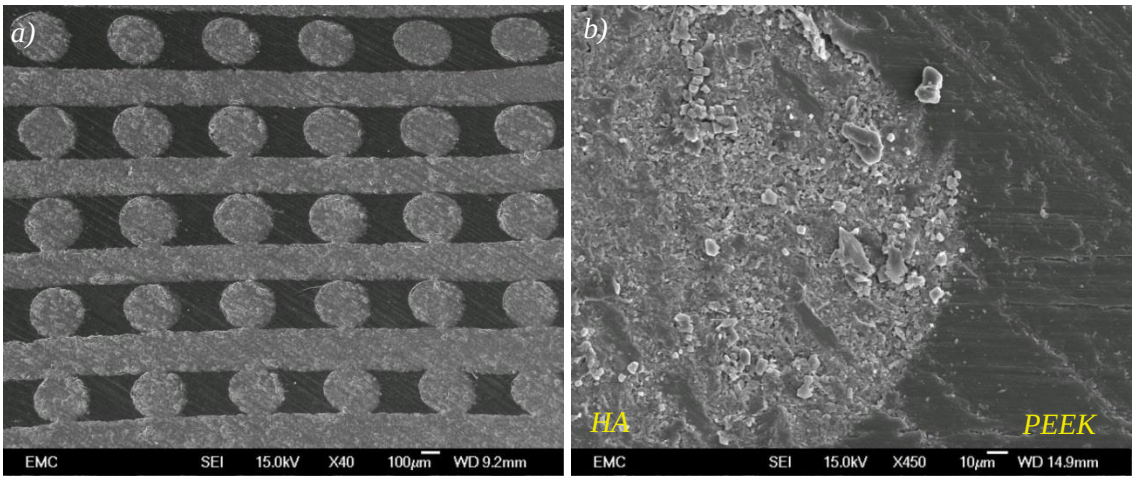

Figure 4.4 Bioactive PEEK/HA composite, scaffold size 10×10×3mm, HA scaffold filament size: 250 μm, pore size 200 μm, moulding temperature: 400 ºC, dwelling time: 20 min, heating rate: 20 C/min, static pressure: 0.39 MPa, **(a)** a vertical section, and **(b)** close view of PEEK–HA interface

Fig. 4.4 depict SEM images of vertical sections from typical PEEK/HA composite produced successfully through the optimized compression moulding using static loading, and PEEK-HA interface (the magnified view). As seen in **Fig. 4.4a**, HA scaffolds are fully infiltrated by PEEK in both vertical (infiltration depth is 3 mm) and lateral directions, while maintaining the HA network structure and uniformity. Whilst a good interface between HA filaments and PEEK matrix is realized, this may not affect the mechanical properties of the composite. In CFR-PEEK, good bonding between PEEK matrix and carbon fibers is critical and determines the

overall strength of the composite as it enables load transfer from PEEK to carbon fibers. However, in these PEEK/HA composites, the interface bonding might not be as important in CFR-PEEK since brittle HA filaments are used for its bioactivity, rather than its load-bearing properties. In contrast, HA scaffold volume fraction and filament diameter/layer orientation could be pivotal in determining the mechanical properties of the final composite, which is discussed further. The interface achieved between HA filaments and PEEK matrix as shown in **Fig. 4.4b** proves that the moulding temperature and pressure were appropriate selections.

4.4 Computed Tomography (CT) Analysis

As mentioned earlier, remarkable entrapped air was observed within PEEK matrix in the PEEK/HA composites produced by dynamic loading. CT analysis revealed that PEEK/HA composites produced by static loading has much less entrapped air than those produced by dynamic loading. This indicated that using dynamic load air inside PEEK matrix did not have sufficient time to release from designed ventilation in the mould. This was observed in almost all the samples were made using dynamic loading. It is important to minimise entrapped air as it reduces mechanical properties of the PEEK/HA composite. CT analysis of PEEK/ HA composites where proportion of HA ranges from approximately 41% (v/v) to 78% (v/v) and are prepared by static loading, resulted in an average of 1.5% (v/v) air within the composite (**Table 4.3**). A small variation (up to approx. 5%) in HA percentage volume calculated by the image processing application (VG Studio Max 2.1) for the samples with the same HA filament/pore size in **Table 4.3** proves repeatability and accuracy of the 3D printing process. No specific correlation between pore size and air bubbles formation was found, with 400 μm pore size resulting in the greatest volume of air (3.2%). **Fig. 4.5** shows representative 3D images obtained using CT, imaging various cross sections of a typical PEEK/HA composite. The majority of air bubbles (which can be realized in white color) are located superiorly in the images, which corresponds to the inferior surface of the mould where air release would be most likely to be impeded.

Table 4.3 Results of CT analysis of compression moulded PEEK/HA composites

HA scaffolds		PEEK /vol.%	HA /vol.%	Air bubble /vol.%
Filament /μm	pore /μm			
250	200	38.6	60.3	1.1
250	200	36.5	62.4	1.1
250	250	42.4	56.1	1.5
250	250	47.6	51.6	0.8
250	400	55.9	40.9	3.2
400	250	21.3	77.7	1.0
400	400	39.4	58.3	2.4
400	550	48.7	50.1	1.2

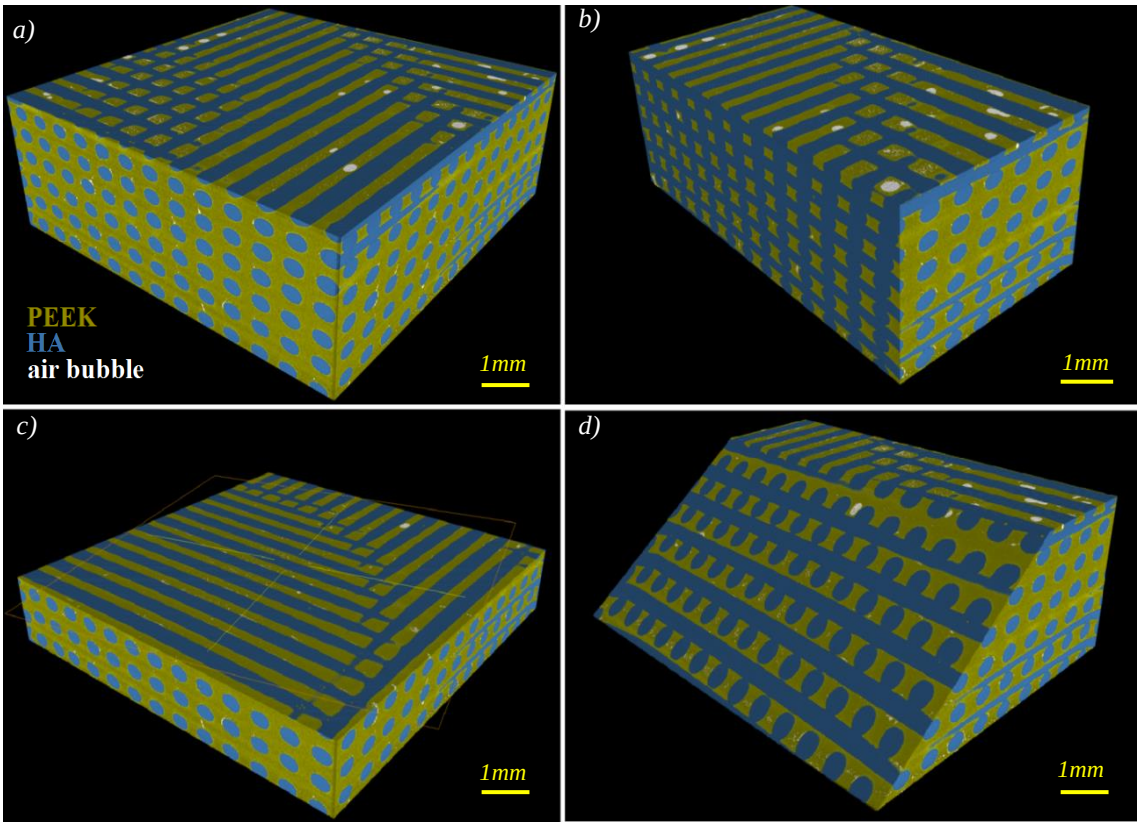

Figure 4.5 3D images constructed from CT scan of a PEEK/HA composite with: HA filament size 400 µm/pore size 400 µm. Volume percentages: HA 58.3%, air bubble 2.4%, PEEK 39.4%. (**a)** isometric view (total volume: 220.72 mm3), (**b)** vertical section view, (**c)** horizontal section view, (**d)** oblique section view

4.5 Porous PEEK

Critical material properties for orthopaedic tissue engineering include: (i) sufficient pore interconnectivity for cell infiltration and perfusion of nutrients, and (ii) adequate pore size to facilitate vascularisation, while still affording sufficient mechanical strength **(Jarman-Smith et al, 2012)**. The channels could help the alignment and differentiation of cells **(Bhuthalingam et al., 2015)**.

Porous PEEK structures were produced by cutting off the PEEK/HA composite from the overmoulded sample to expose the HA filament, then soaking the composites in HCl (37%, Fisher Scientific, UK) solution for 72 hr. The HCl solution dissolved the HA network, leaving interconnected channels within the composite. **Fig. 4.6** shows porous PEEK samples with the hollow channels suitable for bone cell attachment, infiltration and proliferation.

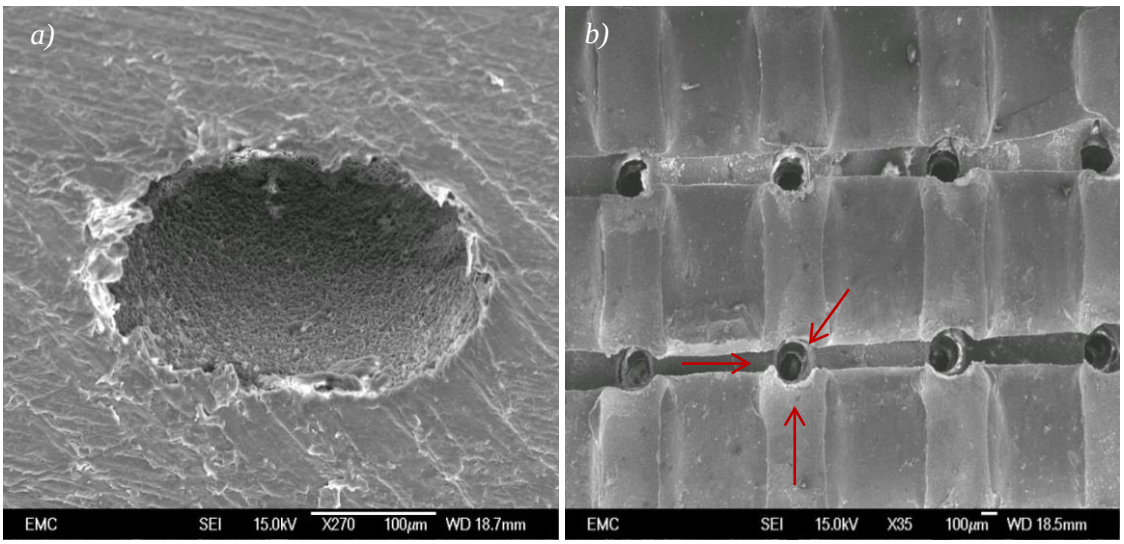

Figure 4.6 (a) A 250 μm hole produced in PEEK by soaking PEEK/HA composite into HCl solution; **(b)** top view of the porous PEEK sample showing interconnectivity of the channels, red arrows indicate crossed channels

The use of extrusion freeforming in this research work permitted excellent control on porosity (and thus mechanical properties of the porous structure), pore distribution, and ensured interconnectivity of the pores (**Fig. 4.6b**) which is necessary for bone-ingrowth. As mentioned in chapter 2, conventional techniques such as particulate leaching has poor control on porosity, and suffers from limitations such as inconsistency and the requirement for manual intervention. Using the proposed novel technique, porous PEEK can be easily produced with much higher control level on porosity and enhanced reproducibility, a key requirement in production of medical devices. Furthermore, the technique is a low-cost process in comparison with the SLS process, while affording greater control of pore size (the minimum achievable pore size in SLS is currently ~500 μm as pore size get smaller it gets more difficult to remove excess unsintered PEEK powders trapped inside pores). Therefore, while SLS as an AM technology has great control on pore size and architecture, its use in clinical applications is currently limited to those in which pore sizes above 500 μm are required. This range of pore size can meet the requirements recommended in literatures for bone in-growth and vascularization but might not be the optimal for bone cell attachment and proliferation where pores ranging 200 μm to 350 μm is normally required **(Gibbs et al., 2014, Jarman-Smith et al., 2012)**. The limitation in minimum pore size makes it difficult to design an implant with desired strength as well. Moreover, the very low recycle rate of PEEK powder makes SLS an extremely expensive and non-eco-friendly process. Conversely, with the use of the proposed technique a wide range of pore sizes (200-1000 μm) is achievable. This makes

the technique a versatile approach, enabling formation of porous PEEK which can be tailored to specific biomechanical requirements of a variety of clinical applications.

Further analysis of the SEM images revealed that the replica of the surface of HA filaments is produced onto the surface of channels in PEEK following HA removal (see **Fig. 4.7a**). This demonstrated that despite the high viscosity of molten PEEK, micropores on the surface of the HA filaments could be filled by PEEK through compression moulding. This guarantees a good interface between PEEK and HA filaments in PEEK/HA composite and more critically the rough surface of channels within porous PEEK can enhance bone cell attachment, proliferation, and differentiation **(Kumar et al., 2012, Evans et al., 2015)**. Kumar et al. **(2012)** demonstrated that etched extrusion freeformed PCL scaffolds with a roughened topography (surface roughness of up to 1.06 μm) can support hBMSC proliferation, while also inducing osteogenic differentiation, for maximal generation of bone-like tissue. The etched scaffolds induced osteogenic differentiation of hBMSCs while the un-etched scaffolds did not. Etched scaffolds also supported same levels of hBMSC proliferation as un-etched scaffolds. In addition, the hBMSCs present on un-etched scaffolds demonstrated greater migration, while hBMSCs on etched scaffolds were more rounded, indicating that surface roughness had an effect on hBMSCs morphology **(Kumar et al., 2012)**.

Optical profilometry (Alicona, Germany) was used to measure surface roughness of a typical 400 μm HA filament and hollow channels following the acid treatment. To this end, two HA scaffolds with a same filament/pore size were printed, both from a same HA paste with equal solvent content, and then one of them was used to produce PEEK/HA composite, and further porous PEEK. Next, single HA filaments from the first printed HA scaffold and the PEEK channels in the porous PEEK were subjected to surface roughness measurement. Surface roughness from 5 areas was recorded and their mean was used for comparison. Profile surface measurements were performed with 100 nm vertical and 1.4 μm lateral resolutions, and were taken from a 200 μm line that was parallel to the filament and channel to minimize errors resulting from the contribution of curvatures. **Figs. 4.7b** and **4.7c** show the 3D surface height maps captured from the surface of an HA filament, and its replica in PEEK, respectively. As it was very difficult to prepare samples with exactly the same filaments and channels, which requires very precise sample marking before and after infiltration, a direct comparison was not conducted. However it is reasonable to assume that the filaments produced in the same batch have very similar surface morphology. Both the surface of HA filament and the surface of the channel in PEEK (produced from the same batch, and the same size of HA filaments) had the same average surface roughness (Ra) of 0.4 μm, with standard deviations of 37 nm and 54 nm,

respectively. This demonstrates that there is excellent contact between PEEK and HA surfaces within the PEEK/HA composite.

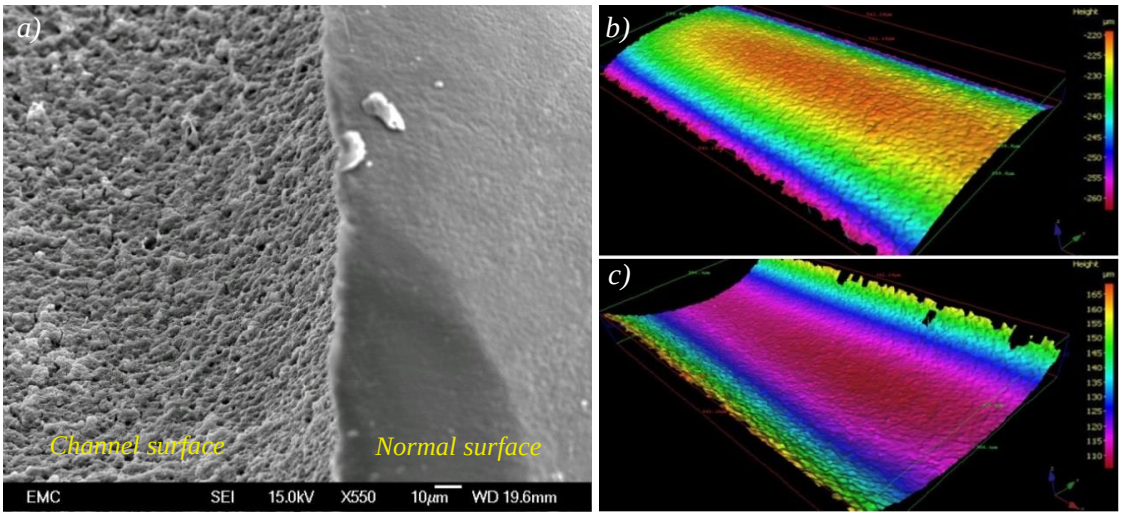

Figure 4.7 (a) Magnified view from surface of a channel within a typical porous PEEK; **(b, c)** representative 3D surface height maps are shown for 400μm HA filament and the channel produced with the use of a same size HA filament: HA filament surface profile **(b)**, and PEEK channel surface profile **(c)**

4.6 Biological Performance of PEEK/HA Composite

After production of the PEEK/HA biocomposites it was necessary to remove any potentially cytotoxic residual manufacturing contaminates and sterilise samples prior to in vitro experimentation. In vitro biocompatibility of the representative PEEK/HA samples was assessed using standard cell viability protocols based on guidelines set out in ISO 10993. Nine PEEK/HA samples were prepared and cut using diamond cutter to approximate size, 4×4×4 mm^3, and polished using silicon carbide papers by sequential wash, rinse and sterilisation stages. Under aseptic conditions, samples were placed in sterile 15 ml conical universal tubes (Corning, USA), and immersed in 10 ml sterile Phosphate Buffered Saline (PBS) (Life Technologies). The samples were placed on a rotary shaker (Spiramix 10, Denley) using 100 rotations per minute (rpm) for 10 minutes at room temperature, and this procedure was performed three times with fresh PBS. The samples were then washed in a 10% Triton X (Sigma Aldrich) distilled water solution, at 100 rpm overnight at 4 °C. Detergent solution was rinsed 5 times using the process previously described. Following the washing process the samples were placed in 10 ml sterile PBS and sterilised using exposure ultra-violet light for 6 hours, with 2 hourly rotations. hBMSCs were isolated using standard laboratory protocols **(Oreffo et al., 1997)**, and plated at density of 1×10^4 onto 75 cm^2 tissue culture flasks (Corning, USA) in α-

Minimum Enrichment Medium (α-MEM, Lonza), containing 10% Foetal Calf Serum (FCS, Lonza) and 1% Penicillin/Streptomycin (Life Technologies), and media changed every 3 days. Cells were passaged at 70-80% confluence using 0.05% Trypsin (Life Technologies), re-plated onto T75 flasks, split in a 1:5 dilution and expanded in culture. Passage 3 cells were trypsinized, and suspended to achieve a 3×10^5 cells/ 100 microliters (µl) of media. Under sterile conditions, each PEEK/HA sample was placed into a well of a 48-well culture plate (Corning) with the surface of interest facing upwards. Two 50 µl droplets of cell suspension were carefully applied to the surface of each sample with care taken to limit droplet exposure only to the region of interest. The samples were then placed incubated at 37.2 °C, 5.2% CO_2 for 1 hour to encourage cell adhesion. Following incubation 500 µl of culture medium was then added to each well, and cultured for 7 days, with media changed every 3 days. Cell viability and adherence were assessed by incubation and fluorescent imaging of Cell Tracker Green and Ethidum Homodimer (Molecular Probes), respectively. After 7 days' incubation, media was removed and the samples were gently washed in PBS. Cell Tracker Green and Ethidium Homodimer solution was prepared as per manufacturer protocol, and 500 µl of it was added to each sample containing well. Samples were left to incubate for 45 minutes then prepared for fluorescent microscopy. The samples were washed 3 times in PBS for 5 minutes before fixation in 4% Paraformaldehyde (PFA) for 10 minutes at 4 °C. Nuclei were counterstained with a 1:1000 diamidino-phenylindole (DAPi) solution for 15 minutes at 4 °C, further washed in PBS and stored prior to fluorescent microscopy. Multi-layered fluorescent images were captured using an AxioCam MRm Monochrome Camera X-Cite® with 200 Fluorescence Microscope Light Source Leica and processed using Axiovision Software V4.0.

Viable, adherent cells are visible under fluorescent microscopy after 7 days in culture. Cell viability at this time point was confirmed by incubation with Cell Tracker Green, the presence of non-viable cells visualized by Ethidium Homodimer incubation and uptake. In **Fig. 4.8**, adherent hBMSC are seen extensively over the surface of the PEEK/HA samples confirming a broad degree of cytocompatibilty across multiple samples, cultured over a biologically relevant time period of 7 days. DAPi stained cell nuclei, shown in blue, aid in visualising cell locality to regions of PEEK/HA interface. Non-quantitative observation suggests a preference in cell adhesion to HA surface areas over PEEK regions within individual samples. The majority of non-viable, non-adherent cells were removed during the PBS rising, which preceded media changes, and incubation with Live/Dead indicators. All remaining, adherent cells were confirmed viable by the absence of observed 617 nm wavelength emission after incubation with Ethidium Homodimer.

Fig. 4.9a shows the result of in vitro test on a sample with HA and rough PEEK channels (following removal of the HA phase). The PEEK channels were simply obtained on the surface after cutting the samples using diamond cutter as HA-PEEK bonding could not bear the high shear stress induced by high speed cutting process. Cells adhered to the HA, and to a lesser extent, the rough PEEK channels. This is an indicator that roughening of the PEEK surface can improve cell adhesion, although further investigation is required to ascertain optimum surface roughness. SEM image of the sample with etched PEEK surfaces (**Fig. 4.9b**) reveals a second cell localizing effect at the boundary between etched and smooth PEEK surface types. SEM imaging helps reveal the cell-surface interaction and adhesion at a) HA surface b) PEEK–HA boundary, and c) Interface of PEEK surface roughness variations. The green arrow in **Fig. 4.9b**, illustrates a bridging effect whereby proliferating cells appear to anchor and branch from the composite HA network and attach to either the rough PEEK channel surface or HA phase on the other side.

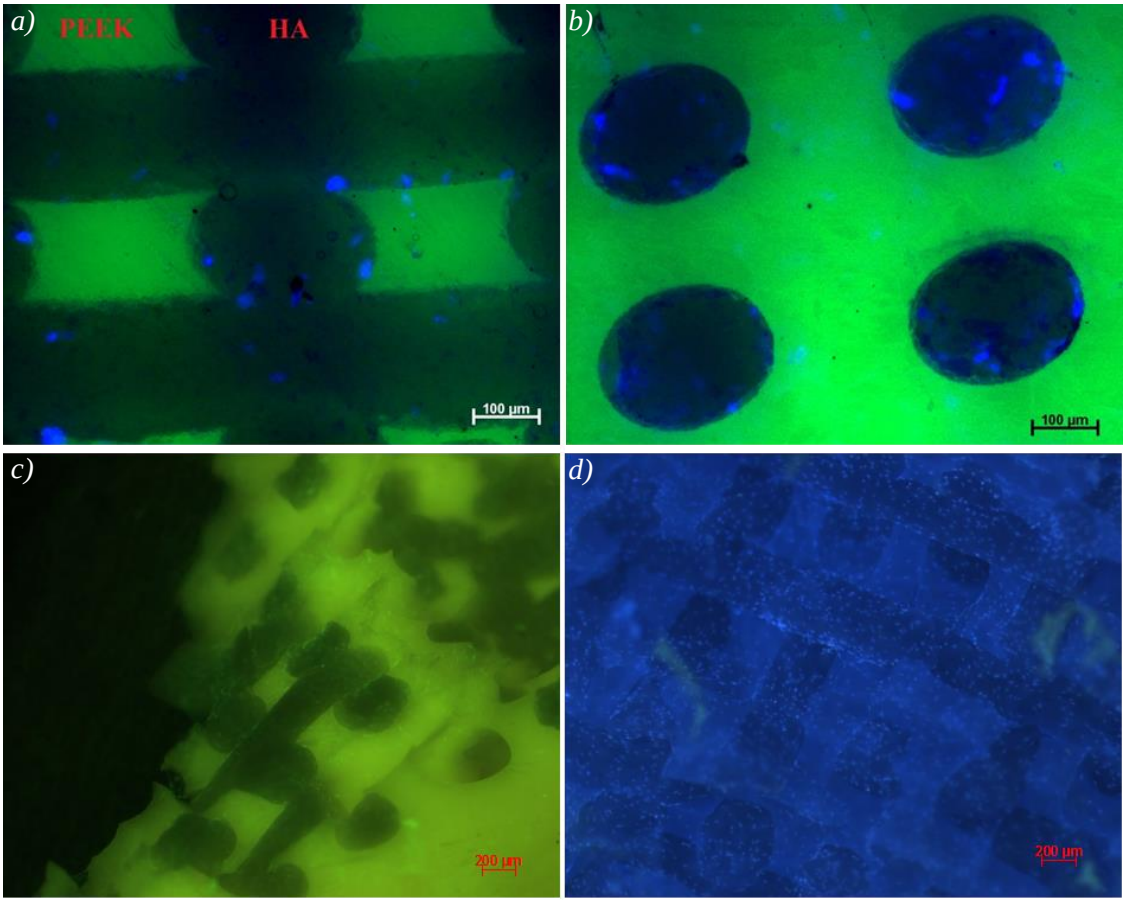

Figure 4.8 Cell attachment on PEEK/HA composite, DAPI nuclear staining (4',6-diamidino-2-phenylindole, blue) indicates the wide scale presence of adherent cells throughout the composite substance. Strong scaffold green-channel auto-fluorescence competes with Cell tracker Green signal in **(c)** which reduces the effectiveness of this assay.

These preliminary results are consistent with various documented techniques detailing the modifying effect of PEEK surface roughness and wettability on cell adhesion and proliferation. Sagomonyants et al. **(2008)** studied machined and injection moulded medical grade PEEK and CFR-PEEK together with polished, and rough medical grade titanium. According to their study, osteoblast adhesion at 4 hours on injection moulded variants of PEEK (Ra = 0.095 µm) and CFR-PEEK (Ra = 0.350 µm) material was comparable to polished (Ra = 0.200 µm) and rough (Ra = 0.554 µm) titanium. Osteoblast adhesion on machined samples of PEEK (Ra = 0.902 µm) and CFR-PEEK (Ra = 1.106 µm) materials were significantly less. Proliferation at 48 h determined by [3H]-thymidine incorporation was the greatest on the smoothest of all materials, the injection moulded unfilled PEEK, which was significantly higher than the rough titanium control. The machined unfilled PEEK had the lowest DNA synthesis. They concluded that surface roughness of 0.095 µm had better adhesion and proliferation response, while for differentiation roughness of 0.902 µm showed a better response. Recently, the effect of surface roughness of CFR-PEEK/nano-HA on in vitro cellular responses of osteoblast-like MG-63 cells (attachment, proliferation, apoptosis, and differentiation) and in vivo osseointegration was investigated **(Deng et al., 2015)**. Three different samples with Ra of 0.93 µm, 1.96 µm, and 2.95 µm were tested. The sample with moderate surface roughness (Ra=1.96 µm) significantly increases cell attachment/proliferation and promotes the production of alkaline phosphatase (ALP) activity and calcium nodule formation compared with the other groups. More importantly, the CFR-PEEK/n-HA implant with appropriate surface roughness (Ra=1.96 µm) exhibited remarkably enhanced bioactivity and osseointegration in vivo in the animal experiment. Surface roughness of 0.4 µm achieved in PEEK channels in this study might have different effect on cell adhesion, proliferation, and differentiation. Nevertheless, the surface morphology of the HA filament can be controlled by different sintering temperature and/or HA/TCP ration **(Yang et al., 2008c)**.

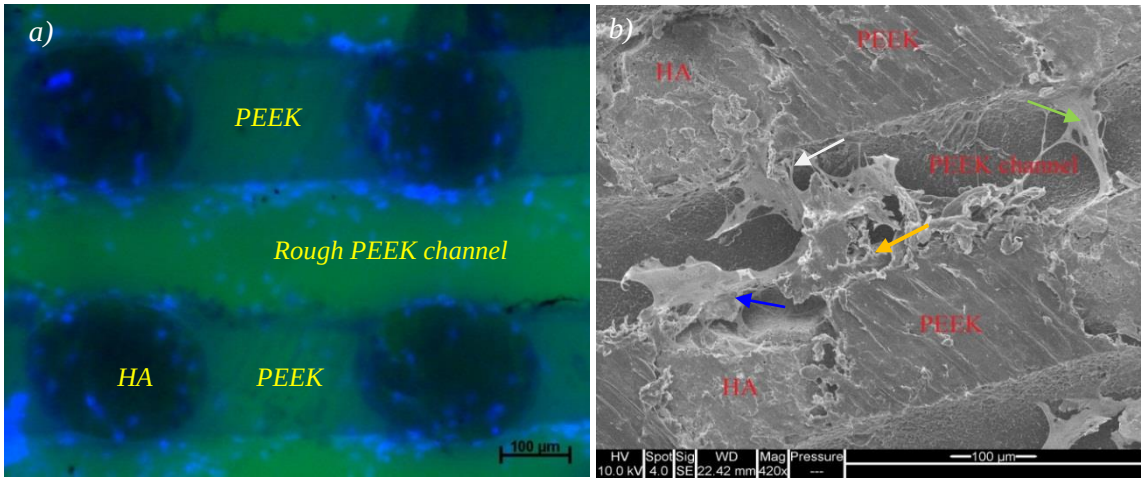

Figure 4.9 (a) Cell attachment on HA and rough PEEK channels within the composite, **(b)** SEM imaging reveals the cell-surface interaction and adhesion at HA surface (blue arrow), PEEK-HA boundary (white arrow) and the interface of PEEK surface roughness variations (orange arrow)

Quality control standards stipulating the testing of medical device biocompatibility require extensive investigation to confirm the true readiness for clinical application. As a pre-cursor to future development it was set out to show preliminary evidence supporting initial biological safety of the technique developed in this study. The protocol used here was only intended as an initial screening process and the authors acknowledge the depth of work yet to be completed to exhaustively document biocompatibility of novel materials. Further studies are planned to include in vitro cell differentiation, proliferation and molecular assays, leading to small in vivo models, and large animal use specific models.

4.7 Mechanical Properties of PEEK/HA

Whilst the addition of bioactive materials to PEEK offers an efficient system to engineer implants with tailored biomechanical properties, it may result in reduced strength of the implant, decrease in fracture energy and the brittleness of the composite materials **(Roeder and Conrad, 2012)**. Mechanical behaviour of conventional PEEK/HA composites has been studied extensively **(Abu Bakar et al., 2003a, Tang et al., 2004, Abu Bakar et al., 2003c, Fan et al., 2004)**. Elastic modulus, compressive strength and micro indentation hardness is enhanced by increasing HA loading, while tensile strength, toughness and strain to failure is decreased. Loading PEEK with 40 vol. % HA has been shown to decrease the ultimate tensile strength (UTS) of the PEEK by 45%, to 44MPa **(Kurtz and Devine, 2007).**

These new composites can be used for either load bearing or non-load bearing applications. The initial intention of this research work was to highlight extrusion freeforming technology as having potential application in production of these new PEEK/HA composites. However, assessment of mechanical properties would be an important metric of performance of these new biocomposites for potential compressive load bearing applications such as spinal cage fusion, etc. To this end, HA scaffolds with filament size of 400 μm and pore size of 700 μm were 3D printed and overmoulded with PEEK using the procedure described earlier. The produced PEEK/HA samples were cut at size 6×6×6mm using diamond cutter and subjected to further CT analysis. The samples with average HA volume percentage of 40% were subjected to unconfined, uniaxial compression test using an Instron 8032 test machine at strain rate of 3×10^{-3} s^{-1}. A 100 kN load cell was used and the test data were collected by Instron's Strainsmart 6200 software. Six samples were tested for reproducibility. The samples were tested in two different directions as illustrated in **Fig. 4.10.** Solid PEEK samples with 0% HA were also compression moulded and tested to compare with those with 40% HA. Due to ductile nature of PEEK in compression, samples were deformed to large strains and all strains referenced in this paper are true strains (logarithmic strains). Compressive yield strength was defined as the stress after which the initial linear region deviated from linearity; yield strain was defined as the strain associated with the compressive yield strength; and modulus of

elasticity was calculated from data representing the slope of the initial linear region **(Espalin et al., 2010)**.

Cyclic compression testing was also carried out on the specimens in direction 1 using the Instron 8032 machine operating under load-controlled mode and using sinusoidal waveform. Testing was carried out at room temperature under compression-compression mode at frequency of 5 Hz and R-value of 0.1 (R is the ratio of minimum to maximum cyclic load). The specimens were subjected to maximum stress of 20 MPa (i.e. approx. 30% of compressive strength). A cooling fan was set up to avoid overheating of the samples during cyclic loading. After 1 million cycles the samples were subjected to static compression test as described earlier in order to evaluate the mechanical durability of the composite. All the PEEK/HA specimens were annealed at 200 °C to achieve a high level of crystallinity before static and cyclic compression tests using the normal protocol for injected moulded PEEK parts (unfilled PEEK-OPTIMA processing guide, Invibio Ltd., UK): first, the samples were dried at 150 °C for three hours; next the samples were heated up at 10 °C/hr to reach to temperature of 200 °C and they were held for four hours at the target temperature; then the samples were cooled down to below 140 °C with rate of 10 °C/hr and the furnace was switched off allowing the samples cooled down to room temperature.

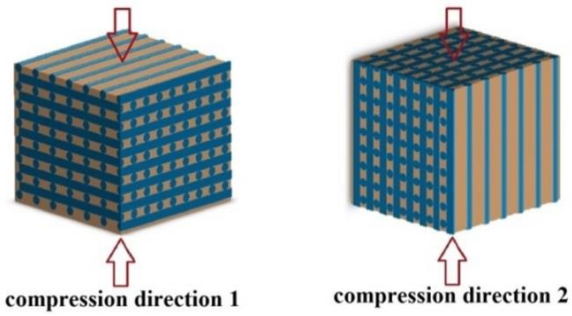

Figure 4.10 Different specimen direction used for compression tests

Figs. 4.11 and **4.12** depict the results of compression tests on the biocomposites with average HA content of 40 vol% tested in two different directions and compared with unfilled PEEK samples. It was observed that the PEEK/HA in both directions had lower yield and compressive strength and moduli than the unfilled samples. It was difficult to compare these results with previous works as other researchers have mainly studied PEEK/HA composites produced using either spherical shape HA particles or HA whisker under tensile loading **(Abu Bakar et al., 2003a, Tang et al., 2004, Abu Bakar et al., 2003c).**

Incorporation of extrusion freeformed HA continuous filaments into PEEK in this work deceased both compressive strength and moduli of the biocomposites. Similar decreasing of compressive moduli has been reported by Roeder's group **(Converse et al., 2009)** for porous PEEK/HA composites. Although Roeder's group has reported a similar effect with regard to

decrease in compressive moduli, their work may not be that comparable to this study since there are some noticeable differences in the biocomposites tested; their PEEK/HA samples had 75% porosity and HA whisker with average length of 21.6 μm and an aspect ratio of 7.6 distributed randomly within the composite, while the samples tested in this study had porosity less than 5% and continuous HA filaments with 400 μm diameter and an aspect ratio of 15 with computer-controlled distribution. Furthermore, the compression moulding procedures used by Roeder's group is relatively different in terms of moulding pressure and PEEK powder densification.

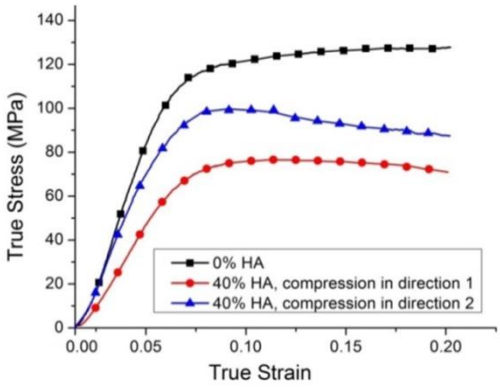

Figure 4.11 Stress–strain plot for PEEK/HA biocomposite with 40 vol.% HA compressed in different directions

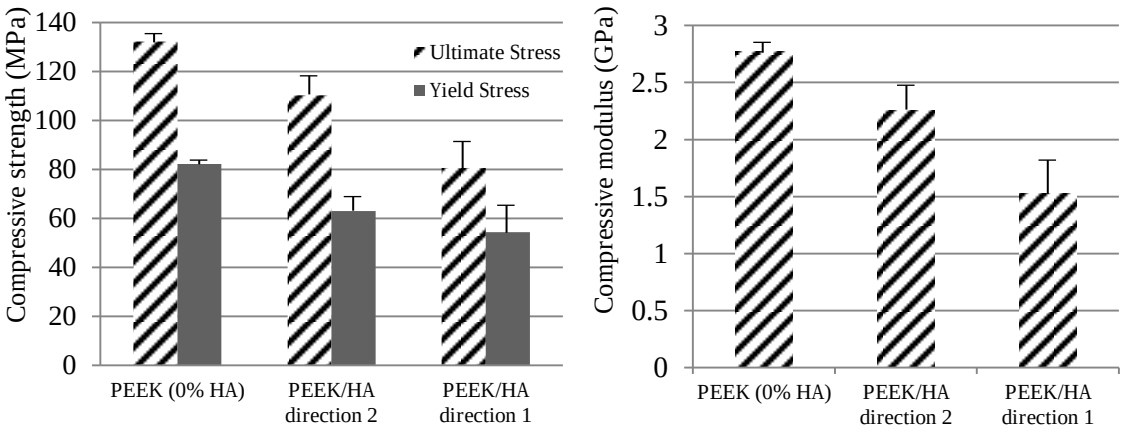

Figure 4.12 Compressive elastic modulus, ultimate and yield stress determined for PEEK and PEEK/HA specimens compressed in different directions

The samples tested in direction 2 had higher compressive modulus, yield and compressive strength than the sample tested in direction 1. It could be considered that having HA filaments oriented parallel to load axis produces remarkably higher compressive moduli and strength that has been reported for short **(Rasheva et al., 2010)** and continuous CFR-PEEK **(Almajid et al., 2011).**

Table 4.4 depicts comparison between compressive properties of the produced unfilled PEEK, the PEEK/HA composites with 40% HA, and human cortical bone (data for human cortical bone taken from **Öhman et al., 2011**). As seen in **Table 4.4**, the mechanical properties of unfilled PEEK are close to that of human cortical bone which has been already reported in the literatures **(Wang et al., 2010b).** The PEEK/HA possesses yield and compressive strength within the range of cortical bone. In particular, the compressive modulus of the PEEK/HA is very close to cortical bone and this is an advantage compared to metal biomaterials. The mismatched compressive moduli of metal biomaterials with bone can cause stress shielding. For this reason metal biomaterials used must be of sufficient porosity for orthopaedic application, which can add significantly to production costs and time. The use of AM systems for direct 3D printing of porous metal implant with tailored stiffness could shorten production time, yet is a relatively inexpensive approach. The compressive moduli of titanium alloy (Ti6Al4V) with porosity of approx. 70%, fabricated by ARCAM's electron beam melting (EBM) AM process, was reported as 3.7-6.7 GPa that is within the range of cortical bone **(Wieding et al., 2012)**. Conversely, the PEEK/HA composites with compressive moduli very close to cortical bone can be produced with much lower cost in a short period.

Table 4.4 Compressive properties of the produced PEEK/HA (with 40% HA) in direction 1 and unfilled PEEK versus human cortical bone taken from **(Öhman et al., 2011)**

	Human cortical bone		**Unfilled PEEK**	**PEEK/HA**
	transverse	longitudinal		
Compressive moduli (GPa)	N/A	4-22	2.8	1.6-2.5
Compressive yield strength (MPa)	N/A	50-200	83	54-63
Compressive strength (MPa)	50-70	70-280	134	80-110

Weibull reliability distribution curves for yield stress and elastic modulus were plotted for samples tested in direction 1 (**Fig. 4.13**). The "two-parameter Weibull distribution" was used to determine ultimate stress, yield stress and elastic modulus in this study. The calculation method is presented in the Appendix 1. According to Weibull reliability curves, about 93% of the samples had compressive yield strength of above 20 MPa, and elastic modulus above 0.8 GPa. Taking this into consideration, another set of samples with same HA content were prepared and subjected to compressive-compressive cyclic loading with maximum and minimum stress of 20 MPa and 2 MPa for 1 million cycles. Afterward, the samples were subjected to compression to failure test in order to evaluate cyclic loading endurance of the biocomposites. No significant difference in compressive strength was observed between the cyclic loaded samples and the normal samples (**Fig. 4.14**). The cyclic loaded samples had relatively similar yield and ultimate strength, but smaller yield strain, and higher elastic modulus of 1.93 GPa. Previous studies on tension-tension fatigue behaviour of the PEEK/HA

composites prepared using compression moulding showed that spherical HA particles in PEEK/HA composites could debond from the PEEK matrix during long-term cyclic loading due to the poor interfacial adhesion **(Tang et al., 2004)**. To improve PEEK-HA interface, well-dispersed HA nanoparticles **(Ma et al., 2014, Deng et al., 2015,Wang et al., 2010, Wang et al., 2011)** can be used although agglomeration of HA nanoparticles becomes an issue when the loading is over 10 vol.% **(Wang et al., 2010)**.

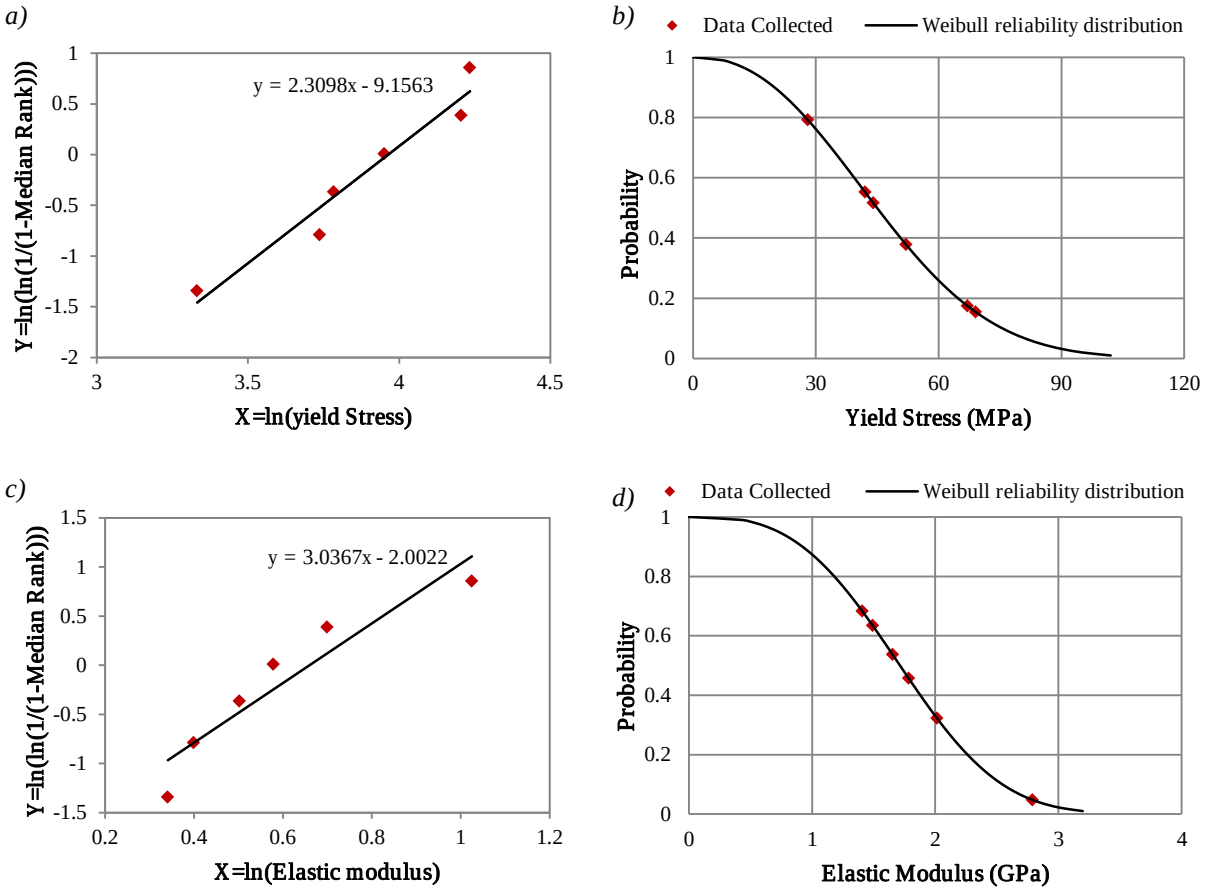

Figure 4.13 (a) Regression line for estimating compressive yield stress, **(b)** Weibull reliability distribution for yield stress, **(c)** Regression line for estimating compressive elastic modulus, **(d)** Weibull reliability distribution for elastic modulus

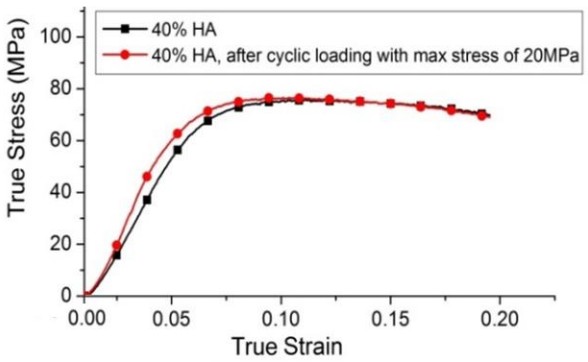

Figure 4.14 Compressive stress-strain plot for PEEK/HA composites with 40 Vol% HA before and after 1 million cyclic loading in direction 1

Fig. 4.15a shows sequential images of the PEEK/HA biocomposites during compression in different directions. As can be seen, in both test directions the samples experienced barrelling due to variation of frictional force (e.g. minimum at the centre and maximum at the edges) under compressive load. In particular, physical inspection of the specimens at both macro and microscopic levels revealed that compression in direction 2 results in anisotropic behaviour of the biocomposites (see **Figs. 4.15b** to **4.15f**). As seen in **Fig. 4.15b** and **4.15c,** the unfilled PEEK sample and PEEK/HA tested in direction 1 have similar strain amounts in X and Y directions, while the PEEK/HA sample tested in direction 2 have a much higher strain in direction Y than direction X (**Fig. 4.15d**). Existence of the long HA fibres might be the main reason for this anisotropic behaviour of the composite when tested in direction 2. PEEK needs to fracture the long HA fibres to flow in direction X, while in Y direction PEEK can flow through pores and has no need to fracture the HA structure. The side view of the sample tested in direction 2 (**Fig. 4.15e**) shows the flow of PEEK between fractured HA filaments. Unfortunately, it was very difficult to use a strain gauge to measure strain in different directions due to small size of the samples. Further experiments are needed on larger specimens to enable investigation of the anisotropic behaviour of these biocomposites.

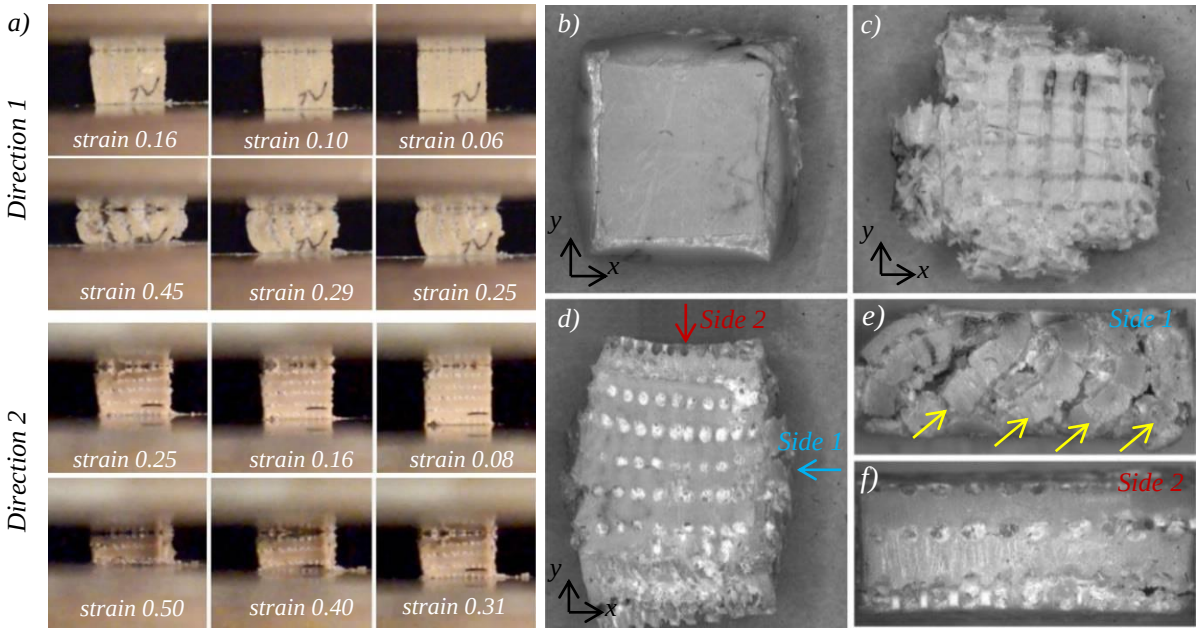

Figure 4.15 (a) Sequential images of PEEK/HA biocomposites at size 6×6×6mm with 40 vol.% HA during compression in different directions, **(b-f)** optical images of the samples after compression test: **(b)** top view of unfilled PEEK sample, **(c)** top view of PEEK/HA compressed in direction 1, **(d)** top view of PEEK/HA compressed in direction 2, **(e, f)** front and side view of PEEK/HA compressed in direction 2

As a consequence of what was discussed, incorporation of a high HA volume into the PEEK matrix significantly affects the mechanical properties of the PEEK/HA composite. However,

interconnectivity of PEEK matrix in the composites achieved through this technique is an advantage as this gives the PEEK matrix a high level of structural integrity. Therefore, a greater proportion of bioactive material can be incorporated into PEEK where required with minimum effect on mechanical properties of the composite as the PEEK matrix remains fully interconnected. Hierarchical HA scaffolds with varied pore size can be served to make functionally graded PEEK/HA composites with partially controlled mechanical and biological performances. A potential future application of these functionally graded PEEK/HA material in spinal arthrodesis is shown in **Fig. 4.16**. As demonstrated, the greatest mechanical strength is achieved in the zone where HA has larger spacing (lower HA content), and enhanced biological performance in regions in contact with bone, where HA lattice has smaller spacing (greater HA content). Computer-controlled distribution of HA in these composites ensures uniform distribution of load onto the device after implantation as well.

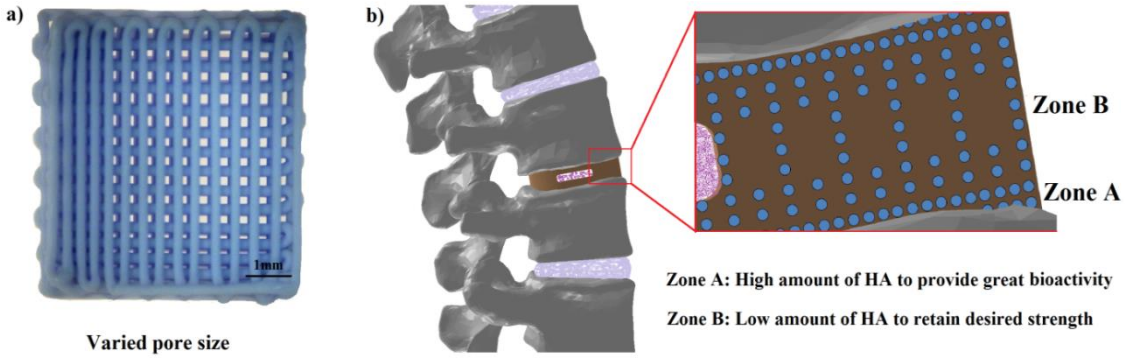

Figure 4.16 (a) A typical 3D printed hierarchical HA scaffold with computer-controlled varied spacing suitable to make functionally graded PEEK/HA composites, **(b)** schematic of the use of functionally graded PEEK/HA in spinal cage fusion

4.8 Summary

In this chapter, a new technique was proposed for production of bioactive PEEK/HA composite and porous PEEK. The technique integrates extrusion freeforming and compression moulding processes. The main advantage of the technique over injection moulding and compression moulding is the greater control on the distribution of the bioactive phase and the 100% interconnectivity of both PEEK and bioactive phase which is superior to existing microstructural designs. A static pressure of 0.39 MPa, dwell time of 20 min and temperature of 400 ºC were identified to be optimal for compression moulding of HA scaffolds of size 10×10×3 mm with filament size of above 250 µm and pore size of above 200 µm. Porous PEEK structures were produced by soaking the biocomposite into HCl solution. Interconnected channels were formed within PEEK matrix with an average surface roughness of 0.4µm.

The results of unconfined, uniaxial compressive tests on these new PEEK/HA biocomposites with 40 vol.% HA under both static and cyclic mode were promising, showing the composites possess yield and compressive strength within the range of human cortical

bone suitable for load bearing applications. The biocomposites could survive in one million compression-compression cyclic loading at 30% of their compressive strength without any degradation in compressive properties. In addition, preliminary evidence supporting initial biological safety of the new technique developed is demonstrated in this chapter. Sufficient cell attachment, sustained viability in contact with the sample over a 7 day period, evidence of cell bridging all confirmed excellent biocompatibility.

Chapter 5

High-Temperature Extrusion Freeforming of PEEK

Chapter 5: High-Temperature Extrusion Freeforming of PEEK

5.1 Introduction

There has been a trend in recent years to develop PEEK-based medical devices. Different manufacturing techniques such as injection moulding, particulate leaching, compression moulding, and SLS have been used to produce porous PEEK for biomedical applications **(Tan et al., 2003, Converse et al., 2007, Abu Bakar et al., 2003a)**. SLS process has made a great breakthrough in PEEK implant design and manufacturing due to its capability to 3D print directly using CAD file with high level of repeatability. However, it is a high cost AM process which suffers from limitations such as achievable pore size and very low recycle rate of PEEK powder.

The results presented in the previous chapters proved that extrusion freeforming, as a low-cost AM method, offers a great control on macro/microarchitecture, and guarantees reproducibility. Although there has been a large number of publications in the field of extrusion freeforming, so far there have been very few preliminary technical **(Valentan et al., 2013)** and commercial reports (INDMATEC GmbH, www.indmatec.com) on extrusion AM of PEEK. It is quite challenging to process PEEK through extrusion freeforming due to its very high melting temperature in comparison with other thermoplastics or biopolymers such as acrylonitrile butadiene styrene (ABS) and poly(lactic acid) (PLA). The preliminary report on extrusion AM of PEEK is promising **(Valentan et al., 2013)**. However, very small parts could be printed with insufficient quality (e.g. defects such as part warpage and/or delamination) and no further discussion on the main challenges and obstacles, and mechanical properties has been presented. In this chapter, successful extrusion AM of medical grade PEEK structures is reported for the first time with in-depth discussion on extrusion system, the main challenges, and the process parameters need to be adjusted. Furthermore, mechanical properties of the extrusion freeformed porous PEEK parts are investigated for the first time in this chapter.

Like SLS process, both external shape and porosity of the structure is computer controlled in extrusion freeforming process and advantageously it is a low-cost process which makes it an economic and efficient method to produce fully functional biomedical PEEK implants. Furthermore, extrusion freeforming does not possess limitation of SLS process in terms of pore size so that it can theoretically meet the pore size requirements for any site of human bone defects with desire mechanical properties.

5.2 Materials and Methods

Two different high-temperature extrusion-based AM systems with different extrusion head configurations were set up and tested: syringe-based (**Fig. 5.1a**) and filament-based extrusion head designs (**Fig. 5.1b**). In both techniques, one nozzle was used for deposition of both part and support materials.

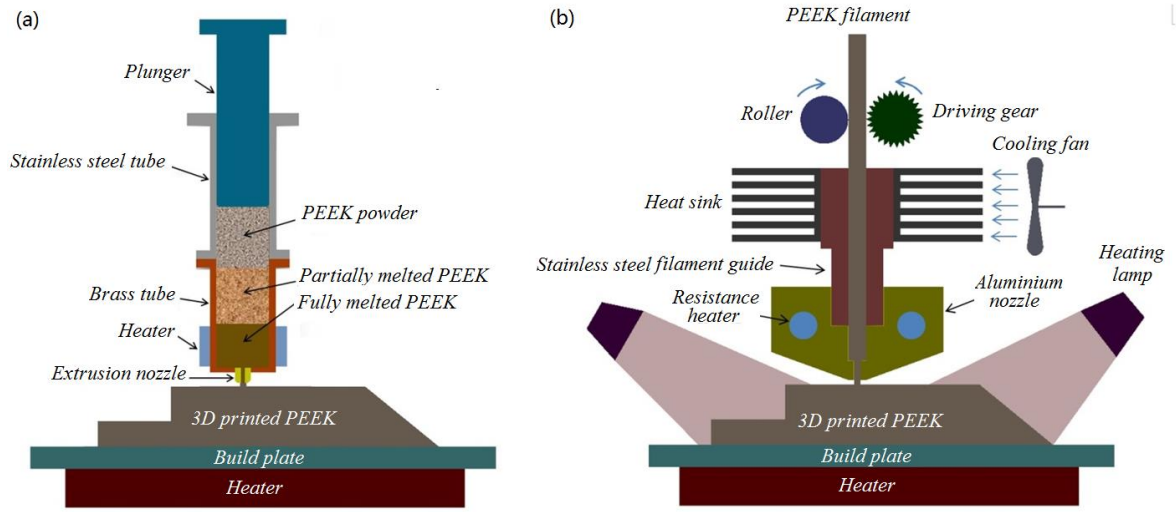

Figure 5.1 Schematic of **(a)** the syringe-based, and **(b)** the filament-based device set up for 3D printing of PEEK

As for the syringe-based method, the pre-set device suitable for low-temperature printing of bioceramic scaffolds **(Vaezi and Yang, 2015)** was modified in order to reach nozzle temperature up to 450 °C for PEEK extrusion. The extrusion syringe was made from two different metal tubes coupled together: a brass tube with an internal diameter of 17 mm with good thermal conductivity attached to a 500 µm nozzle (high-pressure sapphire nozzle-type 60, Quick-ohm, Germany) and a stainless steel tube with high strength and lower thermal conductivity. Using the brass tube, PEEK can absorb sufficient energy to get fully melted and easy to extrude through a nozzle. In the other region (within stainless steel tube), PEEK has lower temperature since there is less thermal conductivity, and thus less chance to get overheated and degraded. A self-adhesive etched foil silicone heater was also used to get the substrate heated (up to 170 °C) in order to transfer heat to the printed PEEK parts continuously to minimise thermal stress. As for filament-based system, a driving gear feeding system was used to extrude PEEK through a 0.4mm nozzle and deposited layer by layer to build up complex 3D structures. For this end, an UP 3D printer (www.pp3dp.com) was modified so that nozzle temperature up to 460 °C and heated build plate of 130 °C could be achieved. In addition, heating lamps surrounding the build area were used to control ambient temperature (approx. 80 °C) to avoid severe part warpage and delamination.

PEEK-OPTIMA LT3 powder was used as received from Invibio for the experiments using the syringe-based device. PEEK-OPTIMA LT3 is an easy flow grade PEEK that was used to minimise friction between PEEK and syringe's wall, and thus reduction of extrusion pressure. Victrex® PEEK 450G filaments with a diameter of 1.75 mm (type 8110, ZYEX, UK) were used for the experiments using the filament-based device. Victrex® PEEK 450G has a molecular weight of 115,000 which is similar to medical grade PEEK-OPTIMA LT1 which has been developed to meet with FDA requirements. The materials were dried at 150 °C for three hours before using in 3D printing process.

The filament-based device was identified more stable and efficient than the syringe-based method. A series of experiments were conducted to define the optimum nozzle temperature range in accordance with mass flow rate. Nozzle temperatures from 350 to 450 °C were tested with an extrusion flow rate of 2.2 mg/s (that is suitable for printing with a build layer thickness of 0.2 mm) and an ambient temperature of 80 °C to define the extrusion temperature range with no nozzle clogging and polymer degradation.

The 3D printed porous samples were cut using a diamond cutter for microstructural analysis. The morphologies of the 3D printed parts and porous scaffolds were examined using optical microscopy and SEM. In addition, the printed PEEK scaffolds were characterized in terms of porosity and mechanical properties. Porosity was measured by correlating PEEK scaffolds' geometrical dimensions and material density as per ASTM F 2450-04:

$$\textbf{Porosity}\ (\%) = \frac{\left(\mathbf{V_T} - \frac{\mathbf{m}}{\boldsymbol{\rho}}\right)}{\mathbf{V_T}} \times \mathbf{100} \qquad (5.1)$$

where V_T is the total volume occupied by the network of pores (determined from calliper measurements of length, width, and height), $\boldsymbol{\rho}$ is the material density (1.30 g/cm^3 for Victrex® PEEK 450G), m is specimen's mass measured using a Mettler AE240 micro-balance (LET, USA).

Based on the standard compressive test method specified by ASTM D695-02a, the stress-strain responses were investigated on the printed closed-cell porous specimens with dimensions of 12.5 mm (diameter) by 25 mm (height). The specimens had an average porosity of 38% with a strut width of 600 μm, a strut height of 200 μm, and a pore size of 450 μm, 3D printed using a nozzle temperature of 410 °C, build plate heated to 100 °C, and an ambient temperature of 80 °C. The samples were tested using the Instron 8032 test machine at a strain rate of 10^{-3} s^{-1}. A 100 kN load cell was used and the test data were collected by Instron's Strainsmart 6200 software. Solid PEEK-OPTIMA LT1 samples (porosity 0%) were also tested to compare those with 38% porosity. Three samples were tested for each group for reproducibility. Due to the ductile nature of PEEK in compression, samples were deformed to large strains and all strains referenced in this study are true

strains (logarithmic strains). Compressive yield strength was defined as the stress after which the initial linear region deviated from linearity; yield strain was defined as the strain associated with the compressive yield strength; and modulus of elasticity was calculated from data representing the slope of the initial linear region **(Espalin et al., 2010)**.

Simplified tensile test bars with rectangular cross section were also printed using 100% infill rate with the aim of achieving maximum density. The samples were printed at size 60×4.5×3 mm^3 in the X direction (e.g. build height of 3 mm) with +45º/-45º criss-cross raster orientation. An Instron 4204 tensile test machine with 50 kN load cell was used for tensile test at a strain rate of $2\times10^{-3}s^{-1}$ and a room temperature of 23 °C. In addition, specimens with a lower infill rate of 80% were printed at size 60×11×3.5 mm^3 and were subjected to tensile test for investigating the effect of incorporating porosity into PEEK.

The three-point flexural test was also conducted according to the ISO 178 standard procedure using an Instron 5569 machine to compare bending behaviour of the 3D printed PEEK with some other available AM materials and techniques, as follows:

- Acrylate-based resin (clear resin as received from Formlabs, USA) printed using a Formlab's Form 1 stereolithography (SLA) machine (www.formlabs.com)
- ABS M30 and ABSPlus printed using commercial Stratasys' Fortus 400mc and Dimension 1200es FDM machines (www.stratasys.com), respectively.
- Polyamide (PA12) and alumide (aluminium/polyamide composite called PA12-Al) printed by an external online 3D printing service company (www.i.materialise.com) using an EOS P730 SLS machine.
- Victrex PEEK 450G printed using the developed filament-based 3D printing system

The flexural test specimens were printed at size 10×4×80 mm^3 and tested in a similar build direction (build layers were parallel to the loading span in all test specimens). All the compression, flexural and tensile test specimens were annealed at 200 °C to achieve a high level of crystallinity using the normal protocol for injected moulded PEEK parts **(unfilled PEEK-OPTIMA processing guide, Invibio Ltd, UK)**: first, the samples were dried at 150 °C for three hours; next, the samples were heated up at 10 °C/h to reach a temperature of 200 °C and they were held for four hours at the target temperature; then the samples were cooled down to below 140 °C with a rate of 10 °C/h and the furnace was switched off allowing the samples to cool down to room temperature.

5.3 The 3D printed PEEK

The critical factors in PEEK extrusion freeforming are high-temperature extrusion head design, and environmental heat management to achieve continuous printing without nozzle clogging or polymer degradation, good layer bonding and minimised part warpage (in

particular detachment of first printed layer from build plate which yields failure of printing). According to the results of the experiments, syringe-based extrusion head design does not provide sufficient heat management over PEEK feedstock inside a syringe. It was difficult to control viscosity of PEEK extrudate, and to avoid thermal degradation of the material inside a syringe. In addition, using syringe-based system parts with limited volume can be printed. **Fig. 5.2** depicts the preliminary results using the syringe-based extruder in which the printed three layer PEEK scaffold detached from the heated build plate of 170 °C (which is above glass transition temperature of PEEK) during printing process. It should be noted that the printed three layer scaffold was not uniform due to insufficient heat management on the PEEK inside the extrusion syringe. As can be seen in **Fig. 5.2b**, PEEK extrudates were too viscose in the second and third layers due to over-heating and could not retain their shape upon deposition (red arrows).

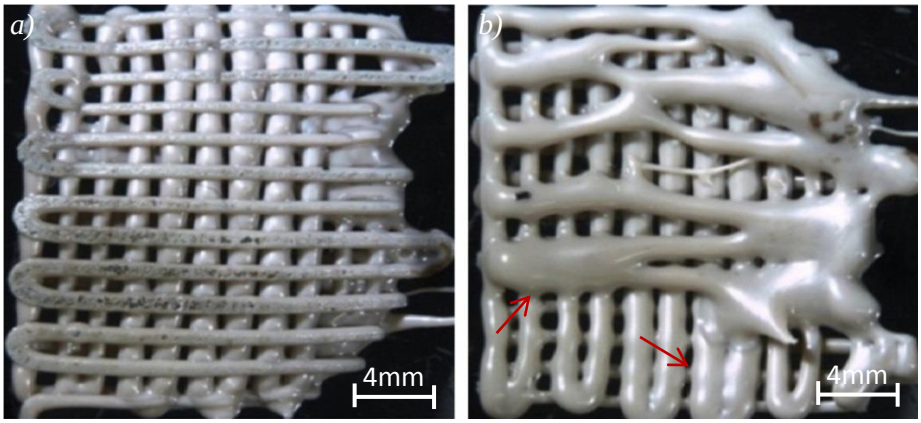

Figure 5.2 PEEK extrusion freeforming using the syringe-based extrusion system and heated build plate (170 °C), printing process failed due to the first-layer detachment from build plate: **(a)** back side, and **(b)** top side

Conversely, using the filament-based extrusion system it was possible to minimise the heat affected zone in the PEEK feedstock with the use of an efficient heat sink as illustrated schematically in **Fig. 5.1b**. High temperature of PEEK melt causes a remarkable thermal stress on PEEK extrudate upon deposition which results in defects such as delamination (insufficient layer bonding) and part warpage. Current available material melting extrusion AM systems use either temperature controlled build chamber or heated build plate to avoid these defects in thermoplastics such as ABS and PLA with melt temperature below 250 °C. As for PEEK, the thermal stress effect is much more significant and necessary to be managed. Although both heated build plate and heating lamps (instead of build chamber) were used to minimise the thermal stress, the printed PEEK detached from heated build plate during printing process (**Fig. 5.3a**). Using a raft structure (patterning very thick filaments under part) was identified as an asset to keep the PEEK filaments stocked on the heated build

plate for longer time (**Fig. 5.3b**), however, it was necessary to use an appropriate technique to have sufficient bonding between the first printed layer and substrate.

Substrate from different polymeric and metallic materials including aluminium, polyimide film (kapton tape), stainless steel, and glass were tested for the aim of achieving adequate PEEK/substrate bonding. None of them provided adequate bonding with PEEK after deposition. This problem has been one of the main challenges in PEEK extrusion freeforming and needed to be solved to be able to successfully print a PEEK part. To solve this problem, a new build plate design was proposed so that there are many fine holes at size less than 1 mm with negative angels to entrap PEEK after deposition. As illustrated in **Fig 5.3c**, the PEEK filaments can fill these holes after deposition and upon solidification they get fixed as the negative angel in the holes avoid any further displacement of the material. A custom designed build plate with features to hold the first deposited layer made from printed circuit board (PCB) heated up to 130 °C and heating lamps surrounding the build area so that ambient temperature could reach to 80 °C was identified as a suitable platform for successful 3D printing of PEEK parts using an extrusion temperature of 410–430 °C.

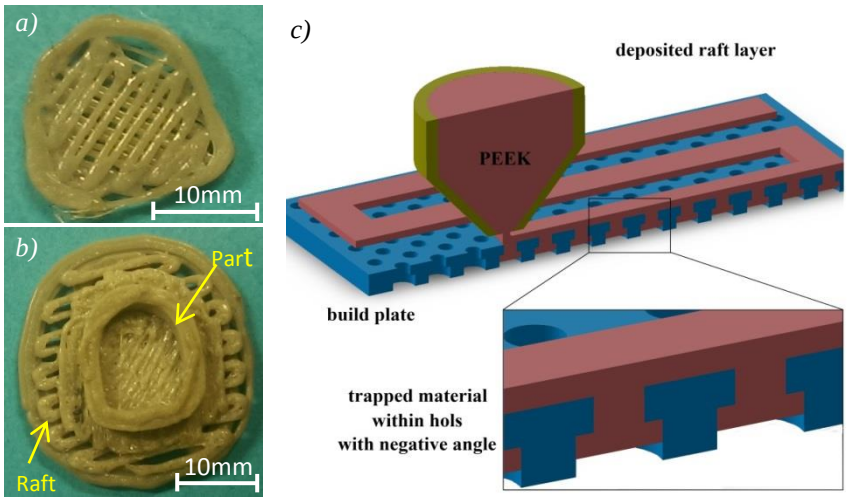

Figure 5.3 3D printed PEEK parts using filament-based extrusion system: **(a)** without raft, **(b)** with raft structure, and **(c)** schematic of the custom designed build plate with features to entrap the deposited PEEK

Also, extrusion temperature needs to be set appropriately since it can affect the level of crystallinity, and thus mechanical properties of the final 3D printed PEEK structure. Furthermore, if the extrusion temperature is too high the material may degrade or the extrudate cannot retain its shape upon deposition which results in filament deformation and dimensional inaccuracy. On the other hand, if the extrusion temperature is not high enough the material does not have enough time to get fully melted and this can cause nozzle clogging. In particular, nozzle clogging more likely occurs when the filament-based extrusion head is used since the heat-affected zone is much

less than the syringe-based extrusion head, and in turn the PEEK filament has less time to absorb energy and get fully melted. A low extrusion temperature can also result in delamination as the material does not have enough energy to make a good contact fusion bonding with the previous layer. Furthermore, there is correlation between nozzle temperature and extrusion flow rate in the filament-based extrusion system. For instance, if a high flow rate is required (for shortening build time using thicker printing layers) the material has a shorter time to absorb energy and consequently nozzle clogging occurs. Therefore, a higher nozzle temperature is required to avoid nozzle clogging at high flow rates.

As a consequence of what was discussed earlier, it was necessary to define the optimum extrusion temperature range in accordance with extrusion rate, ambient temperature and feedstock filament size so that the PEEK filament can retain its shape upon deposition, and there is no polymer degradation, nozzle clogging, and delamination. The melting temperature of PEEK-OPTIMA LT1 is 337 °C, however, it is normally processed through injection moulding at temperatures of 360–400 °C **(Kurtz, 2012)**. To cover this processing range, extrusion temperatures from 350 °C to 450 °C were tested in this research with a flow rate of 2.2 mg/s using PEEK feedstock filaments with a diameter of 1.75 mm, and an ambient temperature of 80 °C. PEEK degradation could be detected by either colour change or formation of entrapped voids inside PEEK filaments after deposition as illustrated in **Fig. 5.4**. Delamination and filament deformation could be detected by visual and optical microscope inspection of the specimens.

Figure 5.4 The 3D printed PEEK scaffold using filament-based extrusion system with entrapped bubbles due to polymer degradation

According to the results, temperature of 400–430 °C was identified as an applicable range so that temperatures below 400 °C caused either nozzle clogging or delamination and above 430 °C resulted in either considerable filament deformation or material degradation over a long time extrusion. This temperature range can be further narrowed by taking into consideration other factors such as dimensional accuracy, mechanical properties and biological performance.

Further dimensional analysis, mechanical and biological experiments are required to define the optimum temperature for printing PEEK parts with high accuracy, maximized mechanical strength with sufficient biocompatibility.

Fig. 5.5a depicts some parts 3D printed successfully using a filament-based device with a build layer thickness of 0.2mm and a nozzle temperature of 410 °C. As can be seen, the 3D printed parts have very good quality with no warpage and delamination due to their strong layer bonding (**Fig. 5.5b**). The use of extrusion freeforming in this research work permitted excellent control on pore size and interconnectivity which is necessary for bone ingrowth. Conventional techniques such as particulate leaching have poor control on porosity, and suffer from limitations such as inconsistency and manual intervention. Using the extrusion freeforming method, porous PEEK implants could be rapidly printed with a much higher control level on external shape and porosity with enhanced reproducibility, a key requirement in the production of medical devices. **Fig. 5.5c** illustrates the capability of the process to make porous PEEK structures with controlled pore size down to 150 µm using computer design. In **Fig. 5.5c**, PEEK filament size is 300 µm and there are two different spacing, namely, 150 µm (red arrow) and 300 µm (blue arrow). Possibility of varying pore size through the part and controlling of external shape by computer design are the main advantages of extrusion freeforming process over other traditional techniques such as particulate leaching and compression moulding. Furthermore, extrusion freeforming is a low-cost AM process in comparison with the SLS process and more importantly it does not subject to limitation in terms of pore size.

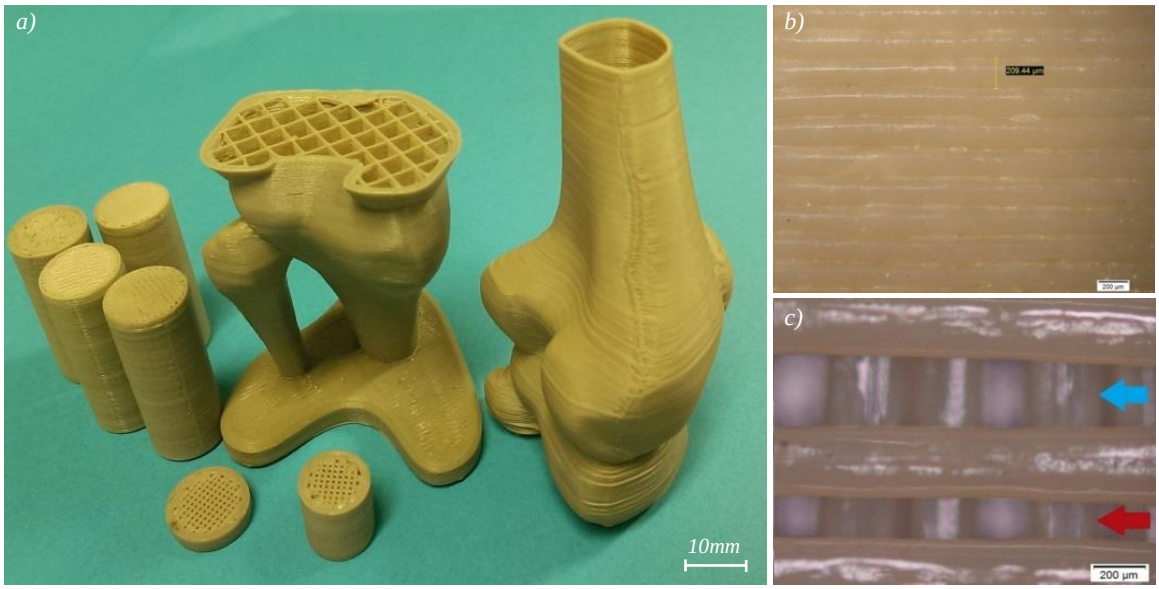

Figure 5.5 (a) PEEK samples 3D printed in 0.2 mm layer thickness; **(b)** microscopic image from the surface of the 3D printed part, showing a good layer bonding, scale bar 200 µm; **(c)** 3D printed PEEK scaffold with varying pore sizes (red: 150 µm, blue: 300 µm), showing capability of the process to control pore size within layers, scale bar 200 µm

PEEK's mechanical properties is influenced by the level of crystallinity of the material, and it has erstwhile been reported that increasing crystallinity can increase elastic modulus and yield strength, while conferring lower toughness **(Chivers and Moore, 1994, Kurtz and Devine, 2007, Jaekel et al., 2011)**. The level of crystallinity is affected by thermal history and material cooling rate. Hence, the level of crystallinity of PEEK is normally controlled by mould temperature in the injection moulding process **(Kurtz, 2012)**. In addition to mould temperature control, injection moulded part may be subjected to further annealing to achieve the optimal level of crystallinity.

Similarly, the cooling rate needs to be controlled in extrusion freeforming process so that deposited materials are cooled down slowly to allow creation of crystalline PEEK structure. Skin colour change occurred either in different layers (**Fig. 5.6a**) or in the same layers but different regions (**Figs. 5.6b** to **5.6e**) in the 3D printed large human bone structures with non-uniform cooling rate. These colour changes should not be confused with degraded material and can be interpreted as different levels of crystallinity: darker parts have more amorphous structure, whereas the brighter areas have a higher level of crystallinity **(Kurtz, 2012)**. The brown amorphous skins could be eliminated by further annealing.

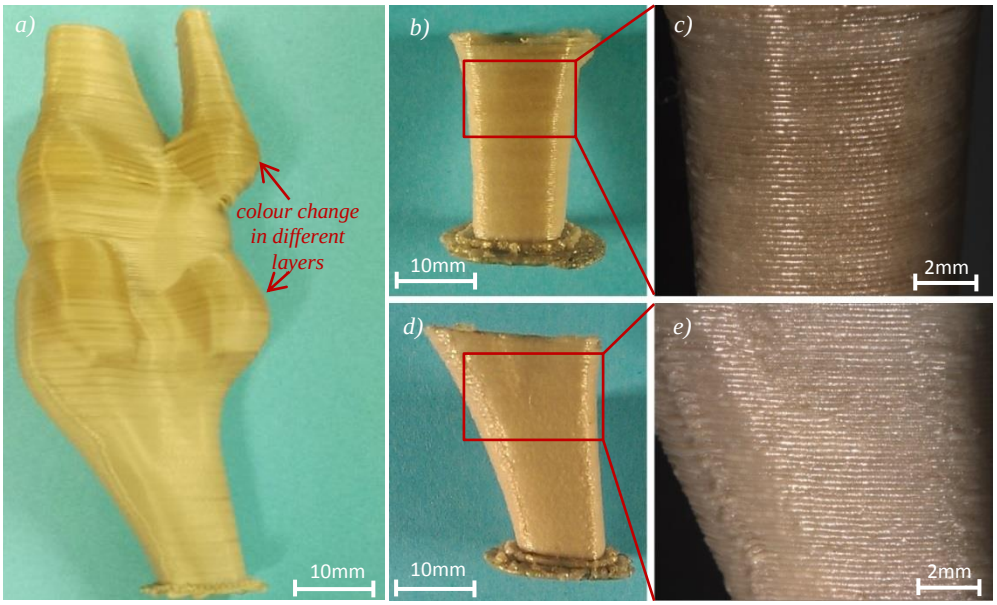

Figure 5.6 (a) A typical 3D printed human bone structure showing surface colour change in different layers due to a different level of crystallinity; **(b)-(e)** a 3D printed sample with colour change in the same layers. **(b)** and **(c)** front view with a high level of amorphous structure in dark brown colour, **(d)** and **(e)** side view with a high level of crystallinity in normal PEEK beige colour.

5.4 Mechanical Properties of the 3D printed PEEK

Fig. 5.7a shows microstructure of a typical 3D printed Victrex PEEK 450G compression test specimen with a strut width of 600 μm, a strut height of 200 μm, and a pore size of 450

μm. As can be seen, the deposited struts have relatively uniform shape which insures interconnectivity of the pores suitable for cell attachment and in-growth. **Fig. 5.7b** depicts compressive response of the 3D printed closed-cell porous Victrex PEEK 450G samples with 38% porosity and solid PEEK-OPTIMA LT1 samples (porosity 0%) compressed at a stain rate of 10^{-3} s^{-1}. Yield strength of 102.38 MPa and 29.34 MPa and yield strain of 0.056 and 0.044 were determined through the curves for solid samples and the sample with 38% porosity, respectively. Average compressive modulus was determined as 1.82 GPa for the solid PEEK samples which is very close to the value that has been reported in the literatures for a similar compression condition **(Rae et al., 2007)**. Both curves show work hardening by plastic deformation; after a strain of 0.45 for the solid PEEK and after a strain of 0.10 for the sample with 38% porosity. From the stress–strain plots, by incorporation of 38% porosity into PEEK, the yield strength decreases by approx. 71%. It was not possible to directly compare this value with porous PEEK prepared by other methods; however, it can be concluded from the test results that incorporating a high level of porosity into the PEEK necessary for gaining early bone apposition can yield considerable reduction of mechanical properties.

The 3D printed porous PEEK can be used for either load bearing or non-load bearing applications. Solid PEEK has matching compressive properties with cortical bone which is in the range of 106–215 MPa **(Lawson and Czernuszka, 1998)**, however, incorporation of a high level of porosity using extrusion-based 3D printing needs to be implemented with care. This can limit applications of these porous PEEK structures as load bearing bone implants since materials without sufficient strength are considered risky to use as they increase chance of baleful failure of implants.

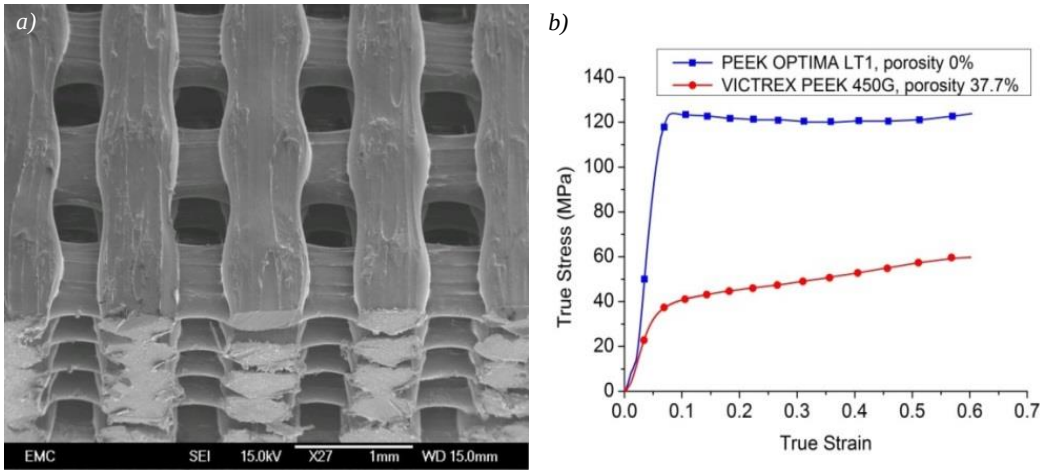

Figure 5.7 (a) SEM image of the compression test specimen with 38% porosity; **(b)** compressive stress–strain plots for PEEK-OPTIMA and Victrex 450G with 0% and 38% porosity, respectively. Strain rate of 10^{-3} s^{-1} at 25 °C

The 3D printed PEEK tensile test specimens were investigated through macro/microscopic observations and porosity measurement. The samples printed with 100% and 80% infill rates had average porosity of 14% and 31%, respectively. The 14% porosity in samples with 100% raster infill rate is mainly due to the formation of air gap between deposited filaments within layers. Different types of air gap are normally produced in extrusion freeformed parts. The air gaps can be formed between layers due to inherent limitation of this process in filament's geometry. Also, the filament's geometry limits materials filling in each layer so that there are undesirable gaps between layer's perimeter and infill filaments. These air gaps tend to be formed more in the first printing layers where the part bonds to the base material. The other types of air gaps are those produced between adjacent infill filaments caused by either variation in feedstock filament diameter or temporary change in proportion between XY table speed and extrusion rate. In addition to air gaps, micro-air bubbles and voids can be entrapped inside extrudate in order to high processing temperature, air bubble inside feedstock filament, and moisture. All these defects induce porosity into the extrusion freeformed PEEK parts and subsequently reduction of mechanical properties.

Fig. 5.8 represents the tensile stress–strain curve of the 3D printed samples using 420 °C nozzle temperature in comparison with injection moulded PEEK and 3D printed polyetherimide (PEI) with the trade name Ultem 9085 which is the highest strength material currently available for use in commercial Stratasys' FDM machines. The 3D printed PEEK samples with 14% and 31% porosity had a smaller strain to failure in comparison with Ultem 9085 and injection moulded PEEK. The printed sample with 14% porosity had UTS at break of 75.06 MPa which is approx. 33% less that injection moulded PEEK that is 113 MPa at the same strain rate **(Rae et al., 2007)**. Conversely, the 3D printed PEEK has remarkably higher UTS than Ultem 9085, although it has less elongation at break. It should be noted that random formation of air gaps and micro-bubbles in the PEEK test specimens and inconsistency in solidification of the material upon deposition had led to relatively inconsistent test results for UTS with a standard deviation of 4.1 MPa.

The UTS determined for the extrusion freeformed PEEK is within the range reported for cortical bone that is 50–150MPa **(Abu Bakar et al., 2003b)**. The printed PEEK with 31% porosity had a UTS of 49.22 MPa and a strain to failure of 0.31. Hence, incorporation of 17% porosity (increasing porosity from 14% to 31%) into 3D printed samples resulted in approx. 35% and 13% reduction in UTS and strain to failure, respectively. It should also be noted that the UTS of the printed porous PEEK samples are comparable to those reported for PEEK/hydroxyapatite (HA) composites with a similar HA content. For instance, the UTS of 78–80 MPa with a strain to failure of 0.15 has been reported for annealed PEEK/HA composites with 15% HA **(Converse et al., 2007, Abu Bakar et al., 2003a)** that is comparable to the 3D printed samples with 14% porosity.

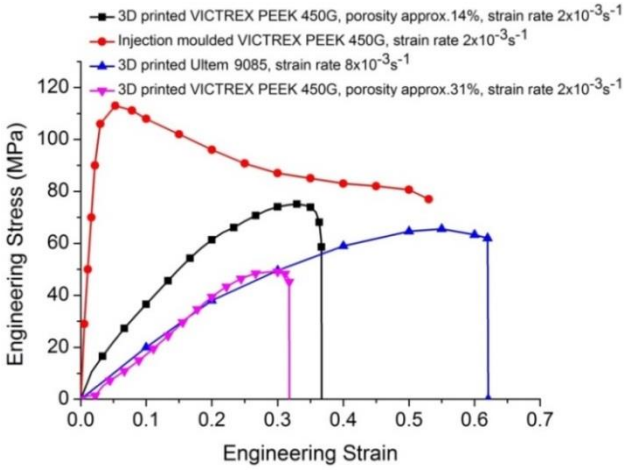

Figure 5.8 Tensile stress–strain curve of different materials including injection moulded PEEK **(Rae et al., 2007)**, 3D printed Ultem 9085 **(Bagsik et al., 2010)**, and 3D printed PEEK with 14% and 31% porosity

The noticeable difference in the stress–strain curve of the 3D printed and injection moulded PEEK parts can be attributed to their different fracture mechanisms. **Fig 5.9** depicts failure mode of a typical specimen with +45º/-45º criss-cross raster orientation with air gaps in the first layer (**Fig. 5.9a**) discussed earlier. The extrusion freeformed parts consist of many individual filaments that each one can be treated as a single component for fracture analysis. Thus, it is important to form and deposit the PEEK filaments with minimum entrapped micro-air bubbles that are considered as the main reason of decrease in filaments' strength. In addition to the strength of individual filaments, a good filament-to-filament bonding is critical in extrusion freeforming to have maximum structural integrity and energy absorption under load. The tensile strength of extrusion freeformed parts is influenced much more by the filament-to-filament bonding rather than the strength of the filaments themselves **(Ziemian et al., 2012, Sung-Hoon et al., 2002)**. Using a high processing temperature is an asset to achieve sufficient filament-to-filament bonding. This can also minimise the formation of air gap between infill filaments since the PEEK extrudate has lower viscosity and thus spread more in the lateral direction upon deposition, although it may affect dimensional accuracy.

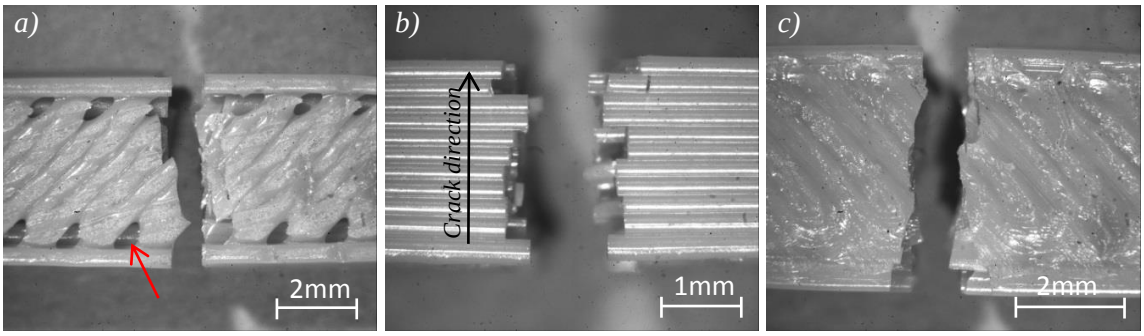

Figure 5.9 Fracture mode of a typical tensile specimen printed with +45º/-45º criss-cross raster orientation; **(a)** bottom view showing air gaps in the first build layer, **(b)** side view with a narrow showing crack propagation direction, and **(c)** top view

Fig. 5.10 depicts fracture surface of a typical extrusion freeformed PEEK sample with +45°/-45° raster orientation printed using a high extrusion temperature of 430 °C. As shown in **Fig. 5.10b**, no welding line between infill and perimeter filaments is evident that proves excellent filament-to-filament bonding in each layer. Welding line between layers (the yellow arrow) could be realized, yet there was sufficient interlayer bonding. This strong filament-to-filament bonding in each layer influences failure behaviour of the extrusion freeformed PEEK. The PEEK specimens printed in low temperature, having evident welding line between infill filaments, exhibit multiple failures of infill filaments in both shear and tension. Failure occurs via pulling and probabilistic fracturing of individual filaments whereby the filaments detached at +45° and -45° angle relative to the tensile load. In contrast, the samples processed in high temperatures, with ideally no clear welding lines, can be analysed as a laminated material. Hence, the materials fracture at 90° angle relative to the tensile load as can be seen in **Fig. 5.10a** since no shear stress on infill filaments is applied.

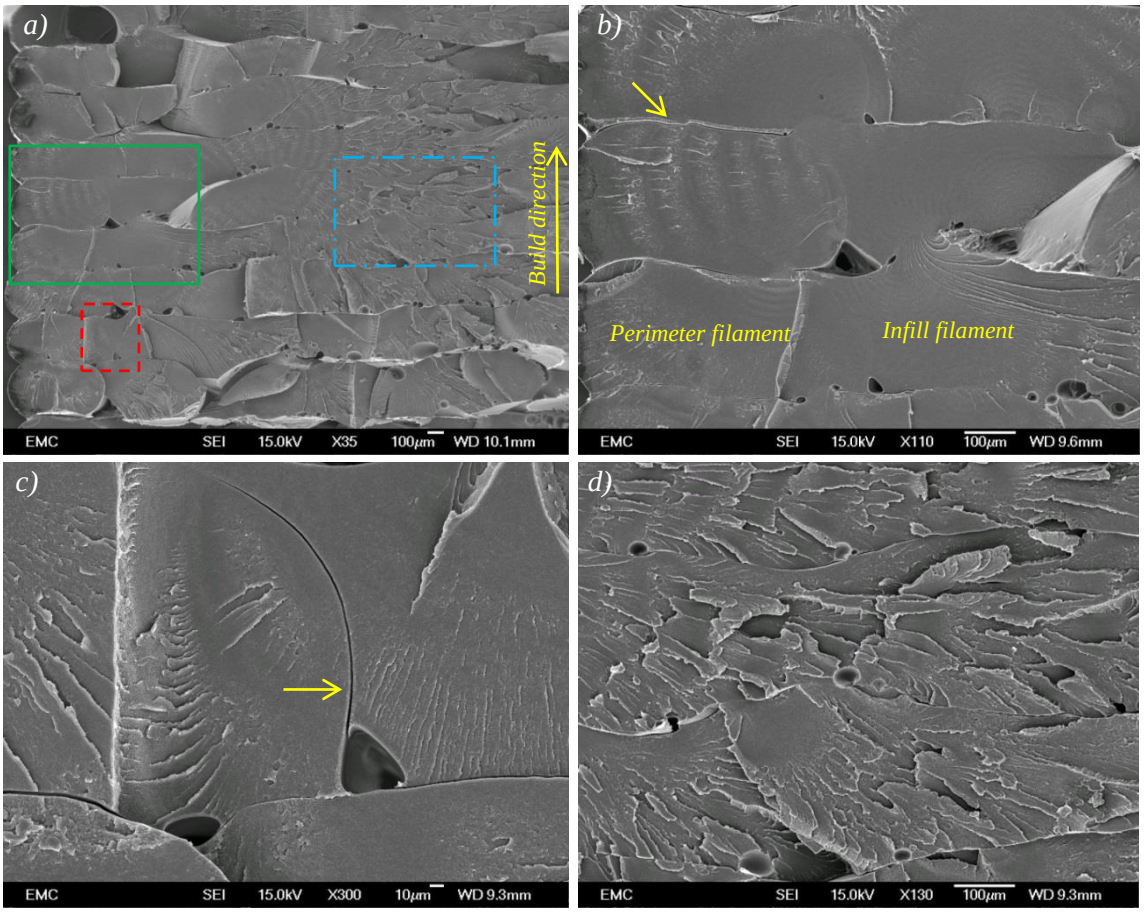

Figure 5.10 (a) Fracture surface of PEEK tensile test sample showing excellent infill filaments bonding in each layer; **(b)** magnified view of the green solid inset box; **(c)** magnified view of the red dash inset box; and **(d)** magnified view of the blue dash dot inset box

The air gaps influence the strength of the extrusion freeformed samples by locally decreasing physical cross-sectional area of material specimens and micro-crack formation under tension **(Ziemian et al., 2012)**. A typical micro-crack initiated from the existing air gap can be seen in **Fig. 5.10c.** The micro-crack was formed and propagated in the direction where two filaments get welded upon deposition. The failure mechanism of the specimen can be explained with eventual rupturing of perimeter filaments (left area in **Fig. 5.10a**) and the weak region in the incipient build layers (down area in **Fig. 5.10a**). The air gaps close to perimeter filaments contributed in initiation of micro-cracks and consequently propagation and rupture of more infill filaments from left to right (i.e. centre of the specimen). Meanwhile, more material has ruptured from down toward the centre of the specimen. The centre of the specimen (the blue box in **Fig. 5.10a**) is the last region has torn due to its strong material bonding and less amount of air gaps. As seen in **Fig. 5.10d**, this region possesses an excellent filament-to-filament and interlayer bonding, although it possess micro-bubbles inside filaments.

Fig. 5.11 represents the results of three point flexural test on the 3D printed PEEK and other AM materials and processes. The 3D printed PEEK had the highest flexural and failure strength of 132.37 MPa and 117.09 MPa, respectively (approx. twice the samples printed from ABS) and flexural modulus of 2.43 GPa. The difference between the failure strength and the maximum strength is how much plastic deformation the specimen can sustain. If there is less difference, that means the specimens snapped cleanly, without any plastic deformation. Similarly, the specimen can withstand more stress before it breaks if the gap between the two values is bigger.

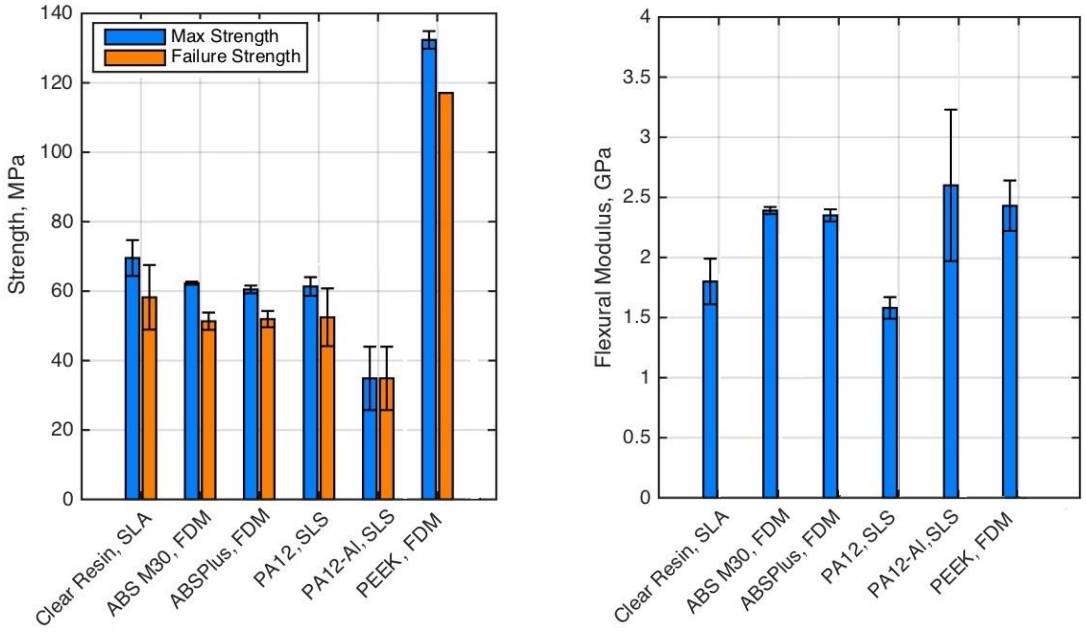

Figure 5.11 Comparison graph of **(a)** the maximum and failure strength, and **(b)** flexural moduli

As can be seen from the error bars (determined from 10 records for each material), there was quite a spread in both modulus and the maximum strength of the samples printed using

SLA and SLS processes than those printed using FDM. The variations in SLA samples might be due to varying degrees of post-curing for the specimens, since inadequate control of the post-curing process can lead to highly varying properties. As for SLS samples, the alumide (PA12-Al) showed a remarkable variation in both strength and modulus than the polyamide samples. This can be explained as a wide range of physical properties of aluminium and polyamide particles (e.g. particle size, shape, and density) negates efficient and consistent mixing, and thus non-uniform distribution of these materials in each layer results in variation in flexural properties of different specimens. The variation in strength and modulus of the 3D printed PEEK samples can also be described by inconsistency in solidification of the material upon deposition. As the ambient temperature was controlled using lamps surrounding printed part there might be less control in the cooling rate as discussed earlier. The random formation of the air gaps and micro-bubbles could be an alternative source for variation. The samples printed from ABS using commercial FDM systems had the least variation as they were printed in a heat-controlled chamber.

5.5 Summary

High-temperature extrusion freeforming of PEEK for biomedical applications is reported for the first time in this chapter. Filament-based extrusion system was identified as more suitable approach than syringe-based method due to its higher control on materials temperature, and thus viscosity. A good PEEK-substrate and PEEK interlayer bonding was achieved through control of ambient temperature and nozzle temperature with regard to flow rate. According to the test results for extrusion rate of 2.2 mg/s, an ambient temperature of 80°C and a nozzle temperature of 400–430°C should be used for 3D printing of defect-free PEEK parts. A well-designed heated build plate (up to 130°C) with many fine holes (each with negative angel) is also necessary to avoid part-substrate detachment. In addition, heat distribution in the environment surrounding the part could affect the level of crystallinity in the 3D printed PEEK structure. Compressive yield strength of 102.38 MPa and 29.34MPa and yield strain of 0.056 and 0.044 were determined for the solid samples with 0% and 38% porosity, respectively. According to the test results, the 3D printed solid samples had UTS of 75.06 MPa that is 33% reduction in injection moulded PEEK due to incorporation of 14% porosity. The printed PEEK samples had a flexural modulus of 2.43 GPa and a flexural strength of 132.37 MPa that was significantly higher than flexural strength of the specimens printed from acrylate-based resin, ABS, polyamide, and alumide using other AM techniques.

Chapter 6

Conclusions and Future Works

Chapter 6: Conclusions and Future Works

6.1 Conclusion

The current study has investigated both low-temperature extrusion freefroming of ceramic bone TE scaffolds and high-temperature extrusion freeforming of PEEK. In addition, novel techniques were proposed for production of PEEK-based biocomposites and porous PEEK structures. Initially, a literature review was undertaken to establish the state–of–the–art of the technology and background knowledge of the extrusion-based AM and bioactive PEEK-based composites, thereby providing insights for the project objectives, experimental design, and interpretation of the results. Herein the principal conclusions and major findings for this research work are presented:

- This project has successfully helped to bring a greater understanding of the factors involved in the design and production of highly accurate 3D printed HA scaffolds for use in tissue engineering applications. Low-temperature extrusion freeforming provides the possibility to print ceramic structures with sufficient control on microstructure and composition. The printed scaffolds were highly uniform, and the production process was consistent and repeatable. It was identified that a sintered scaffold experience shrinkage in the X, Y and Z directions, but also in the filament and pore size. This understanding allows for more accurate shrinkage tolerances to be incorporated into the initial scaffold design. CT analysis of the printed HA scaffolds showed there are air bubbles entrapped inside filaments in addition to the sintering-induced pores. The Archimedes' principle was successfully used to facilitate the calculation of both marcoporosity and mircoporosity in the printed scaffolds. A consistent microporosity of between 7 and 10% (average 8.2%) was found through all samples measured. This indicated fairly consistent levels of air remaining within the filament post sintering, and that microporosity within this range could be accepted as normal
- The key feature of the used SEF method is its nozzle design and paste formulation. Using Benbow's model the HA paste could be characterized, although assumptions incorporated to this model could affect its prediction accuracy. The experiments and ANOVA results proved that extrudate velocity, paste solvent content, and L/D have significant effect on extrusion pressure. HA scaffolds with filaments as fine as 30 μm could be printed for the first time using a conical nozzle design and a paste with sufficiently high solvent content and carefully tuning ram velocity. Agglomerates and LPM phenomena were found as the main source of dimensional inaccuracy in printing of fine HA filaments
- The use of HA in tissue engineering scaffold construction is limited due to its brittle nature, however this can be overcome by forming a composite with more

elastic compounds. In this study, low-temperature extrusion freeforming of high resolution PLA/HA scaffolds was reported with a high level of microstructural uniformity. The elastic behaviour of the biocomposite could be tailored by PLA loading. Porous PLA/HA tubes could be formed by rolling the printed flexible PLA/HA scaffold.

- A good blood vessel formation, call adhesion and proliferation were observed through CAM model and in vitro analysis in the printed HA scaffolds. It can be implied from the results that spacing of 200-250 μm would be suitable range for cell adhesion and proliferation and larger spacing of 350-400 μm is recommended for vascularization. With good biocompatibility, bioactivity and osteoconduction, HA is currently used as common filler material to prepare PEEK composite. In this study, a new technique based on extrusion freeforming and compression moulding was introduced for preparation of bioactive PEEK/HA composite. The technique provides a high level of control on the distribution of the bioactive phase. A static pressure of 0.39 MPa, dwelling time of 20 min and temperature of 400 ºC were identified to be optimal for compression moulding of HA scaffolds of size 10×10×3mm with filament size of above 250 μm and pore size of above 200μm. The technique is also an efficient method for production of porous PEEK with controlled porosity and 100% interconnected channels with an average surface roughness of 0.4μm. The produced PEEK/HA biocomposites exhibited a good biocompatibility and cell attachment, while incorporation of HA into PEEK could result in degradation of mechanical properties. The biocomposites exhibited an excellent sustainability under compression-compression cyclic loading which is quite promising for load bearing applications.

- Successful extrusion-based AM of PEEK parts with high level of control on macro/microstructure was reported in this research project. The method used in this study has potential for further development due to its design freedom to make porous PEEK parts with perceptibly reduction in time and production cost. Proper adjustment of extrusion temperature and ambient temperature was necessary for achieving a good PEEK-substrate and PEEK interlayer bonding, and to avoid warpage and delamination. Nozzle temperature within the range of 400 °C to 430 °C, ambient temperature of 80 °C, and heated custom-designed build plate up to 130 °C were realized as applicable conditions for extrusion rate of 2.2 mg/s. The 3D printed PEEK with 38% porosity had compressive strength of 29.34MPa and yield strain of 0.044 with potential for both load bearing and non-load bearing application. The 3D printed PEEK samples had micro-porosity of about 14% that that could reduce the

UTS of the printed parts to 75.06MPa, that is still comparable with injection moulded PEEK. The 3D printed PEEK samples had flexural strength and modulus perceptibly higher than the samples printed using other AM techniques.

6.2 Future works

Although using a hairdryer was cheap and sufficient for the purpose of preparing HA paste (to evaporate solvent), it allowed little control over the solvent evaporation rate. In addition, heat distribution and paste consistency could be very uniform if constant mechanical stirring could be applied to the ceramic/polymer mixture. With the use of constant and controllable heating rate, a mechanical stirring and known volume of solvent in the ceramic/polymer solution, variations in the paste viscosity would become negligible. The printer calibration process would also become much easier, as extrusion and nozzle speed settings could be standardised for specific materials. This would make the process more quantifiable and the characterization of any ceramic paste using the Benbow's model would be more accurate.

As mentioned earlier, presence of micro-air bubbles was discovered in the prepared pastes that has an adverse effect on the structural integrity of filaments and the bonding between layers, so reducing these bubbles is desirable. One way to do this would be to use a vacuum chamber during paste preparation, rather than stirring it by hand in open air. This would not only remove air from the paste, but would also improve its purity by significantly reducing its contact with dust and other particles in the surrounding environment. Therefore, an automatic paste preparation device should be developed which includes a vacuum chamber with a mechanical stirring system incorporated with heated air blowing system. After evaporation of solvent for a known time (determined through experiments) and achieving proper viscosity, the stirring and vacuum system is stopped and the paste can be loaded into extrusion syringe inside the chamber. A solvent blowing system can also be incorporated to avoid solvent evaporation during paste loading into syringe.

The results from mechanical tests in this study on the PEEK/HA composites proved that the addition of extrusion freeformed HA into PEEK degrades the compressive property of pure PEEK. The effect of HA filament orientation on the mechanical properties was investigated, however, the correlation between microstructural design (i.e. HA loading and distribution, filament size, etc.) and mechanical properties remains unknown. More PEEK/HA test samples with different HA network design, HA percentage, and filament/pore size need to be subjected to compression test to increase the amount of available data. As the proposed technique is a multi-step process there are several noise factors affecting reproducibility, and thus variation in results for samples with similar HA content. In

particular, the small size of the specimens used in this study (6×6×6mm) made it very difficult to cut them precisely into the designed mechanical test sample size. In addition to machining error, existence of air bubbles in the composites was another source of inconsistency in the PEEK/HA samples. All the produced samples were subjected to CT analysis before compression test to make sure they have similar air bubble percentage. However, the location, size and shape of the air bubbles inside the PEEK matrix are varying in different samples. All these noise factors could affect the results of the compression test on the PEEK/HA specimens. Therefore, study of the effect of HA content or filament size on compressive response of these biocomposite is not a matter to be taken lightly. Using PEEK/HA samples at noticeably larger size is considered as a good measure to reduce the effect of these noise factors on the response. Unfortunately, it was not possible to produce larger PEEK/HA samples in this study due to the limitation in size of the HA samples using the developed technique. Currently HA scaffolds with high level of uniformity can be printed in open air environment at maximum height of 6-7 mm due to drying-induced shrinkage. Thus, for printing larger HA scaffolds there is demand for development of a build chamber to control solvent evaporation in printing environment and minimize the shrinkage/deformation during print.

In addition, it is worth to explore the application of plastic molding simulation software (e.g. Autodesk Simulation Moldflow) to study PEEK's melt flow through HA pores, although the current simulation software allow analysis of very basic compression moulding cases. In particular, the use of simulation can be useful for studying size and location of air bubble trapped in PEEK using different ventilation design, moulding temperature and pressure, and location of HA scaffold in the mould. The use of an advanced computer simulation method from one side and application of optimization algorithms (e.g. genetic algorithm) from other side are suggested as future works to be conducted in order to optimize PEEK/HA compression molding process.

The medical sector is currently taking the advantage of PEEK's excellent biocompatibility and mechanical strength, and this trend would be increased by emerging novel bioactive PEEK compounds. Consequently, there will be a huge market, not only medical sector, for AM of complex PEEK parts with a significant reduction in production time and cost. There is currently no commercial AM system in the market with the ability to print high quality PEEK parts economically. Therefore, development of a robust, viable and low-cost PEEK extrusion AM system with the ability to fulfil the key end-user requirements needed for the high-tech industries is expected to be an exciting research topic. The results of this PhD project on AM of PEEK are quite promising. However, there are still some limitations such as insufficient control on process parameters that need to be addressed to be able to serve this 3D printing

technology for industries. Improving the current developed PEEK 3D printing technology in terms of part size, dimensional accuracy, and mechanical properties would be further expansion to the current research work. More experimental works need to be performed to optimize extrusion process to achieve optimum mechanical and biological performance. The correlation between diameter of PEEK feedstock filament and nozzle temperature, and the applicable extrusion temperature with regard to different extrusion rates can be explored with the aim of optimization of dimensional accuracy, mechanical properties with no adverse effect on biocompatibility. This work can be further improved by incorporation of reinforcement or bioactive particles/fibre to fabricate porous PEEK compounds with unique features and mechanical/biological functionality.

Appendix 1

Weibull distribution:

The standard three-parameter cumulative Weibull distribution is given as **(Dirkolu et al., 2002)**:

$$F(x;\ a, b, c) = 1 - e^{\left[-\left(\frac{x-a}{b}\right)^c\right]} \quad a, b, c \geq 0 \tag{1}$$

where a is location parameter; b is scale parameter; and c is shape parameter. Frequently, the location parameter is not used, and the value for this parameter can be set to zero. When this is the case, a=0 in Equation (1), the equation of two-parameter Weibull distribution is obtained:

$$F(x;\ b, c) = 1 - e^{\left[-\left(\frac{x}{b}\right)^c\right]} \quad b, c \geq 0 \tag{2}$$

Normally, three-parameter Weibull distribution is used in conditions where the determined extreme value is not less than "a". Therefore two-parameter Weibull distribution is used to determine ultimate stress, yield stress and elastic modulus in this study. The function of F(x;b,c) represents the probability that the desired mechanical property (ultimate stress, yield stress or elastic modulus) is equal or less than collected data value of x. Assume a reliability function R(x;b,c), and let F(x;b,c) + R(x;b,c) =1, the reliability R(x;b,c) therefore represents the probability of this desired mechanical property is at least x. The equation can be written as:

$$R(x;\ b, c) = 1 - e^{\left[-\left(\frac{x}{b}\right)^c\right]} \quad b, c \geq 0 \tag{3}$$

To determine parameters b and c, a linear regression method is applied. The method involves transforming Equation (2) in to the form of $e^{\left[-\left(\frac{x}{b}\right)^c\right]} = 1 - F(x; b, c)$. Note left hand side of the equation is the reliability function R(x;b,c). Then to take the double logarithms of both sides of the equation, the linear regression model of Y=pX+q is obtained.

$$\ln\left[\ln\left(\frac{1}{1-F(x;b,c)}\right)\right] = c\ \ln(x) - c \ln b \tag{4}$$

The only unknown term in the equation is F(x;b,c), will be obtained by estimation from a median rank, which has the formula:

$$\text{Median Rank} = F(x_i; b, c) = \frac{i-0.3}{(n+0.4)} \tag{5}$$

This equation is also known as Benard's approximation. To calculate median rank value, the total number of data n is needed. These values are sorted from the smallest to the largest, denoting the i_{th} smallest value as x_i. For example, i=1 for the first smallest value which corresponds to x_1, i=2 for the second smallest value which corresponds to x_2, until the n_{th} data where i=n corresponds to x_n. Then linear regression can be plotted in x-y coordinates by point (Xi) where X=ln(x), Y=ln[ln(1/F(x;b,c))] base on Equation (4). The results are shown for plotting the regression line for ultimate stress, yield stress and elastic modulus. In order to compute b and c, a trend line is created where c is the slope of the trend line and b will be the inverse logarithm of the Y-axis intersection.

References:

DIRKOLU, H., AKTAS, A. & BIRGOREN, B. 2002. Statistical Analysis of Fracture Strength of Composite Materials Using Weibull Distribution. TURKISH JOURNAL OF ENGINEERING AND ENVIRONMENTAL SCIENCES, 26**,** 45-48.

Appendix of Figures

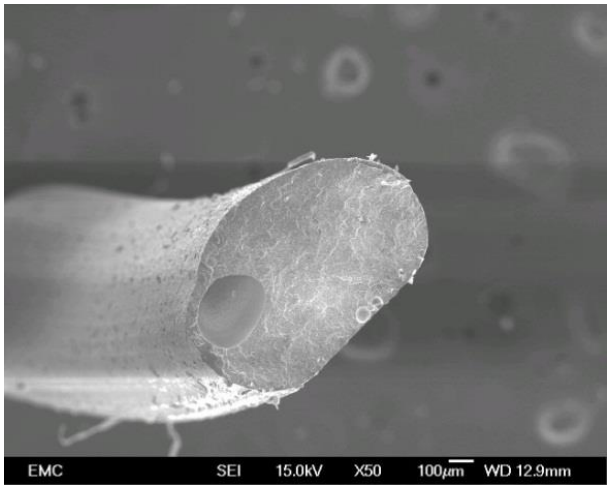

Figure A_1 Air bubble trapped inside extruded HA filament using home-made nozzle

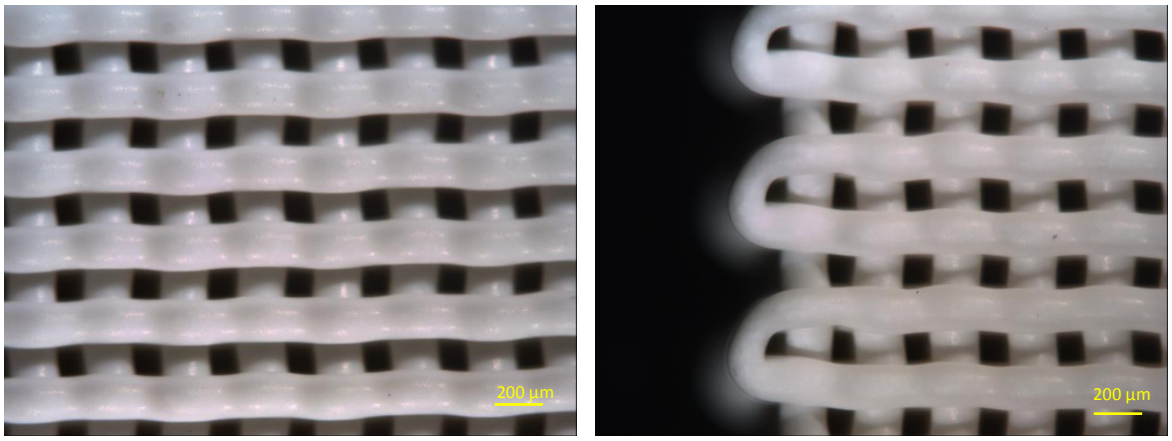

Figure A_2 Zirconia scaffold printed using 200 µm nozzle and nozzle/layer gap of 200 µm

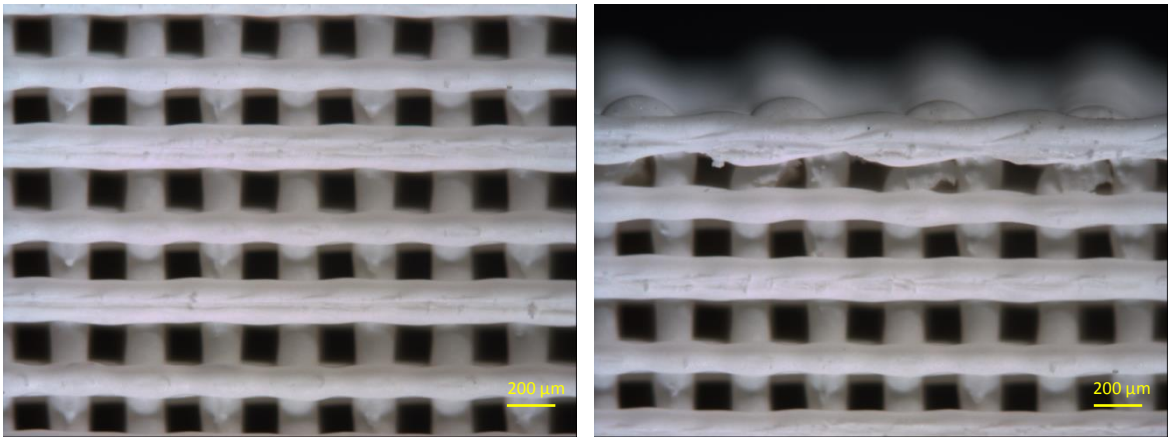

Figure A_3 Zirconia scaffold printed using 200 µm nozzle and nozzle/layer gap of 170 µm

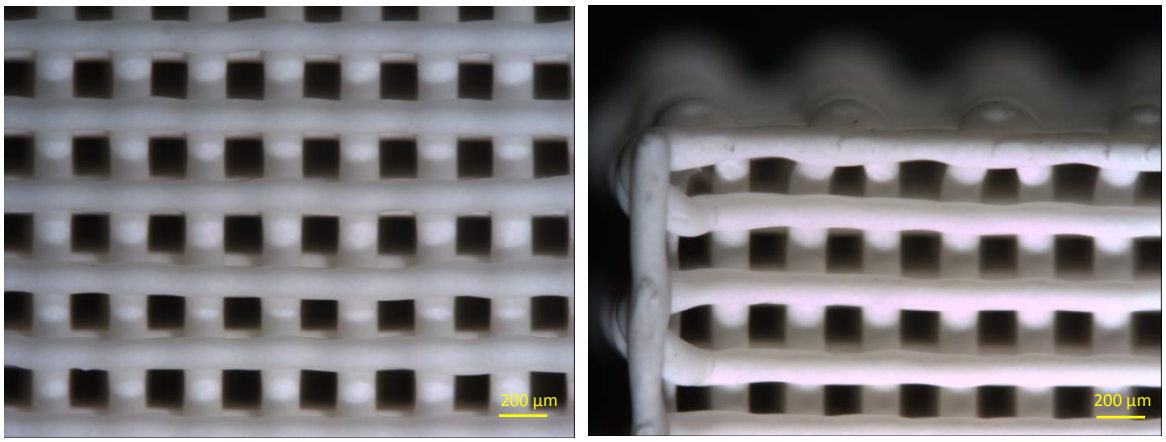

Figure A_4 Zirconia scaffold printed using 200 µm nozzle and nozzle/layer gap of 190 µm

Note: Using nozzle/layer gap of 200 µm (**Fig. A_2**), filaments are not uniform and they have curved shape which indicates the gap between nozzle and built layer is too big and the paste is free to deform before sticking to previous layer. On the other hand, the nozzle/layer gap that is not sufficiently large can result in smash of filaments (**Fig. A_3**). In contrast, filaments are relatively uniform in **Fig. A_4** where the gap is selected properly (190 µm).

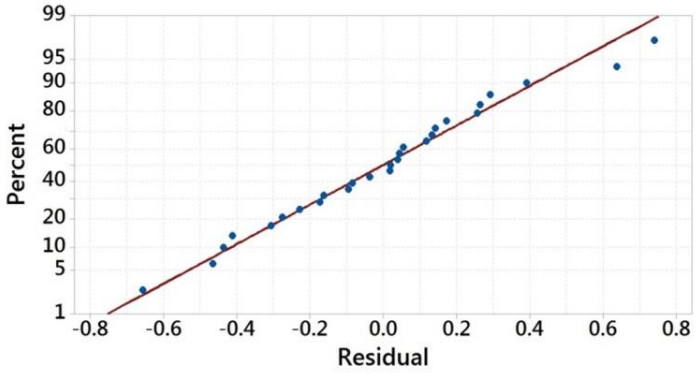

Figure A_5 Normal probability plot of residuals

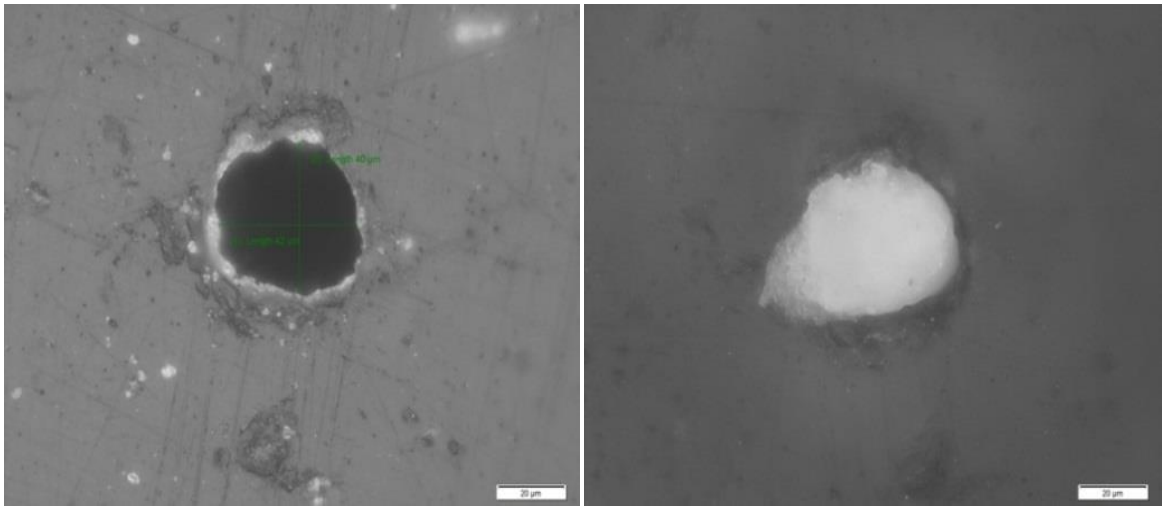

Figure A_6 The 40 µm home-made nozzle used for high resolution printing of HA scaffolds: **(a)** before printing, and **(b)** after nozzle clogging due to quick drying on the nozzle tip (Scale bars 20 µm)

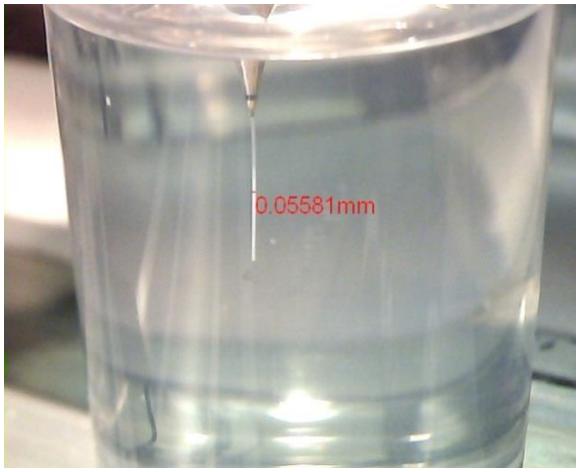

Figure A$_7$ The 50 μm nozzle kept in a bottle containing propan-2-ol solution before printing to avoid drying

Figure A$_8$ Non-uniform extruded PLA/HA filaments (HA 20 vol.%)- dioxin solvent

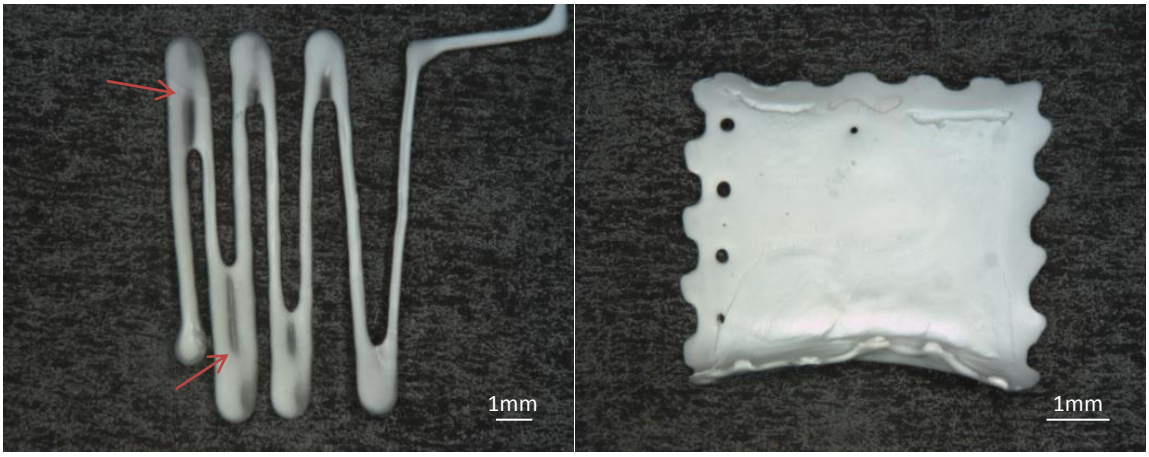

Figure A$_9$ PLA/HA/PEG (20 vol.% HA)- the lines printed using 400 μm nozzle and a paste with solvent (dioxin) content of 23.4 wt.%

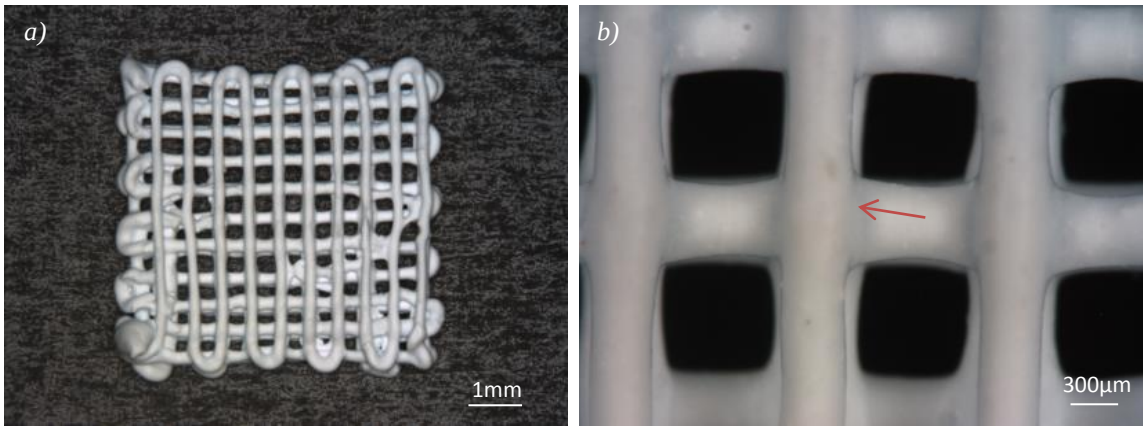

Figure A$_{10}$ PLA/HA/PEG (20 vol.% HA)- scaffold printed using 400 μm nozzle and a paste with 19.7 wt% solvent (dioxin)

Appendix of Tables

Table A_1 Results of filament/pore shrinkage for HA scaffolds with varying filament and pore size

HA scaffold	Before sintering (mean)	After sintering (mean)	Shrinkage (%)
Sample 1 filament size	350 µm	285 µm	18.6
Sample 1 pore size	620 µm	580 µm	6.4
Sample 2 filament size	360 µm	301 µm	16.1
Sample 2 pore size	300 µm	281 µm	6.3

Table A_2 Results of filament/pore shrinkage for zirconia scaffolds with varying filament and pore size

Zirconia scaffold	Before sintering (mean)	After sintering (mean)	Shrinkage (%)
Sample 1 filament size	296 µm	238 µm	19.6
Sample 1 pore size	244 µm	178 µm	7.0
Sample 2 filament size	370 µm	281 µm	23.1
Sample 2 pore size	300 µm	260 µm	7.2

Table A_3 Results of filament/pore shrinkage for alumina scaffolds with varying filament and pore size

Alumina scaffold	Before sintering (mean)	After sintering (mean)	Shrinkage (%)
Sample 1 filament size	243 µm	203 µm	16.5
Sample 1 pore size	258 µm	243 µm	5.8
Sample 2 filament size	373 µm	320 µm	14.2
Sample 2 pore size	307 µm	290 µm	5.4

References

ABU BAKAR, M. S., CHEANG, P. & KHOR, K. A. 1999. Thermal processing of hydroxyapatite reinforced polyetheretherketone composites. Journal of Materials Processing Technology, 89–90**,** 462-466.

ABU BAKAR, M. S., CHEANG, P. & KHOR, K. A. 2003a. Mechanical properties of injection molded hydroxyapatite-polyetheretherketone biocomposites. Composites Science and Technology, 63**,** 421-425.

ABU BAKAR, M. S., CHEANG, P. & KHOR, K. A. 2003b. Tensile properties and microstructural analysis of spheroidized hydroxyapatite–poly (etheretherketone) biocomposites. Materials Science and Engineering: A, 345**,** 55-63.

ABU BAKAR, M. S., CHENG, M. H. W., TANG, S. M., YU, S. C., LIAO, K., TAN, C. T., KHOR, K. A. & CHEANG, P. 2003c. Tensile properties, tension–tension fatigue and biological response of polyetheretherketone–hydroxyapatite composites for load-bearing orthopedic implants. Biomaterials, 24**,** 2245-2250.

AKIMA, H. 1970. A New Method of Interpolation and Smooth Curve Fitting Based on Local Procedures. J. ACM, 17**,** 589-602.

ALGE, D. L. & CHU, T.-M. G. 2010. Calcium phosphate cement reinforcement by polymer infiltration and in situ curing: A method for 3D scaffold reinforcement. Journal of Biomedical Materials Research Part A, 94A**,** 547-555.

ALLAHVERDI, M., DANFORTH, S. C., JAFARI, M. & SAFARI, A. 2001. Processing of advanced electroceramic components by fused deposition technique. Journal of the European Ceramic Society, 21**,** 1485-1490.

ALMAJID, A., FRIEDRICH, K., FLOECK, J. & BURKHART, T. 2011. Surface Damage Characteristics and Specific Wear Rates of a New Continuous Carbon Fiber (CF) / Polyetheretherketone (PEEK) Composite under Sliding and Rolling Contact Conditions. Applied Composite Materials, 18**,** 211-230.

ANG, T. H., SULTANA, F. S. A., HUTMACHER, D. W., WONG, Y. S., FUH, J. Y. H., MO, X. M., LOH, H. T., BURDET, E. & TEOH, S. H. 2002. Fabrication of 3D chitosan-hydroxyapatite scaffolds using a robotic dispensing system. Materials Science & Engineering C-Biomimetic and Supramolecular Systems, 20**,** 35-42.

BAGSIK, A., SCHÖPPNER, V. & KLEMP, E. 2010. FDM Part Quality Manufactured with Ultem*9085. 14th International Scientific Conference. Halle, Germany.

BANG, L. T., KAWACHI, G., NAKAGAWA, M., MUNAR, M., ISHIKAWA, K. & OTHMAN, R. 2013. The use of poly (ε-caprolactone) to enhance the mechanical strength of porous Si-substituted carbonate apatite. Journal of Applied Polymer Science, 130**,** 426-433.

BARRON, J. A., WU, P., LADOUCEUR, H. D. & RINGEISEN, B. R. 2004. Biological laser printing: A novel technique for creating heterogeneous 3-dimensional cell patterns. Biomedical Microdevices, 6**,** 139-147.

BARRY, R. A., SHEPHERD, R. F., HANSON, J. N., NUZZO, R. G., WILTZIUS, P. & LEWIS, J. A. 2009a. Direct-Write Assembly of 3D Hydrogel Scaffolds for Guided Cell Growth. Advanced Materials, 21**,** 2407-+.

BARRY, R. A., SHEPHERD, R. F., HANSON, J. N., NUZZO, R. G., WILTZIUS, P. & LEWIS, J. A. 2009b. Direct-Write Assembly of 3D Hydrogel Scaffolds for Guided Cell Growth. Advanced Materials, 21**,** 2407-2410.

BARTOLO, P. J. & BIDANDA, B. 2008. Bio-Materials and Prototyping Applications in Medicine, New York, USA, Springer.

BARTOLO, P., KRUTH, J.P., SILVA, J., LEVY, G., MALSHE, A., RAJURKAR, K., MITSUISHI, M., CIURANA, J., LEU, M., 2012. Biomedical production of implants by additive electro-chemical and physical processes. CIRP Annals - Manufacturing Technology, 61, 635-655.

BENBOW, J. J. & BRIDGWATER, J. 1993. Paste Flow and Extrusion, Oxford University Press.
BILLIET, T., VANDENHAUTE, M., SCHELFHOUT, J., VAN VLIERBERGHE, S. & DUBRUEL, P. 2012. A review of trends and limitations in hydrogel-rapid prototyping for tissue engineering. Biomaterials, 33**,** 6020-6041.
BHUTHALINGAM, R., LIM, P.Q., IRVINE, S.A., AGRAWAL, A., MHAISALKAR, P.S., AN, J., ET, A.L. 2015. A novel 3D printing method for cell alignment and differentiation. International Journal of Bioprinting,1:57-65
BOCCACCINI, A. R. & BLAKER, J. J. 2005. Bioactive composite materials for tissue engineering scaffolds. Expert Review of Medical Devices, 2**,** 303-317.
BOINARD, E., PETHRICK, R. A. & MACFARLANE, C. J. 2000. The influence of thermal history on the dynamic mechanical and dielectric studies of polyetheretherketone exposed to water and brine. Polymer, 41**,** 1063-1076.
BOSE, S., DARSELL, J., KINTNER, M., HOSICK, H. & BANDYOPADHYAY, A. 2003. Pore size and pore volume effects on alumina and TCP ceramic scaffolds. Materials Science & Engineering C-Biomimetic and Supramolecular Systems, 23**,** 479-486.
BRIEM, D., STRAMETZ, S., SCHRÖODER, K., MEENEN, N. M., LEHMANN, W., LINHART, W., OHL, A. & RUEGER, J. M. 2005. Response of primary fibroblasts and osteoblasts to plasma treated polyetheretherketone (PEEK) surfaces. Journal of Materials Science: Materials in Medicine, 16**,** 671-677.
CEBE, P., CHUNG, S. Y. & HONG, S.-D. 1987. Effect of thermal history on mechanical properties of polyetheretherketone below the glass transition temperature. Journal of Applied Polymer Science, 33**,** 487-503.
CESARANO, J. 1999. A review of robocasting technology. In: DIMOS, D., DANFORTH, S. C. & CIMA, M. J. (eds.) Solid Freeform and Additive Fabrication. Warrendale: Materials Research Society.
CHEAH, C. M., CHUA, C. K., LEONG, K. F., CHEONG, C. H. & NAING, M. W. 2004. Automatic algorithm for generating complex polyhedral scaffold structures for tissue engineering. Tissue Engineering, 10**,** 595-610.
CHEN, S. H., WANG, X. L., XIE, X. H., ZHENG, L. Z., YAO, D., WANG, D. P., LENG, Y., ZHANG, G. & QIN, L. 2012. Comparative study of osteogenic potential of a composite scaffold incorporating either endogenous bone morphogenetic protein-2 or exogenous phytomolecule icaritin: An in vitro efficacy study. Acta Biomaterialia, 8**,** 3128-3137.
CHIVERS, R. A. & MOORE, D. R. 1994. The effect of molecular weight and crystallinity on the mechanical properties of injection moulded poly(aryl-ether-ether-ketone) resin. Polymer, 35**,** 110-116.
CHUA, C.K., LEONG, K.F., AND LIM, C.S., 2010. Rapid prototyping: principles and applications. Singapore: World Scientific.
CHUA, C. K., LEONG, K. F. & AN, J. 2014. 1 - Introduction to rapid prototyping of biomaterials. In: NARAYAN, R. (ed.) Rapid Prototyping of Biomaterials. Woodhead Publishing.
CHUANG, W. & JINGYAN, D. 2013. Direct fabrication of high-resolution three-dimensional polymeric scaffolds using electrohydrodynamic hot jet plotting. Journal of Micromechanics and Microengineering, 23**,** 025017.
CONG BANG, P., KAH FAI, L., TZE CHIUN, L. & KERM SIN, C. 2008. Rapid freeze prototyping technique in bio-plotters for tissue scaffold fabrication. Rapid Prototyping Journal, 14**,** 246-253253.
CONRAD, T. L., JAEKEL, D. J., KURTZ, S. M. & ROEDER, R. K. 2013. Effects of the mold temperature on the mechanical properties and crystallinity of hydroxyapatite whisker-reinforced polyetheretherketone scaffolds. Journal of Biomedical Materials Research Part B: Applied Biomaterials, 101B**,** 576-583.
CONVERSE, G. L., CONRAD, T. L., MERRILL, C. H. & ROEDER, R. K. 2010. Hydroxyapatite whisker-reinforced polyetherketoneketone bone ingrowth scaffolds. Acta Biomaterialia, 6**,** 856-863.

CONVERSE, G. L., CONRAD, T. L. & ROEDER, R. K. 2009. Mechanical properties of hydroxyapatite whisker reinforced polyetherketoneketone composite scaffolds. Journal of the Mechanical Behavior of Biomedical Materials, 2**,** 627-635.

CONVERSE, G. L., YUE, W. & ROEDER, R. K. 2007. Processing and tensile properties of hydroxyapatite-whisker-reinforced polyetheretherketone. Biomaterials, 28**,** 927-935.

DENG, Y., LIU, X., XU, A., WANG, L., LUO, Z., ZHENG, Y., ET, AL. 2015. Effect of surface roughness on osteogenesis in vitro and osseointegration in vivo of carbon fiber-reinforced polyetheretherketone–nanohydroxyapatite composite. International Journal of Nanomedicine, 10:1425—47.

DOMINGOS, M., CHIELLINI, F., GLORIA, A., AMBROSIO, L., BARTOLO, P. & CHIELLINI, E. 2012. Effect of process parameters on the morphological and mechanical properties of 3D Bioextruded poly(epsilon-caprolactone) scaffolds. Rapid Prototyping Journal, 18**,** 56-67.

DOMINGOS, M., DINUCCI, D., COMETA, S., ALDERIGHI, M., BARTOLO, P. J. & CHIELLINI, F. 2009. Polycaprolactone Scaffolds Fabricated via Bioextrusion for Tissue Engineering Applications. International journal of biomaterials, 2009**,** 239643.

DUOSS, E. B., TWARDOWSKI, M. & LEWIS, J. A. 2007. Sol-Gel Inks for Direct-Write Assembly of Functional Oxides. Advanced Materials, 19**,** 3485-3489.

EDWARDS, S., WERKMEISTER, J. A., RAMSHAW, J. A. M., MCLEAN, K. & JARMAN-SMITH, M. 2010. Polyetheretherketone multifilament and monofilament woven tissue engineering scaffolds. Transactions Society for Biomaterials. Seattle, Washington: Society for Biomaterials.

ESPALIN, D., ARCAUTE, K., RODRIGUEZ, D., MEDINA, F., POSNER, M. & WICKER, R. 2010. Fused deposition modeling of patient‐specific polymethylmethacrylate implants. Rapid Prototyping Journal, 16**,** 164-173.

EVANS, N.T., TORSTRICK, F.B., LEE, C.S.D., DUPONT. K.M., SAFRANSKI, D.L., CHANG, W.A., ET AL. 2015. High-strength, surface-porous polyether-ether-ketone for load-bearing orthopedic implants. Acta Biomaterialia, 13:159-67.

FAN, J. P., TSUI, C. P., TANG, C. Y. & CHOW, C. L. 2004. Influence of interphase layer on the overall elasto-plastic behaviors of HA/PEEK biocomposite. Biomaterials, 25**,** 5363-5373.

FANG, Z., STARLY, B. & SUN, W. 2005. Computer-aided characterization for effective mechanical properties of porous tissue scaffolds. Computer-Aided Design, 37**,** 65-72.

FEDOTOV, A. Y., BAKUNOVA, N. V., KOMLEV, V. S. & BARINOV, S. M. 2013. Increase in mechanical properties of porous materials by polymer impregnation. Inorganic Materials: Applied Research, 4**,** 7-11.

GEBHARDT, A., 2003. Rapid prototyping. Munich, Germany: Hanser Gardner.

GEUN HYUNG, K. & JOON GON, S. 2009. 3D polycarprolactone (PCL) scaffold with hierarchical structure fabricated by a piezoelectric transducer (PZT)-assisted bioplotter. Applied Physics A: Materials Science & Processing, 94**,** 781-785785.

GHOSH, S., PARKER, S. T., WANG, X. Y., KAPLAN, D. L. & LEWIS, J. A. 2008. Direct-write assembly of microperiodic silk fibroin scaffolds for tissue engineering applications. Advanced Functional Materials, 18**,** 1883-1889.

GIBBS, D., VAEZI, M., YANG, S., OREFFO, R.O.C. 2014. Hope versus hype: what can additive manufacturing realistically offer trauma and orthopedic surgery. Regenerative Medicine, 9,(4), 535-549.

GIBSON, I., 2006. Advanced manufacturing technology for medical applications: Reverse engineering, software conversion and rapid prototyping. West Sussex, England: Wiley.

GIBSON, I., ROSEN, D.W., AND STUCKER, B., 2010. Additive manufacturing technologies. New York, NY, USA: Springer.

GRATSON, G. M. & LEWIS, J. A. 2004. Phase Behavior and Rheological Properties of Polyelectrolyte Inks for Direct-Write Assembly. Langmuir, 21**,** 457-464.

GRATSON, G. M., XU, M. & LEWIS, J. A. 2004. Microperiodic structures: Direct writing of three-dimensional webs. Nature, 428**,** 386-386.

GREENWALD A.S., BODEN S.D., GOLDBERG V.M., KHAN Y., LAURENCIN C.T. & R.N.;, R. 2003. Bone Graft Substitutes: Facts, Fictions & Applications. American Academy of Orthopaedic Surgeons, 70th annual meeting. Louisiana.

GREULICH, M., GREUL, M. & PINTAT, T. 1995. Fast, functional prototypes via multiphase jet solidification. Rapid Prototyping Journal, 1**,** 20-25.

GRIDA, I. & EVANS, J. R. G. 2003. Extrusion freeforming of ceramics through fine nozzles. Journal of the European Ceramic Society, 23**,** 629-635.

GRIFFITHS V. 2013. 3D printing of bioceramic tissue engineering scaffolds for bone regeneration. University of Southampton.

HA, S. W., GISEP, A., MAYER, J., WINTERMANTEL, E., GRUNER, H. & WIELAND, M. 1997. Topographical characterization and microstructural interface analysis of vacuum-plasma-sprayed titanium and hydroxyapatite coatings on carbon fibre-reinforced poly(etheretherketone). Journal of Materials Science: Materials in Medicine, 8**,** 891-896.

HA, S. W., MAYER, J., KOCH, B. & WINTERMANTEL, E. 1994. Plasma-sprayed hydroxylapatite coating on carbon fibre reinforced thermoplastic composite materials. Journal of Materials Science: Materials in Medicine, 5**,** 481-484.

HAMDAN, S. & SWALLOWE, G. M. 1996. The strain-rate and temperature dependence of the mechanical properties of polyetherketone and polyetheretherketone. Journal of Materials Science, 31**,** 1415-1423.

HAN, C.M., LEE, E.J., KIM, H.E., KOH, Y.H., KIM, K.N., HA, Y., et al. 2010. The electron beam deposition of titanium on polyetheretherketone (PEEK) and the resulting enhanced biological properties. Biomaterials, 31:3465-70.

HOPKINSON, N., HAGUE, R., AND DICKENS, P., 2006. Rapid manufacturing: An industrial revolution for the digital age. West Sussex, England: John Wiley & Sons.

HENGKY, C., KELSEN, B., SARASWATI & CHEANG, P. 2009. Mechanical and Biological Characterization of Pressureless Sintered Hydroxapatite-Polyetheretherketone Biocomposite. In: LIM, C. & GOH, J. H. (eds.) 13th International Conference on Biomedical Engineering. Springer Berlin Heidelberg.

HOLLISTER, S. J. 2006. Porous scaffold design for tissue engineering (vol 4, pg 518, 2005). Nature Materials, 5**,** 590-590.

HOLLISTER, S. J. & KIKUCHI, N. 1994. HOMOGENIZATION THEORY AND DIGITAL IMAGING - A BASIS FOR STUDYING THE MECHANICS AND DESIGN PRINCIPLES OF BONE TISSUE. Biotechnology and Bioengineering, 43**,** 586-596.

HOLLISTER, S. J., LEVY, R. A., CHU, T. M., HALLORAN, J. W. & FEINBERG, S. E. 2000. An image-based approach for designing and manufacturing craniofacial scaffolds. International Journal of Oral and Maxillofacial Surgery, 29**,** 67-71.

HOLLISTER, S. J., MADDOX, R. D. & TABOAS, J. M. 2002. Optimal design and fabrication of scaffolds to mimic tissue properties and satisfy biological constraints. Biomaterials, 23**,** 4095-4103.

HOQUE, M. E., SAN, W. Y., WEI, F., LI, S. M., HUANG, M. H., VERT, M. & HUTMACHER, D. W. 2009. Processing of Polycaprolactone and Polycaprolactone-Based Copolymers into 3D Scaffolds, and Their Cellular Responses. Tissue Engineering Part A, 15**,** 3013-3024.

HUNG-JEN, Y., CHING-SHIOW, T., SHAN-HUI, H. & CHING-LIN, T. 2009. Evaluation of chondrocyte growth in the highly porous scaffolds made by fused deposition manufacturing (FDM) filled with type II collagen. Biomedical Microdevices, 11**,** 615-624624.

HUNTER, A., ARCHER, C. W., WALKER, P. S. & BLUNN, G. W. 1995. Attachment and proliferation of osteoblasts and fibroblasts on biomaterials for orthopaedic use. Biomaterials, 16**,** 287-295.

JAEKEL, D. J., MACDONALD, D. W. & KURTZ, S. M. 2011. Characterization of PEEK biomaterials using the small punch test. Journal of the Mechanical Behavior of Biomedical Materials, 4**,** 1275-1282.

JARMAN-SMITH, M., BRADY, M., KURTZ, S. M., CORDARO, N. M. & WALSH, W. R. 2012. Chapter 12 - Porosity in Polyaryletheretherketone. PEEK Biomaterials Handbook. Oxford: William Andrew Publishing.

JAYASINGHE, S. N. 2007. Bio-electros prays: The development of a promising tool for regenerative and therapeutic medicine. Biotechnology Journal, 2**,** 934-937.

JOYCE, T. J., RIEKER, C. & UNSWORTH, A. 2006. Comparative in vitro wear testing of PEEK and UHMWPE capped metacarpophalangeal prostheses. Bio-Medical Materials and Engineering, 16**,** 1-10.

KALITA, S. J., BOSE, S., HOSICK, H. L. & BANDYOPADHYAY, A. 2003. Development of controlled porosity polymer-ceramic composite scaffolds via fused deposition modeling. Materials Science & Engineering C-Biomimetic and Supramolecular Systems, 23**,** 611-620.

KANCZLER, J. M., SMITH, E. L., ROBERTS, C. A. & OREFFO, R. O. 2012. A novel approach for studying the temporal modulation of embryonic skeletal development using organotypic bone cultures and microcomputed tomography. Tissue Eng Part C Methods, 18**,** 747-60.

KATZER, A., MARQUARDT, H., WESTENDORF, J., WENING, J. V. & VON FOERSTER, G. 2002. Polyetheretherketone—cytotoxicity and mutagenicity in vitro. Biomaterials, 23**,** 1749-1759.

KHALIL, S., NAM, J. & SUN, W. 2005. Multi-nozzle deposition for construction of 3D biopolymer tissue scaffolds. Rapid Prototyping Journal, 11**,** 9-17.

KIM, I. Y., SUGINO, A., KIKUTA, K., OHTSUKI, C. & CHO, S. B. 2009. Bioactive Composites Consisting Of PEEK And Calcium Silicate Powders. Journal of Biomaterials Applications, 24**,** 105-118.

KOCH, K. U., BIESINGER, B., ARNHOLZ, C. & JANSSON, V. 1998. Time- Compression Technologies '98 Conferences. Rapid News Publications.

KUMAR, G., WATERS, M. S., FAROOQUE, T. M., YOUNG, M. F. & SIMON JR, C. G. 2012. Freeform fabricated scaffolds with roughened struts that enhance both stem cell proliferation and differentiation by controlling cell shape. Biomaterials, 33**,** 4022-4030.

KURTZ, S. M. 2012. Chapter 1 - An Overview of PEEK Biomaterials. In: KURTZ, S. M. (ed.) PEEK Biomaterials Handbook. Oxford: William Andrew Publishing.

KURTZ, S. M. & DEVINE, J. N. 2007. PEEK biomaterials in trauma, orthopedic, and spinal implants. Biomaterials, 28**,** 4845-4869.

LANDERS, R., HUBNER, U., SCHMELZEISEN, R. & MULHAUPT, R. 2002. Rapid prototyping of scaffolds derived from thermoreversible hydrogels and tailored for applications in tissue engineering. Biomaterials, 23**,** 4437-4447.

LANDERS, R. & MULHAUPT, R. 2000. Desktop manufacturing of complex objects, prototypes and biomedical scaffolds by means of computer-assisted design combined with computer-guided 3D plotting of polymers and reactive oligomers. Macromolecular Materials and Engineering, 282**,** 17-21.

LANDES, C. A., BALLON, A. & ROTH, C. 2006. In-patient versus in vitro degradation of P(L/DL)LA and PLGA. Journal of Biomedical Materials Research Part B: Applied Biomaterials, 76B**,** 403-411.

LAWSON, A. C. & CZERNUSZKA, J. T. 1998. Collagen-calcium phosphate composites. Proceedings of the Institution of Mechanical Engineers, Part H: Journal of Engineering in Medicine, 212**,** 413-425.

LEE, B.T., QUANG, D., YOUN, M.H. & SONG, H.Y. 2008. Fabrication of biphasic calcium phosphates/polycaprolactone composites by melt infiltration process. Journal of Materials Science: Materials in Medicine, 19**,** 2223-2229.

LEE, J.H., JANG, H.L., LEE, K.M., BAEK, H.R., JIN, K., HONG, K.S., et al. 2013. In vitro and in vivo evaluation of the bioactivity of hydroxyapatite-coated polyetheretherketone biocomposites created by cold spray technology. Acta Biomaterialia, 9:6177-87.

LEE, Y. B., POLIO, S., LEE, W., DAI, G. H., MENON, L., CARROLL, R. S. & YOO, S. S. 2010. Bio-printing of collagen and VEGF-releasing fibrin gel scaffolds for neural stem cell culture. Experimental Neurology, 223**,** 645-652.

LEWIS, J. A. 2008. Novel Inks for Direct-Write Assembly of 3-D Periodic Structures. Material Matters, 3**,** 4-9.

LEWIS, J. A. & GRATSON, G. M. 2004. Direct writing in three dimensions. Materials Today, 7**,** 32-39.

LI, X., HE, J., BIAN, W., LI, Z., ZHANG, W., LI, D., et al. 2014. A novel silk-based artificial ligament and tricalcium phosphate/polyether ether ketone anchor for anterior cruciate ligament reconstruction – Safety and efficacy in a porcine model. Acta Biomaterialia, 10:3696-704.

LI, G., WEI, F., HUTMACHER, D. W., YOKE SAN, W., HAN TONG, L. & FUH, J. Y. H. 2005. Direct writing of chitosan scaffolds using a robotic system. Rapid Prototyping Journal, 11**,** 90-9797.

LI, K., YEUNG, C. Y., YEUNG, K. W. K. & TJONG, S. C. 2012. Sintered Hydroxyapatite/Polyetheretherketone Nanocomposites: Mechanical Behavior and Biocompatibility. Advanced Engineering Materials, 14**,** B155-B165.

LI, L. H., KOMMAREDDY, K. P., PILZ, C., ZHOU, C. R., FRATZL, P. & MANJUBALA, I. 2010. In vitro bioactivity of bioresorbable porous polymeric scaffolds incorporating hydroxyapatite microspheres. Acta Biomaterialia, 6**,** 2525-2531.

LI, S. J., XIONG, Z., WANG, X. H., YAN, Y. N., LIU, H. X. & ZHANG, R. J. 2009a. Direct Fabrication of a Hybrid Cell/Hydrogel Construct by a Double-nozzle Assembling Technology. Journal of Bioactive and Compatible Polymers, 24**,** 249-265.

LI, S. J., YAN, Y. N., XIONG, Z., WENG, C. Y., ZHANG, R. J. & WANG, X. H. 2009b. Gradient Hydrogel Construct Based on an Improved Cell Assembling System. Journal of Bioactive and Compatible Polymers, 24**,** 84-99.

LIANG, J.-Z. 2004. A relationship between extrudate swell ratio and entry stored elastic strain energy during die flow of tyre compounds. Polymer Testing, 23**,** 441-446.

LIAO, K. 1994. PERFORMANCE CHARACTERIZATION AND MODELING OF A COMPOSITE HIP PROSTHESIS. Experimental Techniques, 18**,** 33-38.

LIN, C. Y., HSIAO, C. C., CHEN, P. Q. & HOLLISTER, S. J. 2004a. Interbody fusion cage design using integrated global layout and local microstructure topology optimization. Spine, 29**,** 1747-1754.

LIN, C. Y., KIKUCHI, N. & HOLLISTER, S. J. 2004b. A novel method for biomaterial scaffold internal architecture design to match bone elastic properties with desired porosity. Journal of Biomechanics, 37**,** 623-636.

LIN, T. W., CORVELLI, A. A., FRONDOZA, C. G., ROBERTS, J. C. & HUNGERFORD, D. S. 1997. Glass peek composite promotes proliferation and osteocalcin production of human osteoblastic cells. Journal of Biomedical Materials Research, 36**,** 137-144.

LIOU, F.W., 2007. Rapid prototyping and engineering applications: a toolbox for prototype development. Boca Raton, US: CRC Press.

LIU, H., LIU, J., LEU, M., LANDERS, R. & HUANG, T. 2013. Factors influencing paste extrusion pressure and liquid content of extrudate in freeze-form extrusion fabrication. The International Journal of Advanced Manufacturing Technology, 67**,** 899-906.

LIU, L., XIONG, Z., YAN, Y. N., ZHANG, R. J., WANG, X. H. & JIN, L. 2009a. Multinozzle Low-Temperature Deposition System for Construction of Gradient Tissue Engineering Scaffolds. Journal of Biomedical Materials Research Part B-Applied Biomaterials, 88B**,** 254-263.

LIU, L., XIONG, Z., ZHANG, R. J., JIN, L. & YAN, Y. N. 2009b. A Novel Osteochondral Scaffold Fabricated via Multi-nozzle Low-temperature Deposition Manufacturing. Journal of Bioactive and Compatible Polymers, 24**,** 18-30.

LU, T., WEN, J., QIAN, S., CAO, H., NING, C., PAN, X., et al. 2015. Enhanced osteointegration on tantalum-implanted polyetheretherketone surface with bone-like elastic modulus. Biomaterials, 51:173-83.

LU, X., CHEN, L., AMINI, N., YANG, S., EVANS, J. G. & GUO, Z. 2012a. Novel methods to fabricate macroporous 3D carbon scaffolds and ordered surface mesopores on carbon filaments. Journal of Porous Materials, 19**,** 529-536.

LU, X., LEE, Y., YANG, S., HAO, Y., EVANS, J. & PARINI, C. 2009a. Extrusion freeforming of millimeter wave electromagnetic bandgap (EBG) structures. Rapid prototyping journal, 15**,** 42 - 51.

LU, X., LEE, Y., YANG, S., HAO, Y., EVANS, J. R. G. & PARINI, C. G. 2009b. Extrusion freeforming of millimeter-wave electromagnetic bandgap (ebg) photonic crystals. Tsinghua Science and Technology, 14**,** 168-174.

LU, X., LEE, Y., YANG, S., HAO, Y., EVANS, J. R. G. & PARINI, C. G. 2009c. Fine lattice structures fabricated by extrusion freeforming: Process variables. Journal of Materials Processing Technology, 209**,** 4654-4661.

LU, X., LEE, Y., YANG, S., HAO, Y., EVANS, J. R. G. & PARINI, C. G. 2010. Solvent-based paste extrusion solid freeforming. Journal of the European Ceramic Society, 30**,** 1-10.

LU, X., LEE, Y., YANG, S., HAO, Y., UBIC, R., EVANS, J. R. G. & PARINI, C. G. 2008. Fabrication of electromagnetic crystals by extrusion freeforming. Metamaterials, 2**,** 36-44.

LU, X., LEE, Y., YANG, S., HAO, Y., UBIC, R., EVANS, J. R. G. & PARINI, C. G. 2009d. Fabrication of Millimeter-Wave Electromagnetic Bandgap Crystals Using Microwave Dielectric Powders. Journal of the American Ceramic Society, 92**,** 371-378.

LU, X. S., CHEN, L. F., AMINI, N., YANG, S. F., EVANS, J. R. G. & GUO, Z. X. 2012b. Novel methods to fabricate macroporous 3D carbon scaffolds and ordered surface mesopores on carbon filaments. Journal of Porous Materials, 19**,** 529-536.

LUO, H., XIONG, G., YANG, Z., RAMAN, S. R., LI, Q., MA, C., LI, D., WANG, Z. & WAN, Y. 2014. Preparation of three-dimensional braided carbon fiber-reinforced PEEK composites for potential load-bearing bone fixations. Part I. Mechanical properties and cytocompatibility. Journal of the Mechanical Behavior of Biomedical Materials, 29**,** 103-113.

MA, R., FANG, L., LUO, Z., WENG, L., SONG, S., ZHENG, R., SUN, H. & FU, H. 2014. Mechanical performance and in vivo bioactivity of functionally graded PEEK–HA biocomposite materials. Journal of Sol-Gel Science and Technology, 70**,** 339-345.

MA, R. & TANG, T. 2014. Current Strategies to Improve the Bioactivity of PEEK. International Journal of Molecular Sciences, 15**,** 5426.

MA, R., TANG, S., TAN, H., LIN, W., WANG, Y., WEI, J., et al. 2014b. Preparation, characterization, and in vitro osteoblast functions of a nano-hydroxyapatite/polyetheretherketone biocomposite as orthopedic implant material. International Journal of Nanomedicine, 9:3949—61.

MA, R., WENG, L., BAO, X., NI, Z., SONG, S. & CAI, W. 2012a. Characterization of in situ synthesized hydroxyapatite/polyetheretherketone composite materials. Materials Letters, 71**,** 117-119.

MA, R., WENG, L., BAO, X., SONG, S. & ZHANG, Y. 2013. In vivo biocompatibility and bioactivity of in situ synthesized hydroxyapatite/polyetheretherketone composite materials. Journal of Applied Polymer Science, 127**,** 2581-2587.

MA, R., WENG, L., FANG, L., LUO, Z. & SONG, S. 2012b. Structure and mechanical performance of in situ synthesized hydroxyapatite/polyetheretherketone nanocomposite materials. Journal of Sol-Gel Science and Technology, 62**,** 52-56.

MAHER, P. S., KEATCH, R. P., DONNELLY, K., MACKAY, R. E. & PAXTON, J. Z. 2009. Construction of 3D biological matrices using rapid prototyping technology. Rapid Prototyping Journal, 15**,** 204-210.

MANNING, A. 2012. Additive Manufacturing Used to Create First Laser-Sintered Cranial Implant Geometry. Advanced Materials & Processes, 170**,** 33-36.

MARIANI, M., ROSATINI, F., VOZZI, G., PREVITI, A. & AHLUWALIA, A. 2006. Characterization of tissue-engineered scaffolds microfabricated with PAM. Tissue Engineering, 12**,** 547-557.

MARTÍNEZ-VÁZQUEZ, F. J., PERERA, F. H., MIRANDA, P., PAJARES, A. & GUIBERTEAU, F. 2010. Improving the compressive strength of bioceramic robocast scaffolds by polymer infiltration. Acta Biomaterialia, 6**,** 4361-4368.

MASOOD, S. H. & SONG, W. Q. 2004. Development of new metal/polymer materials for rapid tooling using Fused deposition modelling. Materials & Design, 25**,** 587-594.

MATHIEU, L. M., BOURBAN, P. E. & MÅNSON, J. A. E. 2006. Processing of homogeneous ceramic/polymer blends for bioresorbable composites. Composites Science and Technology, 66**,** 1606-1614.

MAY, R. 2002. Polyetheretherketones. Encyclopedia of Polymer Science and Technology. John Wiley & Sons, Inc.

MELCHELS, F. P. W., DOMINGOS, M. A. N., KLEIN, T. J., MALDA, J., BARTOLO, P. J. & HUTMACHER, D. W. 2012. Additive manufacturing of tissues and organs. Progress in Polymer Science, 37**,** 1079-1104.

MICHNA, S., WU, W. & LEWIS, J. A. 2005. Concentrated hydroxyapatite inks for direct-write assembly of 3-D periodic scaffolds. Biomaterials, 26**,** 5632-5639.

MIRANDA, P., PAJARES, A., SAIZ, E., TOMSIA, A. P. & GUIBERTEAU, F. 2008. Mechanical properties of calcium phosphate scaffolds fabricated by robocasting. Journal of Biomedical Materials Research Part A, 85A**,** 218-227.

MIRANDA, P., SAIZ, E., GRYN, K. & TOMSIA, A. P. 2006. Sintering and robocasting of beta-tricalcium phosphate scaffolds for orthopaedic applications. Acta Biomaterialia, 2**,** 457-466.

MIRONOV, V., PRESTWICH, G. & FORGACS, G. 2007. Bioprinting living structures. Journal of Materials Chemistry, 17**,** 2054-2060.

MORONI, L., DE WIJN, J. R. & VAN BLITTERSWIJK, C. A. 2006. 3D fiber-deposited scaffolds for tissue engineering: Influence of pores geometry and architecture on dynamic mechanical properties. Biomaterials, 27**,** 974-985.

MORRISON, C., MACNAIR, R., MACDONALD, C., WYKMAN, A., GOLDIE, I. & GRANT, M. H. 1995. In vitro biocompatibility testing of polymers for orthopaedic implants using cultured fibroblasts and osteoblasts. Biomaterials, 16**,** 987-992.

MRSE, A. M. & PIGGOTT, M. R. 1993. Compressive properties of unidirectional carbon fibre laminates: II. The effects of unintentional and intentional fibre misalignments. Composites Science and Technology, 46**,** 219-227.

NANDAN, B., KANDPAL, L. D. & MATHUR, G. N. 2003. Poly(ether ether ketone)/poly(aryl ether sulfone) blends: Relationships between morphology and mechanical properties. Journal of Applied Polymer Science, 90**,** 2887-2905.

NGUYEN, K. T. & WEST, J. L. 2002. Photopolymerizable hydrogels for tissue engineering applications. Biomaterials, 23**,** 4307-4314.

NIEMINEN, T., KALLELA, I., WUOLIJOKI, E., KAINULAINEN, H., HIIDENHEIMO, I. & RANTALA, I. 2008. Amorphous and crystalline polyetheretherketone: Mechanical properties and tissue reactions during a 3-year follow-up. Journal of Biomedical Materials Research Part A, 84A**,** 377-383.

NOISET, O., SCHNEIDER, Y.-J. & MARCHAND-BRYNAERT, J. 2000. Adhesion and growth of CaCo2 cells on surface-modified PEEK substrata. Journal of Biomaterials Science, Polymer Edition, 11**,** 767-786.

NOROTTE, C., MARGA, F.S., NIKLASON, L.E., FORGACS, G., 2009. Scaffold-free vascular tissue engineering using bioprinting. Biomaterials, 30(30):5910-5917.

ÖHMAN, C., BALEANI, M., PANI, C., TADDEI, F., ALBERGHINI, M., VICECONTI, M. & MANFRINI, M. 2011. Compressive behaviour of child and adult cortical bone. Bone, 49**,** 769-776.

OREFFO, R.O., VIRDI, A.S., TRIFFITT, J.T. 1997. Modulation of osteogenesis and adipogenesis by human serum in human bone marrow cultures. Eur J Cell Biol, 74:251-61.

OXMAN, N., 2011. Variable property rapid prototyping. Virtual & Physical Prototyping, 6: 3-31

PAN, Y., SHEN, Q., CHEN, Y. 2013. Fabrication and characterisation of functional gradient hydroxyapatite reinforced poly (ether ether ketone) biocomposites. Micro & Nano Letters, 8:357-61.

PARK, S., PARK, D., SHIN, J., KANG, Y., KIM, H., YOON, T. & SHIN, J.-W. 2012. Scaffolds for bone tissue engineering fabricated from two different materials by the rapid prototyping technique: PCL versus PLGA. Journal of Materials Science: Materials in Medicine, 23**,** 2671-2678.

PARKER, S. T., DOMACHUK, P., AMSDEN, J., BRESSNER, J., LEWIS, J. A., KAPLAN, D. L. & OMENETTO, F. G. 2009. Biocompatible Silk Printed Optical Waveguides. Advanced Materials, 21**,** 2411-+.

PETILLO, O., PELUSO, G., AMBROSIO, L., NICOLAIS, L., KAO, W. J. & ANDERSON, J. M. 1994. In vivo induction of macrophage Ia antigen (MHC class II) expression by biomedical polymers in the cage implant system. Journal of Biomedical Materials Research, 28**,** 635-646.

PETROVIC, L., POHLE, D., MÜNSTEDT, H., RECHTENWALD, T., SCHLEGEL, K. A. & RUPPRECHT, S. 2006. Effect of βTCP filled polyetheretherketone on osteoblast cell proliferation in vitro. Journal of Biomedical Science, 13**,** 41-46.

PFISTER, A., LANDERS, R., LAIB, A., HUBNER, U., SCHMELZEISEN, R. & MULHAUPT, R. 2004. Biofunctional rapid prototyping for tissue-engineering applications: 3D bioplotting versus 3D printing. Journal of Polymer Science Part a-Polymer Chemistry, 42**,** 624-638.

PHAM, D.T. AND DIMOV, S.S., 2000. Rapid manufacturing - Technologies for rapid prototyping and tooling. London: Springer-Verlag.

POHLE, D., PONADER, S., RECHTENWALD, T., SCHMIDT, M., SCHLEGEL, K. A., MÜNSTEDT, H., NEUKAM, F. W., NKENKE, E. & VON WILMOWSKY, C. 2007. Processing of Three-Dimensional Laser Sintered Polyetheretherketone Composites and Testing of Osteoblast Proliferation in vitro. Macromolecular Symposia, 253**,** 65-70.

POWELL, J., ASSABUMRUNGRAT, S. & BLACKBURN, S. 2013. Design of ceramic paste formulations for co-extrusion. Powder Technology, 245**,** 21-27.

RAE, P. J., BROWN, E. N. & ORLER, E. B. 2007. The mechanical properties of poly(ether-ether-ketone) (PEEK) with emphasis on the large compressive strain response. Polymer, 48**,** 598-615.

RAO, P.J., PELLETIER, M.H., WALSH, W.R., MOBBS, R.J. 2014. Spine Interbody Implants: Material Selection and Modification, Functionalization and Bioactivation of Surfaces to Improve Osseointegration. Orthopaedic Surgery, 6:81-9.

RASHEVA, Z., ZHANG, G. & BURKHART, T. 2010. A correlation between the tribological and mechanical properties of short carbon fibers reinforced PEEK materials with different fiber orientations. Tribology International, 43**,** 1430-1437.

RIVARD, C.-H., RHALMI, S. & COILLARD, C. 2002. In vivo biocompatibility testing of peek polymer for a spinal implant system: A study in rabbits. Journal of Biomedical Materials Research, 62**,** 488-498.

ROEDER, R. K. & CONRAD, T. L. 2012. Chapter 11 - Bioactive Polyaryletherketone Composites. In: KURTZ, S. M. (ed.) PEEK Biomaterials Handbook. Oxford: William Andrew Publishing.

ROUGH, S. L., BRIDGWATER, J. & WILSON, D. I. 2000. Effects of liquid phase migration on extrusion of microcrystalline cellulose pastes. International Journal of Pharmaceutics, 204**,** 117-126.

ROUGH, S. L., WILSON, D. I. & BRIDGWATER, J. 2002. A Model Describing Liquid Phase Migration Within an Extruding Microcrystalline Cellulose Paste. Chemical Engineering Research and Design, 80**,** 701-714.

RUST-DAWICKI, A. M. & COOK, S. D. Preliminary evaluation of titanium-coated PEEK implants. Biomedical Engineering Conference, 1995., Proceedings of the 1995 Fourteenth Southern, 7-9 Apr 1995 1995. 75-77.

SACHLOS, E. & CZERNUSZKA, J. T. 2003. Making tissue engineering scaffolds work: Review on the application of solid freeform fabrication technology to the production of tissue engineering scaffolds. European Cells & Materials, 5**,** 29-40.

SAGOMONYANTS, K. B., JARMAN-SMITH, M. L., DEVINE, J. N., ARONOW, M. S. & GRONOWICZ, G. A. 2008. The in vitro response of human osteoblasts to polyetheretherketone (PEEK) substrates compared to commercially pure titanium. Biomaterials, 29**,** 1563-1572.

SCHIELE, N. R., KOPPES, R. A., CORR, D. T., ELLISON, K. S., THOMPSON, D. M., LIGON, L. A., LIPPERT, T. K. M. & CHRISEY, D. B. 2009. Laser direct writing of combinatorial libraries of idealized cellular constructs: Biomedical applications. Applied Surface Science, 255**,** 5444-5447.

SHIM, J. H., LEE, J-S., KIM, J. Y., CHO, D-w. 2012. Bioprinting of a mechanically enhanced three-dimensional dual cell-laden construct for osteochondral tissue engineering using a multi-head tissue/organ building system. Journal of Micromechanics and Microengineering, 22, 085014.

SCHMIDT, M., POHLE, D. & RECHTENWALD, T. 2007. Selective Laser Sintering of PEEK. CIRP Annals - Manufacturing Technology, 56**,** 205-208.

SCHRÖDER, K., MEYER-PLATH, A., KELLER, D. & OHL, A. 2002. On the Applicability of Plasma Assisted Chemical Micropatterning to Different Polymeric Biomaterials. Plasmas and Polymers, 7**,** 103-125.

SCHUURMAN, W., KHRISTOV, V., POT, M. W., VAN WEEREN, P. R., DHERT, W. J. A. & MALDA, J. 2011. Bioprinting of hybrid tissue constructs with tailorable mechanical properties. Biofabrication, 3**,** 021001.

SEOL, Y.-J., PARK, D. Y., PARK, J. Y., KIM, S. W., PARK, S. J. & CHO, D.-W. 2013. A new method of fabricating robust freeform 3D ceramic scaffolds for bone tissue regeneration. Biotechnology and Bioengineering, 110**,** 1444-1455.

SERRA, T., PLANELL, J. A. & NAVARRO, M. 2013. High-resolution PLA-based composite scaffolds via 3-D printing technology. Acta Biomaterialia, 9**,** 5521-5530.

SHEPHERD, J. N. H., PARKER, S. T., SHEPHERD, R. F., GILLETTE, M. U., LEWIS, J. A. & NUZZO, R. G. 2011. 3D Microperiodic Hydrogel Scaffolds for Robust Neuronal Cultures. Advanced Functional Materials, 21**,** 47-54.

SHOR, L., GUCERI, S., CHANG, R., GORDON, J., KANG, Q., HARTSOCK, L., AN, Y. H. & SUN, W. 2009. Precision extruding deposition (PED) fabrication of polycaprolactone (PCL) scaffolds for bone tissue engineering. Biofabrication, 1.

SHOR, L., GUCERI, S., WEN, X. J., GANDHI, M. & SUN, W. 2007. Fabrication of three-dimensional polycaprolactone/hydroxyapatite tissue scaffolds and osteoblast-scaffold interactions in vitro. Biomaterials, 28**,** 5291-5297.

SIGMUND, O. 1994. MATERIALS WITH PRESCRIBED CONSTITUTIVE PARAMETERS - AN INVERSE HOMOGENIZATION PROBLEM. International Journal of Solids and Structures, 31**,** 2313-2329.

SIMON, J. L., MICHNA, S., LEWIS, J. A., REKOW, E. D., THOMPSON, V. P., SMAY, J. E., YAMPOLSKY, A., PARSONS, J. R. & RICCI, J. L. 2007. In vivo bone response to 3D periodic hydroxyapatite scaffolds assembled by direct ink writing. Journal of Biomedical Materials Research Part A, 83A**,** 747-758.

SMAY, J. E., GRATSON, G. M., SHEPHERD, R. F., CESARANO, J. & LEWIS, J. A. 2002. Directed colloidal assembly of 3D periodic structures. Advanced Materials, 14**,** 1279-+.

SPIERINGS, A. B., SCHNEIDER, M. & EGGENBERGER, R. 2011. Comparison of density measurement techniques for additive manufactured metallic parts. Rapid Prototyping Journal, 17**,** 380-386.

STUCKER, B., 2011. Additive manufacturing technologies: technology introduction and business implications. In: Frontiers of Engineering: Reports on Leading-Edge Engineering from the 2011 Symposium The National Academies press, US, pp. 5-14.

SUN, L., PARKER, S. T., SYOJI, D., WANG, X., LEWIS, J. A. & KAPLAN, D. L. 2012. Direct-Write Assembly of 3D Silk/Hydroxyapatite Scaffolds for Bone Co-Cultures. Advanced Healthcare Materials, 1**,** 729-735.

SUNG‐HOON, A., MICHAEL, M., DAN, O., SHAD, R. & PAUL, K. W. 2002. Anisotropic material properties of fused deposition modeling ABS. Rapid Prototyping Journal, 8, 248-257.

SUTERA, S. P. & SKALAK, R. 1993. The History of Poiseuille's Law. Annual Review of Fluid Mechanics, 25**,** 1-20.

TAI, N. H., MA, C. C. M. & WU, S. H. 1995. Fatigue behaviour of carbon fibre/PEEK laminate composites. Composites, 26**,** 551-559.

TAN, K. H., CHUA, C. K., LEONG, K. F., CHEAH, C. M., CHEANG, P., ABU BAKAR, M. S. & CHA, S. W. 2003. Scaffold development using selective laser sintering of polyetheretherketone–hydroxyapatite biocomposite blends. Biomaterials, 24**,** 3115-3123.

TAN, K. H., CHUA, C. K., LEONG, K. F., CHEAH, C. M., GUI, W. S., TAN, W. S. & WIRIA, F. E. 2005a. Selective laser sintering of biocompatible polymers for applications in tissue engineering. Bio-Medical Materials and Engineering, 15**,** 113-124.

TAN, K. H., CHUA, C. K., LEONG, K. F., NAING, M. W. & CHEAH, C. M. 2005b. Fabrication and characterization of three-dimensional poly(ether-ether-ketone)/-hydroxyapatite biocomposite scaffolds using laser sintering. Proceedings of the Institution of Mechanical Engineers, Part H: Journal of Engineering in Medicine, 219**,** 183-194.

TANG, S. M., CHEANG, P., ABUBAKAR, M. S., KHOR, K. A. & LIAO, K. 2004. Tension–tension fatigue behavior of hydroxyapatite reinforced polyetheretherketone composites. International Journal of Fatigue, 26**,** 49-57.

TANNER, R. I. 1970. A theory of die-swell. Journal of Polymer Science Part A-2: Polymer Physics, 8**,** 2067-2078.

TARTARISCO, G., GALLONE, G., CARPI, F. & VOZZI, G. 2009. Polyurethane unimorph bender microfabricated with Pressure Assisted Microsyringe (PAM) for biomedical applications. Materials Science & Engineering C-Materials for Biological Applications, 29**,** 1835-1841.

TAY, B.Y., EVANS, J.R.G., AND EDIRISINGHE, M.J., 2003. Solid freeform fabrication of ceramics. International Materials Reviews, 48, 341-370.

TELLIS, B. C., SZIVEK, J. A., BLISS, C. L., MARGOLIS, D. S., VAIDYANATHAN, R. K. & CALVERT, P. 2008. Trabecular scaffolds created using micro CT guided fused deposition modeling. Materials Science & Engineering C-Biomimetic and Supramolecular Systems, 28**,** 171-178.

TIRELLA, A., DE MARIA, C., CRISCENTI, G., VOZZI, G. & AHLUWALIA, A. 2012. The PAM(2) system: a multilevel approach for fabrication of complex three-dimensional microstructures. Rapid Prototyping Journal, 18**,** 299-307.

TIRELLA, A., ORSINI, A., VOZZI, G. & AHLUWALIA, A. 2009. A phase diagram for microfabrication of geometrically controlled hydrogel scaffolds. Biofabrication, 1.

TIRELLA, A., VOZZI, G. & AHLUWALIA, A. 2008. Biomimicry of PAM Microfabricated Hydrogel Scaffold, Springfield, Soc Imaging Science & Technology.

TOTH, J. M., WANG, M., ESTES, B. T., SCIFERT, J. L., SEIM III, H. B. & TURNER, A. S. 2006. Polyetheretherketone as a biomaterial for spinal applications. Biomaterials, 27**,** 324-334.

VACCARO, A. R. 2002. The role of the osteoconductive scaffold in synthetic bone graft. Orthopedics, 25**,** S571.

VAEZI, M., CHIANRABUTRA, S., MELLOR, B. & YANG, S. 2013a. Multiple material additive manufacturing – Part 1: a review. Virtual and Physical Prototyping, 8**,** 19-50.

VAEZI, M., SEITZ, H. & YANG, S. 2013b. A review on 3D micro-additive manufacturing technologies. The International Journal of Advanced Manufacturing Technology, 67**,** 1721-1754.

VAEZI, M. & YANG, S. 2014. 2 - Freeform fabrication of nanobiomaterials using 3D printing. In: NARAYAN, R. (ed.) Rapid Prototyping of Biomaterials. Woodhead Publishing.

VAEZI, M. & YANG, S. F. 2015. A novel bioactive PEEK/HA composite with controlled 3D interconnected HA network. International Journal of Bioprinting, 1, 66-76.

VALENTAN, B., KADIVNIK, Z., BRAJLIH, T., ANDERSON, A. & DRSTVEN{EK, I. 2013. Processing Poly(Ether Etherketone) On A 3d Printer For Thermoplastic Modelling. Materials and technology, 47, 715–721.

VAN CLEYNENBREUGEL, T., VAN OOSTERWYCK, H., VANDER SLOTEN, J. & SCHROOTEN, J. 2002. Trabecular bone scaffolding using a biomimetic approach. Journal of Materials Science-Materials in Medicine, 13**,** 1245-1249.

VON WILMOWSKY, C., VAIRAKTARIS, E., POHLE, D., RECHTENWALD, T., LUTZ, R., MÜNSTEDT, H., KOLLER, G., SCHMIDT, M., NEUKAM, F. W., SCHLEGEL, K. A. & NKENKE, E. 2008. Effects of bioactive glass and β-TCP containing three-dimensional laser sintered polyetheretherketone composites on osteoblasts in vitro. Journal of Biomedical Materials Research Part A, 87A**,** 896-902.

VOZZI, G. & AHLUWALIA, A. 2007. Microfabrication for tissue engineering: rethinking the cells-on-a scaffold approach. Journal of Materials Chemistry, 17**,** 1248-1254.

VOZZI, G., FLAIM, C., AHLUWALIA, A. & BHATIA, S. 2003. Fabrication of PLGA scaffolds using soft lithography and microsyringe deposition. Biomaterials, 24**,** 2533-2540.

VOZZI, G., FLAIM, C. J., BIANCHI, F., AHLUWALIA, A. & BHATIA, S. 2002. Microfabricated PLGA scaffolds: a comparative study for application to tissue engineering. Materials Science & Engineering C-Biomimetic and Supramolecular Systems, 20**,** 43-47.

VOZZI, G., PREVITI, A., CIARAVELLA, G. & AHLUWALIA, A. 2004. Microfabricated fractal branching networks. Journal of Biomedical Materials Research Part A, 71A**,** 326-333.

WAKE, M. C., PATRICK, C. W. & MIKOS, A. G. 1994. PORE MORPHOLOGY EFFECTS ON THE FIBROVASCULAR TISSUE-GROWTH IN POROUS POLYMER SUBSTRATES. Cell Transplantation, 3**,** 339-343.

WAKELIN, E.A., KONDYURIN, A.V., WISE, S.G., MCKENZIE, D.R., DAVIES, M.J., BILEK, M. 2015. Bio-Activation of Polyether Ether Ketone Using Plasma Immersion Ion Implantation: A Kinetic Model. Plasma Processes and Polymers, 12:180-93.

WANG, A., LIN, R., STARK, C. & DUMBLETON, J. H. 1999. Suitability and limitations of carbon fiber reinforced PEEK composites as bearing surfaces for total joint replacements. Wear, 225–229, Part 2**,** 724-727.

WANG, F., SHOR, L., DARLING, A., KHALIL, S., SUN, W., GUCERI, S. & LAU, A. 2004. Precision extruding deposition and characterization of cellular poly-epsilon-caprolactone tissue scaffolds. Rapid Prototyping Journal, 10**,** 42-49.

WANG, L., WENG, L., SONG, S. & SUN, Q. 2010. Mechanical properties and microstructure of polyetheretherketone–hydroxyapatite nanocomposite materials. Materials Letters, 64**,** 2201-2204.

WANG, H., XU, M., ZHANG, W., KWOK, D.T.K., JIANG, J., WU, Z., et al. 2010b. Mechanical and biological characteristics of diamond-like carbon coated poly aryl-ether-ether-ketone. Biomaterials, 31:8181-7.

WANG, L., WENG, L., SONG, S., ZHANG, Z., TIAN, S. & MA, R. 2011. Characterization of polyetheretherketone–hydroxyapatite nanocomposite materials. Materials Science and Engineering: A, 528**,** 3689-3696.

WIEDING, J., JONITZ, A., BADER, R. 2012. The Effect of Structural Design on Mechanical Properties and Cellular Response of Additive Manufactured Titanium Scaffolds. Materials, 5:1336.

WENZ, L. M., MERRITT, K., BROWN, S. A., MOET, A. & STEFFEE, A. D. 1990. In vitro biocompatibility of polyetheretherketone and polysulfone composites. Journal of Biomedical Materials Research, 24**,** 207-215.

WOHLERS, T. 2015. Wohlers report 2015: Additive manufacturing and 3D printing, state of the industry. Colorado, USA: Wohlers Associates.

WONG, K. L., WONG, C. T., LIU, W. C., PAN, H. B., FONG, M. K., LAM, W. M., CHEUNG, W. L., TANG, W. M., CHIU, K. Y., LUK, K. D. K. & LU, W. W. 2009. Mechanical properties and in vitro response

of strontium-containing hydroxyapatite/polyetheretherketone composites. Biomaterials, 30**,** 3810-3817.

WOODFIELD, T. B. F., MALDA, J., DE WIJN, J., PETERS, F., RIESLE, J. & VAN BLITTERSWIJK, C. A. 2004. Design of porous scaffolds for cartilage tissue engineering using a three-dimensional fiber-deposition technique. Biomaterials, 25**,** 4149-4161.

WU, X., LIU, X., WEI, J., MA, J., DENG, F., WEI, S. 2012. Nano-TiO2/PEEK bioactive composite as a bone substitute material: in vitro and in vivo studies. International Journal of Nanomedicine, 7:1215—25.

XIONG, Z., YAN, Y., WANG, S., ZHANG, R. & ZHANG, C. 2002a. Fabrication of porous scaffolds for bone tissue engineering via low-temperature deposition. Scripta Materialia, 46**,** 771-776.

XIONG, Z., YAN, Y. N., WANG, S. G., ZHANG, R. J. & ZHANG, C. 2002b. Fabrication of porous scaffolds for bone tissue engineering via low-temperature deposition. Scripta Materialia, 46**,** 771-776.

XIONG, Z., YAN, Y. N., ZHANG, R. J. & SUN, L. 2001. Fabrication of porous poly(L-lactic acid) scaffolds for bone tissue engineering via precise extrusion. Scripta Materialia, 45**,** 773-779.

XU, A., LIU, X., GAO, X., DENG, F., DENG, Y., WEI, S. 2015. Enhancement of osteogenesis on micro/nano-topographical carbon fiber-reinforced polyetheretherketone–nanohydroxyapatite biocomposite. Materials Science and Engineering: C, 48:592-8.

XUESONG, L., YOONJAE, L., SHOUFENG, Y., YANG, H., EVANS, J. R. G. & PARINI, C. G. 2009. Fine lattice structures fabricated by extrusion freeforming: process variables. Journal of Materials Processing Technology, 209**,** 4654-46614661.

XUESONG, L., YOONJAE, L., SHOUFENG, Y., YANG, H., EVANS, J. R. G. & PARINI, C. G. 2010. Solvent-based paste extrusion solid freeforming. Journal of the European Ceramic Society, 30**,** 1-1010.

YAMADA, A., NIIKURA, F. & IKUTA, K. 2008. A three-dimensional microfabrication system for biodegradable polymers with high resolution and biocompatibility. Journal of Micromechanics and Microengineering, 18**,** 025035.

YANG, H., YANG, S., CHI, X. & EVANS, J. R. G. 2006. Fine ceramic lattices prepared by extrusion freeforming. Journal of Biomedical Materials Research Part B: Applied Biomaterials, 79B**,** 116-121.

YANG, H. Y., CHI, X. P., YANG, S. & EVANS, J. R. G. 2010. Mechanical strength of extrusion freeformed calcium phosphate filaments. Journal of Materials Science: Materials in Medicine, 21**,** 1503-1510.

YANG, H. Y., THOMPSON, I., YANG, S. F., CHI, X. P., EVANS, J. R. G. & COOK, R. J. 2008a. Dissolution characteristics of extrusion freeformed hydroxyapatite-tricalcium phosphate scaffolds. Journal of Materials Science-Materials in Medicine, 19**,** 3345-3353.

YANG, H. Y., YANG, S. F., CHI, X. P., EVANS, J. R. G., THOMPSON, I., COOK, R. J. & ROBINSON, P. 2008b. Sintering behaviour of calcium phosphate filaments for use as hard tissue scaffolds. Journal of the European Ceramic Society, 28**,** 159-167.

YANG, S., YANG, H., CHI, X., EVANS, J. R. G., THOMPSON, I., COOK, R. J. & ROBINSON, P. 2008c. Rapid prototyping of ceramic lattices for hard tissue scaffolds. Materials & Design, 29**,** 1802-1809.

YANG, S. F., HONGYI, Y., XIAOPENG, C., EVANS, J. R. G., THOMPSON, I., COOK, R. J. & ROBINSON, P. 2008d. Rapid prototyping of ceramic lattices for hard tissue scaffolds. Materials & Design, 29**,** 1802-18091809.

YANG, S. F., LEONG, K. F., DU, Z. H. & CHUA, C. K. 2001. The design of scaffolds for use in tissue engineering. Part 1. Traditional factors. Tissue Engineering, 7**,** 679-689.

YONGNIAN, Y., ZHUO, X., YUNYU, H., SHENGUO, W., RENJI, Z. & CHAO, Z. 2003. Layered manufacturing of tissue engineering scaffolds via multi-nozzle deposition. Materials Letters, 57**,** 2623-26282628.

YU, S., HARIRAM, K. P., KUMAR, R., CHEANG, P. & AIK, K. K. 2005. In vitro apatite formation and its growth kinetics on hydroxyapatite/polyetheretherketone biocomposites. Biomaterials, 26**,** 2343-2352.

ZEIN, I., HUTMACHER, D. W., TAN, K. C. & TEOH, S. H. 2002. Fused deposition modeling of novel scaffold architectures for tissue engineering applications. Biomaterials, 23**,** 1169-1185.

ZHANG, Y., HAO, L., SAVALANI, M. M., HARRIS, R. A., DI SILVIO, L. & TANNER, K. E. 2009. In vitro biocompatibility of hydroxyapatite-reinforced polymeric composites manufactured by selective laser sintering. Journal of Biomedical Materials Research Part A, 91A**,** 1018-1027.

ZHUO, X., YONGNIAN, Y., SHENGUO, W., RENJI, Z. & CHAO, Z. 2002. Fabrication of porous scaffolds for bone tissue engineering via low-temperature deposition. Scripta Materialia, 46**,** 771-776776.

ZIEMIAN, C., SHARMA, M. & ZIEMIAN, S. 2012. Anisotropic Mechanical Properties of ABS Parts Fabricated by Fused Deposition Modelling. In: GOKCEK, M. (ed.) Mechanical Engineering.